

This file is part of the following work:

**Madanayaka, Thushara Asela (2018) *Method of fragments (MoF) solutions for double-walled, circular and rectangular cofferdam seepage problems*. PhD Thesis, James Cook University.**

Access to this file is available from:

<https://doi.org/10.25903/5c99693025545>

Copyright © 2018 Thushara Asela Madanayaka

The author has certified to JCU that they have made a reasonable effort to gain permission and acknowledge the owners of any third party copyright material included in this document. If you believe that this is not the case, please email

[researchonline@jcu.edu.au](mailto:researchonline@jcu.edu.au)

**Method of fragments (MoF) solutions for  
double-walled, circular and rectangular cofferdam  
seepage problems**

By

Thushara Asela Madanayaka BSc (Eng) Hons, M.Eng.

This thesis submitted for the  
Degree of Doctor of Philosophy  
(Geotechnical Engineering)

College of Science and Engineering  
James Cook University

December 2018

## STATEMENT OF ACCESS

I, the undersigned, the author of this thesis, understand that James Cook University will make it available for use within the University Library and, by microfilm or other means, allow access to users in other approved libraries.

All users consulting this thesis will have to sign the following statement:

In consulting this thesis, I agree not to copy or closely paraphrase it in whole or in part without the written consent of the author; and to make proper public written acknowledgement for any assistance which I have obtained from it.

Beyond this, I do not wish to place any restriction on access to this thesis.

.....

Signature

.....

Date

## STATEMENT OF SOURCES

### DECLARATION

I declare that this thesis is my own work and has not been submitted in any form of another degree or diploma at any university or other institution of tertiary education. Information derived from the published or unpublished work of others has been acknowledged in the text and a list of references is given.

.....

Signature

.....

Date

### DECLARATION – ELECTRONIC COPY

I, the undersigned, the author of this work, declare that to the best of my knowledge, the electronic copy of this thesis submitted to the library at James Cook University is an accurate copy of the printed thesis submitted.

.....

Signature

.....

Date

## **STATEMENT OF CONTRIBUTION OF OTHERS**

- Grants** : This research work was supported by the scholarship (JCU PRS) and research grants (to participate international conferences) of Graduate Research School of James Cook University (JCU), and also, Doctoral Completion Grant provided by the College of Science and Engineering of JCU.
- Supervision** : A/Prof. Nagaratnam Sivakugan was the primary supervisor (JCU) for this Ph.D. and the additional supervision was provided by Dr. Peter To (JCU).
- Editorial Assistance** : The editorial assistance for both thesis and research articles (journal and conference) was provided by the A/Prof. Nagaratnam Sivakugan and Dr. Peter To. Also, Dr. Jay Ameratunga (Principal Geotechnical Engineer at Golder Associates) provided the editorial assistance for the conference article published in 19th International Conference on Soil Mechanics and Geotechnical Engineering (ICSMGE 2017) held in Seoul, South Korea.

## ACKNOWLEDGEMENTS

Firstly, I would like to express my sincere gratitude to my primary supervisor Prof. Nagaratnam Sivakugan for the continuous advice and support of my Ph.D., for his patience, motivation, and immense knowledge. His invaluable guidance helped me in all the time of research and writing of this thesis. Thank you, Prof. Siva, without your untiring efforts and guidance, my Ph.D. research would not have been a success.

Besides my primary supervisor, I would like to thank my secondary supervisor Dr. Peter To for his insightful comments and encouragement. Also, my sincere thank is to Dr. Jay Ameratunga (Principal Geotechnical Engineer at Golder Associates) for his kind advises.

My sincere thanks also go to Mr. Warren O'Donnell (Former geomechanics laboratory manager) and current laboratory managers Mr. Shaun Robinson and Mr. Troy Poole for providing laboratory and research facilities and for their guidance. I thank my university colleagues and all the staff of College of Science and Engineering for their constant support. In particular, I am grateful to Mrs. Norton Melissa for her priceless assistance.

In addition, I wish to acknowledge the Graduate Research School (GRS) providing me the scholarship, the living stipend, and GRS grants (for international conference participations) during my candidature. Also, my sincere gratitude to College of Science and Engineering for providing financial support (Student Support Allocation) and Doctoral Completion Grant.

Last but not the least, I would like to thank my family: my beloved wife, Sajee, my son, Akein, my mother and my sister for supporting me spiritually throughout during my Ph.D. studies and my life.

*To my family and teachers*

## ABSTRACT

Cofferdams are temporary structures used in construction sites. Long-narrow (double-walled), circular, square and rectangular are the commonly seen cofferdam shapes, and flow rate and maximum exit hydraulic gradient are two of the main design parameters required. Commonly, these are evaluated through the 2D ground water flow model solved using flow nets or numerical methods. However, when the flow pattern is 3D, such as flow into the square or rectangular cofferdams, predictions by the 2D models underestimate the flow rate and maximum exit hydraulic gradient values considerably.

Method of fragment (MoF) is an approximate technique which can be used for quick estimates of the flow rate and maximum exit hydraulic gradient values for double-walled cofferdams. The accuracy of the MoF solutions depends on the validity of the assumption that the equipotential line at the tip of the cut-off wall is vertical, dividing the flow domain into two fragments. In this research, validity of this assumption was assessed through the extensive numerical simulations, and it was found that, MoF predictions are within acceptable limits, and the effect of deviating from the assumption is always onto the conservative side. Further, MoF was extended to solve circular cofferdam problems, defining two new axisymmetric fragment types. Through a range of numerical simulations, design charts were developed to obtain the required axisymmetric form factors and normalised exit hydraulic gradient values. These were validated against detailed numerical solutions, analytical solutions, and experimental results reported in the literature. Also, a small-scale laboratory model was developed for analysing the circular cofferdam, and using that, series of tests were carried out. Then, the experimental results were compared against solutions derived using the proposed MoF solutions and showed a good agreement. Further, simple analytical expressions were developed and validated for the

form factors and normalised exit gradient estimations of both double-walled and circular cofferdams enabling quicker computations and the MoF be implemented in spreadsheets.

In addition, a simple method for evaluating the cofferdam safety against possible piping failure is presented. Through a series of finite element simulations, simple expressions were developed and validated to estimate the maximum exit hydraulic gradient for both double-walled and circular cofferdams considering only the shortest seepage path, known as creep length. The proposed solutions, including mean, lower and upper bound values for the exit hydraulic gradient at a given creep length can be applied in both isotropic and anisotropic soil conditions. Using them, a first-order estimate of the required creep length to limit the exit hydraulic gradient to a specific value can be determined. Alternatively, for a given configuration of the cofferdam, the exit hydraulic gradient can also be estimated. These equations can be valuable tools for back-of-the-envelope calculations in the preliminary analysis while selecting the dimensions in a cofferdam.

Furthermore, simple expressions were developed and validated for accurately estimating the flow rate and maximum exit hydraulic gradient values of square and rectangular cofferdams founding on an isotropic and homogeneous soil medium. However, when the soil medium is anisotropic and homogeneous, proposed solutions are still applicable with a reasonable level of accuracy. In the proposed solutions, the 3D flow effects of square and rectangular cofferdams have been incorporated through the correction factors. Suggestions are made to improve the expressions given in the Canadian Foundation Engineering Manual, widely used in practice.

The solutions proposed in this research can be very useful as a design tool in providing realistic first estimates of the flow rate and maximum exit hydraulic gradients of cofferdams, especially in preliminary assessments and for carrying out parametric studies, before going for a detailed analysis.

## LIST OF PUBLICATIONS

### Book

1. Madanayaka, T. A., and Sivakugan, N. Confined Flow Through Soils: The Method of Fragments Approach. CRC Press (*draft in progress*).

### Journal Articles

1. Madanayaka, T. A., and Sivakugan, N. (2016). Approximate equations for the method of fragment. *International Journal of Geotechnical Engineering*, 10(3), 297-303.
2. Madanayaka, T. A., and Sivakugan, N. (2017). Adaptation of Method of Fragments to Axisymmetric Cofferdam Seepage Problem. *International Journal of Geomechanics, ASCE* (9), doi: 10.1061/(ASCE)GM.1943-5622.0000955.
3. Madanayaka, T. A., and Sivakugan, N. (2018). Simple solutions for square and rectangular cofferdam seepage problems. *Canadian Geotechnical Journal* (*In print*).
4. Madanayaka, T. A., and Sivakugan, N. (2017) “ Validity of the method of fragments for seepage analysis in circular cofferdams” *Geotechnical & Geological Engineering*, (*Under the second review*).
5. Madanayaka, T. A., and Sivakugan, N. “ Relationship between minimum creep length and exit gradient in cofferdams ” *Geotechnical & Geological Engineering*, (*draft ready for submission*).

## **Refereed conference proceedings**

1. Madanayaka, T., and Sivakugan, N. (2016) Simplified method of fragments based two dimensional seepage solution for the double-wall cofferdam. *Proc., 19th Southeast Asian Geotechnical Conference*, 1047-1051, 31 May-03 June 2016, Kuala Lumpur, Malaysia.
2. Madanayaka, T., Sivakugan, N., Ameratunga J (2017) Validity of the method of fragments for seepage analysis in double-wall cofferdams. *Proc., 19th International Conference on Soil Mechanics and Geotechnical Engineering*, 2921-2924, 18-22, September 2017, Seoul, South Korea.

## Table of Contents

Statement of Access	ii
Statement of Sources	iii
Statement of Contribution of Others	iv
Acknowledgements	v
Abstract	vii
List of Publications	x
Table of Contents	xii
List of Figures	xix
List of Tables	xxvi
CHAPTER 1 INTRODUCTION	1
1.1 General	1
1.2 Cofferdams	2
1.3 Current State-of-the-Art	6
1.4 Objectives and scope of research	7
1.5 Relevance of the research	8
1.6 Thesis overview	9
CHAPTER 2 LITERATURE REVIEW	12
2.1 Overview	12
2.2 Soil permeability	12
2.2.1 Factors affecting the soil permeability	13
2.2.2 Laboratory determination of soil permeability	14
2.2.3 Empirical relations for soil permeability	17
	xii

2.2.4	Permeability anisotropy	19
2.3	Darcy' law and range of validity	22
2.3.1	Reynolds number	23
2.3.2	Laboratory study on Reynolds number	25
2.4	Hydraulic failure mechanisms of cofferdams	32
2.4.1	Piping failure mechanism	32
2.4.2	Heaving failure mechanism	33
2.4.3	Critical failure mechanism	34
2.5	Seepage solution methods for cofferdams	35
2.5.1	Seepage solution methods for double-walled cofferdams	36
2.5.2	Seepage solution methods for circular cofferdams	41
2.5.3	Seepage solution methods for square and rectangular cofferdams	44
2.5.4	Design charts	46
2.5.5	Method of fragments (MoF)	47
2.6	Summary and conclusions	52

## CHAPTER 3 VALIDITY OF METHOD OF FRAGMENTS (MOF) SOLUTIONS

	FOR DOUBLE- WALLED COFFERDAMS	53
3.1	Introduction	53
3.2	Method of fragments (MoF) solutions for double-walled cofferdams	53
3.2.1	Flow rate $q$ estimation	55
3.2.2	Exit hydraulic gradient $i_E$ estimation	56
3.3	Accuracy of MoF solutions for double-walled cofferdams	56
3.3.1	Numerical modeling of double-walled cofferdams	57
3.3.2	Sensitivity analysis and model validation	59

3.3.3	Accuracy assessment of the MoF solutions	60
3.3.4	Effects of assumption deviation on the seepage solutions	63
3.4	Expressions for form factors and exit gradient estimations	66
3.4.1	Expressions for fragment type <i>C</i>	66
3.4.2	Expression for fragment type <i>A</i>	71
3.4.3	Validation of proposed form factors and exit hydraulic gradient expressions	73
3.5	Summary and conclusions	73
CHAPTER 4 METHOD OF FRAGMENTS (MOF) SOLUTIONS FOR CIRCULAR COFFERDAM SEEPAGE PROBLEMS		76
4.1	Introduction	76
4.2	Numerical simulation of circular cofferdams	76
4.2.1	Axisymmetric numerical model validation	77
4.3	Flow net solutions for circular cofferdams	81
4.4	Adaptability of method of fragments (MoF) solutions for circular cofferdams	85
4.4.1	Validity assessment of the assumption for equipotential line behaviour	86
4.5	Development of method of fragments (MoF) for circular cofferdams	88
4.5.1	Development of design charts required for axisymmetric MoF solution	89
4.6	Validation of MoF solutions for circular cofferdams	94
4.6.1	Comparison against finite element solutions	95
4.6.2	Comparison against analytical solutions	97
4.6.3	Comparison against experimental results	100
4.7	Development of expressions for axisymmetric form factors and exit hydraulic gradient estimations	112
4.7.1	Fragment <i>D</i> form factor	113

4.7.2	Fragment $E$ form factor	113
4.7.3	Fragment $D$ normalised exit hydraulic gradient	114
4.7.4	Validation of the proposed expressions	115
4.8	Summary and conclusions	116
CHAPTER 5 RELATIONSHIP BETWEEN MINIMUM CREEP LENGTH		
AND MAXIMUM EXIT HYDRAULIC GRADIENT IN		
DOUBLE-WALLED AND CIRCULAR COFFERDAMS		
		119
5.1	Introduction	119
5.2	Factor of safety applied against piping failure	119
5.3	Line of creep method	120
5.4	Line of creep method for double-walled cofferdams	123
5.4.1	Relationship between creep length and maximum exit hydraulic gradient of double-walled cofferdams	124
5.4.2	Upper and lower bound curves for double-walled cofferdams	128
5.4.3	Validation of the proposed solutions for double-walled cofferdams	132
5.5	Line of creep method for circular cofferdams	134
5.5.1	Relationship between creep length and maximum exit hydraulic gradient of circular cofferdams	135
5.5.2	Boundary curves for circular cofferdams	138
5.5.3	Validation of the proposed solutions for circular cofferdams	139
5.6	Approximate creep ratios for cofferdams	140
5.7	Summary and conclusions	143

CHAPTER 6	SIMPLE SOLUTIONS FOR SQUARE AND RECTANGULAR	
	COFFERDAM SEEPAGE PROBLEMS	145
6.1	Introduction	145
6.2	Seepage solutions for square cofferdams	145
6.2.1	Numerical simulations of square cofferdams	146
6.2.2	Accuracy assessment of current approximate seepage solution methods for square cofferdams	152
6.2.3	Proposed solution method for square cofferdams	160
6.3	Seepage solution for rectangular cofferdams	163
6.3.1	Numerical simulations of rectangular cofferdams	163
6.3.2	Accuracy assessment of double-walled approximation to the seepage solutions for rectangular cofferdams	165
6.3.3	Proposed solution method for rectangular cofferdams	169
6.4	Summary and conclusions	175
CHAPTER 7	SUMMARY, CONCLUSIONS AND RECOMENDATIONS	177
7.1	Summary	177
7.2	Conclusions	181
7.2.1	Method of Fragments (MoF) solutions for double-walled and circular cofferdams	181
7.2.2	Creep length solutions for piping failure assessment of double-walled and circular cofferdams	182
7.2.3	Approximate seepage solutions for square cofferdams	182
7.2.4	Approximate seepage solutions for rectangular cofferdams	183

7.3	Recommendation for future research	183
7.3.1	Method of Fragments (MoF) solutions for double-walled cofferdams	184
7.3.2	Method of Fragments (MoF) solutions for circular cofferdams	184
7.3.3	Creep length solutions for piping failure assessment of double-walled and circular cofferdams	185
7.3.4	Seepage solutions for square and rectangular cofferdams	185
7.4	Final comments	186
REFERENCES		187
APPENDIX A1	Comparison of Griffiths (1984) fragment <i>C</i> form factor values with the derived values in this desertion	197
APPENDIX A2	Comparison of Griffiths (1984) fragment <i>C</i> normalised exit hydraulic gradient values with the derived values in this desertion	198
APPENDIX A3	Comparison of Griffiths (1984) fragment <i>A</i> form factor values with the derived values in this desertion	199
APPENDIX B1	Developed axisymmetric form factor values of fragment <i>D</i>	200
APPENDIX B2	Developed axisymmetric form factor values of fragment <i>E</i>	201
APPENDIX B3	Developed normalised exit gradient values of fragment <i>D</i>	202
APPENDIX B4	Laboratory simulation results of circular cofferdams	203
APPENDIX C1	$i_E/h$ values of double-walled cofferdams	204
APPENDIX C2	$i_E/h$ values of circular cofferdams	206
APPENDIX D1	Relation of double-walled cofferdam flow rate to the rectangular flow rate	208

APPENDIX D2	Relation of double-walled cofferdam $i_E$ to the $i_{EL}$ of rectangular cofferdams	209
APPENDIX D3	Relation of double-walled cofferdam $i_E$ to the $i_{ES}$ of rectangular cofferdams	210
APPENDIX D4	Relation of double-walled cofferdam $i_E$ to the $i_{EC}$ of rectangular cofferdams	211

## List of Figures

<b>Figure</b>	<b>Description</b>	<b>page</b>
1.1	Cofferdam shapes: (a) long-narrow; (b) circular; (c) square; (d) rectangular	3
1.2	(a) Elevation; (b) plan views (section X-X) of a cofferdam under four possible flow patterns	5
2.1	Schematic diagram of constant head test set-up [adopted from Das and Sivakugan (2016)]	15
2.2	Schematic diagram of falling head test set-up [adopted from Das and Sivakugan (2016)]	16
2.3	Equivalent permeability determination in stratified soil	20
2.4	Grain size distributions for three samples	26
2.5	Permeameter apparatus	27
2.6	Constant head permeability test set-up	28
2.7	Observed Darcy and nonlinear flow behaviours	29
2.8	$i-v$ plots for laminar flow regime	31
2.9	Failure due to heaving in front of a single row of sheet pile (Das 2013)	34
2.10	Experimental model geometry studied by Marsland (1953)	35
2.11	Flow element in two-dimensions	36
2.12	Flow net for the double-walled cofferdam in 2D Cartesian plane (Craig 2004)	38
2.13	Numerical model geometry for double-walled cofferdams	41
2.14	Axisymmetric plane in cylindrical coordinate system for circular cofferdams Neveu (1972)	42
2.15	3D numerical model geometry for square cofferdams	45

<b>Figure</b>	<b>Description</b>	<b>page</b>
2.16	Required penetration of cut-off wall against piping or heaving [adopted from U.S. Department of the Navy (1982)]	47
2.17	Method of fragments for concrete dam	48
3.1	Adoption of MoF for double-walled cofferdams	54
3.2	Form factor charts: (a) fragment <i>A</i> ; (b) fragment <i>C</i> [adopted from Griffiths (1984)]	54
3.3	Normalised exit gradient chart for fragment <i>C</i> [adopted from Griffiths (1984)]	55
3.4	Numerical model geometry used for simulating double-walled cofferdams	57
3.5	Initial dewatering condition of double-walled cofferdams for the onshore excavations	58
3.6	Double-walled cofferdam model validation: (a) flow rate; (b) exit hydraulic gradient	61
3.7	Behaviour of the equipotential lines with double-walled cofferdam geometry	62
3.8	Comparison of predictions from MoF and full numerical model (Full NM) solutions when $\alpha = 0$ : (a) seepage quantity; (b) exit hydraulic gradient	64
3.9	Effect of cofferdam geometry on the accuracy of MoF solutions: (a) seepage quantity; (b) exit hydraulic gradient	65
3.10	Numerical model geometry used for fragment <i>C</i> simulations	67
3.11	Form factor $\Phi_C$ values for fragment <i>C</i> (from finite element simulation)	69
3.12	Exit hydraulic gradient values for fragment <i>C</i> (from finite element simulation)	70
3.13	Fragment <i>A</i> geometries: (a) actual geometry; (b) equivalent fragment <i>C</i> geometry used for numerical simulations	72
3.14	Form factor $\Phi_A$ values for fragment <i>A</i> at $b = 0$ (from finite element simulation)	72
3.15	Comparison of proposed expressions solutions with full numerical model (NM) solutions: (a) seepage quantity; (b) exit hydraulic gradient	75

<b>Figure</b>	<b>Description</b>	<b>page</b>
4.1	Axisymmetric numerical model geometry used for circular cofferdams	77
4.2	Axisymmetric numerical model validation for flow rate estimation of circular cofferdams	79
4.3	Axisymmetric model validation for average exit hydraulic gradient $i_{E_{Avg}}/h$ estimation of circular cofferdams	80
4.4	Circular cofferdam in axisymmetric configuration: (a) elevation view; (b) plan view	82
4.5	Flow nets: (a) double-walled cofferdam; (b) circular cofferdam	85
4.6	Proposed Axisymmetric fragment types: (a) fragment $D$ ; (b) fragment $E$	86
4.7	Behaviour of the equipotential lines with circular cofferdam geometries	87
4.8	Numerical model geometry used for axisymmetric fragments: (a) fragment $D$ ; (b) fragment $E$	90
4.9	Convergence of axisymmetric form factor and dimensionless exit hydraulic gradient values to single sheet pile wall values: (a) form factors; (b) exit hydraulic gradient	91
4.10	Form factor $\beta_D$ values for fragment $D$ (from finite element simulation)	92
4.11	Form factor $\beta_E$ values for fragment $E$ (from finite element simulation)	93
4.12	Exit gradient values for fragment $D$ (from finite element simulation)	94
4.13	Comparison of predictions from axisymmetric MoF and full numerical model (Full NM) solutions when $\alpha = 0$ : (a) seepage quantity; (b) exit hydraulic gradient	95
4.14	Effect of cofferdam geometry on the accuracy of axisymmetric MoF solutions: (a) seepage quantity; (b) exit hydraulic gradient	97

<b>Figure</b>	<b>Description</b>	<b>page</b>
4.15	Comparison of seepage quantities estimated by proposed axisymmetric MoF solutions against analytical solutions by Neveu (1972): (a) $\alpha=0$ ; (b) $\alpha=0.505$ ; (c) $\alpha=0.808$	99
4.16	Grain size distributions for three sand samples	100
4.17	Constant head test set-up used for permeability values determination	103
4.18	Relation between permeability and relative density ( $D_r$ )	104
4.19	a) The schematic diagram of the laboratory test set-up (to scale); (b) a photograph of the test set-up	105
4.20	Comparison of seepage quantities estimated by proposed axisymmetric MoF solutions against experimental results	109
4.21	Comparison of seepage quantities estimated by proposed axisymmetric MoF solutions against experimental results by Davidenkoff and Franke (1965)	111
4.22	Comparison of proposed expressions solutions with full numerical model (NM) solutions: (a) seepage quantity; (b) exit hydraulic gradient	116
5.1	Line of creep method for a dam problem	121
5.2	Creep length calculation for double-walled cofferdams	124
5.3	Changing the normalised $i_E$ values with cofferdam width in double-walled cofferdams: (a) $s/T = 0.2$ ; (b) $s/T = 0.4$ ; (c) $s/T = 0.8$	126
5.4	Normalised $i_E$ vs creep ratio $C_c$ relationship for double-walled cofferdams: (a) $0.1 \leq LR/T < 0.5$ ; (b) $LR/T \geq 0.5$	127
5.5	Boundary curves for $0.1 \leq LR/T < 0.5$ : (a) Upper bound curve; (b) Lower bound curve	129
5.6	Both upper and lower bound curves for normalised $i_E$ of double-walled cofferdams: (a) $0.1 \leq LR/T < 0.5$ ; (b) $LR/T \geq 0.5$	131

<b>Figure</b>	<b>Description</b>	<b>page</b>
5.7	Validity assessment for double-walled cofferdams: (a) $0.1 \leq LR/T < 0.5$ ;(b) $LR/T \geq 0.5$	133
5.8	Changing the normalised $i_E$ values with cofferdam width in circular cofferdams: (a) $s/T = 0.2$ ; (b) $s/T = 0.4$ ; (c) $s/T = 0.8$	136
5.9	Normalised $i_E$ vs creep ratio $C_c$ relationship for circular cofferdams: (a) $0.1 \leq rR/T < 0.5$ ; (b) $rR/T \geq 0.5$	137
5.10	Both upper and lower bound curves for normalised $i_E$ of circular cofferdams: (a) $0.1 \leq rR/T < 0.5$ ; (b) $rR/T \geq 0.5$	138
5.11	Validity assessment for circular cofferdams: (a) $0.1 \leq rR/T < 0.5$ ; (b) $rR/T \geq 0.5$	140
5.12	Summary of the equations and curves for the double-walled (DW) and circular (Cir.) cofferdams: (a) $0.1 \leq (\frac{LR}{T} \text{ or } \frac{rR}{T}) < 0.5$ ; (b) $(\frac{LR}{T} \text{ or } \frac{rR}{T}) \geq 0.5$	144
6.1	Numerical model used for square cofferdams: (a) model geometry; (b) 3D mesh	147
6.2	Square cofferdam model validation: (a) flow rate; (b) average exit hydraulic gradient at middle of a side $i_{EMAvg.}/h$ ; (c) average exit hydraulic gradient at corner $i_{ECAvg.}/h$	149
6.3	Sensitivity analysis results for square cofferdams: (a) flow rate; (b) exit hydraulic gradient at mid-point $i_{EM}$ ; (c) exit hydraulic gradient at corner $i_{EC}$	151
6.4	Relationships between 2D flow rates ( $q_c$ and $q_d$ ) to the 3D flow rate $q_s$ into square cofferdam: (a) axisymmetric flow; (b) Cartesian flow	153
6.5	Deviation of the flow rate predictions of square cofferdam by Eq. 6 and Eq. 8 From the actual flow rate	155
6.6	Double-walled cofferdam geometry and form factors chart used in CFEM (2006) [adopted from (CFEM 2006)]	156

<b>Figure</b>	<b>Description</b>	<b>page</b>
6.7	Relationships between 2D exit hydraulic gradient $i_E$ values and $i_{EM}$ and $i_{EC}$ values of square cofferdams: (a) circular cofferdam; (b) double-walled cofferdam	157
6.8	Comparison of the exit gradient predictions using 2D flow patterns: (a) circular cofferdam; (b) double-walled cofferdam	159
6.9	Comparison of the flow rate predictions for square cofferdams using 2D flow patterns : (a) circular cofferdam; (b) double-walled cofferdam	161
6.10	Equipotential lines distributions: (a) square cofferdams; (b) circular cofferdams; (c) double-walled cofferdams	162
6.11	Numerical model geometry used for rectangular cofferdams	165
6.12	Relationship between double-walled flow rate to the 3D flow rate into rectangular cofferdam at $l/B = 3$	166
6.13	Relationship between double-walled exit gradient to the actual exit gradient values of rectangular cofferdams at $l/B = 3$	168
6.14	Relationship of $a$ value to the $l/B$ ratio	170
6.15	Comparison of the flow rate predictions for rectangular cofferdam at $l/B = 3$	171
6.16	Relationship of $b$ value to the $l/B$ ratio on $i_{EL}$ estimation	172
6.17	Comparison of the exit hydraulic gradient predictions for rectangular cofferdams: (a) $i_{EC}$ ; (b) $i_{ES}$ ; (c) $i_{EL}$	174
D1.1	Relationship between double-walled flow rate to the 3D flow rate into rectangular cofferdams	208
D2.1	Relationship between double-walled $i_E$ to the actual $i_{EL}$ of rectangular cofferdams	209
D3.1	Relationship between double-walled $i_E$ to the actual $i_{ES}$ of rectangular cofferdams	210

D4.1 Relationship between double-walled  $i_E$  to the actual  $i_{EC}$  of rectangular  
cofferdams

211

## List of Tables

<b>Table</b>	<b>Description</b>	<b>page</b>
2.1	Typical values of soil permeability in saturated soils [adopted from (Das and Sivakugan 2016)]	13
2.2	Proposed values for Hazen's constant $c$	18
2.3	Empirical relationships for the Forchheimer coefficients of $a$ and $b$ determination [adopted from (Van Lopik et al. 2017)]	25
2.4	Determined index properties	26
2.5	Summary of the test results	30
2.6	Confined flow fragments and their form factors, Harr (1962, 1977)	50
2.7	Confined flow fragments by Griffiths (1984)	51
3.1	Cofferdam geometries used for numerical model validations	60
3.2	Double-walled cofferdam geometries used for equipotential lines behaviour Studied	61
4.1	Cofferdam geometries used for validating the axisymmetric numerical model for circular cofferdams	78
4.2	Circular cofferdam geometries used for equipotential lines behaviour studied	87
4.3	Cofferdam geometries used for axisymmetric MoF comparisons against analytical solution by Neveu (1972)	98
4.4	Result of grain size distribution tests	101
4.5	Tests and the list of standards used for determining the physical properties of sand	101
4.6	Physical properties of sand 1	101
4.7	Sequence of the laboratory tests conducted	107
4.8	Relative errors between experimental results and MoF Predictions	109

<b>Table</b>	<b>Description</b>	<b>page</b>
4.9	Relative errors between experimental results (using electrical analogy model) and MoF Predictions	112
5.1	Lane's recommended values for weighted creep ratio $C_w$	123
5.2	Summary of the validity assessment for double-walled cofferdams	134
5.3	Summary of the validity assessment for circular cofferdams	140
5.4	Summary of the estimated creep ratio $C_c$ values for cofferdams	142
6.1	Cofferdam geometries used for validating the 3D numerical model for square cofferdam	148
6.2	Geometry range used for square cofferdam analysis	153
6.3	Summary of the flow rate analysis of rectangular cofferdam	167
6.4	Summary of the exit gradient estimation relations for rectangular cofferdam	169
A1.1	Griffiths (1984) fragment $C$ form factor $\Phi_C$ values	197
A1.2	Developed fragment $C$ form factors $\Phi_C$ values using finite element simulations	197
A2.1	Griffiths (1984) fragment $C$ normalised exit hydraulic gradient $i_{ES_C}/h_C$ values	198
A2.2	Developed fragment $C$ normalised exit hydraulic gradient $i_{ES_C}/h_C$ values using finite element simulations	198
A3.1	Griffiths (1984) fragment $A$ form factor $\Phi_A$ values when $b = 0$	199
A3.2	Derived fragment $C$ form factor $\Phi_C$ values when $L = 2T_C$ using finite element simulations	199
B1.1	Developed fragment $D$ form factors $\beta_D$ values using finite element simulations	200
B2.1	Developed fragment $E$ form factors $\beta_E$ values using finite element simulations	201
B3.1	Developed fragment $D$ normalised exit gradient $i_{ES_D}/h_D$ values using finite element simulations	202
B4.1	Laboratory simulation results of circular cofferdams	203

C1.1	Normalised exit hydraulic gradient $i_E/h$ of double-walled cofferdams	204
C2.1	Normalised exit hydraulic gradient $i_E/h$ of circular cofferdams	206

## Chapter 1 Introduction

### 1.1 General

Excavations are used in construction sites to create foundations for structures such as buildings, bridges, dams etc. When an excavation takes place below the ground water level, it is required to control water seepage into the excavation to provide a dry and safe working environment to the workers within the excavations. Commonly used seepage controlling methods can be identified under three basic groups as follows (Powers 1992):

1. Open pumping: a method that allows water to flow into the excavation and pumps them away from sumps and ditches.
2. Predrain method: a method that lowers the ground water table before commencing the excavation using wells, well points or drains.
3. Cut-off method: a method that cuts-off water entering into the excavation using a vertically driven structure.

Open pumping is suitable for excavations where the slope is relatively flat (Kavvas et al. 1992). This is the cheapest method, but conditions should be favorable, i.e., flat and stable slope is required. Otherwise, it can overrun the cost and delay the project. In worst scenarios, it can lead even to a catastrophic failure (Powers 1992). Therefore, open pumping is not a feasible method for controlling water specially in urban areas. The second method, predrain, involves lowering the ground water table below the excavation base level, and hence, it lowers the ground water table beyond the excavation boundary, too. This increases the effective stress in the surrounding area, and hence, settlement induced damages can occur to the surrounding structures. This risk associated with predrain reduces its potential as a seepage control method.

The third one is to apply a water cut-off structure using sheet piling walls, diaphragm walls or grout walls acting as a ground support structure, in addition to reducing the water entering the excavation (Powers 1992). Further, Kavvadas et al. (1992) defined some other unique advantages of water cut-off structures as below:

1. It reduces water seepage into the excavation significantly because of vertically driven structures making barriers to the horizontal flow. This is due to the soil permeability is larger in horizontal direction compared to that in the vertical direction.
2. It lowers the ground water table which is away from the excavation boundary only a small amount compared to that of the predrain method. So, there is less risk to adjacent structures by settlement induced damages.
3. It decreases the exit hydraulic gradient considerably because vertical structures are driven well below the excavation base, and hence, provides adequate factor of safety with respect to possible hydraulic failure (heaving or piping).

Due to above advantages, water cut-off structures are among the widely used seepage control methods. Water cutoff structures made using sheet piles are usually known as cofferdams and are most suitable for sandy soils and stratified soil systems (Powers 1992). Also, steel is the often seen material for sheet piles for its as high structural strength, driveability, water tightness, reusability and quick construction.

## **1.2 Cofferdams**

Cofferdams are temporary structures and are constructed by making enclosures using walls of sheet piles driven into the ground. Long-narrow, circular, square and rectangular are the commonly seen cofferdam shapes in plan view. Fig. 1.1 shows the real applications of these types of cofferdams. In long-narrow type, length is considerably large compared to its width, and hence, the effect of the shorter sides is negligible. Therefore, this type of cofferdam is

termed as double-walled cofferdams (Harr 1962; Griffiths 1984; Banerjee and Muleshkov 1992; Banerjee 1993), and the same term is used in this thesis also, to define the long-narrow cofferdams. Double-walled cofferdams are commonly used for constructions of foundations for bridge piers, concrete dams and harbour walls (King and Cockroft 1972). For constructions of water treatment plant, sewers, bridge piers, and abutment and shaft, circular cofferdams are employed (Koltuk and Azzam 2016) while square or rectangular cofferdams are encountered with the foundation constructions for buildings, small bridges etc.



**Fig. 1.1** Cofferdam shapes: (a) long-narrow; (b) circular; (c) square; (d) rectangular (Fig. 1.1 a courtesy of Eng. L Wenzel, Wenzel Engineering, Inc., United States, Fig. 1.1 b courtesy of Eng. P. Brady, Brady marine and civil, Australia, Fig. 1.1 c and d courtesy of Prof. N. Sivakugan, James Cook University, Australia)

All the cofferdam shapes discussed above are similar in the cross-sectional elevation view as shown in Fig. 1.2a where the seepage flow is taking place under the total head difference of  $h$ . Water seeping into the cofferdam generates the hydraulic gradient, and hence, excavation base failure can occur. Also, presence of a hydraulic gradient affects the stability of sheet pile wall, changing the distribution and magnitude of the water and earth pressure components (Kaiser and Hewitt 1982; Soubra et al. 1999; Benmebarek et al. 2006). Therefore, seepage analysis is a vital factor for designing any shape of cofferdam, and flow rate  $Q$  and maximum exit hydraulic gradient  $i_E$  are two important variables that are computed. The flow rate is necessary to estimate the required pump capacity, maintaining the excavation base dry while exit hydraulic gradient is to assess the stability with respect to possible piping failure. Here, exit hydraulic gradient  $i_E$  is the hydraulic gradient *at the excavation base right next to the sheet pile wall* (see Fig. 1.2a) since, exit hydraulic gradient is maximum at that point (Griffiths 1984).

Flow into the cofferdams are actually three-dimensional (3D) for all the cases, but flow patterns are different. However, for double-walled cofferdams, it is considered as a parallel flow (top left one of Fig. 1.2b) ignoring the effect of the two shorter side. Therefore, these problems are analysed as 2D problems in the Cartesian plane. Flow pattern into the circular cofferdams is an axisymmetric one as shown in the top right of Fig. 1.2b; therefore, these problems can also be analysed as 2D problem, but in the cylindrical coordinate system. The flow pattern of bottom left in Fig. 1.2b is for square cofferdams while the bottom right is for the rectangular cofferdam. 3D analysis is required for these two cases.

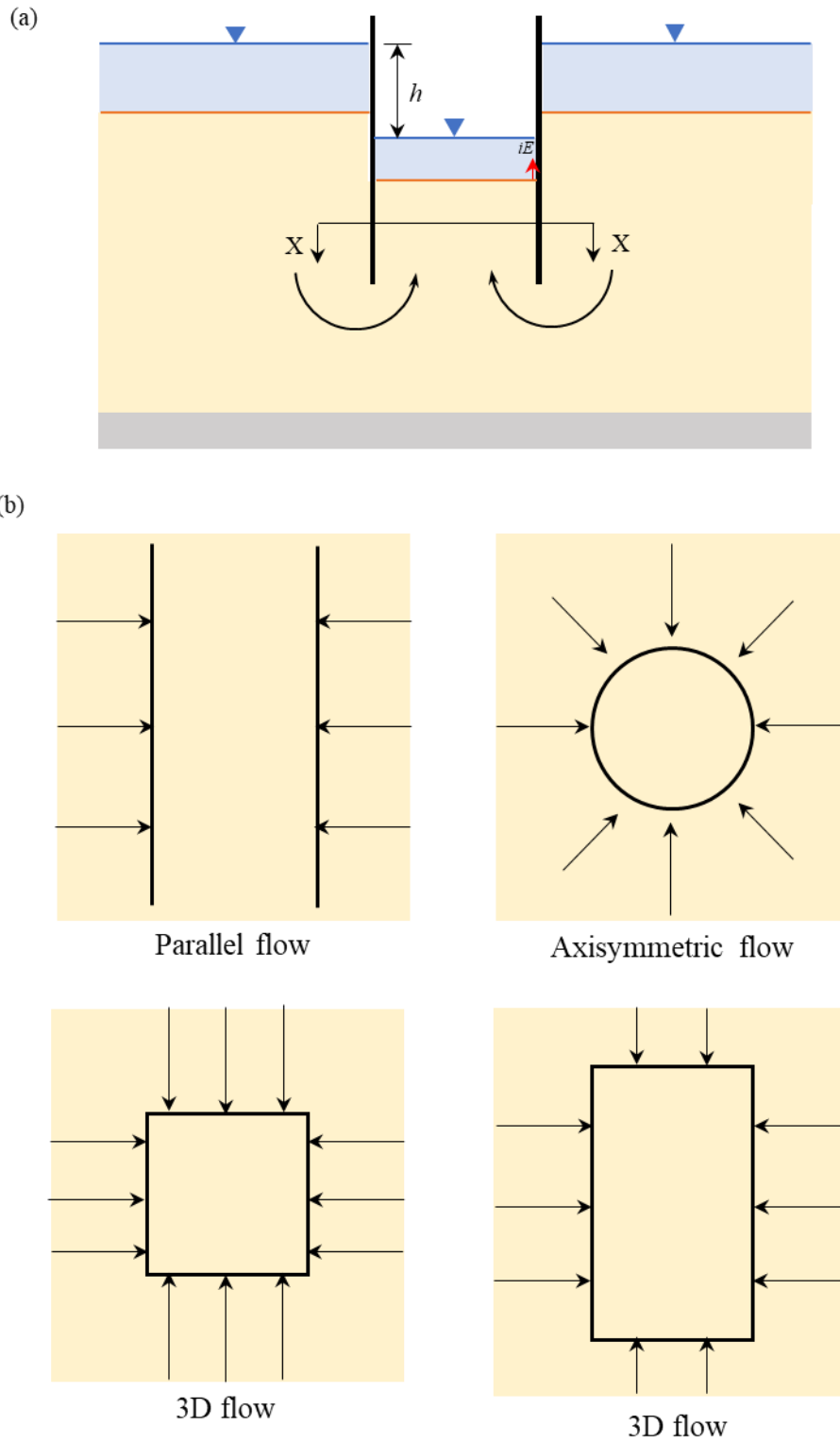


**Fig. 1.2** (a) Elevation; (b) plan views (section X-X) of a cofferdam under four possible flow patterns

### 1.3 Current State-of-the-Art

For double-walled cofferdams, available seepage solution methods are the following: flow net, analytical, numerical, and method of fragments (MoF). Out of these methods, MoF proposed by Griffiths (1984) has a place as a simple and quick method to estimate flow rate and maximum exit hydraulic gradient. Also, it has the ability to incorporate the effect of soil anisotropy, too. However, the accuracy of this method depends on the validity of the assumption that the equipotential lines at tip of the sheet piles are vertical; therefore, the method's accuracy varies with the cofferdam geometry.

For cofferdam types where the flow patterns are 3D (circular, square and rectangular), there are no simple and accurate solution methods such as MoF. Drawing a flow net is a possible method, but it requires to consider 3D flow effect, and hence, it is a tedious task. Also, analytical solution is available only for circular cofferdams and was proposed by Neveu (1972) to provide only the flow rate estimations. Approximate solution methods proposed by Becker and Moore (2006) are available for circular and square cofferdams using correction factors to the corresponding values of double-walled cofferdam. However, the accuracy of this method is low since the correction factors cannot simulate the effect of 3D flow correctly. For rectangular cofferdams, only approximate solution method available is to consider it as a double-walled cofferdam. But, this approximation can jeopardize safety because actual flow into the rectangular cofferdam is 3D, and hence, what is predicted assuming a double-walled cofferdam underestimates the values of flow rate and maximum exit hydraulic gradient (Miura et al. 2000; Tanaka et al. 2000). Therefore, there is a perceived benefit of having a simple, but accurate seepage solution method for circular, square and rectangular cofferdam problems.

Considering all, it can be concluded that, although MoF provides simple and quick seepage solutions for double-walled cofferdam problems, it is still required to assess the effect of violating the assumption (that the equipotential line at the tip of sheet pile is vertical) on the accuracy of the result over a wider range of geometries. Also, it is very useful to have MoF solution method for circular cofferdams. Further, solution methods that can incorporate the effect of 3D flow into the square and rectangular cofferdams will also be more beneficial.

#### **1.4 Objectives and scope of research**

The primary goal of this study is to critically assess the adaptability of MoF as a seepage solution method for cofferdams of different geometries, with particular interest on the flow rate and maximum exit hydraulic gradient estimations. Following objectives are established in order to achieve the thesis aim.

1. To assess the effect of violating the assumption that the equipotential line at the tip is vertical on the MoF solutions for double-walled cofferdams.
2. To develop axisymmetric MoF solutions for circular cofferdams which are applicable to both isotropic and anisotropic soil conditions and validate them over wider range of geometries.
3. To develop and validate a relationship between shortest seepage path (creep length) and maximum exit hydraulic gradient in both double-walled and circular cofferdams in order to use as the first-order approximations in ensuring the safety against piping.
4. To develop and validate a simple and more accurate solution method for analyzing seepage into square cofferdams and compare against the existing solutions.
5. To develop and validate a simple seepage solution method for rectangular cofferdams.

In this study, numerical, analytical and experimental techniques are used to compare against each other, and to validate the proposed solutions. The research will contribute to:

1. Better understanding of the effect of violating the assumption (that the equipotential line at the sheet pile tip is vertical) on the accuracy of the MoF for double-walled cofferdams.
2. Provide a simple and accurate seepage solution method to circular cofferdams.
3. Enhance the safety of square and rectangular cofferdams using more accurate solution methods incorporating the effect of 3D flow.

### **1.5 Relevance of the research**

Cofferdams are among the widely used hydraulic structures in waterfront construction sites. However, cofferdam failure induced by water seepage is also not a rare incident, and several researchers reported case histories on this (Bauer 1984; Tanaka et al. 1994; Tanaka et al. 2002; Cai and Ugai 2003; Tanaka 2003; Cai and Ugai 2004). Also, these failures are rapid with little advance warning and are responsible for catastrophic situations. Therefore, having a simple and accurate solution method is essential to minimize these incidents. Since, MoF is a simple and quick solution method, extending this further for double-walled and circular cofferdams will provide realistic first estimates of the flow rate and maximum exit hydraulic gradients. Further, proposing a method to predict the possibility for piping failure only considering the shortest seepage path in both double-walled and circular cofferdams will also be beneficial as a first-order solution method.

Also, cofferdam design based on the 2D approximations while flow pattern is actually 3D has caused failure, and some case histories and laboratory model tests on this have been discussed by several researchers (Bauer 1984; Tanaka et al. 2002; Tanaka and Yokoyama 2005;

Bouchelghoum and Benmebarek 2011; Koltuk and Iyisan 2013; Tanaka et al. 2013). Therefore, seepage solutions proposed herein for square and rectangular cofferdams with incorporating the effect of 3D flow will be more effective for the designs at preliminary stage.

## **1.6 Thesis overview**

Chapter 1 introduces cofferdam types and flow patterns, seepage solution methods, research problem, objectives, and the relevance of the research. Finally, the thesis overview is presented.

In chapter 2, a review of previous studies that discuss the soil permeability, hydraulic failure mechanisms and existing solution methods for analyzing the cofferdam seepage problems are presented.

Chapter 3 validates the MoF as a feasible seepage solution method for double-walled cofferdam and provides simple analytical equations to estimate the flow rate and exit hydraulic gradient values. The work reported in this chapter was published in:

1. Madanayaka, T. A., and Sivakugan, N. (2016). "Approximate equations for the method of fragment." *Int. J. Geotech. Eng.*, 10(3), 297-303.
2. Madanayaka, T., and Sivakugan, N. "Simplified method of fragments based two dimensional seepage solution for the double-wall cofferdam." *Proc., 19th Southeast Asian Geotechnical Conference*, Kuala Lumpur, Malaysia, 1047-1051.
3. Madanayaka, T., Sivakugan, N., and Ameratunga, J. (2017). "Validity of the method of fragments for seepage analysis in double-wall cofferdams." *Proc., 19th International Conference on Soil Mechanics and Geotechnical Engineering*, Seoul, South Korea, 2921-2924.

Chapter 4 describes the development of axisymmetric MoF solution for circular cofferdams using the finite element computer package *RS2 9.0*, developed by Rocscience. It includes proposing new axisymmetric fragments with their form factors and exit hydraulic gradient charts to provide simple seepage solutions. Also, simple analytical expressions have been proposed for estimating the form factors and maximum exit hydraulic gradients. These expressions enable the MoF be implemented in spreadsheet, and hence, can be used as an effective tool for parametric studies. Some of the content from this chapter were published in:

1. Madanayaka, T. A., and Sivakugan, N. (2017). "Adaptation of Method of Fragments to Axisymmetric Cofferdam Seepage Problem." *International Journal of Geomechanics, ASCE* (9), doi: 10.1061/(ASCE)GM.1943-5622.0000955.
2. Madanayaka, T. A., and Sivakugan, N. " Validity of the method of fragments for seepage analysis in circular cofferdams" *Geotechnical & Geological Engineering, (Draft ready for second submission)*.

Chapter 5 proposes and validates simple solution methods to provide first-order approximations in ensuring safety against piping failure for double-walled and circular cofferdams just only considering the shortest seepage path. This chapter is being under the second review for the publication in *International Journal of Geomechanics (ASCE)* as Madanayaka, T. A., and Sivakugan, N. "Relationship between minimum creep length and exit gradient in cofferdams".

Chapter 6 discusses the development and validation of approximate solution methods to estimate the flow rate and exit hydraulic gradient for square and rectangular cofferdams considering the effect of 3D flow using the 3D finite element software package, *RS3 2.0* developed by Rocscience. The work reported in this chapter has been published by the

Canadian Geotechnical Journal as Madanayaka, T. A., and Sivakugan, N. “Simple solutions for square and rectangular cofferdam seepage problems”.

Chapter 7 provides a summary and conclusion of the research, and at the end, some recommendations suggested for future research.

## Chapter 2 Literature review

### 2.1 Overview

Structural stability of the sheet piles and the bracing system is a main concern in evaluating the performance of cofferdams (Banerjee and Muleshkov 1992). As noted before, flow rate into the cofferdam and excavation base stability against hydraulic failure are also two other concerns which are equally important. Soil permeability  $k$  is a key parameter used in the Darcy's law in order to estimate the flow rate into the cofferdams. For the homogeneous and isotropic soils, soil permeability does not have an effect on the excavation base stability, but for the anisotropic soils, it is a factor to be considered (Koltuk and Iyisan 2013). There are various solution methods available for estimating the flow rate and excavation base stability against hydraulic failures of cofferdams.

This chapter gives a broad review emphasizing soil permeability, Darcy's law and its range of validity, hydraulic failure mechanisms of cofferdams, and current seepage solution methods for various shapes of cofferdams. However, literature review is not limited only to this chapter. An extensive description of method of fragments (MoF) in double-walled cofferdams, axisymmetric flow net construction, application of method of fragments in 3D flow situations, and physical modeling of cofferdams is given in later chapters.

### 2.2 Soil permeability

Soil permeability  $k$  is the parameter used to measure the ability of a fluid passing through the soils. Water is the fluid involved mostly; therefore, the term, soil permeability is used to define the ability of water passing through the soils in this dissertation. Permeability is the soil property having the widest variation (Cedergren 1977) and Table 2.1 shows typical values of soil permeability for saturated soils.

**Table 2.1** Typical values of soil permeability in saturated soils [adopted from (Das and Sivakugan 2016)]

Soil type	k (cm/s)
Clean gravel	100-1
Coarse sand	1.0-0.01
Fine sand	0.01-0.001
Silty sand	0.001-0.00001
Clay	<0.000001

### 2.2.1 Factors affecting the soil permeability

There are several factors that affect the soil permeability. Most of them are the soil properties and are listed below (Das and Sivakugan 2016).

- Pore-size distribution
- Grain-size distribution
- Void ratio
- Roughness of the mineral particles
- Degree of saturation

Soil permeability is significantly lower when it is unsaturated compared to that for the saturated condition. The two fluid properties that can change the permeability are the dynamic viscosity  $\mu$  and unit weight  $\gamma_w$ , and they are related to the soil permeability in the way of (Das and Sivakugan 2016):

$$k = \frac{\gamma_w}{\mu} \bar{K} \quad (2.1)$$

where  $\bar{K}$  is the absolute permeability and is independent from the fluid properties.

In clayey soils, some other factors should also be considered on the permeability assessment. They are, soil structure, ionic concentration, and thickness of water layers attached to the clay

particles (Das and Sivakugan 2016). In this review, permeability of clayey soils is not considered specifically, since cofferdams are generally applied in sandy soils.

### 2.2.2 Laboratory determination of soil permeability

In laboratory, constant head permeability test is used to determine the permeability of coarse-grained soils (AS 1289.6.7.1; ASTM D2434) while falling head permeability test is used for fine-grained soils (AS 1289.6.7.2; ASTM D5856). For sandy soils, reconstituted samples are commonly used because undisturbed samples are difficult to obtain, but the soils require to be compacted to a specific density simulating the field condition (Sivakugan and Das 2009). Also, Hatanaka et. al. (1997; 2001) showed that there is no significant difference between the permeability values measured in undisturbed and reconstituted samples for sandy and gravelly soils. Therefore, laboratory permeability estimates using reconstituted samples are sufficient for most of the cofferdam designing purposes in sandy soils.

#### Constant head test

Fig. 2.1 shows the schematic diagram of a constant head test set-up where the flow direction is downward. In this test, water is allowed to drain until the flow rate has reached a steady state value at a constant head difference  $h$ . Then, total volume of water  $Q$  collected in a measuring cylinder for a known period  $t$  is measured. Then,  $Q$  can be expressed as:

$$Q = Avt \quad (2.2)$$

where  $A$  is the cross-sectional area of the soil sample,  $v$  is the discharge velocity, and  $t$  is the duration of water collection. Applying Darcy's law,  $v = ki$ , where  $k$  is the soil permeability and  $i$  is the hydraulic gradient into Eq. 2.2,  $Q$  can be estimated as:

$$Q = Akit \quad (2.3)$$

Note that, Darcy's law will be discussed later (Sec. 2.3) in more detail. Also,  $i$  can be expressed as  $h/L$  where  $L$  is the sample length. Then Eq. 2.3 can be rewritten as:

$$Q = Ak \frac{h}{L} t \quad (2.4)$$

Thus, soil permeability  $k$  can be estimated by:

$$k = \frac{QL}{Aht} \quad (2.5)$$

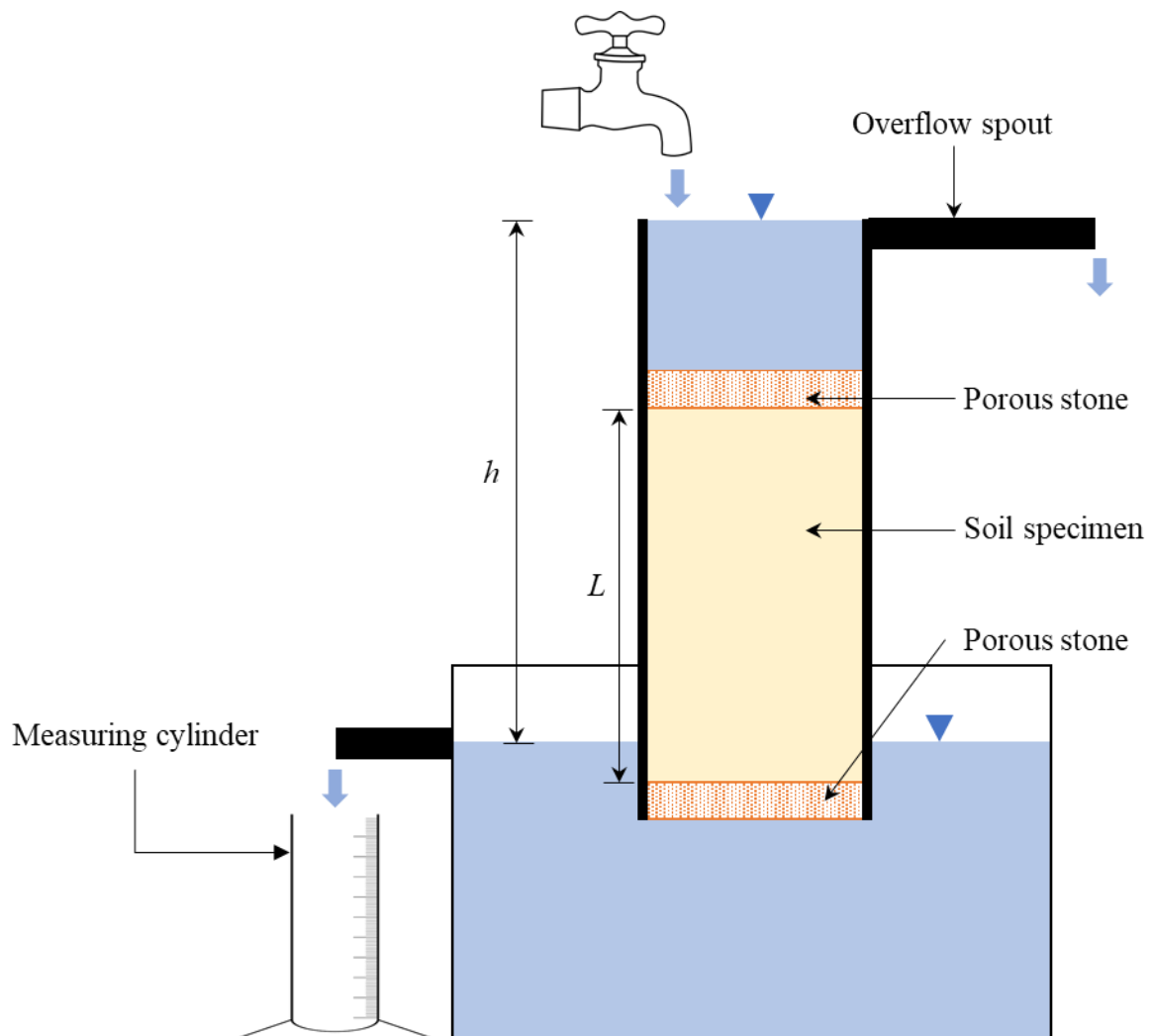


**Fig. 2.1** Schematic diagram of constant head test set-up [adopted from Das and Sivakugan (2016)]

Falling head test

A schematic diagram of falling head test set-up is shown in Fig. 2.2. In this test, water is allowed to flow from standpipe through the soil specimen for a given time period  $t$  while head difference drops from  $h_1$  to  $h_2$ .

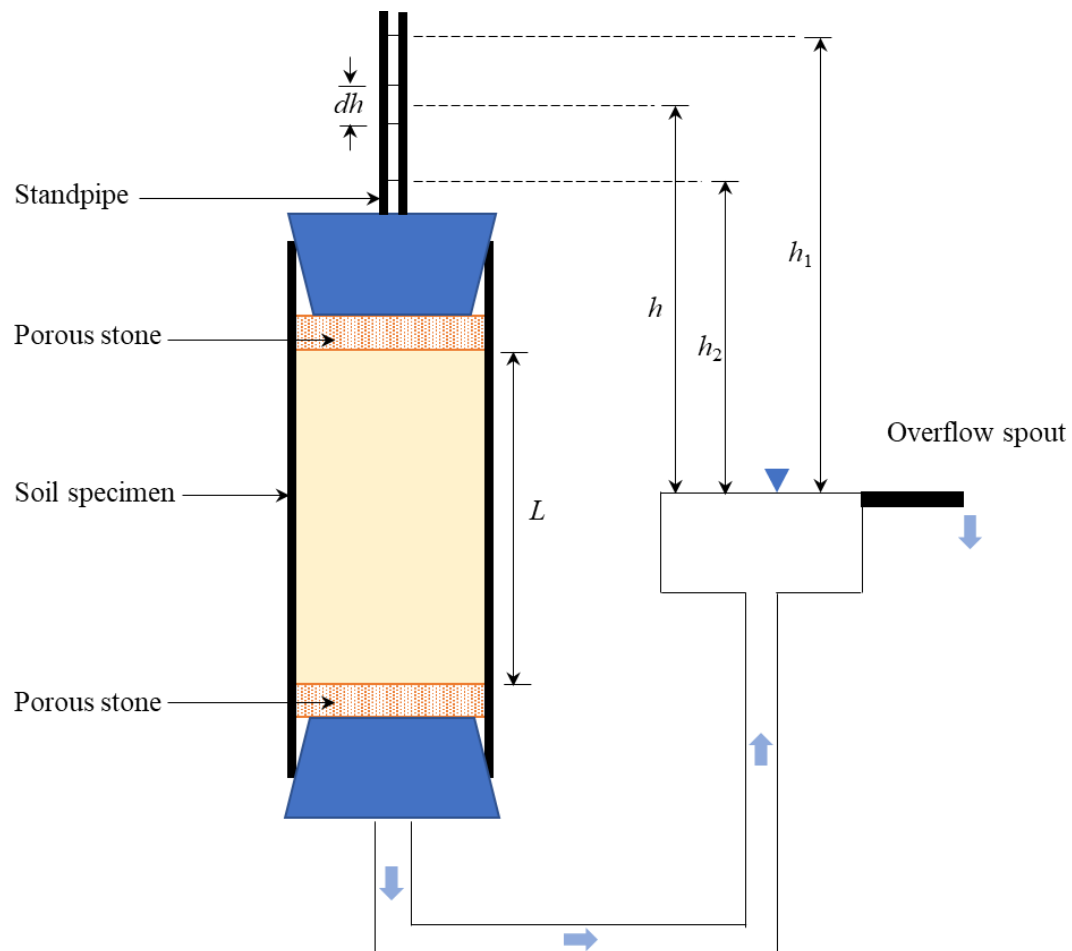


**Fig. 2.2** Schematic diagram of falling head test set-up [adopted from Das and Sivakugan (2016)]

Using Darcy's law, equating the flow rate  $q$  through the sample and the standpipe, at any given time  $t$  can be expressed as:

$$q = k \frac{h}{L} A = -a \frac{dh}{dt} \quad (2.6)$$

where  $A$  and  $a$  are the cross-sectional area of soil specimen, and standpipe, respectively. Next, Eq. 2.6 can be rearranged in to the form:

$$dt = \frac{aL}{Ak} \left( -\frac{dh}{h} \right) \quad (2.7)$$

Then, Eq. 2.7 can be integrated considering the limits of time and head difference from 0 to  $t$  and  $h_1$  to  $h_2$ , respectively, and hence, a relation to estimate the soil permeability can be derived as:

$$k = \frac{aL}{At} \ln \frac{h_1}{h_2} \quad (2.8)$$

### 2.2.3 Empirical relations for soil permeability

Seelheim (1880) [vide Chapuis (2004)] suggested that the possibility of predicting the soil permeability  $k$  of granular soils using the squared value of an effective grain size. Since then, several studies have developed relations for estimating the  $k$  using experimental models (empirical relations), hydraulic radius theories, capillary models and statistical models; however, the equation proposed by Hazen (1930) is used widely because of its simplicity compared to other equations (Chapuis 2004). Hazen (1930) developed a relationship for the permeability of clean filter sand in the form given by:

$$k \left( \frac{cm}{s} \right) = cD_{10}^2 \quad (2.9)$$

where,  $c$  is a constant and  $D_{10}$  is the effective grain size in mm. Several studies have suggested various values for the constant  $c$ , and some of the values given in geotechnical textbooks are shown in Table 2.2. However, Carrier (2003) pointed that the value of  $c$  can be varied by three orders of magnitude. Also having a small quantity of silts and clay may change the permeability significantly. Therefore, permeability value given by Eq. 2.9 is not very reliable.

**Table 2.2** Proposed values for Hazen's constant  $c$ 

Proposed by	Constant $c$ value
Cedergren (1977)	0.9 – 1.2
Holtz and Kovacs (1981)	0.4 – 1.2
Terzaghi et al. (1996)	0.5 – 2.0
Coduto (1999)	0.8 - 1.2
Das (2013)	1.0 – 1.5
Das and Sivakugan (2016)	1.0 – 1.5

The equation proposed by Kozeny (1927) and Carman (1938, 1956) gives reasonably good result in estimating the permeability of sandy soils and also, for some silts (Das 2013). The Kozeny-Carman equation is semi-empirical and semi-theoretical and gives the permeability  $k$  as:

$$k = \frac{1}{C_s S_s^2 T^2} \frac{\gamma_w}{\mu} \frac{e^3}{1 + e} \quad (2.10)$$

where,

$C_s$  is the shape factor

$S_s$  is the specific surface area

$T$  is the tortuosity of flow channel

$\mu$  is the dynamic viscosity of permeant

$\gamma_w$  is the unit weight of water

$e$  is the void ratio

Further to above equations, U.S. Department of the Navy (1974) provides graphical solutions for estimating the permeability values of clean sand and gravel using the  $D_{10}$  and void ratio  $e$  values. This is also among the widely used methods due to its simplicity.

### 2.2.4 Permeability anisotropy

Witt and Brauns (1983) identified three reasons which make the permeability anisotropic for most of the soils. They are, macro-stratification, micro-stratification, and flatness and orientation of particles. Anisotropy caused by macro-stratification can be estimated using thickness and permeability values of each layer, but for the micro stratification, in situ pumping test is required. The third one, effect of flatness and orientation can also be quantified using the measurements of number of particles (Witt and Brauns 1983). Hatanaka et. al. (1997; 2001) studied high quality undisturbed sands and gravelly soils and found that permeability in horizontal direction is larger than that of the vertical. However, maximum deference observed was 70%, and hence, sandy or gravelly soils can be assumed as isotropic in general. Therefore, in cofferdam designing, soil anisotropy is mainly encountered when the founding soil consists of layered (stratified) soil systems. For these stratified soil systems, considering an equivalent permeability is required.

#### Equivalent permeability in stratified soil

Consider the stratified soil system shown in Fig. 2.3 consisting of  $n$  homogeneous and isotropic soil layers with thickness of  $d_1, d_2, \dots, d_n$ . Here, coefficients of permeability of individual layers are  $k_1, k_2, \dots, k_n$ . For horizontal flow direction (in the direction of stratification), total flow  $q$  through the cross-section of unit thickness in unit time can be written as:

$$q = v(d \times 1) = v_1(d_1 \times 1) + v_2(d_2 \times 1) + \dots + v_n(d_n \times 1) \quad (2.11)$$

where,

$v$  = average discharge velocity through the entire soil bed

$d$  = sum of the thickness of each layer

$v_1, v_2, \dots, v_n$  = discharge velocities of flow in layers 1, 2, ..., and  $n$ , respectively.

From Darcy's law,

$$v = k_{H(eq)}i_{eq}; v_1 = k_1i_1; v_2 = k_2i_2; \dots v_n = k_ni_n \quad (2.12)$$

where,

$k_{H(eq)}$  = equivalent permeability in horizontal direction

$i_{(eq)}$  = equivalent hydraulic gradient

$i_1, i_2, \dots, i_n$  = hydraulic gradient through layers of 1, 2, ..., and  $n$  respectively.

For the horizontal flow,

$$i_{eq} = i_1 = i_2 = \dots = i_n \quad (2.13)$$

Substitution of velocity and hydraulic gradient relations given in Eq. 2.12 and 2.13, respectively in Eq. 2.11 gives  $k_{H(eq)}$  as:

$$k_{H(eq)} = \frac{1}{d}(k_1d_1 + k_2d_2 + \dots k_nd_n) \quad (2.14)$$

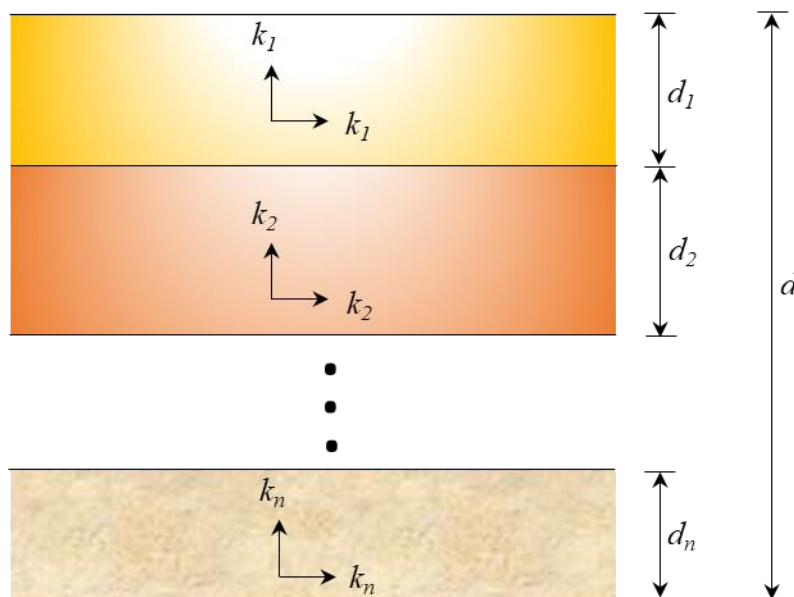


**Fig. 2.3** Equivalent permeability determination in stratified soil

For the vertical flow (in the perpendicular direction to the stratification), flow velocity is the same through all layers, and hence,

$$v = v_1 = v_2 = \dots = v_n \quad (2.15)$$

Applying Darcy's law, Eq. 2.15 becomes,

$$k_{v(eq)} \frac{h}{d} = k_1 \frac{h_1}{d_1} = k_2 \frac{h_2}{d_2} = \dots = k_n \frac{h_n}{d_n} \quad (2.16)$$

where,

$h$  = sum of the head losses in each layer

$h_1, h_2, \dots, h_n$  = head loss in layers 1, 2, ..., and  $n$ , respectively.

Also,

$$h = h_1 + h_2 + \dots + h_n \quad (2.17)$$

Solving Eqs. 2.16 and 2.17,  $k_{V(eq)}$  can be obtained as:

$$k_{V(eq)} = \frac{d}{\left(\frac{d_1}{k_1}\right) + \left(\frac{d_2}{k_2}\right) + \dots + \left(\frac{d_n}{k_n}\right)} \quad (2.18)$$

From Eqs. 2.14 and 2.18, it can be showed that the equivalent permeability in horizontal direction  $k_{H(eq)}$  is greater than that in vertical direction  $k_{V(eq)}$ . Harr (1962) proved this for two layers. In this dissertation, it is extended to three layers system where  $d_1, d_2, d_3$  and  $k_1, k_2, k_3$  are the thickness and coefficients of permeability of each layer, respectively. Assuming  $d_1/d_2 = \delta$  and  $d_2/d_3 = \beta$ , and using Eqs. 2.14 and 2.18  $k_{H(eq)} > k_{V(eq)}$  can be written as:

$$\frac{k_1\delta + k_2 + k_3/\beta}{\delta + 1 + 1/\beta} > \frac{\delta + 1 + 1/\beta}{\delta/k_1 + \delta/k_2 + 1/\beta k_3} \quad (2.19)$$

Then, Eq. 2.19 simplifies to the true statement given by:

$$k_3\beta^2\delta(k_1 - k_3)^2 + k_2\delta\beta(k_1 - k_3)^2 + k_1\beta(k_2 - k_3)^2 > 0 \quad (2.20)$$

Similarly, it can be proved that  $k_{H(eq)} > k_{V(eq)}$  for a layered system having any number of homogeneous and isotropic layers.

Griffiths (1984) introduced a factor  $R$  to treat the permeability anisotropy of the homogeneous single layer soil medium as:

$$R = \sqrt{k_V/k_H} \quad (2.21)$$

where  $k_V$  and  $k_H$  are the permeability coefficients of vertical and horizontal directions of soil medium, respectively. Therefore, seepage solution for the cofferdam where founding soil medium consists of thin, homogeneous and isotropic (within the layer) soil layers can be obtained considering the equivalent anisotropy factor  $R_{eq}$  given by:

$$R_{eq} = \sqrt{k_{V(eq)}/k_{H(eq)}} \quad (2.22)$$

### 2.3 Darcy' law and range of validity

A French engineer, Henry Darcy (1856) [vide Verruijt (1970)] proved a linear relationship between discharge velocity  $v$  and hydraulic gradient  $i$  for the laminar state flow as:

$$v = ki \quad (2.23)$$

The range where the Darcy's law is valid has been studied extensively using experimental works, and a detailed summary of these is given in Muskat and Wyckoff (1937). Reynolds (1883) observed that the relation between  $i$  and  $v$  is linear only at small velocities (laminar flow), and flow becomes irregular with increasing flow velocities. Also, he proposed a relationship between  $i$  and  $v$  for this condition as:

$$i = a_1v + b_1v^{n_1} \quad (2.24)$$

where  $a_1$  and  $b_1$  are constants.  $n_1$  is a variable between 1 and 2. However Lindquist (1933) [vide Harr (1977)] reported that  $n_1$  is exactly 2.

### 2.3.1 Reynolds number

Reynolds number  $R_e$  is the criteria used to determine the laminar range where the Darcy's law is valid. There is a critical value for the Reynold number  $R_{ecr}$ , beyond which flow velocity  $v$  is no longer lineally proportional to the  $i$ . This concept was originally proposed by Stokes (1851), but the term, Reynolds number is introduced by Sommerfeld (1908) [vide (Rott 1990)] considering its extensive applications by Reynolds (1883) for studying the flow behaviour through pipes and is defined as:

$$R_e = \frac{vD\rho}{\mu} \quad (2.25)$$

where,

$v$  is the discharge velocity, cm/s

$D$  is the diameter of the median grain size, cm

$\rho$  is the density of water, g/cm<sup>3</sup>

$\mu$  is the dynamic viscosity of water, g/cm.s

#### Critical Reynolds number ( $R_{ecr}$ )

In literature, a wider range of values has been suggested by various researches for the critical Reynolds number. For instance, the range was between 1 and 15 according to Bear (1972), Hassanizadeh and Gray (1987) and Ma and Ruth (1993) while it extends to 75 according to Scheidegger (1958). However, Muskat and Wyckoff (1937) recommended to consider Reynolds number equals to 1 as a safe lower limit ensuring the flow is laminar. Also, it was noted that the Reynolds number at which flow becomes turbulent is much higher than the critical Reynolds number where the flow regime transfers from the Darcy flow to the nonlinear laminar flow condition (Chauveteau and Thirriot 1967; Seguin et al. 1998). Seguin et al. (1998) mentioned that the flow regime transition from Darcy flow to nonlinear laminar flow and

finally, nonlinear laminar flow to turbulent flow in a gradual process. Also, several researchers (Venkataraman and Rao 1998; Sidiropoulou et al. 2007; Moutsopoulos et al. 2009; Sedghi-Asl et al. 2014; Salahi et al. 2015; Li et al. 2017) have shown that this process can be represented by the Forchheimer equation (Forchheimer 1901). According to Cedergren (1977), Forchheimer equation can be presented in more general form and is given by:

$$i = av + bv^2 \quad (2.26)$$

where  $a$  and  $b$  are constants and can be estimated through curve fitting. Van Lopik et al. (2017) showed that constant  $a$  equal to the reciprocal of the permeability ( $a = 1/k$ ), and hence, linear section of the flow where the Darcy's law is valid can be written as:

$$i = av \quad (2.27)$$

Several studies have proposed empirical relationships for estimating the  $a$  and  $b$ , and a summary of them is given in Table 2.3.

#### Recent studies on critical Reynolds number

Recently, Van Lopik et al. (2017) studied nonlinear behaviour of uniformly graded coarse material ranged from medium sands to gravel, considering 11 samples where median grain size  $d_{50}$  varied between 0.39 mm to 6.34 mm. They found that Eq. 2.26 accurately predicts the nonlinear flow behaviour in all the cases, and the critical Reynolds number ranged between 2.21 to 4.13 falling within the limit 1-15 recommended in the literature. Also, for sands, corresponding critical discharge velocities varied between 0.21 cm/s to 0.71 cm/s and increases while  $d_{50}$  value decreases. However, they have not studied the effect of relative density and shape of the particle on the critical Reynolds number. Therefore, a laboratory study was conducted in this dissertation, in an attempt to study the effects of relative density and particle shape on critical Reynolds number.

**Table 2.3** Empirical relationships for the Forchheimer coefficients of  $a$  and  $b$  determination

[adopted from (Van Lopik et al. 2017)]

Proposed by	$a$ (s/m)	$b$ (s <sup>2</sup> /m <sup>2</sup> )
Schneebeil (1955)	$1100 \frac{\eta}{gd^2}$	$12 \frac{1}{gd}$
Ward (1964)	$360 \frac{\eta}{gd^2}$	$10.44 \frac{1}{gd}$
Ergun-type	$A \frac{(1-n)^2 \eta}{gn^3 d^2}$	$B \frac{(1-n)}{gn^3 d}$
Carman (1937)	$A = 180$	-
Ergun (1952)	$A = 150$	$B = 1.75$
Kovacs (1981)	$A = 144$	$B = 2.4$
Macdonald et al. (1979)	$180 \frac{(1-n)^2 \eta}{gn^{3.6} d^2}$	$1.8 \frac{(1-n)}{gn^{3.6} d}$
Kadlec and Knight (1996)	$255 \frac{(1-n)\eta}{gn^{3.7} d^2}$	$2 \frac{(1-n)}{gn^3 d}$
Sidiropoulou et al. (2007)	$0.0033d^{-1.5}n^{0.0603}$	$0.194d^{-1.27}n^{-1.14}$
Geertsma (1974)	-	$\frac{0.005}{g} (\bar{K}10000)^{-0.5}n^{-5.5}$

where,  $\eta$  is the kinematic viscosity (m<sup>2</sup>/s),  $d$  is the median particle diameter (m),  $n$  is the porosity,  $g$  is the acceleration due to gravitational force (m/s<sup>2</sup>), and  $\bar{K}$  is the absolute permeability (m<sup>2</sup>).

### 2.3.2 Laboratory study on Reynolds number

The study was conducted using three types of material, namely zeolite, Leighton Buzzard sand, and glass beads. For each of the samples tested, index properties (moisture content, particle size distribution, specific gravity, minimum and maximum density values) were determined as

per the Australian standards and are given in Table 2.4. All three samples are uniformly graded, and glass beads and Leighton Buzzard sand are similar in grain size distribution as shown in Fig. 2.4. Also, it was observed that the glass beads consist of well rounded particles compared to other two material studied.

**Table 2.4** Determined index properties

Index property	Sample Name		
	Zeolite (A)	Leighton Buzzard sand (B)	Glass beads (C)
Moisture content (%)	4.0	0.10	0.10
$d_{10}$ (mm)	1.71	0.64	0.62
$d_{30}$ (mm)	1.75	0.74	0.72
$d_{50}$ (mm)	1.80	0.85	0.85
$d_{60}$ (mm)	1.85	0.90	0.90
$C_u$	1.08	1.41	1.45
$C_c$	0.97	0.95	0.93
Specific gravity	2.42	2.64	2.49
Minimum density (g/cm <sup>3</sup> )	1.15	1.53	1.49
Maximum density (g/cm <sup>3</sup> )	1.28	1.75	1.56

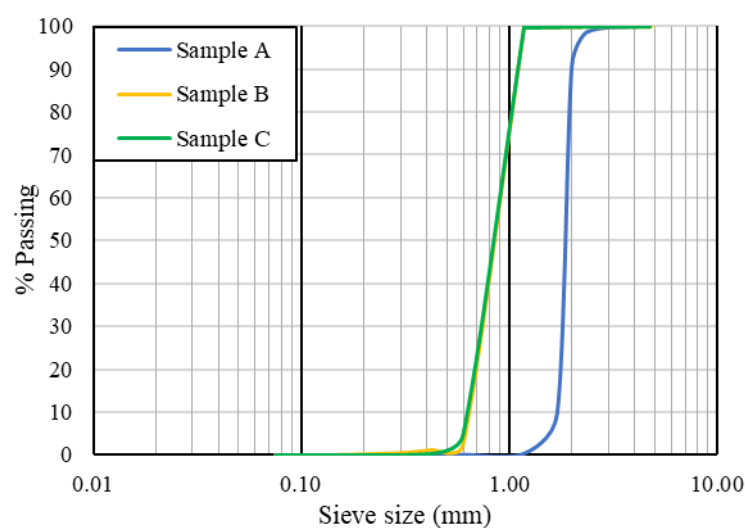


**Fig 2.4** Grain size distributions for three samples

Constant head permeability tests were conducted to study the flow behaviour for all three samples since material used are coarse-grained. The permeameter and constant head test set-up were designed as per the Australian standard AS 1289.6.7.1 and are shown in Figs. 2.5 and 2.6, respectively. The inner diameter of the permeameter was 100 mm while length of the sample height studied was 258 mm. Five tests were conducted at different relative density values covering two for zeolite at 69% and 90%, one for Leighton Buzzard sand at 50%, and two for glass beads at 23% and 83%.

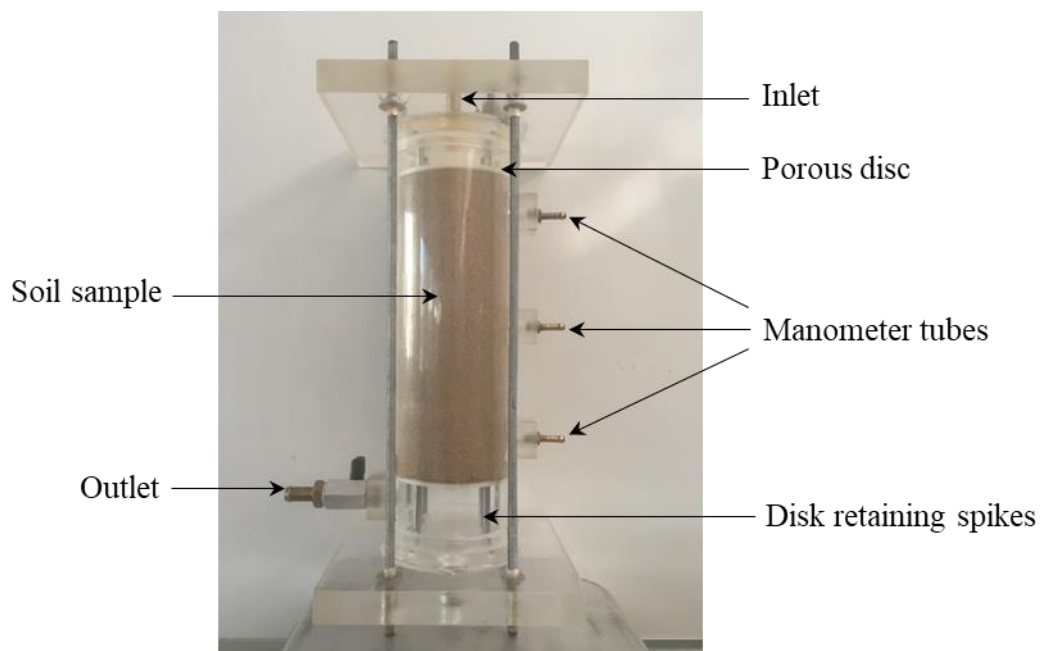


**Fig. 2.5** Permeameter apparatus

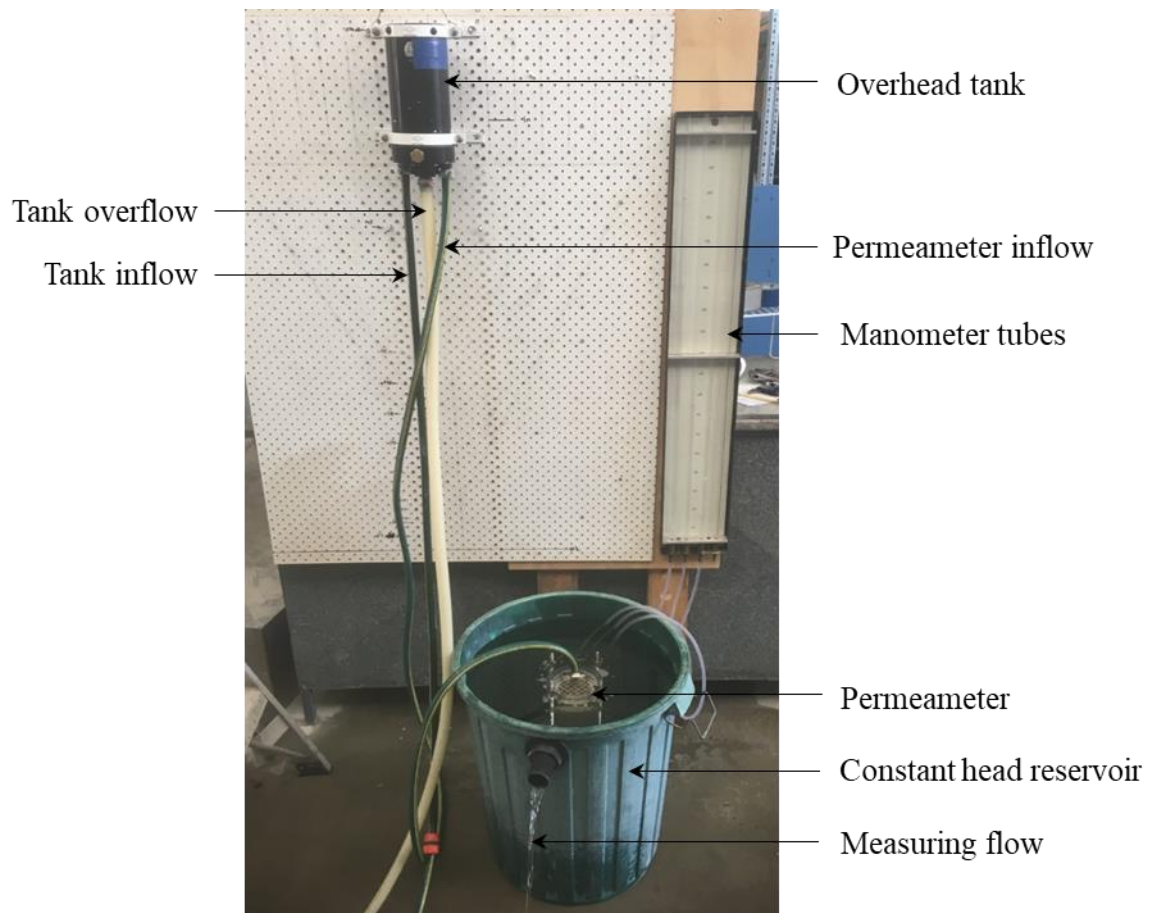


**Fig. 2.6** Constant head permeability test set-up

### Laboratory test results

For each test, discharge velocity  $v$  values were determined for a range of hydraulic gradient  $i$  values changing the height of the overhead tank shown in Fig. 2.6, and observed  $i - v$  plots for all five tests are shown in Fig. 2.7. Flow behaviors of all five cases given in Fig. 2.7 show an excellent agreement ( $R^2 > 0.99$ ) to the Forchheimer relation described by Eq. 2.26. Linear flow behaviour described by Darcy's law ( $i = av$ ) is also plotted in each case to show the deviation of flow from linear to nonlinear while increasing the flow velocity. Then Reynolds number was calculated using the discharge velocity given by Forchheimer relation at which relative difference between Forchheimer and Darcy's velocity is 5%. This criteria was defined by Van Lopik et al. (2017). In addition, minimum and maximum Reynolds number were also computed

using the minimum and maximum discharge velocity values obtained for each test, and the summary of the results including Forchheimer coefficients for each case is given in Table 2.5.

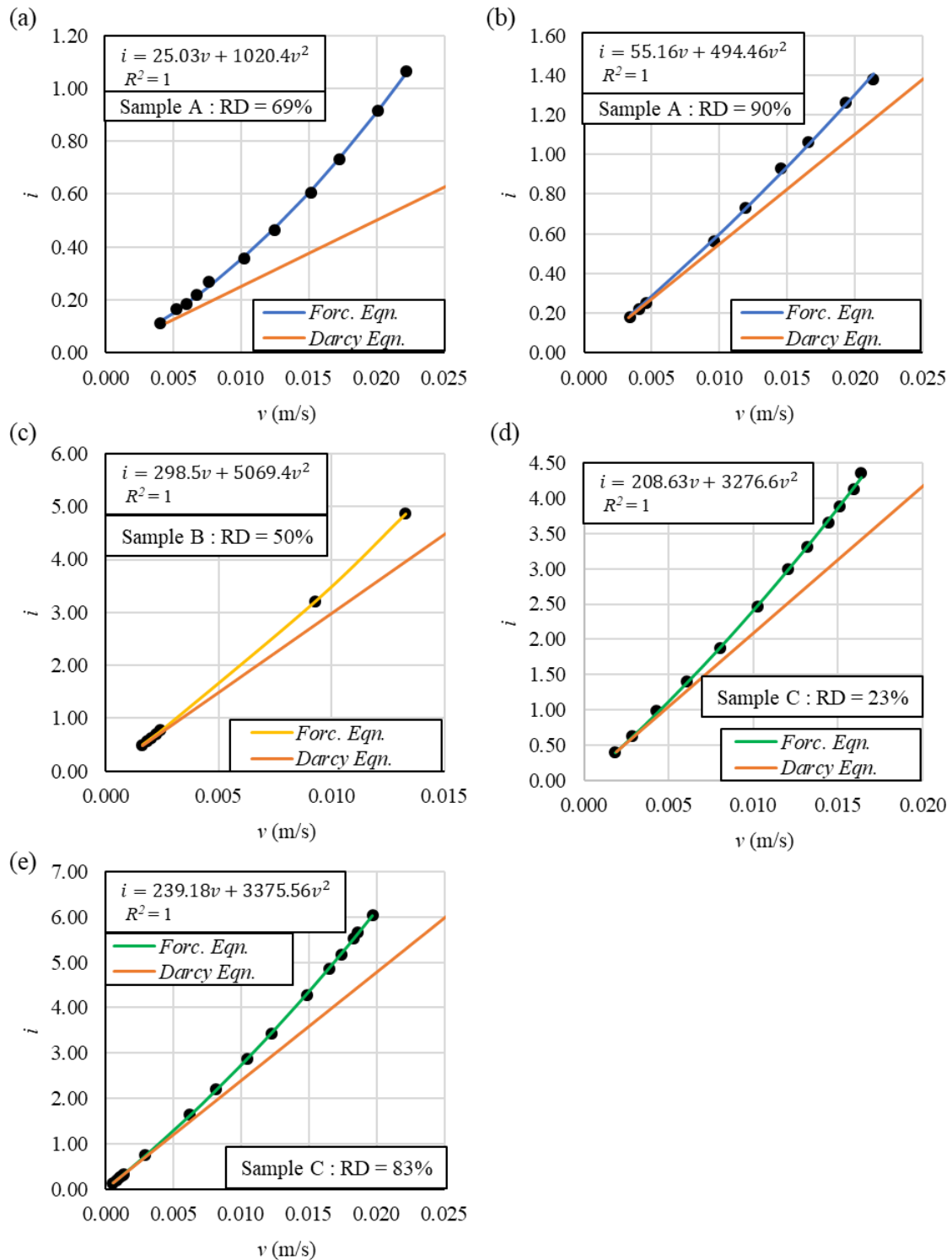


Fig. 2.7 Observed Darcy and nonlinear flow behaviours

**Table 2.5.** Summary of the test results

Sample	$d_{50}$	$D_r$ (%)	Forc. Coeff.		Darcy Coeff. $a$ ( $\text{sm}^{-1}$ )	Discharge velocity $v$ ( $\text{ms}^{-1}$ )			$R_{emin}$	$R_{emax}$	$R_{ecr}$
			$a$ ( $\text{sm}^{-1}$ )	$b$ ( $\text{s}^2\text{m}^{-2}$ )		$v_{min}$	$v_{max}$	$v_{cri}$			
A	1.80	69	25.0	1020.4	-	0.0040	0.0222	0.0012	7.2	39.9	2.2
	1.80	90	55.2	494.5	53.9	0.0034	0.0214	0.0056	6.1	38.5	10.0
B	0.85	50	298.5	5069.4	310.0	0.0016	0.0133	0.0029	1.4	11.3	2.5
C	0.85	23	208.6	3276.6	-	0.0018	0.0164	0.0032	1.6	13.9	2.7
	0.85	83	239.2	3375.5	249.9	0.0005	0.0197	0.0035	0.5	16.8	3.0

Results in Table 2.5 show that critical Reynolds numbers obtained in this study are between 2.2 to 10.0 falling to the ranged recommended in the literature (1-15). Also, it increases with increasing the relative density  $D_r$  for a given sample (see Sample A and C). Further, critical Reynolds number for sample C is slightly higher than the sample B value, even though both samples are more or less identical in grain size distributions. This may be due to the pore structure difference between samples B and C since sample C particles are well rounded compared to the sample B. Also, it is noted that, effect of relative density of sample A is significant compared to that for the sample C. This was evident by larger deviations of critical Reynolds numbers and Forchheimer coefficients when relative density changing from 69% to 90% of sample A while there is only a slight change in the critical Reynolds number and Forchheimer coefficients for the sample C with larger difference of relative density (23% to 83%) between two tests. This is also due to the pore structure difference at different relative density values. Sample C pore structure does not influence much with increasing relative density compared to the sample A since sample C particles are well rounded compared to the sample A. Also, critical velocity obtained for sand (sample B) in this study was 0.29 cm/s and is comparable to the values calculated for Van Lopik et al. (2017).

Further, there were multiple data points (more than 2 points) in Darcy region (velocity less than critical discharge velocity) for the tests of sample A at relative density 90%, sample B at relative density 50% and sample C at relative density 83%. Therefore, these points were plotted in ( $i$ - $v$ ) graphs as shown in Fig. 2.8 and Darcy's coefficient  $a$  values were obtained for each case through the linear regression analysis. These results (Darcy's coefficient  $a$  values) were well comparable with the Forchheimer coefficients shown in Table 2.5 with the maximum relative error of 4%. This is similar to the agreement observed by Van Lopik et al. (2017).

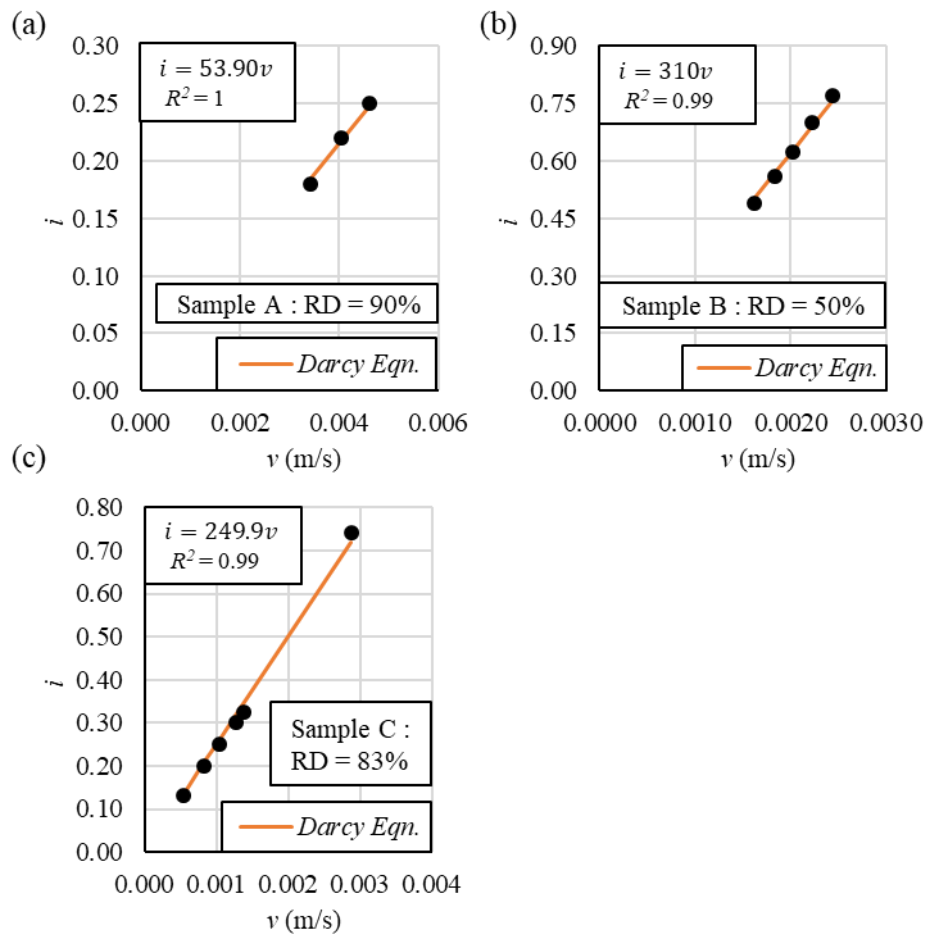


**Fig. 2.8**  $i$ - $v$  plots for laminar flow regime

In summary, it is observed that Forchheimer equation represents nonlinear flow behavior more accurately, and assuming critical Reynolds number equals to one provides conservative upper limit for laminar flow regime in sandy soils. Also, critical velocity beyond which flow becomes nonlinear fall within 0.2 cm/s - 0.7 cm/s in most of the sandy soils. However, Holtz and Kovacs (1981) concluded that, water flow velocity in most soils is adequately smaller compared to the observed velocity (0.2 cm/s - 0.7 cm/s), and hence, considering the laminar flow is a reasonable assumption in cofferdam seepage analysis in sands. Also, they mentioned that water is relatively incompressible for stress levels encountered in most seepage problems. Therefore, validity of Darcy's law and soil/water incompressibility are reasonable assumptions for studying the seepage into cofferdams.

## **2.4 Hydraulic failure mechanisms of cofferdams**

McNamee (1949) identified two excavation base failure mechanisms, namely, local failure and general upheaval. Local failure, also known as piping failure, initiates at the point downstream where the uppermost stream line emerges, i.e., next to the sheet pile wall on the excavation base. Although piping initiation involves only a small volume of soil, it progresses up to the upstream side, forming a free water channel and makes the structure fails within a short period. Conversely, general upheaving is a widespread failure where a soil prism adjacent to the sheet pile wall rises due to the upward hydraulic pressure acting on the prism base. This failure mechanism is known as heaving.

### **2.4.1 Piping failure mechanism**

Harza (1935) studied the piping mechanism for hydraulic structures. It is more likely to happen in non-cohesive soil, and he suggested that the critical condition occurs when exit hydraulic

gradient  $i_E$  is equal to the critical hydraulic gradient of soil  $i_c$ . Thus, he defined the factor of safety against piping  $F_p$  as:

$$F_p = \frac{\text{Critical hydraulic gradient } (i_c)}{\text{Maximum exit hydraulic gradient}(i_E)} \quad (2.28)$$

As noted before in Sec. 1.2, for the cofferdams,  $i_E$  is the exit gradient at the excavation base adjacent to sheet pile wall. The critical hydraulic gradient  $i_c$  is the hydraulic gradient at which effective stress become zero, i.e., soil is at the boiling condition (Reddi 2003). Then,  $i_c$  is given by:

$$i_c = \frac{G_s - 1}{1 + e} \quad (2.29)$$

where,  $G_s$  and  $e$  are the specific gravity and void ratio, respectively.

#### 2.4.2 Heaving failure mechanism

Heaving mechanism was studied by Terzaghi (1943) using model tests for a single row of sheet piles. He found that the zone which is susceptible to heave is a prism adjacent to the sheet pile as shown in Fig. 2.9. He assumed that at the instant of failure, no frictional resistance between soil and the sheet pile wall, and hence, he defined the factor of safety against heaving ( $F_h$ ) as:

$$F_h = \frac{W'}{U} \quad (2.30)$$

where,  $W'$  is the submerged weight of the soil prism and  $U$  is the hydraulic uplift pressure.

Considering the unit thickness of the prism, Eq. 2.30 can be written as:

$$F_h = \frac{\frac{1}{2}\gamma' s^2}{\frac{1}{2}\gamma_w s h_a} = \frac{s\gamma'}{h_a\gamma_w} \quad (2.31)$$

where,  $\gamma'$  is the submerged unit weight of soil,  $\gamma_w$  is the unit weight of the water, and  $h_a$  is the average hydraulic (pressure) head at the prism base. Also, Terzaghi (1943) recommended

considering several prisms for other type of structures varying the prism height  $s'$  as  $0 < s' \leq s$  to determine the minimum safety factor value. However, Harr (1962) suggested to use Eq. 2.31 applying the factor of safety value of the order of 4 to 5 for other structures; therefore, Eq. 2.31 can be applied for cofferdam problems discussed in this dissertation, too.

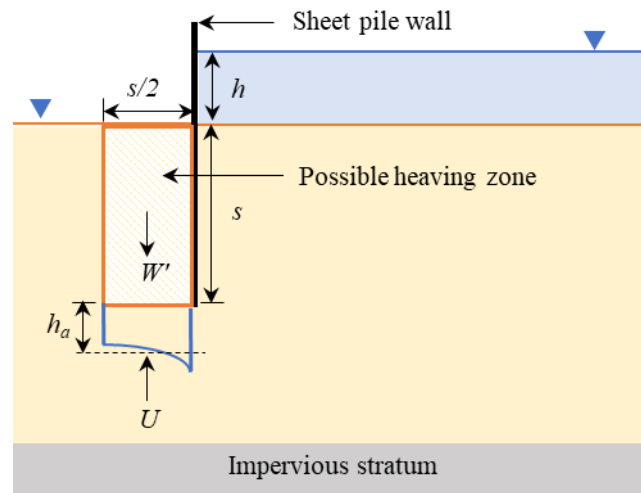


**Fig. 2.9** Failure due to heaving in front of a single row of sheet pile (Das 2013)

### 2.4.3 Critical failure mechanism

Out of the two mechanisms described above, it is not possible to determine which one is more likely to happen in a particular condition (McNamee 1949). However, he suggested that the piping is the criteria for the wider excavations while heaving is for the narrow excavations in homogeneous sand. Marsland (1953) conducted model experiments to determine the failure mode for the double-walled cofferdam geometry shown in Fig. 2.10 using both dense and loose homogeneous sands. In his extensive studies, it was concluded that in loose sand, heaving is the failure mode for narrow cofferdams while piping is for the wider cofferdams. Here, he defined a narrow cofferdam in such a way that  $D_1 > 2L$ , i.e., depth of sheeting penetration  $D_1$  is greater than cofferdam width  $2L$ . Further, in dense sand, he observed that piping was the dominant failure mode in both narrow and wider geometries.

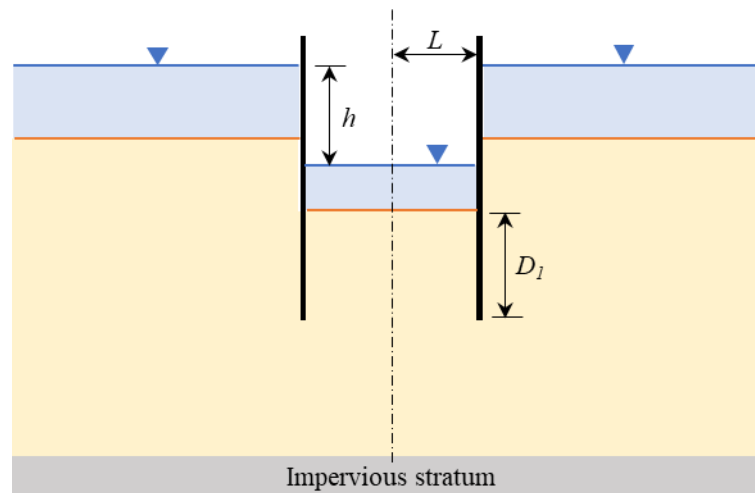


**Fig. 2.10** Experimental model geometry studied by Marsland (1953)

Considering all, it can be concluded that piping is the most common failure mode except the case of narrow excavations in loose sands. However, narrow excavations are rarely applicable in practice since they are not economical, and hence, piping failure is the most significant excavation base failure mode in cofferdams. Therefore, excavation base stability assessment against heaving failure will not be considered specifically in this dissertation. Consequently, total flow rate  $Q$  and maximum exit hydraulic gradient  $i_E$  are two important parameters to be determined for designing the cofferdams of any shape.

## 2.5 Seepage solution methods for cofferdams

There are various solution methods available for finding  $Q$  and  $i_E$ , but their applicability varies depending on the cofferdam shape. In all these methods, validity of Darcy' law and soil/water incompressibility are assumed (Cedergren 1977), and also, the steady state condition is considered.

### 2.5.1 Seepage solution methods for double-walled cofferdams

Seepage solution methods for double-walled cofferdams involve solving a Laplace equation in the two-dimensional Cartesian plane. Consider the flow element shown in Fig. 2.11 where the thickness is one unit.

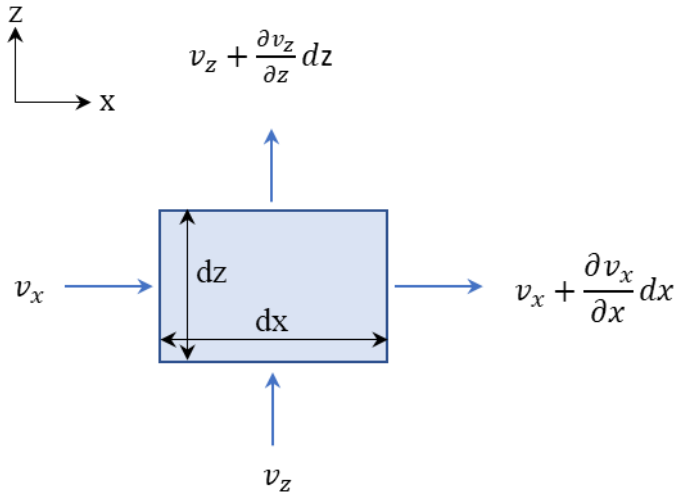


**Fig. 2.11** Flow element in two-dimensions

Under steady state condition, no change in storage, and hence, flow into the element should equal to the flow out. Therefore;

$$v_x(dz \cdot 1) + v_z(dx \cdot 1) = \left(v_x + \frac{\partial v_x}{\partial x} dx\right)(dz \cdot 1) + \left(v_z + \frac{\partial v_z}{\partial z} dz\right)(dx \cdot 1) \quad (2.32)$$

where  $v_x$  and  $v_z$  are the velocity of flow in  $x$  and  $z$  directions, respectively. Then, Eq. 2.32 further simplifies to:

$$\frac{\partial v_x}{\partial x} + \frac{\partial v_z}{\partial z} = 0 \quad (2.33)$$

Using Darcy's law in generalize form (Verruijt 1970) ,

$$v_x = k_x \frac{\partial h}{\partial x} \text{ and } v_z = k_z \frac{\partial h}{\partial z} \quad (2.34)$$

where  $k_x$  and  $k_z$  are permeability coefficients of  $x$  and  $z$  directions, respectively, and  $h$  is the total hydraulic head. From Eqs. 2.33 and 2.34,

$$k_x \frac{\partial^2 h}{\partial x^2} + k_z \frac{\partial^2 h}{\partial z^2} = 0 \quad (2.35)$$

For the isotropic soil,  $k_x = k_z$ , and hence, Eq. 2.35 simplifies to:

$$\frac{\partial^2 h}{\partial x^2} + \frac{\partial^2 h}{\partial z^2} = 0 \quad (2.36)$$

This is the Laplace equation for 2D seepage problems. For the anisotropic soils, Eq. 2.35 can be rewritten to the form given by:

$$\frac{\partial^2 h}{(k_z/k_x)\partial x^2} + \frac{\partial^2 h}{\partial z^2} = 0 \quad (2.37)$$

Considering the substituting  $x' = \sqrt{k_z/k_x} x$ , Eq. 2.37 simplifies to the form of Laplace equation as:

$$\frac{\partial^2 h}{\partial x'^2} + \frac{\partial^2 h}{\partial z^2} = 0 \quad (2.38)$$

There are three possible ways that can solve the Laplace equation in two-dimensional form for cofferdam seepage problems in Cartesian plane. A graphical solution (drawing a flow net) is a one method while analytical solutions or numerical simulations using finite element or finite difference software are the other two methods.

### Flow net solutions

This is an approximate solution method and was formalized by Casagrande (1937). A flow net consists of flowlines (stream lines) and equipotential lines. A flow line represents the path of a water molecule starting at upstream side and finishing at downstream. The area covered by two adjacent flow lines is known as a flow channel. An equipotential line joins the points of same total head and intersects flow lines at  $90^\circ$ . There are thousands of flow lines, but for a flow net, small number of flow lines (3-5) are drawn ensuring the same flow within each flow channel.

Equipotential lines are selected maintaining the same total head difference between two adjacent equipotential lines. Fig. 2.12 shows the flow net of the double-walled cofferdam for the example 2.3 discussed in Craig (2004) founding in an isotropic soil medium. This was generated using the finite element package, *RS2 9.0*.

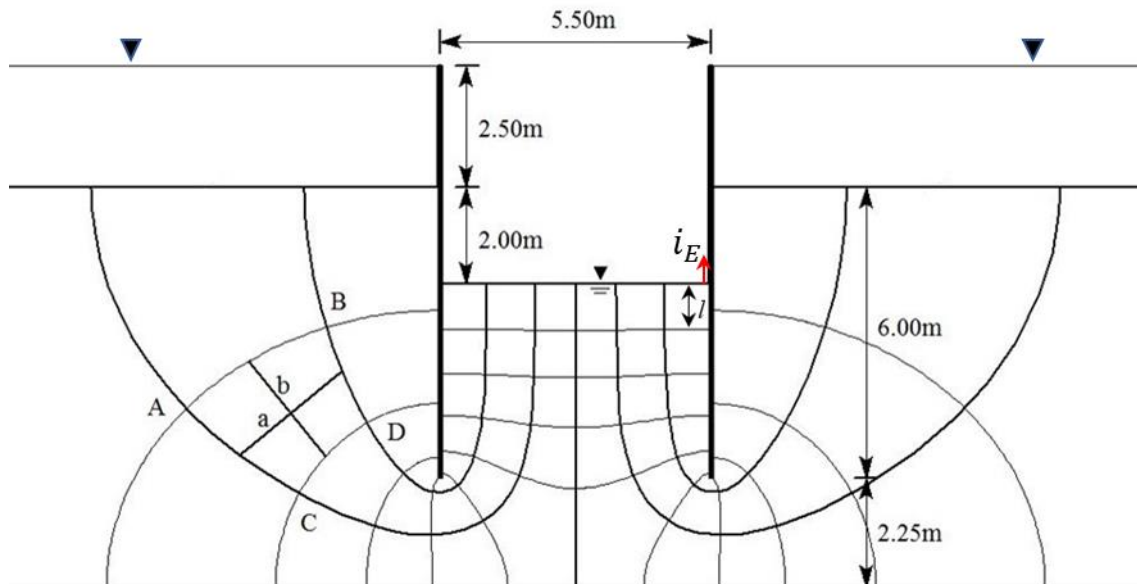


**Fig. 2.12** Flow net for the double-walled cofferdam in 2D Cartesian plane (Craig 2004)

The total flow rate  $Q$  can be computed from the above flow net as follows. Considering the zone ABCD bounded by two adjacent equipotential lines and two adjacent flow lines, flow velocity from AB to CD  $v_{AB-CD}$  can be written as:

$$v_{AB-CD} = k \frac{h_{AB-CD}}{b} \quad (2.39)$$

where,  $k$  is the soil permeability, and  $h_{AB-CD}$  is the head loss from AB to CD. Typically, this is analysed in 2D Cartesian co-ordinates system (treating the third dimension as infinite), and the flow rate through the zone ABCD  $\Delta q$  is calculated by considering a unit thickness perpendicular to the plane as:

$$\Delta q = k \frac{h_{AB-CD}}{b} \quad (a.1) \quad (2.40)$$

Since there are six flow channels, and the flow rate through each channel should be the same, the total flow rate  $Q$  per unit thickness perpendicular to the plane becomes:

$$q = 6kh_{AB-CD} \frac{a}{b} \quad (2.41)$$

Also head loss over two adjacent equipotential lines  $h_{AB-CD}$  can be written as:

$$h_{AB-CD} = \frac{h}{N_d} \quad (2.42)$$

where  $h$  is the total head loss over the cofferdam, and  $N_d$  is the number of equipotential drops.

Therefore, total flow rate  $Q$  can be written in a more general form as:

$$Q = kh \frac{N_f a}{N_d b} \quad (2.43)$$

where  $N_f$  is the total number of flow channels. Besides, flow nets are drawn forming curvilinear squares at every location ( $a/b = 1$  over entire flow net), and hence, Eq. 2.43 can be simplified further to:

$$Q = kh \frac{N_f}{N_d} \quad (2.44)$$

For the anisotropic soils, it requires to consider transformed section in horizontal direction multiplying the horizontal dimensions by  $\sqrt{k_V/k_H}$  where  $k_V$  and  $k_H$  are permeability coefficients of horizontal and vertical directions. Then, flow net can be drawn on transformed section using the similar procedure described above, and flow rate can be calculated using the Eq. 2.44, but  $k$  value should be considered as  $\sqrt{k_V \times k_H}$ . Also maximum exit hydraulic gradient can be estimated using the distance between last two equipotential lines  $l$  in the downstream side (see Fig. 2.12) and is given by:

$$i_E = \frac{h}{N_D l} \quad (2.45)$$

Thus, it is clear that drawing a flow net is a trial and error process, and time can be wasted if the person who draws a flow net has less experience. Further, any small change in geometry requires that the entire flow net be redrawn. In addition, when the soil anisotropy is encountered, the complexity of drawing a flow net increases. Therefore, flow net solution is not a straight forward method.

### Analytical solutions

Analytical solution involves conformal mapping technique using the Schwarz-Christoffel transformation. This method was originally proposed by Pavlovsky (1922). The first analytical solution for the double-walled cofferdam was given by Harr and Deen (1961) considering the case of infinitely deep pervious stratum. Later Harr (1962) proposed solution for the infinitely wide cofferdam where the pervious stratum is at a limited depth, i.e., for the single sheet pile wall. Next, King and Cockroft (1972) developed the solution for double-walled cofferdam problems for pervious stratum at limited depth, but only for the two special cases, i.e., no excavation and full excavation. For partially excavation, his solutions are only approximations. At last, Banerjee and Muleshkov (1992) presented solutions for complete problems; however, their solution is more conservative, compared to the previous solutions by Harr and Deen (1961) and King and Cockroft (1972). Also, all these solutions require computing elliptic integral using tables; therefore, analytical solutions are not a convenient method to use in practice.

### Numerical simulation

Using a finite element or finite difference software package, seepage solutions can be obtained. The numerical model required to simulate is only one-half of the cross section of double-walled

cofferdam considering the symmetry and is shown in Fig. 2.13. Here,  $L$  is the half-width of double-walled cofferdam. The analysis type is the plane strain. For the simulations, boundaries AB and CD should be considered as constant head boundaries with the total head difference of  $h$  while CE and EF are as impermeable boundaries. In addition, sheet piles are required to be simulated by a thin layer of material with its permeability being orders of magnitude lower than the soil. Several researchers have studied double-walled cofferdam seepage using a similar numerical model shown in Fig. 2.12 (Kavvas et al. 1992; Cai and Ugai 2004).

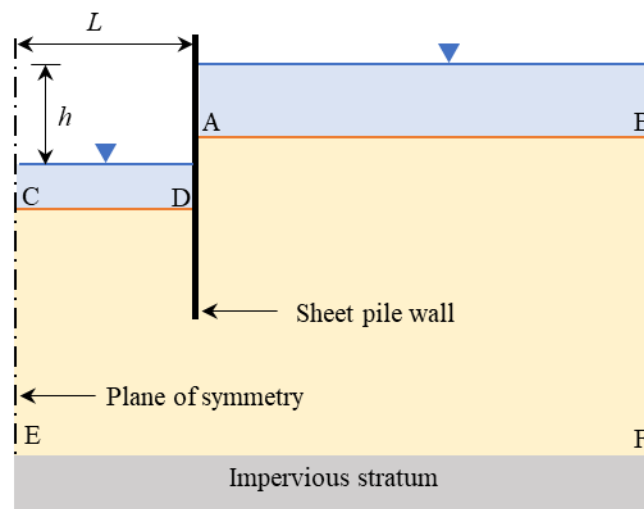


**Fig. 2.13** Numerical model geometry for double-walled cofferdams

### 2.5.2 Seepage solution methods for circular cofferdams

Flow into circular cofferdams is symmetrical around the vertical axis running through the centre of the cofferdam. Therefore, circular cofferdam problems require to be analysed in a radial vertical plane of the cylindrical coordinate system (axisymmetric plane) as shown in Fig. 2.14. Since, the cofferdam is axially symmetrical, soil properties and boundary conditions do not change with  $\theta$ . Therefore, seepage solution methods involve solving a continuity equation given by (Muskat 1938; Neveu 1972; Rao 1999; Merry and Du 2014):

$$\frac{1}{r} \frac{\partial}{\partial r} \left( r k_r \frac{\partial h}{\partial r} \right) + \frac{\partial}{\partial z} \left( k_z \frac{\partial h}{\partial z} \right) = 0 \quad (2.46)$$

where,  $k_r$  and  $k_z$  are permeability coefficients of  $r$  (radial) and  $z$  (vertical) directions, respectively, and  $h$  is the total hydraulic head. For isotropic soils, Eq. 2.46 further simplifies as:

$$\frac{1}{r} \frac{\partial}{\partial r} \left( r \frac{\partial h}{\partial r} \right) + \frac{\partial^2 h}{\partial z^2} = 0 \quad (2.47)$$

Eq. 2.47 is the Laplace equation required to be solved for circular cofferdam seepage problems.

Also, in the anisotropic case, substituting  $r' = \sqrt{k_z/k_r} r$ , Eq. 2.47 can be expressed in Laplace form in the new transformed coordinate system as:

$$\frac{1}{r'} \frac{\partial}{\partial r'} \left( r' \frac{\partial h}{\partial r'} \right) + \frac{\partial^2 h}{\partial z^2} = 0 \quad (2.48)$$

Here, both Eq. 2.47 and 2.48 can also be solved using flow nets, analytical approach or numerical simulation using a computer package.

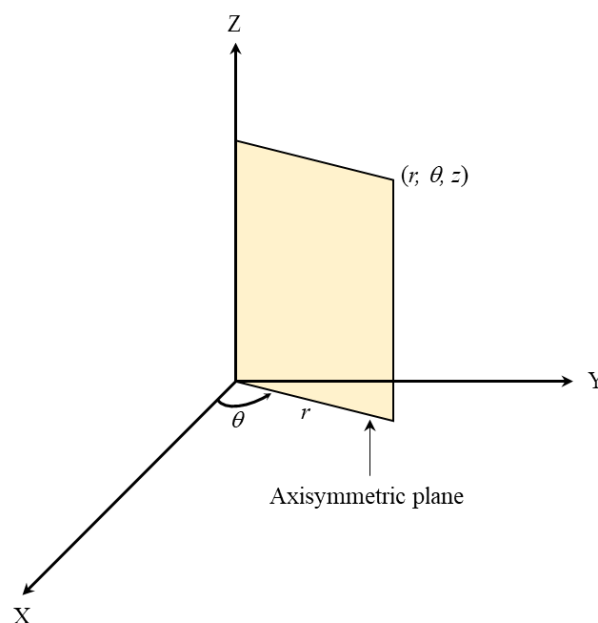


**Fig. 2.14** Axisymmetric plane in cylindrical coordinate system for circular cofferdams

Neveu (1972)

Flow net solutions

Drawing a flow net for circular cofferdam problem is a difficult task compared to the double-walled cofferdams. Here, it is required to consider the effect of 3D because flow rate estimation is per radian generally. Therefore, the zone bounded by two adjacent equipotential lines and two flow lines (see Fig. 2.12) for circular cofferdams should be satisfied the relation of  $\frac{a}{b}r_z = 1$  allowing the 3D effect at every zone, where the geometry configuration is in the unit of meter.  $r_z$  is the radial length to the center of the zone, from the axis of symmetry. Also, when the geometry is scaled up, all the flow lines have to be redrawn for axisymmetric flow nets while entire flow net remains unchanged for double-walled cofferdam. Thus, drawing a flow nets for axisymmetric case requires substantial effort and time compared to that for the double-walled cofferdam. A more detail description will be given on drawing a flow net for circular cofferdams in Chapter 4.

Analytical solutions

There is little specific literature on analytical solutions for circular cofferdams. Neveu (1972) solved Laplace equation in cylindrical form (Eq. 2.47) using Green's Theorem and developed design charts to estimate the flow rate into the circular cofferdams, but his solution does not provide exit gradient values. So, numerical simulation remains as the only method which can provide complete solutions required in practice.

Numerical simulation

For circular cofferdam also, a 2D finite element or finite difference software package can be used. The numerical model required, and the boundary conditions are similar to the case of double-walled cofferdams discussed in Sec. 2.5.1. In circular models, cofferdam radius  $r$  has to apply instead of  $L$  in double-walled models. The only difference is the analysis type, which

is the axisymmetric for circular cofferdams while plane strain is the required one for double-walled cofferdams. Using this simulation procedure, several researchers have studied circular cofferdam seepage problems (Miura et al. 2000; Bouchelghoum and Benmebarek 2011).

### 2.5.3 Seepage solution methods for square and rectangular cofferdams

For square and rectangular cofferdams, flow pattern is 3D, therefore, solution methods require solving Laplace equation in three-dimensional form. Considering an elementary soil prism with the dimensions of  $dx$ ,  $dy$  and  $dz$ , continuity equation in 3D form can be obtained using similar procedure discussed for double-walled cofferdams (Sec. 2.5.1) as:

$$k_x \frac{\partial^2 h}{\partial x^2} + k_y \frac{\partial^2 h}{\partial y^2} + k_z \frac{\partial^2 h}{\partial z^2} = 0 \quad (2.49)$$

For the isotropic soils, Eq. 2.49 can be rewritten as:

$$\frac{\partial^2 h}{\partial x^2} + \frac{\partial^2 h}{\partial y^2} + \frac{\partial^2 h}{\partial z^2} = 0 \quad (2.50)$$

There is no literatures available on flow net or analytical solutions for the square or rectangular cofferdam problems. However, Chien (1952) presented a generalized relaxation formula that can be used for making 3D flow nets, but it is more complicated compared to the 2D flow nets. Therefore, 3D numerical simulation using a finite element or finite difference computer package (e.g., Plaxis 3D, FLAC<sup>3D</sup>, RS3) is the widely used solution method for solving Laplace equation in 3D form.

#### Numerical simulation

Considering the symmetry, only one of the four quadrants needs to study for square and rectangular cofferdams. The geometry of the numerical model required to analyse for square cofferdam is shown in Fig. 2.15 where  $B$  is the half-width of square cofferdam,  $s$  is the depth of the sheet pile and  $T$  is the thickness of the soil layer. In the simulations, impermeable

boundaries are applied for the vertical surfaces (see planes ACDEFG and AHIIJKG of Fig. 2.15) considering the effect of symmetry, and for the bottom plane of the model. In addition, sheet pile wall can be simulated by a thin layer of material with its permeability being orders of magnitude lower than the soil. The ground level outside the excavation and excavation base level should be treated by constant head boundaries with the total head difference of  $h$ . For rectangular cofferdam, a similar model is applicable, and only difference required is to increase the half-length of one side keeping the shorter side with  $B$ . Koltuk and Iyisan (2013) and Koltuk et al. (2015) studied seepage into rectangular and square cofferdam, respectively using a similar model shown in Fig. 2.15.

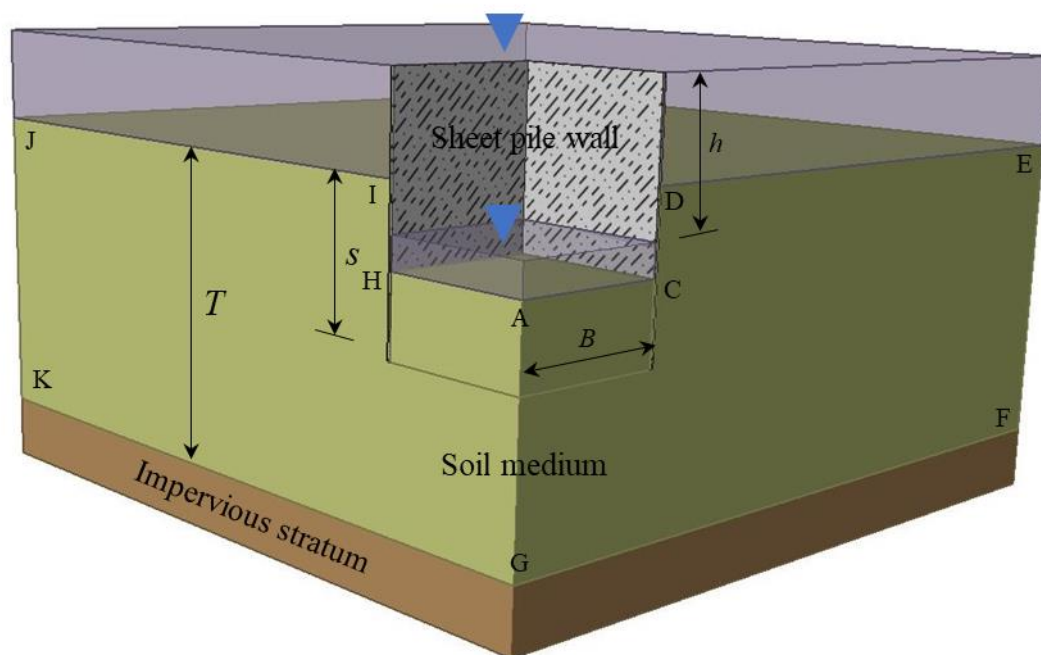


**Fig. 2.15** 3D numerical model geometry for square cofferdams

Considering all, it can be concluded that numerical simulation is the most powerful method for solving seepage problems for all cofferdam types considering the difficulties and limitations of the flow net and analytical solutions. As noted before, double-walled and circular cofferdam

problems can be studied using a 2D simulation package. For square and rectangular cases, 3D simulation is required, and hence, more expensive 3D computer package with technically sound person is required. Therefore, in practice, design charts developed using experimental or numerical analysis or approximate solutions based on method of fragments (MoF) are used most of the time, especially in preliminary stages of designs.

#### 2.5.4 Design charts

##### Double-walled cofferdams

Fox and McNamee (1948) proposed design charts on the basis of numerical solutions, providing the flow rate and exit gradient values for isotropic soils. Also, McNamee (1949) developed charts for estimating the maximum exit hydraulic gradient and penetration depth required using numerical solutions. Marsland (1953) presented design charts providing sheet pile penetration depth required to prevent piping or heaving failures for isotropic soils, and these charts have been applied by U.S. Department of the Navy (1982) as shown in Fig. 2.16.

##### Circular cofferdams

Koltuk and Azzam (2016) developed design charts for circular cofferdams enabling solution for heaving failure assessment using numerical simulations.

It was observed that most of the design charts available are for the case of double-walled cofferdams and to assess the potential of piping or heaving failure in isotropic soils. Also, no design charts available for estimating the flow rate and exit gradient for square or rectangular cofferdams, and also, the available charts for circular cofferdams are mainly for assessing potential heaving failure.

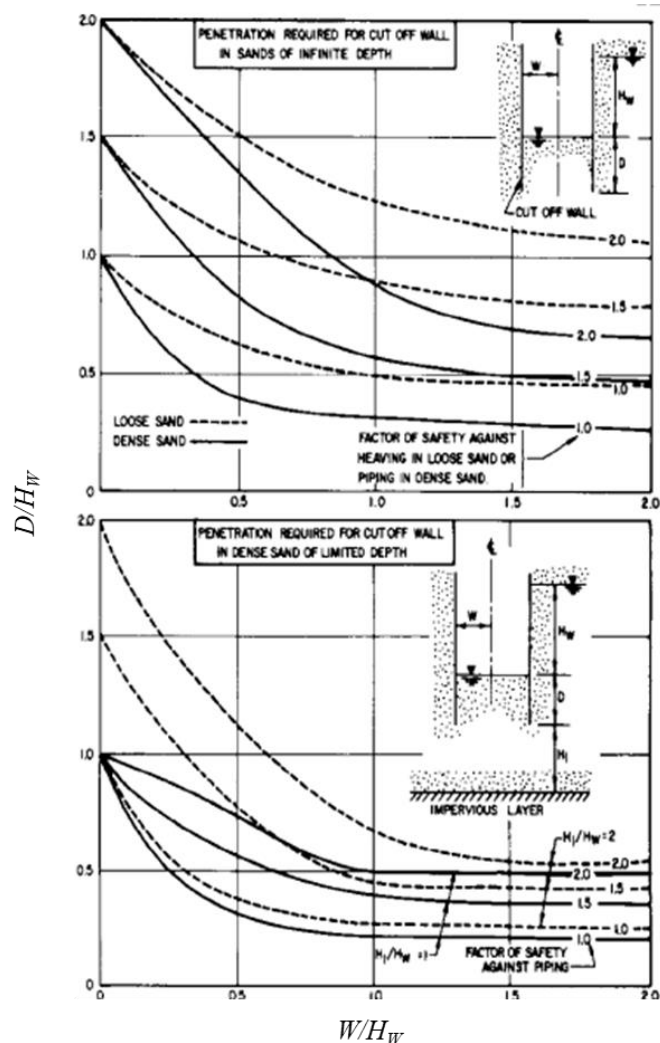


**Fig. 2.16** Required penetration of cut-off wall against piping or heaving [adopted from U.S. Department of the Navy (1982)]

### 2.5.5 Method of fragments (MoF)

This is an approximate, semi-analytical solution method and was originally proposed by Pavlovsky (1956) for two-dimensional seepage problems. Later, Harr (1962, 1977) brought it to the attention of the western world. This is an approximate method because its accuracy relies on the assumption that the equipotential lines at the critical points (e.g., tip of sheet pile) are vertical. Fig. 2.17 shows the concrete dam where the flow domain has been divided into three fragments via two vertical equipotential lines.

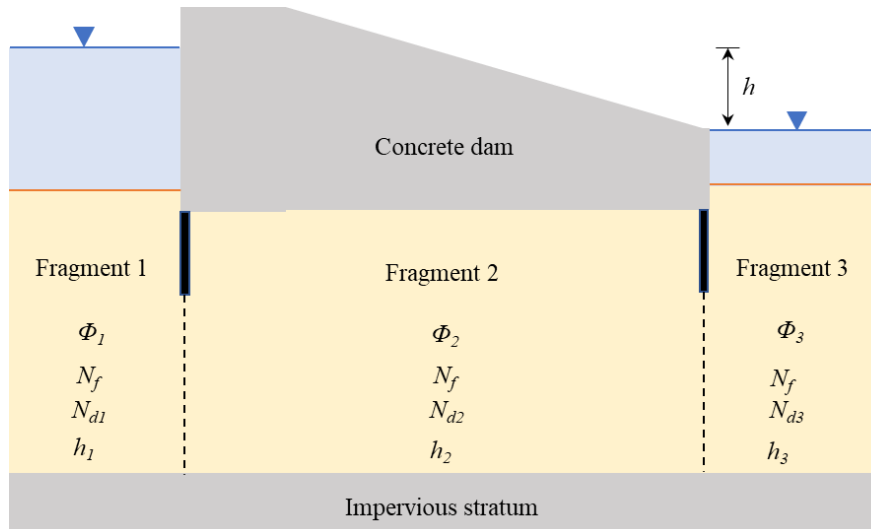


**Fig. 2.17** Method of fragments for concrete dam

Then dimensionless form factor ( $\Phi_i$ ) is defined for each fragment as (Sivakugan and Alaghbari 1993):

$$\Phi_i = \frac{N_{di}}{N_f} \quad (2.51)$$

where,  $N_{di}$  is the number of equipotential drops in the  $i^{\text{th}}$  fragment, and  $N_f$  is the number of flow channels. Considering the flow net theory, number of flow channels  $N_f$  should equals for all three fragments while summation of equipotential drops  $N_{d1}$ ,  $N_{d2}$ , and  $N_{d3}$  of fragments 1, 2, and 3, respectively gives the total equipotential drops over the entire flow domain. Also, head loss over fragments 1, 2, and 3 are  $h_1$ ,  $h_2$  and  $h_3$ , respectively and sum of them should equals to the total head loss of  $h$ . Again, considering the flow net theory (see Eq. 2.44), flow rate beneath concrete dam shown in Fig. 2.17 can be written as:

$$Q = kh \frac{1}{\left( \frac{N_{d1} + N_{d2} + N_{d3}}{N_f} \right)} \quad (2.52)$$

Using Eq. 2.51, Eq. 2.52 can be rewritten as:

$$q = \frac{kh}{\sum \Phi} \quad (2.53)$$

Since flow rate through each fragment is the same,

$$q = \frac{kh}{\sum \Phi} = \frac{kh_1}{\Phi_1} = \frac{kh_2}{\Phi_2} = \dots = \frac{kh_n}{\Phi_n} \quad (2.54)$$

Hence, head loss over a given fragment is given by:

$$h_i = \frac{\Phi_i h}{\sum_{i=1}^n \Phi_i} \quad (2.55)$$

### Form factors

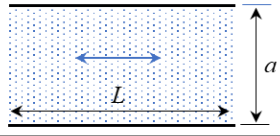
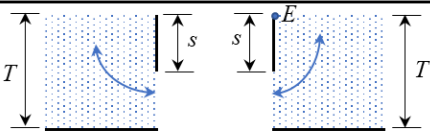
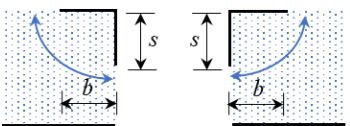
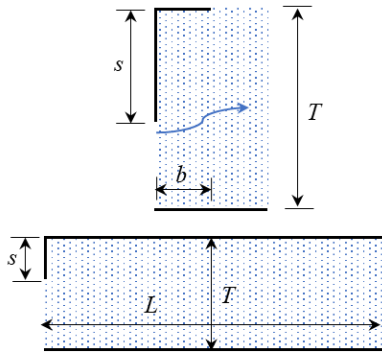
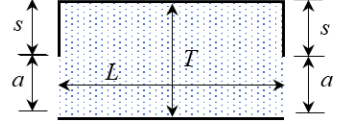
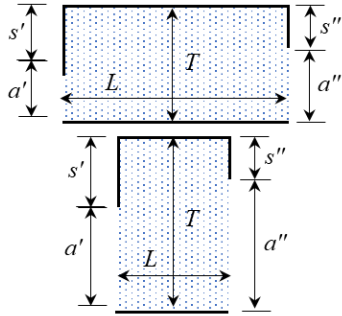
From the Eq. 2.51, it is clear that form factor of any given fragment depends only on the fragment geometry. Harr (1977) defined nine fragments covering both confined and unconfined flow scenarios. Here, first six fragments are for the confined flow and have already been discussed in Harr (1962). Table 2.6 shows Harr's six confined flow fragments and their form factor expressions. Griffiths (1984) condensed Harr's six fragments into two, namely, Fragments *A* and *B* and also defined a new fragment type known as *C* providing solutions for some additional confined flow problems such as double-walled cofferdams which cannot be handled alone with Harr's six fragments. Fragment *A* covers Harr's fragments II and III while fragment *B* is for the fragments I, IV, V and VI. Table 2.7 shows geometries of these three fragments. He developed design charts for estimating the form factor values of three fragments and normalised exit hydraulic gradient values of fragment *C* and also provided the facility to incorporate the anisotropy in soil permeability directly.

### Method of fragments (MoF) solutions for cofferdam problems

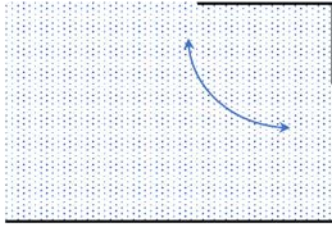
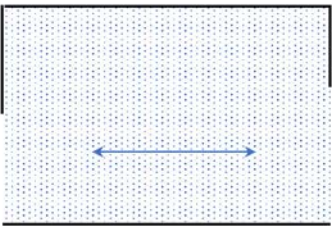
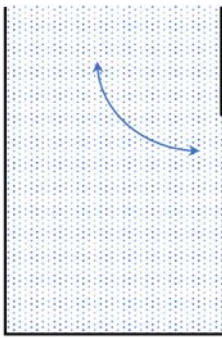
Griffiths (1984) proposed method of fragments solutions for double-walled cofferdam using his fragment types *A* and *C* providing flow rate and exit hydraulic gradient estimations. This will be discussed in more detail in chapter 3. Also Griffiths (1994) discussed the applicability

of MoF in unsymmetric cofferdam problems, too. However, MoF solution for cofferdam problems presented in the literature is limited to the problems in 2D Cartesian plane (double-walled cofferdams) and there are no MoF solutions available for circular, square or rectangular shapes of cofferdams where the flow into the cofferdam is three dimensional (3D). However, Sivakugan and Rankine (2012) and Sivakugan et al. (2013) have developed 3D MoF solutions for analysing the seepage of hydraulic mine fill stopes.

**Table 2.6** Confined flow fragments and their form factors, Harr (1962, 1977)

Frag. No	Fragment geometry	Form factor
I		$\Phi = \frac{L}{a}$
II		$\Phi = \frac{\kappa}{\kappa'}; \quad m = \sin \frac{\pi s}{2T}$ $i_E = \frac{h\pi}{2KTm}$
III		$\Phi = \frac{\kappa}{\kappa'}; \quad m = \cos \frac{\pi s}{2T} \sqrt{\tanh^2 \frac{\pi b}{2T} + \tan^2 \frac{\pi s}{2T}}$
IV		$b \leq 2s:$ $\Phi = \ln \left( 1 + \frac{b}{a} \right)$  $b \geq 2s:$ $\Phi = \ln \left( 1 + \frac{s}{a} \right) + \frac{b-s}{T}$
V		$\Phi = 2 \ln \left( 1 + \frac{L}{2a} \right) \quad : L \leq 2s$ $\Phi = 2 \ln \left( 1 + \frac{s}{a} \right) + \frac{L-2s}{T} \quad : L \geq 2s$
VI		$L \geq s' + s'':$ $\Phi = \ln \left[ \left( 1 + \frac{s'}{a'} \right) \left( 1 + \frac{s''}{a''} \right) \right] + \frac{L - (s' + s'')}{T}$ $L \leq s' + s'':$ $\Phi = \ln \left[ \left( 1 + \frac{b'}{a'} \right) \left( 1 + \frac{b''}{a''} \right) \right]$ where, $b' = \frac{L + (s' - s'')}{2}$ ,and $b'' = \frac{L - (s' - s'')}{2}$

**Table 2.7** Confined flow fragments by Griffiths (1984)

Griffiths (1984) Fragments	Description
 <p data-bbox="533 591 667 618">Fragment A</p>	Covers Harr's (1962) fragments II and III
 <p data-bbox="533 891 667 918">Fragment B</p>	Covers Harr's (1962) fragments I, IV, V and VI
 <p data-bbox="533 1303 667 1330">Fragment C</p>	New fragment

*Validity of method of fragments for confined seepage problems*

As noted before, accuracy of the MoF solutions depends on the validity of the assumption that the equipotential lines at the critical points are vertical. Griffiths and Li (1986) assessed the effects of assumption deviation on the accuracy of MoF solutions for dam seepage problems and found that MoF solutions are in good agreement with the finite element solutions although the assumption deviates noticeably. Further, Sivakugan and Alaghbari (1993) compared MoF solutions against flow net solutions analysing series of dam geometries and single sheet pile wall problem and have observed good agreement between both methods. Therefore, it is

concluded that MoF provides solutions with reasonable accuracy for most of the confined flow problems in 2D Cartesian plane. However, it is still required to assess the effects of assumption deviation on the MoF solutions for double-walled cofferdams.

## **2.6 Summary and conclusions**

A review of literature on existing seepage solution methods for double-walled, circular, square and rectangular cofferdam has been conducted. It was found that approximate solution methods (design charts or method of fragments) are commonly used in double-walled cofferdams specially in preliminary stage of designs even though numerical simulation provides more accurate solutions. Also for the circular cofferdams, numerical solutions remains the only solution method even though it can be analysed in a 2D radial plane. Therefore, having a simple solution method for circular cofferdams based on the MoF will be more beneficial in preliminary designs.

For the square or rectangular cofferdams, 3D numerical simulation is the only available solution method. However, approximating them to 2D problems tends to underestimate the flow rate and exit gradient significantly. Therefore, developing simple solution methods considering the effects of 3D flow will significantly improve the accuracy of approximate solution methods.

---

## Chapter 3 Validity of method of fragments (MoF) solutions for double-walled cofferdams

### 3.1 Introduction

Seepage analysis for double-walled cofferdams is a 2D problem and can be carried out in the Cartesian co-ordinates system, treating the third dimension as infinite. As discussed in Sec. 2.3.3, flow rate  $q$  and exit hydraulic gradient  $i_E$  adjacent to the sheet pile wall are two key parameters required to be determined. Method of fragments (MoF) is the quickest method which can be used to estimate these two parameters, without sacrificing the accuracy much.

### 3.2 Method of fragments (MoF) solutions for double-walled cofferdams

Fig. 3.1 shows a double-walled cofferdam in the cross-sectional elevation view. Two sets of parallel sheet pile walls  $2L$  distance apart are driven into the ground to a depth of  $s$  where the thickness of the soil layer is  $T$ , which is underlain by an impervious stratum. The excavation depth is given by  $\alpha s$  ( $0 < \alpha < 1$ ), and head loss over the flow domain is  $h$ . Due to symmetry, analysis of half the section along the centreline is adequate to estimate the flow rate  $q$  (per unit length) and the maximum exit hydraulic gradient  $i_E$ . So, total flow rate into the cofferdam is  $2q$ . Griffiths (1984) proposed MoF solutions dividing the flow domain (half the section) into fragment types  $A$  and  $C$  at the tip of the sheet pile wall using assumed vertical equipotential line (see Fig. 3.1 for right half section). Also, he developed form factor charts for fragment  $A$  and  $C$  as shown in Fig.3.2, and normalised exit hydraulic gradient chart for fragment  $C$  (Fig. 3.3).

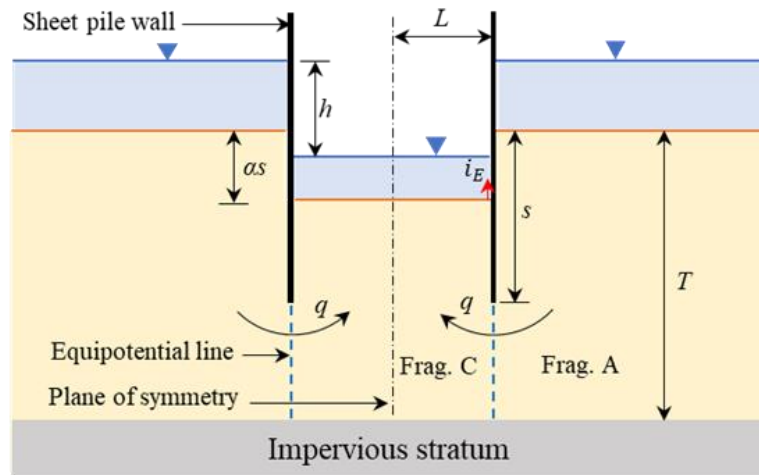


**Fig. 3.1** Adoption of MoF for double-walled cofferdams

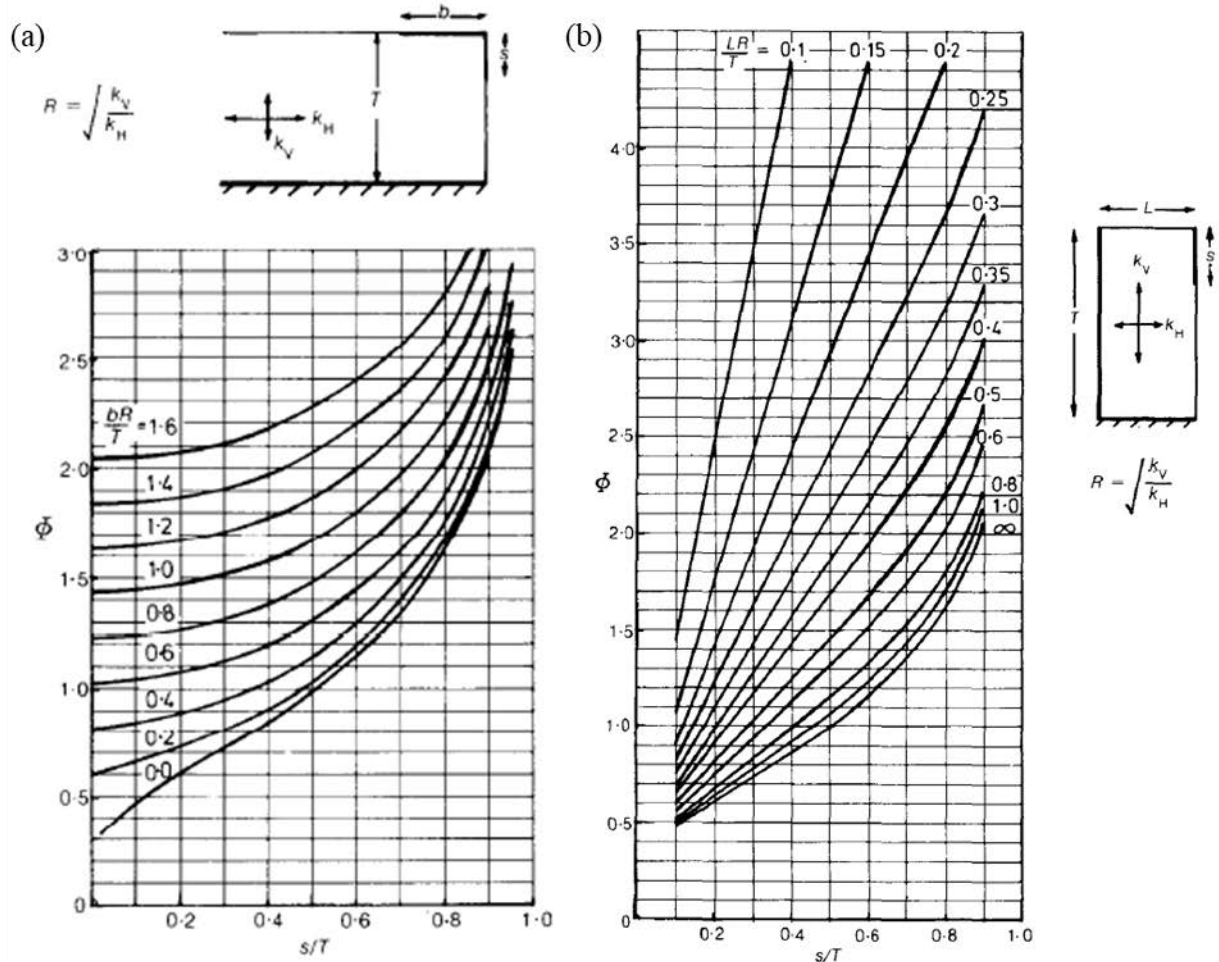


**Fig. 3.2** Form factor charts: (a) fragment A; (b) fragment C [adopted from Griffiths (1984)]

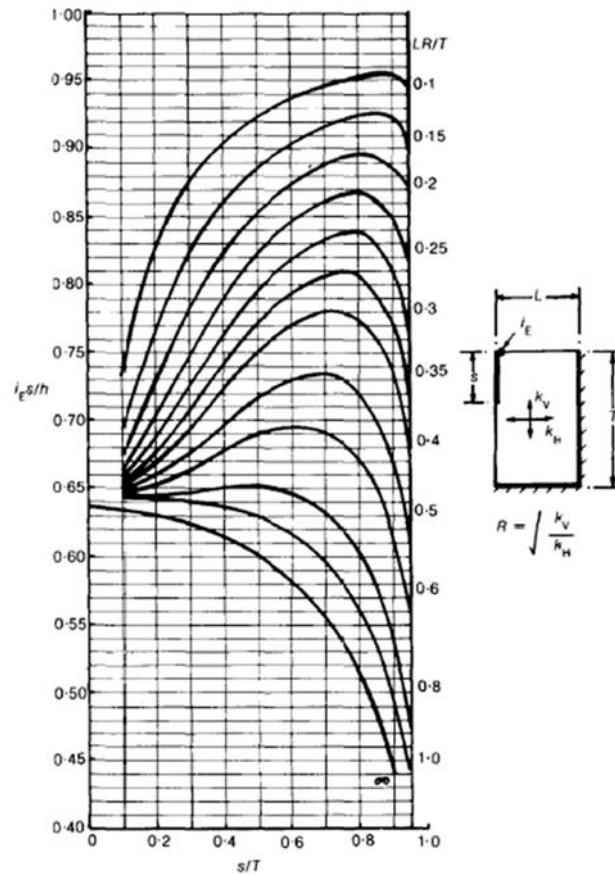


**Fig. 3.3** Normalised exit gradient chart for fragment C [adopted from Griffiths (1984)]

### 3.2.1 Flow rate $q$ estimation

From Eq. 2.53, flow rate  $q$  per half the section can be calculated as:

$$q = \frac{kh}{(\Phi_A + \Phi_C)} \quad (3.1)$$

where  $\Phi_A$  and  $\Phi_C$  are the form factor values of fragments  $A$  and  $C$ , respectively. Total flow rate  $Q$  per unit length of cofferdam is given by  $2q$  and can be written as:

$$Q = \frac{2kh}{(\Phi_A + \Phi_C)} \quad (3.2)$$

Design charts given in Fig. 3.2 provide the required form factor values for fragments  $A$  and  $C$ . Griffiths (1984) has provided the facility to incorporate the anisotropy in soil permeability directly in these charts defining the term, soil anisotropy ratio  $R$  as  $\sqrt{k_V/k_H}$ . When the soil is

homogeneous and anisotropic ( $R \neq 1$ ), corresponding solutions can be obtained considering the cofferdam width  $L$  in the transformed section, i.e.  $LR$  (multiply  $L$  by  $R$ ). Therefore, in this chapter, the half-width of the double-walled cofferdam is termed as  $LR$  in the more general form. Further,  $s/T$ ,  $LR/T$  and  $i_E s/h$  ratios required in fragment  $C$  charts (Figs. 3.2b and 3.3) should be calculated considering only the geometry of the fragment  $C$  region. So, these ratios are termed as  $s_C/T_C$ ,  $LR/T_C$  and  $i_E s_C/h_C$  in a clearer way where  $s_C = s - \alpha s$  and  $T_C = T - \alpha s$  while  $h_C$  gives the head loss within the fragment  $C$  region. Similarly, for the fragment  $A$ ,  $s/T$  ratio should be termed as  $s_A/T_A$ , but  $s_A = s$  and  $T_A = T$ .

### 3.2.2 Exit hydraulic gradient $i_E$ estimation

Using Eq. 2.55, head loss over the fragment  $C$  ( $h_C$ ) can be calculated as:

$$h_C = \frac{\Phi_C h}{\Phi_A + \Phi_C} \quad (3.3)$$

Then,  $i_E$  value can be obtained using the normalized exit hydraulic gradient values ( $i_E s_C/h_C$ ) given in Fig. 3.3.

### 3.3 Accuracy of MoF solutions for double-walled cofferdams

As noted in the above section, MoF solutions involve dividing the flow domain (half-section) into two fragments using an assumed equipotential line at tip of the sheet pile (see Fig. 3.1). Thus, the accuracy of the solutions depends on the validity of this assumption. Also, it is clear that the position of the equipotential line (at tip of the sheet pile) is controlled by geometric parameters of the cofferdam, i.e.,  $LR$ ,  $s$ ,  $T$  and  $\alpha s$ . Therefore, to assess the validity of this assumption, behaviors of equipotential lines over a wider range of geometries were studied using numerical simulation results.

### 3.3.1 Numerical modeling of double-walled cofferdams

The 2D finite element program (*RS2 V9.011*) developed by Rocscience was used for the simulations, and the numerical model geometry used is shown in Fig. 3.4. Only a half section was studied considering the symmetry. The parameters,  $h$ ,  $L$ ,  $s$ ,  $\alpha s$  and  $T$  are similar to those defined in Fig. 3.1.  $L_e$  is the safe distances from sheet pile wall to the model boundary at which the boundary effect on the results is insignificant. For all the simulations, a homogeneous and isotropic soil model was applied ( $R = 1$ ), keeping the soil permeability constant ( $10^{-5}$  m/s) within the entire model. In addition, permeable layer thickness  $T$ , and total head loss over the cofferdam  $h$  were also kept constant for all the runs, with values of 20 m and 10 m, respectively.

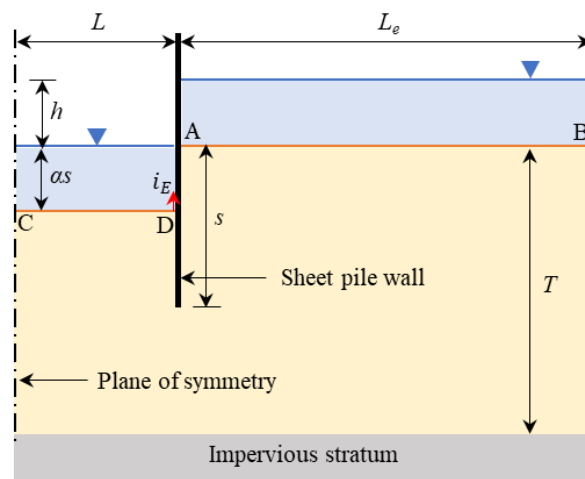


**Fig. 3.4** Numerical model geometry used for simulating double-walled cofferdams

Further, it was assumed that the seepage flow into the excavation does not lower the ground water table, outside the excavation. This assumption is reasonable when the cofferdam is used for the offshore excavations as shown in Fig. 3.4. Moreover, this is a conservative assumption for the onshore excavations, where the water table is below the ground level, outside the excavation. When dewatering the inner excavation is in progress for onshore cofferdams, the water table outside the excavation starts to lower and reaches a steady state condition after some time. The transition time required depends on the soil permeability, depth of the sheet pile penetration below the water table and the width of the excavation (Kavvadas et al. 1992).

However, the most critical flow condition is encountered at the initial dewatering condition, and at which, flow rate, maximum exit hydraulic gradient and hydraulic pressure on the sheet pile wall are the highest. Fig. 3.5 shows the initial dewatering condition of onshore cofferdams. Therefore, all the designing parameters (flow rate, factor of safety against hydraulic failure and the strength of sheet pile wall) of onshore cofferdam must be based on this initial condition. Accordingly, numerical solution results of offshore cofferdams are applicable to the onshore cases, too. However, it is required to measure the parameters  $s$ ,  $\alpha s$  and  $T$  from the water table and not from the original ground level (see Fig. 3.5). Consequently, all simulations in this chapter were conducted for the offshore cofferdam models shown in Fig. 3.4.

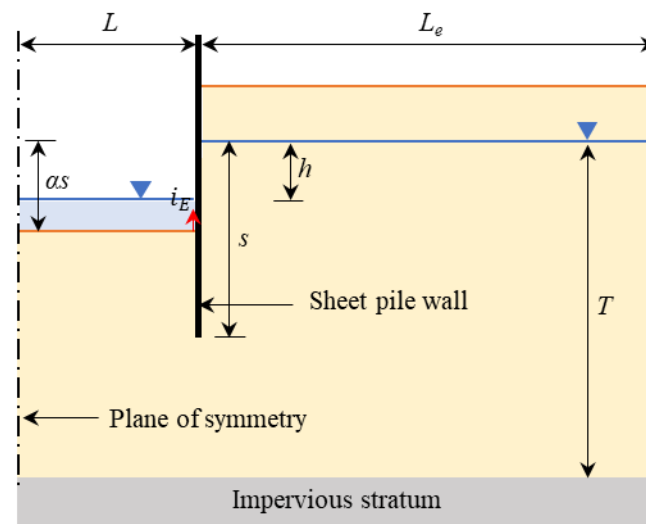


**Fig. 3.5** Initial dewatering condition of double-walled cofferdams for the onshore excavations

In all the simulations, planes of symmetry and impermeable bases were considered as impermeable boundaries. The ground level outside the excavation and the base of the excavation (line AB and CD, respectively in Fig. 3.4) were treated as constant head boundaries (i.e., equipotential surfaces) with the total head difference of  $h$ . In addition, a thin layer of material was used to simulate the sheet pile wall where its permeability is orders of magnitude lower than the soil material. Simulations were carried out as flow only problems (i.e., no

deformations) for a completely saturated soil, and a uniform mesh with four noded quadrilateral elements were used for meshing. Exit hydraulic gradient value for each model was calculated using the “Add Material Query” option available in *RS2 V9.011*. This option allows to define a query anywhere within the model in the form of a single point, a single line segment or an arbitrary polyline of number of line segments. Then, required data can be obtained for a particular point or a line depending on the defined query type. Therefore, in this study, a query (single point form) was defined for the point where the exit hydraulic gradient is sought. This is the point located on the excavation base adjacent to the sheet pile wall (see Fig. 3.4). Using these query points,  $i_E$  values were calculated. Also, “discharge section” option available in *RS2* was used to calculate the  $q$  values.

### 3.3.2 Sensitivity analysis and model validation

Before using models for equipotential line behaviour analysis, a sensitivity analysis was conducted to ensure that the effect of selected safe distance for the model's boundaries ( $L_e$ ) are negligible on the results ( $q$  and  $i_E$ ). It showed that increasing the horizontal distance from the sheet pile wall to the outer boundary  $L_e$  beyond  $2T$  was insensitive, i.e. the percentage increment of  $q$  and  $i_E$  values when  $L_e$  greater than  $2T$  is less than 1%. Therefore, all the models were run with  $L_e$  equals  $2T$ . Also, it was observed that increasing the half-width  $L$  beyond  $2T_C$  did not affect the results. Therefore, a double-walled cofferdam where the half-width  $L$  equals to  $2T_C$  is equivalent to the case of single sheet pile wall (i.e., width of the cofferdam is infinite).

Next, finite element model was calibrated against the results of the analytical solutions ensuring the validity of the size and type of finite elements, and the mesh type used. For the flow rate  $q$  comparison, analytical solution proposed by King and Cockroft (1972) for the no excavation ( $\alpha = 0$ ) condition was used while exit hydraulic gradient  $i_E$  estimation values were compared

against the Harr (1962) solution for single sheet pile wall ( $LR/T = \infty$ ). The geometries considered for the validation are shown in Table 3.1, and the comparison results are given in Fig. 3.6. Numerical solutions are well agreed to the analytical solutions in both cases and deviate less than 5% in general. Therefore, it is verified that the accuracy of the numerical model for analysing the seepage beneath double-walled cofferdams is adequate.

**Table 3.1** Cofferdam geometries used for numerical model validations

Flow rate estimations			Exit gradient estimations		
$\alpha$	$LR/T$	$s/T$	$\alpha$	$LR/T$	$s/T$
0	0.2	0.2	0	$\infty$	0.1
		0.4			0.2
		0.6			0.3
	0.4	0.2			0.4
		0.4			0.5
		0.6			0.6
	0.6	0.2			0.7
		0.4			0.8
		0.6			0.9

### 3.3.3 Accuracy assessment of the MoF solutions

As noted above, the accuracy of the MoF solutions depends on the validity of the assumption that the equipotential line is vertical at tip of the sheet pile. To evaluate this, series of finite element model runs were carried out, and equipotential line was drawn for each case. The geometry range considered is shown in Table 3.2 while Fig. 3.7 shows the equipotential lines drawn.

#### Effect of the cofferdam width and depth of the cut-off wall

In Fig. 3.7,  $s/T$  increases from left to right while  $LR/T$  increases downwards. The equipotential lines are away from the vertical for low values of  $LR/T$  and  $s/T$  ratios. With increasing the

values of  $LR/T$  and  $s/T$ , the equipotential lines become closer to the vertical, making the assumption reasonable.

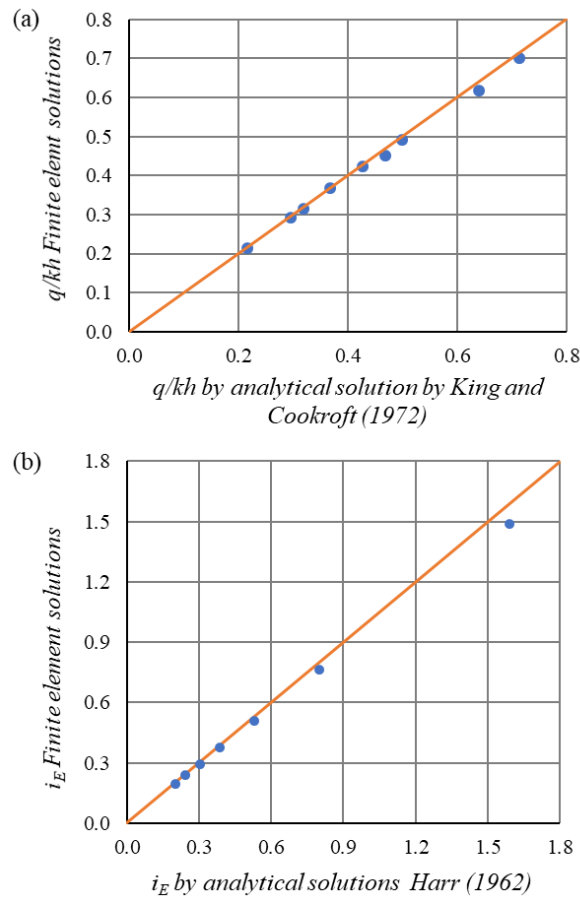


**Fig. 3.6** Double-walled cofferdam model validation: (a) flow rate; (b) exit hydraulic gradient

**Table 3.2** Double-walled cofferdam geometries used for equipotential lines behaviour studied

$LR/T$	$s/T$	$\alpha$
0.1	0.1	0, 0.4, 0.8
	0.4	0, 0.4, 0.8
	0.8	0, 0.4, 0.8
0.4	0.1	0, 0.4, 0.8
	0.4	0, 0.4, 0.8
	0.8	0, 0.4, 0.8
0.8	0.1	0, 0.4, 0.8
	0.4	0, 0.4, 0.8
	0.8	0, 0.4, 0.8

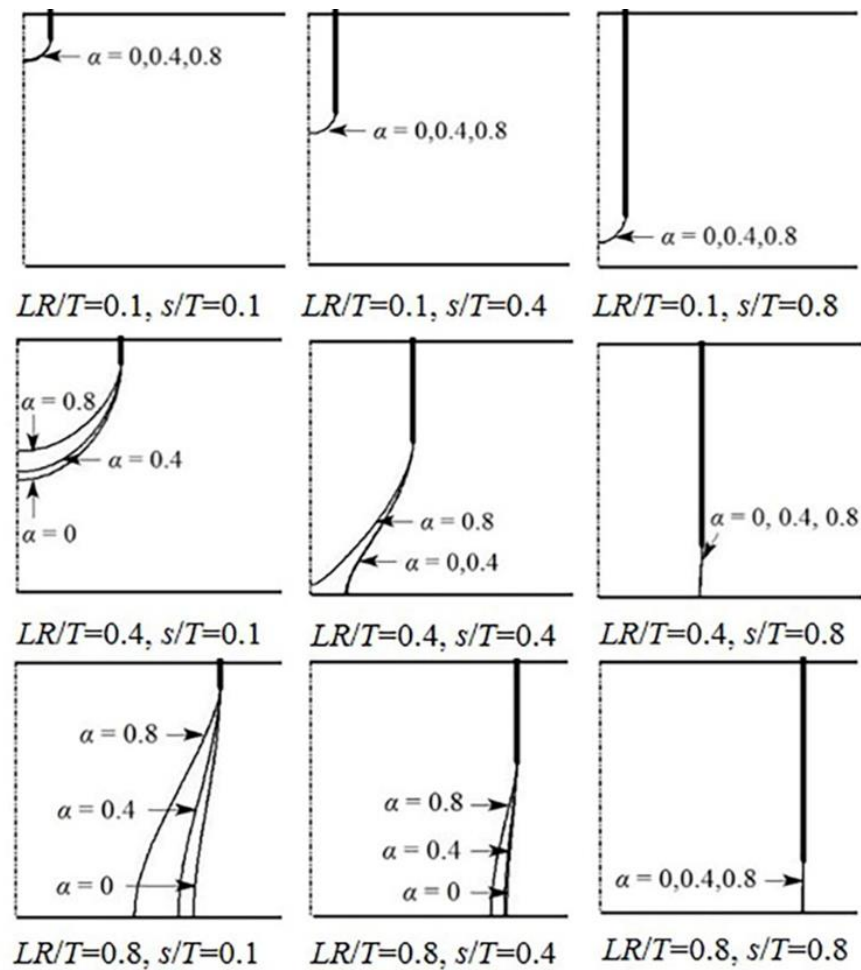


**Fig. 3.7** Behaviour of the equipotential lines with double-walled cofferdam geometry

### Effect of the excavation depth

The effect of the excavation depth ( $\alpha s$ ) on the position of the equipotential line is also shown in Fig. 3.7. When increasing the excavation depths ( $\alpha$  changing from 0 to 0.8) for any given  $LR/T$  particularly at low values of  $s/T$ , the deviation of the equipotential line from the vertical is more pronounced, thus jeopardising the assumption. However, the difference between equipotential lines when  $\alpha$  increases from 0 to 0.4 is only slight, with most of the deviation occurring for the range 0.4-0.8. Therefore, behavior of the equipotential line for moderate excavations is not significantly affected by the excavation depth ( $\alpha$  from 0 to 0.4) and is mostly controlled by the cofferdam width ( $LR$ ) and cut-off wall depth ( $s$ ). Also, the difference between

the equipotential lines when  $\alpha$  increases from 0.4 to 0.8 becomes low when decreasing the  $LR/T$  ratio and increasing the  $s/T$  ratio. So, the effect of the excavation depth on the validity of the assumption is a concern only when excavating to a considerably larger depth ( $\alpha > 0.4$ ) for the geometries where the value of  $LR/T$  is high and  $s/T$  ratio is low. On the other hand, one is unlikely to excavate to a larger depth when  $LR/T$  is high, and  $s/T$  is low; hence, this kind of instances have very little practical significance. Therefore, the effect of the excavation depth is not significant on the accuracy of the MoF solutions in double-walled cofferdams for most geometries encountered in practice.

### 3.3.4 Effects of assumption deviation on the seepage solutions

For this analysis, series of finite element model runs were carried out to adequately represent most cases encountered in practice. The finite element solutions obtained for the hundreds of trials do not make any assumptions about the equipotential line at the tip of the sheet pile being vertical. The values of  $q$  and  $i_E$  computed from these runs were compared with those computed using the MoF charts developed by Griffiths (1984).

#### Effect of non-vertical equipotential line due to cofferdam width and cut-off wall depth

Fig. 3.8 shows the comparisons of the normalized seepage quantity ( $q/kh$ ) and  $i_E$  obtained by the MoF solutions with corresponding full numerical solutions for the series of geometries considered. Here, series of geometries (90 cases) were studied changing the  $LR/T$  from 0.1 to 1 and  $s/T$  from 0.1 to 0.9, while keeping the soil as isotropic ( $R = 1$ ) and depth of excavation as zero ( $\alpha = 0$ ).

Both comparisons show good agreement between the MoF solutions and the finite element solutions. Also, MoF predictions gives higher values compared to that given by the finite

element solutions for all the cases; hence, MoF solutions are always on the safe side (i.e., they are conservative). Further they differ by less than 10% compared to the corresponding finite element solutions for most of the cases (i.e., 87 and 79 cases out of the 90 for  $q/kh$  and  $i_E$ , respectively). The few cases with the substantial deviation (10-20%) correspond to the geometries which are having less applicability in the practice where the cut-off wall depth is too low ( $s/T \leq 0.2$ ) to ensure stability.

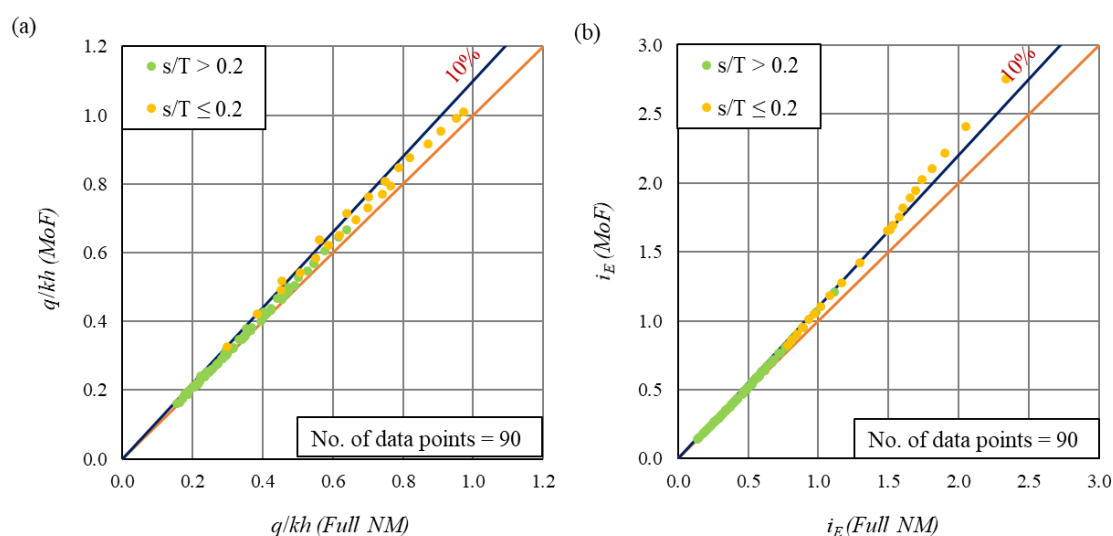


**Fig. 3.8** Comparison of predictions from MoF and full numerical model (Full NM) solutions when  $\alpha = 0$ : (a) seepage quantity; (b) exit hydraulic gradient

### Effect of non-vertical equipotential line due to excavation depth

Fig. 3.9 compares the  $q/kh$  and  $i_E$  at three excavation depths ( $\alpha = 0, 0.4$  and  $0.8$ ) predicted by MoF against corresponding full numerical model predictions for three different cofferdam widths of  $LR/T = 0.1, 0.4$  and  $0.8$  changing  $s/T$  from  $0.1$  to  $0.9$ . For two cases where  $\alpha = 0$  and  $0.4$ , the deviation of MoF solutions from the numerical results is less than 10%, and also, onto the conservative side. So, excavation depth effect is not significant on the results. Conversely, for  $\alpha = 0.8$ , the deviation is slightly larger (relative errors between 10-20%) compared to  $\alpha = 0$  and  $0.4$ , but MoF predictions are conservative in this case, too. Also, the

error decreases with increasing the  $s/T$  values. These two observations are in line with the conclusion made with the Fig. 3.7 above (i.e., effect of the excavation depth on the validity of the assumption is a concern only when excavating to a considerably larger depth). However, the effect of violating this assumption is always on the conservative side (i.e., both the  $q/kh$  and  $i_E$  are overestimated).

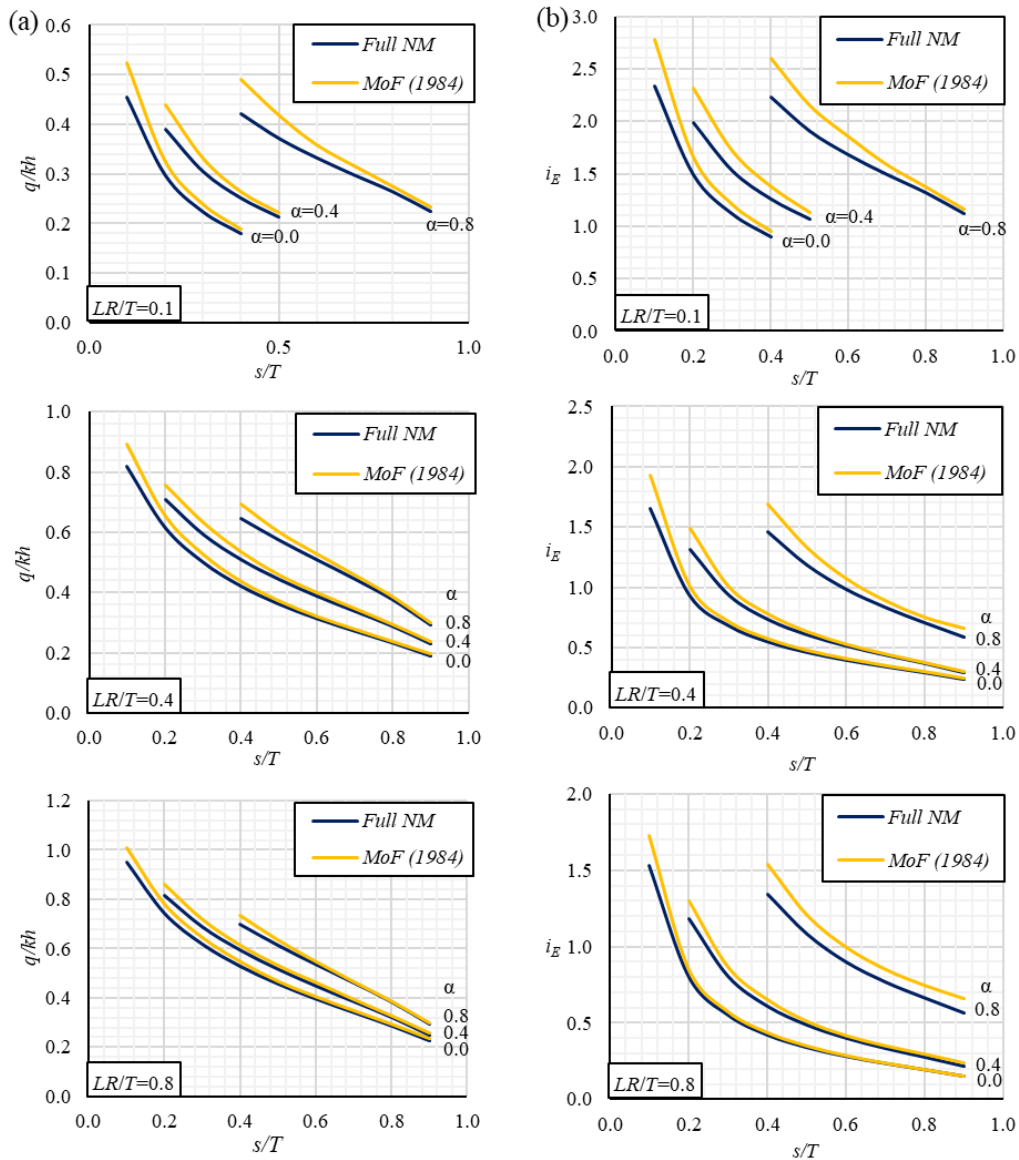


**Fig. 3.9** Effect of cofferdam geometry on the accuracy of MoF solutions:

(a) seepage quantity; (b) exit hydraulic gradient

Considering all above, it can be concluded that MoF is a sufficiently accurate tool for quick estimations of  $q$  and  $i_E$  for the double-walled cofferdam problems. Even when the assumption is violated,  $q$  and  $i_E$  are conservatively overestimated by less than 10% for most practical situations ( $s/T > 0.2$ ). Therefore, simple expressions are proposed herein to estimate the form factors of both fragments  $C$  and  $A$ , and  $i_E s_C/h_C$  for fragment  $C$ , which enable the implementation of the MoF in spreadsheets.

### 3.4 Expressions for form factors and exit gradient estimations

As noted before, two form factor charts shown in Fig. 3.2 and the normalized exit hydraulic gradient chart (in Fig. 3.3) can be used to obtain the MoF solutions for the double walled cofferdams. However, it is required to extrapolate or interpolate them to find the form factors and exit gradient values for some geometries. The graphical nature of the charts, developed for selected  $s_C/T_C$  and  $LR/T_C$  values for fragment type  $C$ , makes the interpolation not easy, and also not very precise for some geometries. Therefore, an attempt is made to develop expressions for estimating the form factors and normalized exit hydraulic gradients of the fragment type  $C$ , and the form factors of special case of fragment type  $A$  with  $b = 0$ . These expressions enable quick estimations of  $q$  and  $i_E$ , without going for the graphical solutions.

#### 3.4.1 Expressions for fragment type $C$

Observing the fragment  $C$  form factor chart (Fig. 3.2a), it can be concluded that the difference between form factor values when  $LR/T_C$  increasing from 1 to  $\infty$  is only a slight, with most of the changes occurring for the range of 0.1-1. For the exit gradient too, the pattern is similar. Therefore, a geometry range was selected covering the situations where  $s_C/T_C = 0.1 - 0.9$ , and  $LR/T_C = 0.1 - 1.0$  for the expressions development. Then, form factor and exit hydraulic gradient charts were redeveloped for the range mentioned above using the procedure described

in following paragraphs. Also redeveloped form factor chart covers few additional cases where (a)  $LR/T_C = 0.1$  and  $s_C/T_C > 0.4$ , (b)  $LR/T_C = 0.15$  and  $s_C/T_C > 0.6$ , and (c)  $LR/T_C = 0.2$  and  $s_C/T_C > 0.8$  which cannot be handled using the form factor chart by Griffiths (1984) shown in Fig. 3.2b.

Fig. 3.10 shows the geometry of the numerical model used to simulate the fragment  $C$  using *RS2 V9.011*. The base of the fragment  $BC$ , the left boundary  $CD$  (i.e., vertical centerline) and the sheet pile  $AE$  were taken as impervious boundaries. The vertical boundary  $AB$  and the horizontal boundary  $DE$  were treated as constant head boundaries with the total head difference of  $h_C$ . Then, series of finite element runs (99 cases) were made covering the geometry range mentioned above ( $LR/T_C = 0.1 - 1.0$  and  $s_C/T_C = 0.1 - 0.9$ ), and  $q$  and  $i_E$  values were computed for each case.

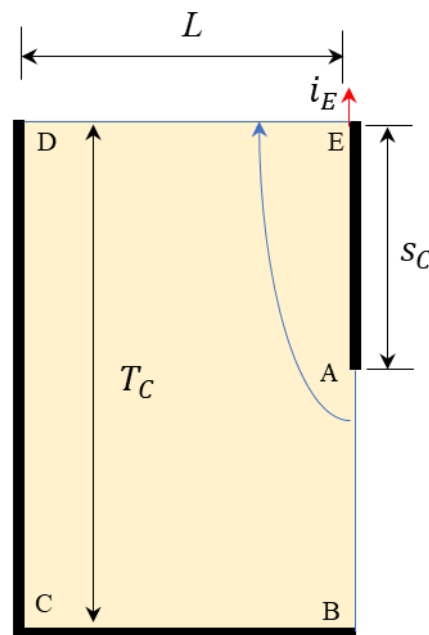


**Fig. 3.10** Numerical model geometry used for fragment  $C$  simulations

Form factor expression

Using the computed flow rate  $q$  values, fragment  $C$  form factor  $\Phi_C$  value was calculated for each case via the relationship given by:

$$\Phi_C = \frac{kh_C}{q} \quad (3.4)$$

Next,  $\Phi_C$  values were presented in a form of design chart as shown in Fig. 3.11. All these values were compared against the Griffiths (1984) values (shown in Fig. 3.2a) and found an excellent agreement (relative errors around 1% for all cases). Appendix A1 shows the Griffiths (1984) fragment  $C$  form factors and the derived fragment  $C$  form factors using finite element simulation in this dissertation. Then, computed  $\Phi_C$  values were used to develop an expression for fragment  $C$  form factor. Considering form factor equations suggested by Harr (1962) for confined flow fragments (see Table 2.6), and the shape of the design chart shown in Fig. 3.11, form factor  $\Phi_C$  can be expressed in the form given by:

$$\Phi_C = \ln\left(1 + \frac{s_C}{T_C}\right) + a(s_C/T_C) + b \quad (3.5)$$

where  $a$  and  $b$  are functions of  $LR/T_C$ . Then  $a$  and  $b$  were determined by plotting them separately against  $LR/T_C$  as:

$$a = \frac{0.85}{LR/T_C} \quad (3.6)$$

$$b = 0.4 \exp^{-0.5LR/T_C} \quad (3.7)$$

Substituting Eqs. 3.6 and 3.7 into Eq. 3.5,  $\Phi_C$  can be rewritten as:

$$\Phi_C = \ln\left(1 + \frac{s_C}{T_C}\right) + 0.85 \frac{s_C}{LR} + 0.4 \exp\left(-\frac{LR}{2T_C}\right) \quad (3.8)$$

For  $LR/T_C > 1$ , it is suggested to use Eq. 3.8 and reduce  $\Phi_C$  by 10%.

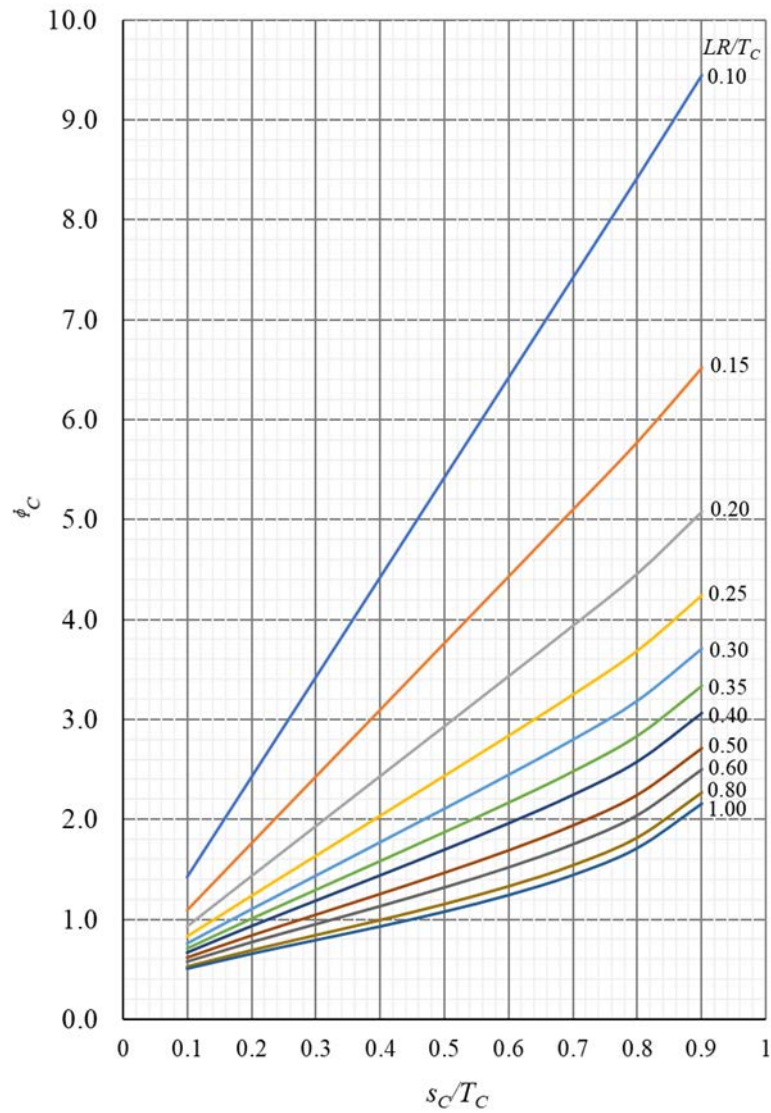


**Fig. 3.11** Form factor  $\Phi_C$  values for fragment  $C$  (from finite element simulation)

#### Exit hydraulic gradient expression

Computed  $i_E$  values were converted into normalised form, i.e.,  $i_E s_C / h_C$ , and then, were presented in the design chart shown in Fig. 3.12. These values also show an excellent agreement to the Griffiths (1984) values (relative errors were less than 1%), and hence, were used to derive the expression [Appendix A2 shows the Griffiths (1984) values and derived normalised exit hydraulic gradient values in this study].

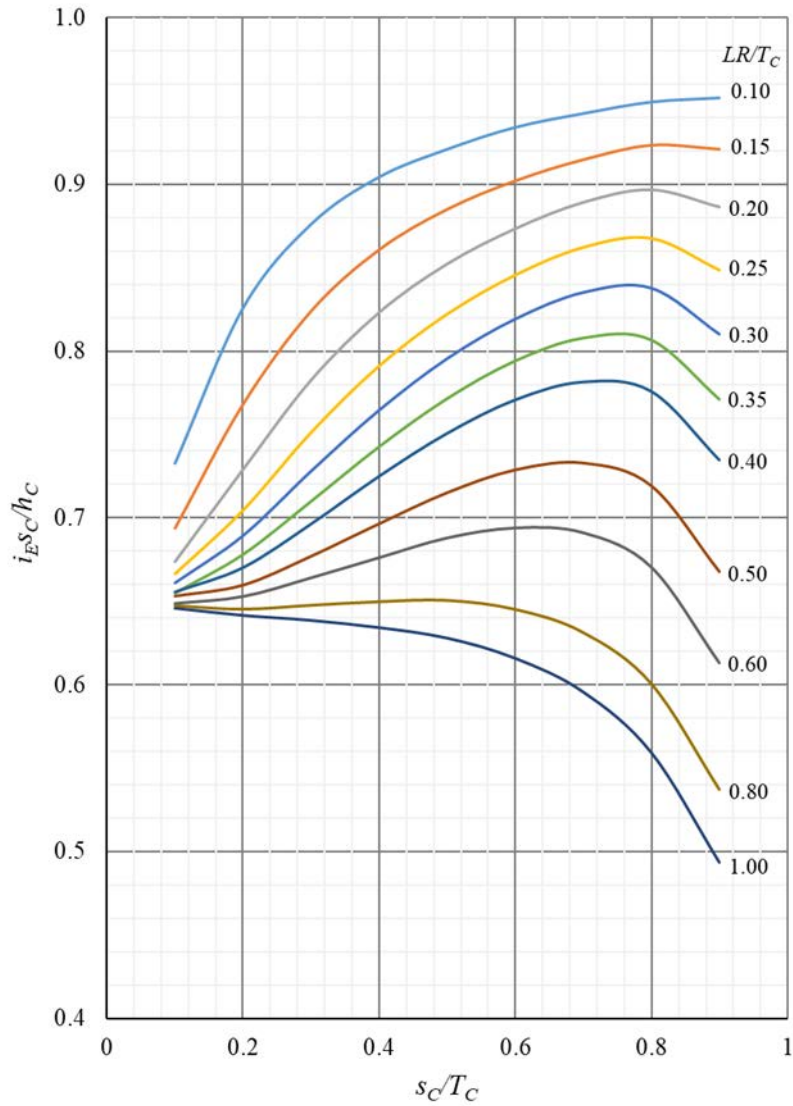


**Fig. 3.12** Exit hydraulic gradient values for fragment  $C$  (from finite element simulation)

It appears that the exit hydraulic gradient patterns at various  $LR/T_C$ ,  $i_{ES_C}/h_C$  can be expressed by the form defined as:

$$i_{ES_C}/h_C = c(s_C/T_C)^d(1 - \exp^{-s_C/T_C}) \quad (3.9)$$

Here also,  $c$  and  $d$  are functions of  $LR/T_C$  and were determined by plotting them separately against  $LR/T_C$  as:

$$c = 1.5 - 0.75 LR/T_C \quad (3.10)$$

$$d = -(0.3 LR/T_C + 0.65) \quad (3.11)$$

Using Eqs. 3.10 and 3.11, Eq. 3.9 can be rewritten as:

$$i_E s_C / h_C = 1.5 \left[ \frac{1 - \exp(-s_C/T_C)}{(s_C/T_C)^{(0.3 LR/T_C + 0.65)}} \right] \left( 1 - 0.5 \frac{LR}{T_C} \right) \quad (3.12)$$

For the case of  $LR/T_C > 1$ , it is suggested to use Eq. 3.12 since the predictions are conservative.

### 3.4.2 Expression for fragment type *A*

As noted before, type *A* fragment involved in the double-walled cofferdam is a special case with  $b = 0$  (see Fig. 3.1 and 3.2a). Hence, this fragment can be modelled as a special case of type *C* with  $L = \infty$  as shown in Fig. 3.13. As discussed before, increasing  $L$  beyond  $2T_C$  has little effect on the flow rate predictions, and hence, has insignificant effect on the form factor values. Therefore, form factors for the type *A* fragment with  $b = 0$  were developed using the numerical simulations of same fragment *C*, but with  $L = 2T_C$  when anisotropic ratio  $R = 1$ . Appendix A3 shows the Griffiths (1984) fragment *A* form factor  $\Phi_A$  values (at  $b = 0$ ) and the derived fragment *C* form factor  $\Phi_C$  values (at  $L = 2T_C$ ) in this study. Then established form factors for fragment *A* at  $b = 0$  are shown in Fig. 3.14 as a function of  $s/T$  and can be approximated as:

$$\Phi_A = 0.43 \exp\left(\frac{5s}{3T}\right) \quad (3.13)$$

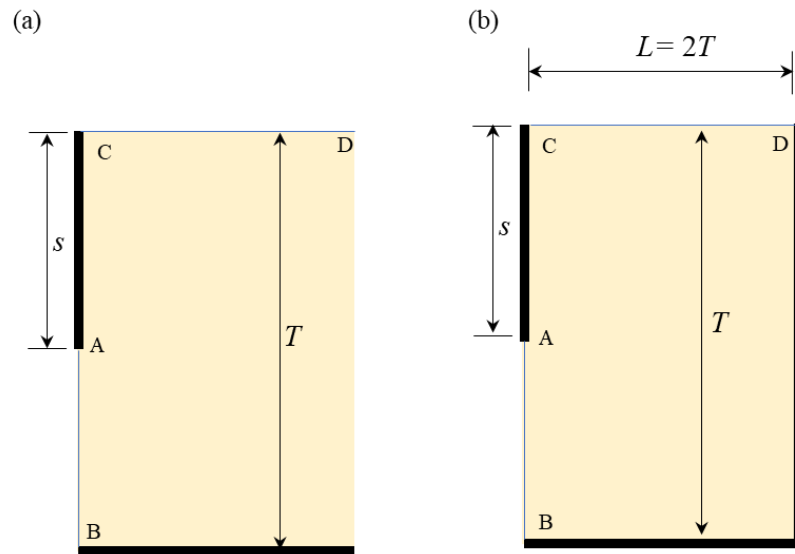


**Fig. 3.13** Fragment  $A$  geometries: (a) actual geometry; (b) equivalent fragment  $C$  geometry used for numerical simulations

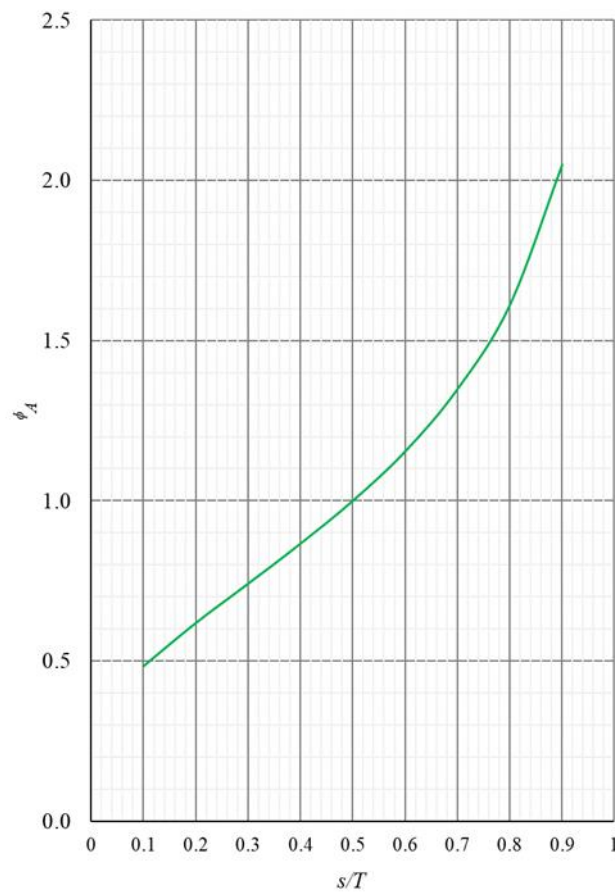


**Fig. 3.14** Form factor  $\Phi_A$  values for fragment  $A$  at  $b = 0$  (from finite element simulation)

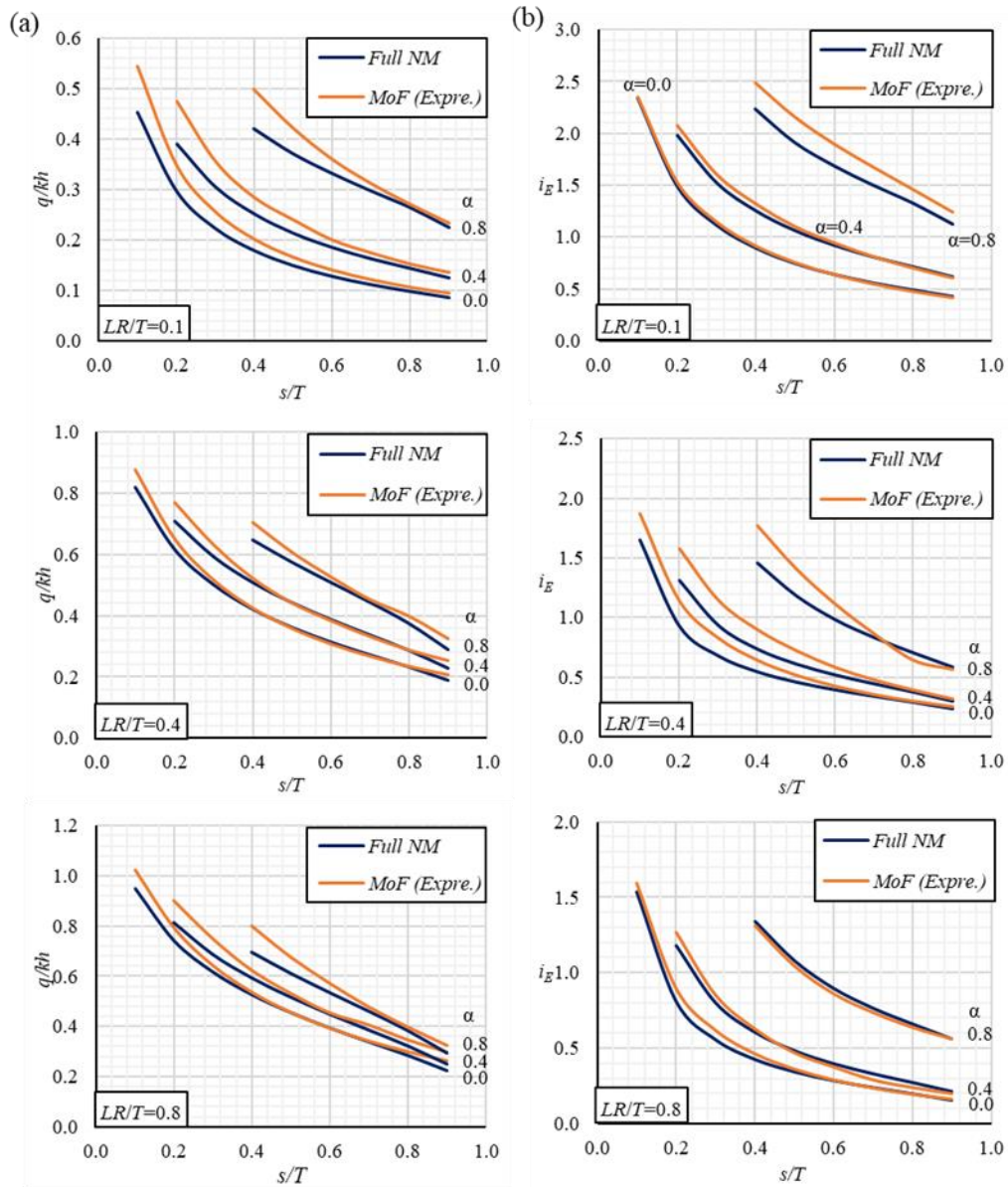
### 3.4.3 Validation of proposed form factors and exit hydraulic gradient expressions

Fig. 3.15 compares the  $q/kh$  and  $i_E$  values predicted using the form factor expressions (Eqs. 3.8 and 3.13) and the exit gradient expression (Eq. 3.12) against the corresponding values calculated by full numerical simulations. When the excavation  $\alpha = 0.4$ , the relation between the predictions by proposed expressions and numerical solutions follow a trend that is similar to no excavation condition ( $\alpha = 0$ ), and the relative errors are less than 10% for both cases. For  $\alpha = 0.8$ , deviation is slightly larger (10 -20% in general). However, the error decreases with increasing the  $s/T$  values. These observations are in line with the observations made with the Fig. 3.9 above, and hence, it can be concluded that  $q$  and  $i_E$  predictions using the expressions proposed herein are reasonably accurate.

### 3.5 Summary and conclusions

The method of fragments (MoF) solutions for double-walled cofferdams relies on the assumption that the equipotential line at the tip of the sheet pile is vertical, which divides the flow domain into two fragments ( $A$  and  $C$ ). An assessment is made in this chapter on the validity of this assumption and the effects of any violation on the computed values of flow rate  $q$  and the maximum exit hydraulic gradient  $i_E$ . It is observed that this equipotential line can be far from vertical, especially for low values of  $LR/T$  and  $s/T$ . However, it is shown that the MoF is adequate for reasonable estimates of the  $q$  and  $i_E$  provided  $s/T > 0.2$ , with relative errors are less than 10%. Also, the effect of assumption deviation is always onto the conservative side. When  $s/T \leq 0.2$ , MoF still provides conservative solutions, but their level of accuracy is low (relative errors are between 10-20%) when compared to the geometries with  $s/T > 0.2$ . Although, the situations where  $s/T \leq 0.2$  are of no practical significance, and hence, this should not be a concern for using MoF in engineering practice.

Three simple analytical expressions (Eqs. 3.8, 3.12 and 3.13) have been proposed and validated to estimate the form factors and normalised exit gradient values of the fragment type  $C$  and the form factors of the fragment type  $A$  with  $b = 0$ , respectively. The direct application of the proposed expressions for fragment  $C$  (Eqs. 3.8 and 3.12) is limited to the geometries in the range of  $0.1 \leq s/T \leq 0.9$  and  $0.1 \leq LR/T \leq 1$ ; but it covers most of the practical situations. Also, for geometries with  $LR/T > 1$ , suggestions have been made for estimating the form factors and normalised exit hydraulic gradients, with a slight error. Proposed Eq. 3.13 can be used to determine the form factor values of the fragment type  $A$  for any geometry in realistic situations, i.e.  $0.1 \leq s/T \leq 0.9$ . One can directly apply these three expressions to find full seepage solutions for any geometry of the cofferdam without using the numerical modelling or MoF chart solutions. Further, these expressions can be implemented through spreadsheets for carrying out parametric studies and for quick determination of the flow rate  $q$  and the exit hydraulic gradient  $i_E$ .



**Fig. 3.15** Comparison of proposed expressions solutions with full numerical model (NM)

solutions: (a) seepage quantity; (b) exit hydraulic gradient

---

## Chapter 4 Method of fragments (MoF) solutions for circular cofferdam seepage problems

### 4.1 Introduction

As discussed in chapter 1, circular cofferdams are widely used for construction of water treatment plant, sewers, bridge piers and abutments, and shaft. Some of the significant case histories on the application of circular cofferdams have been reported by Lefas and Georgiannou (2001), Parashar et al. (2007), Underwood and Weber (2011) and Tan and Wang (2015). In a circular cofferdam also, flow rate  $q$  and maximum exit hydraulic gradient  $i_E$  are two key parameters required to be determined. Seepage flow into circular cofferdams is three dimensional, but seepage analysis is commonly carried out as a 2D problem in the cylindrical coordinate system since the flow is symmetric about vertical axis of the cofferdam (i.e., an axisymmetric problem). As noted in Sec. 2.5.2, numerical simulation using a finite element or finite difference computer package is the widely used seepage solution method for circular cofferdams. Drawing a flow net is also a possible solution method, but it is a more difficult task compared to that of drawing a flow net in 2D Cartesian plane (i.e., flow net for double-walled cofferdam). Method of fragments (MoF) appears to be another possible seepage solution method for circular cofferdams, but it requires proposing new axisymmetric fragments and developing their form factors and dimensionless exit hydraulic gradient values.

### 4.2 Numerical simulation of circular cofferdams

The 2D finite element program *RS2 V9.011* developed by Rocscience was used for the simulations, and the model used is shown in Fig. 4.1. The parameter  $r$  is the cofferdam radius and  $r_e$  is the safe distance from sheet pile wall to the model outer boundary at which the boundary effect on the results is insignificant. Note that, cofferdam radius is termed as  $rR$  in

more general form in this chapter, which is similar to the case discussed for double-walled cofferdams where  $R$  is the soil anisotropy ratio. All the other parameters ( $s$ ,  $T$ ,  $as$  and  $h$ ) are similar to those defined in Fig. 3.1 for double-walled cofferdam. Analysing only the flow along a radial plane is adequate considering the axisymmetry, and the simulation procedure is similar to the one applied for the double-walled cofferdams as discussed in Sec. 3.3.1. The only difference was the analysis type, which is the axisymmetric for circular cofferdams while the plane strain was applied for double-walled cofferdams. Here also, soil model applied was the homogeneous and isotropic ( $R=1$ ) keeping the soil permeability constant ( $10^{-5}$  m/s) within the entire model. Further, permeable layer thickness  $T$ , and total head loss over the cofferdam  $h$  were also kept constant for all the runs, with values of 20 m and 10 m, respectively. Also, all the simulations were conducted considering the offshore cofferdam model (Fig. 4.1) since the results are valid and conservative for onshore cases, too, as pointed in Sec. 3.3.1 for double walled cofferdam analysis.

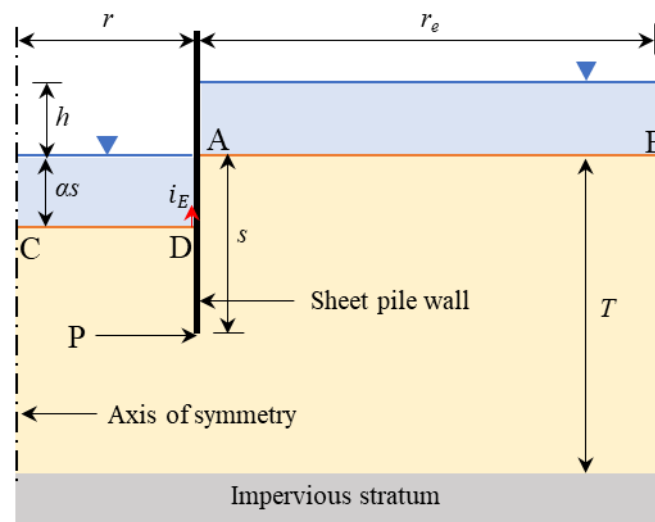


**Fig. 4.1** Axisymmetric numerical model geometry used for circular cofferdams

#### 4.2.1 Axisymmetric numerical model validation

The accuracy of the axisymmetric numerical simulation procedure for estimating the flow rate  $q$  and exit hydraulic gradient  $i_E$  was validated against the extensive experimental study

conducted by the Davidenkoff and Franke (1965) using an electrical analogy model. The geometries considered for the validations are shown in Table 4.1.

**Table 4.1** Cofferdam geometries used for validating the axisymmetric numerical model for

circular cofferdams

Circular cofferdams		
$rR/T$	$s/T$	$\alpha$
0.34	0.13	0.00
	0.13	0.50
	0.25	0.00
	0.25	0.50
	0.50	0.00
	0.50	0.50
	0.80	0.00
	0.80	0.50
0.67	0.11	0.00
	0.11	0.51
	0.26	0.00
	0.26	0.50
	0.51	0.00
	0.50	0.50
	0.80	0.00
	0.80	0.50
1.34	0.21	0.05
	0.21	0.52
	0.51	0.02
	0.51	0.51
	0.80	0.00
	0.80	0.50
3.27	0.51	0.05
	0.51	0.52
	0.76	0.03
	0.76	0.52

Accuracy of flow rate estimation

For the validation, dimensionless flow rate values ( $q/kh$ ) measured using the experimental models by Davidenkoff and Franke (1965) were compared against the corresponding

dimensionless flow rate values ( $q/kh$ ) calculated by the author's numerical simulations. Here,  $q$  is the flow rate per unit length along the perimeter of the circular cofferdam. The comparison results are shown in Fig. 4.2.

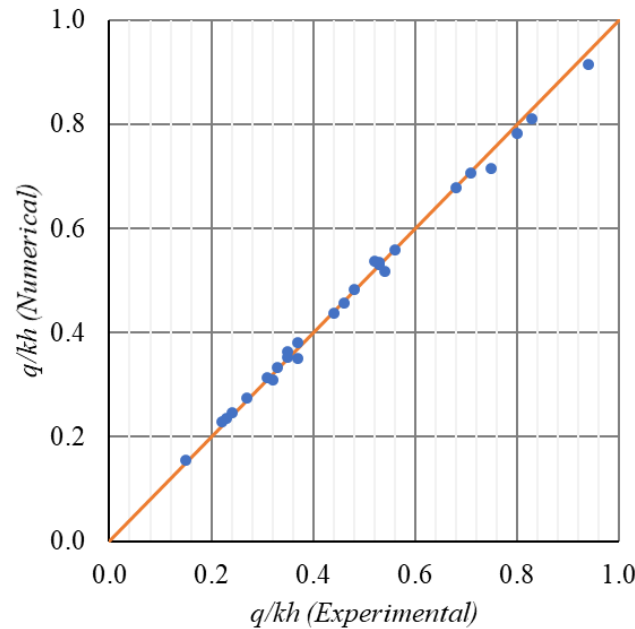


**Fig. 4.2** Axisymmetric numerical model validation for flow rate estimation of circular cofferdams

#### Accuracy of exit hydraulic gradient estimation

In experimental models, maximum exit hydraulic gradient  $i_E$  value calculated is the average value of hydraulic gradient within the sheet pile enclosure, from tip of the sheet pile to the base of the excavation. Therefore, for the accuracy assessment, normalised average exit hydraulic gradient values ( $i_{E_{Avg.}}/h$ ) derived using the experimental results by Davidenkoff and Franke (1965) were compared against the corresponding values calculated using numerical simulations for series of cofferdam geometries shown in Table 4.1. Davidenkoff and Franke (1965) defined the dimensionless parameter  $\phi_s$  which describes the head loss from tip of the sheet pile (point P on Fig. 4.1) to the excavation base as a fraction of the total head loss over the cofferdam as:

$$\phi_s = \frac{\text{Head loss from pile tip to the excavation base}}{\text{Total head loss } (h)} \quad (4.1)$$

Then, average exit hydraulic gradient  $i_{E Avg.}$  can be estimated as:

$$i_{E Avg.} = \frac{\phi_s h}{\text{Length from pile tip to excavation base}} \quad (4.2)$$

Then, substituting the  $\phi_s$  values measured by Davidenkoff and Franke (1965) into Eq. 4.2, experimental  $i_{E Avg.}$  values were calculated for the series of circular cofferdam geometries shown in Table 4.1. Next, for the same geometries, corresponding  $i_{E Avg.}$  values were calculated using the numerical simulation results. Here too, for each numerical model,  $\phi_s$  value was calculated using the total head value measured at pile tip (see Eq.4.1), and then, relevant  $i_{E Avg.}$  value was calculated as per the Eq. 4.2. For the assessment of model validity,  $i_{E Avg.}/h$  values calculated using the experimental and numerical results were compared as shown in Fig. 4.3.

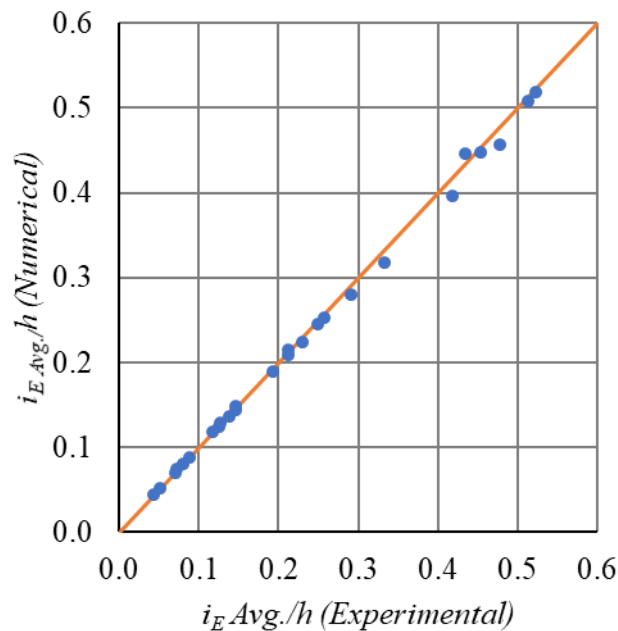


**Fig. 4.3** Axisymmetric model validation for average exit hydraulic gradient  $i_{E Avg.}/h$  estimation of circular cofferdams

In both cases (Figs. 4.2 and 4.3), the numerical model results are closely related to the experimental results. All the flow rate and exit hydraulic gradient predictions by the numerical simulations are within the  $\pm 5\%$  of the corresponding experimental results. Therefore, it is verified that the accuracy of the axisymmetric numerical model is adequate for analysing the seepage beneath the circular cofferdams.

Next, a sensitivity analysis was conducted varying the distance to the outer boundary from the sheet pile wall  $r_e$  between  $2T$  to  $6T$  for the series of cofferdam geometries. Results showed that increasing the distance beyond the  $2T$  was insensitive on the  $q$  and  $i_E$  results. Also Pavlovsky (1922) [vide Neveu (1972)] showed that when the ratio between the radial distance to the outer boundary from the axis of symmetry (i.e.,  $r + r_e$ ) and the radius of cofferdam  $r$  is about 6, the velocity potential distribution and seepage quantity sufficiently represents the case of infinite extension. Hence, it is recommended to use the distance to the outer boundary from the axis of symmetry as the larger of the two scenarios (i.e.,  $2T + r$  or  $6r$ ).

### 4.3 Flow net solutions for circular cofferdams

Fig. 4.4 shows a circular cofferdam in the elevation and the plan view. In the elevation view, both double-walled and circular cofferdams are similar (see Fig. 3.1 and 4.4a). But, for double-walled cofferdams, flow rate is calculated considering a unit thickness perpendicular to the 2D Cartesian plane while it is computed per radian in circular cofferdams using the axisymmetric analysis (see Fig. 4.4b). Therefore, flow net diagram for a circular cofferdam (axisymmetric flow net) should also be drawn reflecting this.

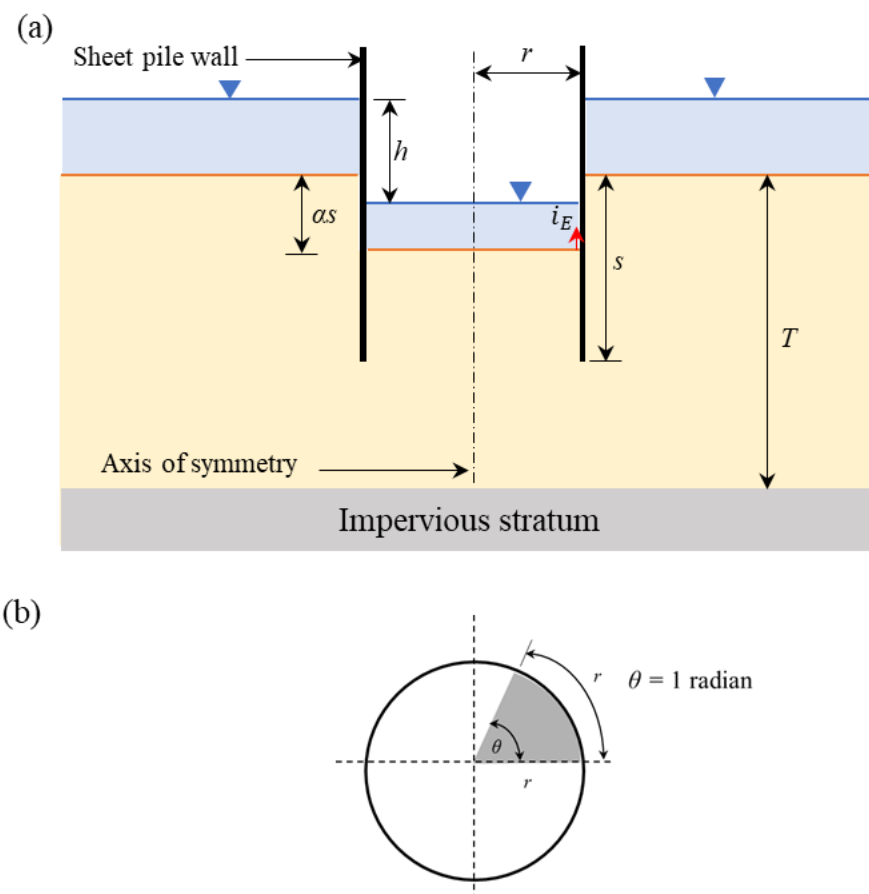


**Fig. 4.4** Circular cofferdam in axisymmetric configuration: (a) elevation view; (b) plan view

Fig. 4.5a shows the flow net for half the section of double-walled cofferdam discussed in example 2.3 by Craig (2004). This was generated using the finite element package, *RS2 V9.011*. Note that, even though the finite element computer package has a facility to draw required number of equipotential lines without selecting the points manually, it is still required to select appropriate start or end points for corresponding flow lines manually on the uppermost (lines AB in Fig. 4.1) or lowest (line CD in Fig. 4.1) equipotential line, respectively forming curvilinear squares ( $a = b$  as shown in Fig. 4.5a) to ensure the accuracy of the flow net. Therefore, after simulating the double-walled cofferdam using equipotential *RS2 V9.011*, equipotential lines were generated considering 10 equipotential drops. Next, corresponding flow lines were generated selecting the end points manually on the lowest equipotential line

(line CD in Fig. 4.5a) because upward flow within the downstream (soil area surrounded by sheet pile walls) side is approximately one dimensional, and hence, equipotential lines closer to the excavation base are horizontal (see Fig. 4.5a). Therefore, shape of curvilinear squares should be approximately square along the equipotential line CD and hence, points for flow lines can be selected more easily and accurately. As discussed in Sec. 2.5.1, total flow rate  $Q$  per unit thickness can be calculated using Eq. 2.44 for the flow net shown in Fig. 4.5a as:

$$Q = 2kh \frac{N_f}{N_d} \quad (4.3)$$

where  $N_f$  and  $N_d$  are the number of flow channels and equipotential drops of half the section.

As noted before, an axisymmetric flow net should be drawn such that it enables computation of the flow rate per radian. Therefore, considering a zone bounded by two adjacent equipotential lines and two flow lines (which is similar to the zone discussed in Fig. 2.12 for double-walled cofferdam), flow rate per radian through this zone can be written as:

$$\Delta q = k \frac{h_z}{b} (a \times r_z) \quad (4.4)$$

Here,  $h_z (= h/N_d)$  is the head loss within the zone, and  $r_z$  is the arc length at the center of the zone, with the axis of symmetry being the center for the arc. Since the flow rate is computed per radian, the arc length is the same as the radial distance to the center of the zone (see Fig. 4.4b). Then total flow rate  $Q$  per radian into the circular cofferdam can be defined using the similar way discussed for the double-walled cofferdam in Eq. 2.43 by:

$$Q = kh \frac{N_f}{N_d} \frac{a}{b} r_z \quad (4.5)$$

To interpret the Eq. 4.5 into the more general form (similar to the Eq. 4.3), it is essential to maintain  $\frac{a}{b} r_z = 1$  m at every zone, where the geometry configuration is in the unit of meter. As

noted before, for the double-walled cofferdams,  $\frac{a}{b} = 1$  (see Fig. 4.5a) making a curvilinear square in each zone whereas, in axisymmetric flow, this ratio  $a/b$  is inversely proportional to the radial distance ( $r_z$ ) of the zone from the axis of symmetry.

Fig. 4.5b shows the axisymmetric flow net drawn for the circular cofferdam having the same configuration to the double-walled cofferdam discussed in Fig. 4.5a. Here also, *RS2 V9.011* computer package was used, and equipotential lines were generated considering 10 equipotential drops. As discussed before, for flow net in double-walled cofferdam, corresponding flow lines were generated selecting the end points manually on the lowest equipotential (line CD in Fig. 4.5a) line because here too, upward flow within the downstream is approximately one dimensional. However, it was required to maintain the relation  $\frac{a}{b} r_z = 1\text{m}$  for all the cases while this was  $a = b$  for the cofferdam drawn for double-walled cases. Fig. 4.5 clearly shows the difference between the  $\frac{a}{b}$  ratios for the two cases. Also, if entire flow net was drawn by hand, the time and effort required for axisymmetric flow net compared to that for the corresponding double-walled cofferdams is significantly higher, and also it is a more difficult task. Also, as pointed in Sec. 2.5.2, it is required to redraw all the flow lines of the axisymmetric flow net when the geometry is scaled up, while entire flow net remains unchanged for the double-walled cofferdam. Thus, flow net solution is not a convenient solution method for circular cofferdams, and hence, method of fragments (MoF) appears to be a better alternative seepage solution method.

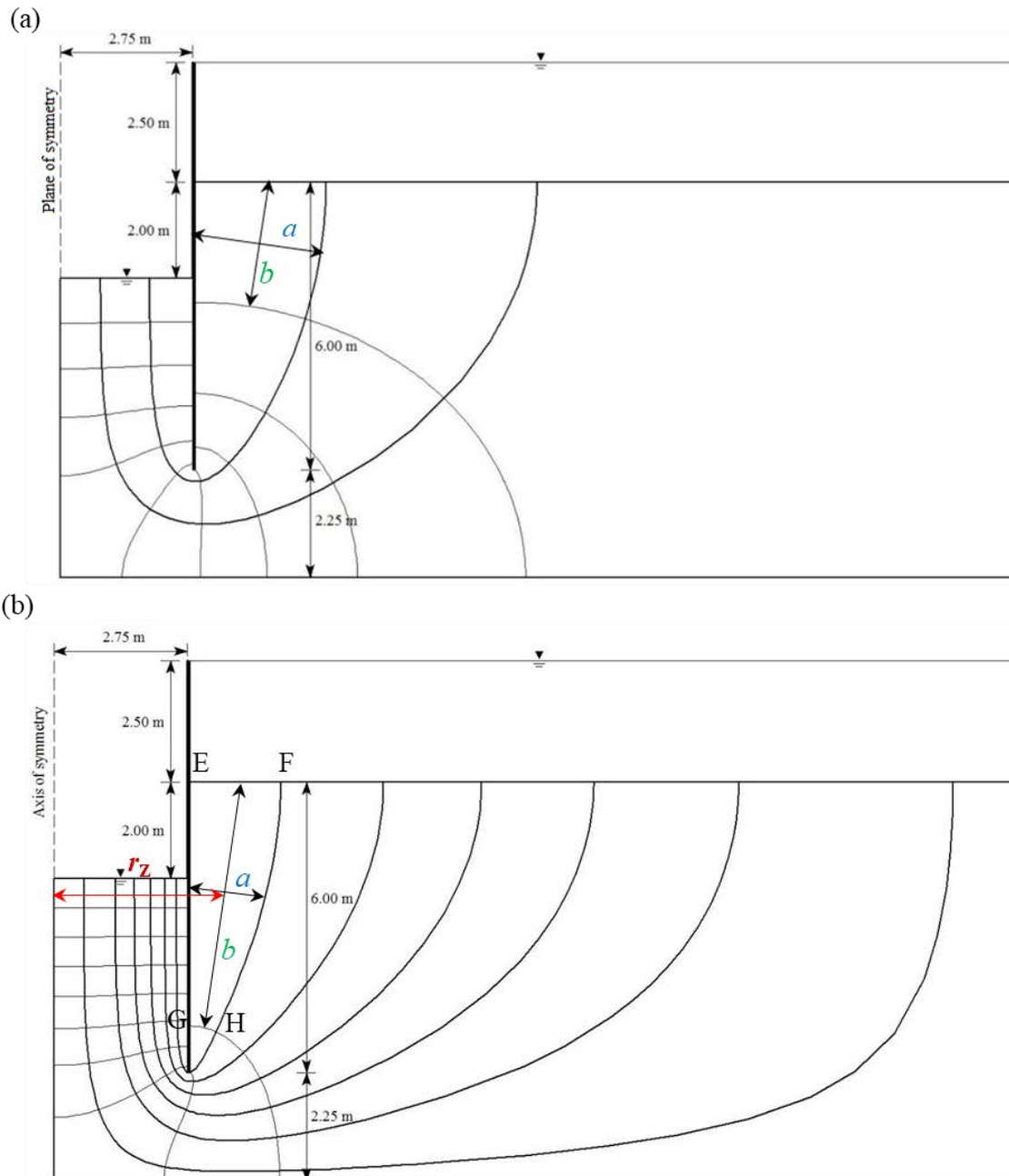


**Fig. 4.5** Flow nets: (a) double-walled cofferdam; (b) circular cofferdam

#### 4.4 Adaptability of method of fragments (MoF) solutions for circular cofferdams

The axisymmetric method of fragments (MoF) approach to be developed herein is similar to the two-dimensional Cartesian one (MoF for double-walled cofferdam). Hence, equipotential line at the tip of the cut-off wall is required to be vertical, and the axis of symmetry acts as an impermeable boundary. Then, flow domain of a radial plane shown in Fig. 4.6 can be divided

into two fragments, namely, an inner fragment  $D$  and outer fragment  $E$ , which are joined at the assumed vertical equipotential surface along perimeter of the cofferdam. Therefore, accuracy of the MoF solutions for circular cofferdams also depends on the validity of this assumption (i.e., equipotential line is vertical at sheet pile tip). Consequently, it is important to see the behavior of the equipotential lines over a range of cofferdam geometries before developing the axisymmetric MoF solutions.

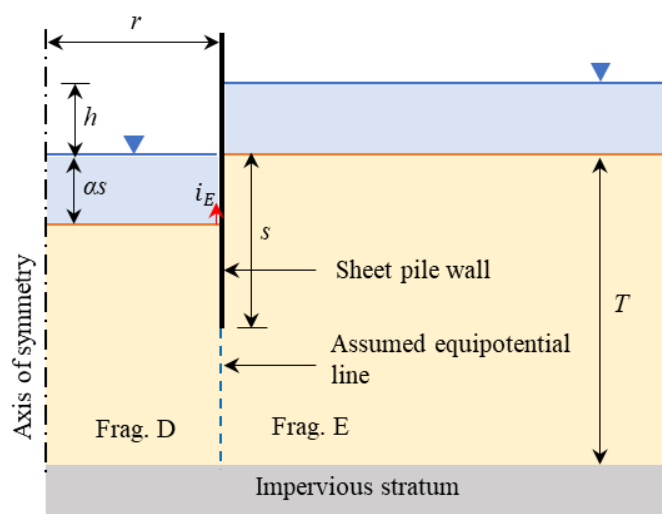


**Fig. 4.6** Proposed Axisymmetric fragment types: (a) fragment  $D$ ; (b) fragment  $E$

#### 4.4.1 Validity assessment of the assumption for equipotential line behaviour

The procedure adopted here was similar to the one applied for assessing the validity of the same assumption for double-walled cofferdams. In a similar manner, behavior of the equipotential line at tip of the sheet pile was studied over a range of geometries shown in Table 4.2. Fig. 4.7 shows the equipotential lines drawn for each case. The equipotential lines are away from the vertical for low values of  $rR/T$  and  $s/T$  ratios and become closer to the vertical while increasing  $rR/T$  and  $s/T$ , making the assumption reasonable. Also, the excavation depth is a concern only when excavating to a considerably larger depth ( $\alpha > 0.4$ ) for the geometries where the value of  $rR/T$  is high and  $s/T$  ratio is low. This pattern of equipotential lines behaviour for circular cofferdam is similar to the one observed for the double-walled cofferdams (see Fig.

3.7); therefore, it can be considered that MoF is a feasible solution method for circular cofferdam problems, too.

**Table 4.2** Circular cofferdam geometries used for equipotential lines behaviour studied

$rR/T$	$s/T$	$\alpha$
0.1	0.1	0, 0.4, 0.8
	0.4	0, 0.4, 0.8
	0.8	0, 0.4, 0.8
0.4	0.1	0, 0.4, 0.8
	0.4	0, 0.4, 0.8
	0.8	0, 0.4, 0.8
0.8	0.1	0, 0.4, 0.8
	0.4	0, 0.4, 0.8
	0.8	0, 0.4, 0.8

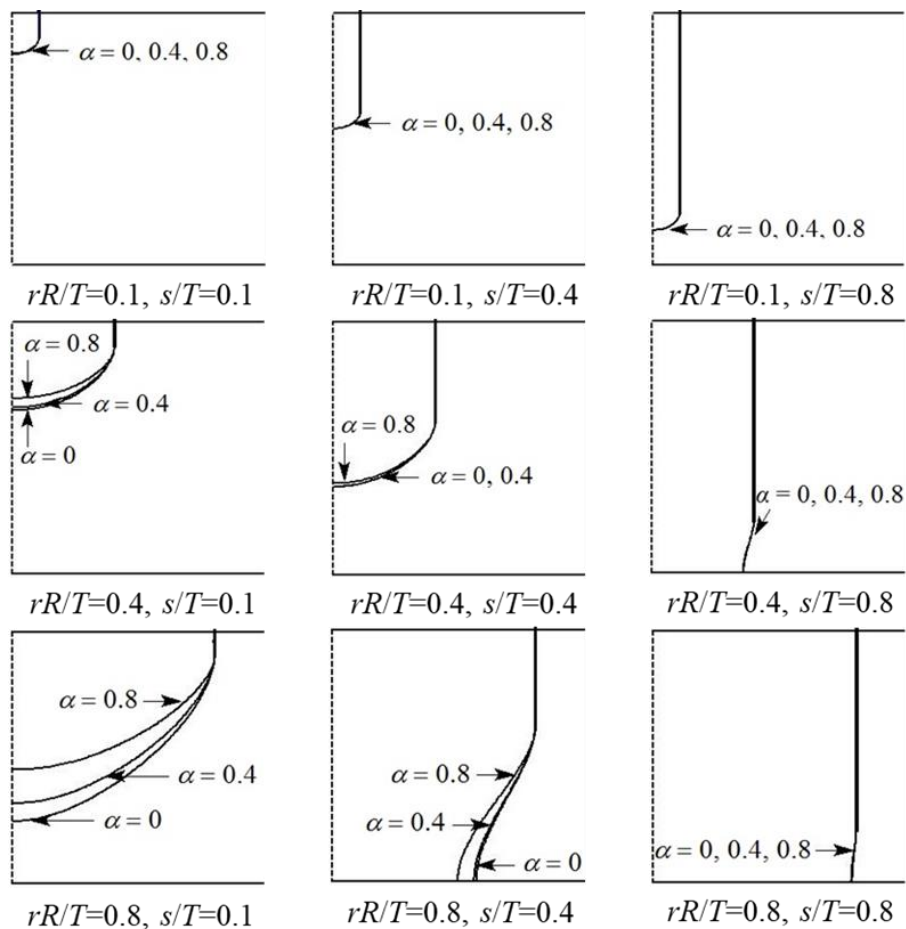


**Fig. 4.7** Behaviour of the equipotential lines with circular cofferdam geometries

#### 4.5 Development of method of fragments (MoF) for circular cofferdams

Similar to the form factors used in the MoF solutions for double-walled cofferdams, axisymmetric form factors denoted by  $\beta_D$  and  $\beta_E$  are used to represent the fragments  $D$  and  $E$ , respectively shown in Fig. 4.6.

The main attributes of the form factors ( $\beta_D$  and  $\beta_E$ ) must be:

- (a) They should be dimensionless numbers,
- (b)  $\beta_{\text{Cofferdam}} = \beta_D + \beta_E$
- (c) The ratio of head losses ( $h_i$ ) and form factors  $\beta_i$  are same for both fragments, i.e.,

$$\frac{h_D}{\beta_D} = \frac{h_E}{\beta_E} = \frac{h}{\beta_D + \beta_E}$$

where  $h = h_D + h_E =$  total head loss over the entire cofferdam, and  $h_D$  and  $h_E$  are the head losses within the fragments  $D$  and  $E$ .

- (d) when the geometry is scaled by  $x$  times, the form factors should remain the same.

In circular cofferdams, when the geometry is scaled by  $x$  times, the total flow is also scaled by  $x$  times while the flow rate per unit length of perimeter remains the same at a constant head loss  $h$ . Therefore, to ensure that the form factor of any fragment  $\beta_i$  remains the same when the geometry is scaled up, the flow rate per unit length of perimeter is used in defining the form factor. Also, both form factors are functions only of the cofferdam geometry described by embedded depth, radius, and thickness of the soil. Hence, form factor ( $\beta_D$  and  $\beta_E$ ) can be written as:

$$\beta_D = \frac{kh_D}{q_D} = f\{s_D, r, T_D, R\} = f\left\{\frac{s_D}{T_D}, \frac{rR}{T_D}\right\} \quad (4.6a)$$

$$\beta_E = \frac{kh_E}{q_E} = f\{s_E, r, T_E, R\} = f\left\{\frac{s_E}{T_E}, \frac{rR}{T_E}\right\} \quad (4.6b)$$

where,  $q_D$  and  $q_E$  are the flow rate per unit length of perimeter of fragment  $D$  and  $E$ , respectively. Also,  $s_D$  and  $T_D$  are the sheet pile embedded depth and the thickness of the soil layer thickness, respectively within fragment  $D$  while  $s_E$  and  $T_E$  are the same parameters within fragment  $E$ . However,  $s_E = s$  and  $T_E = T$  for fragment  $E$  (see Fig. 4.6). Also, flow rate through each fragment is the same, and hence,

$$q = \frac{kh_D}{\beta_D} = \frac{kh_E}{\beta_E} = \frac{kh}{\beta_D + \beta_E} \quad (4.7)$$

#### 4.5.1 Development of design charts required for axisymmetric MoF solution

Fig. 4.8 shows the geometry of the numerical models used to simulate the fragment  $D$  and  $E$  using *RS2 V9.011*. The two fragments separated along the joint shown as a dashed vertical line in Fig. 4.6 (which is assumed to be an equipotential line), and flow lines are assumed perpendicular to that. The bases of the two fragments (BC and BH), the left boundary CD (i.e., vertical centerline) of fragment  $D$  and the sheet pile surfaces (AE and AF) were taken as impervious boundaries. The vertical boundary AB and the horizontal boundary DE of the fragment  $D$  were treated as constant head boundaries with the head difference of  $h_D$ . Similarly, for the fragment  $E$ , vertical boundary AB and the horizontal boundary FG were also treated with constant head boundaries where the difference is  $h_E$ . The inner fragment  $D$  has a radius of  $r$ . The outer fragment  $E$  begins at radius of  $r$  and extends to  $r_e$ . The radial distance  $r_e$  was selected as the larger of the two scenarios (i.e.,  $2T + r$  or  $6r$ ) as discussed in Sec. 4.2.

Although fragments  $D$  and  $E$  are different in geometry, both geometries become similar when  $r$  equals infinity, and the situations can be simulated by a single sheet pile wall in 2D Cartesian system. Hence fragment  $D$  and fragment  $E$  form factors should be the same and equal to the case of single sheet pile wall when  $r$  equals infinity. Also fragment  $D$  exit gradient values at  $r$

$= \infty$  should also be equal to the single sheet pile values. As noted in Chapter 3, single sheet pile wall can be simulated by the fragment  $C$  geometry (discussed for the double-walled cofferdams) with the fragment width  $L$  equals two times the permeable layer thickness  $T_C$  (see Fig. 3.13). Hence, flow rate and maximum exit hydraulic gradient values of fragment  $C$  geometry at  $L = 2T_C$  were used to derive the form factor values of both fragments  $D$  and  $E$  ( $\beta_D$  &  $\beta_E$ ) and normalised exit hydraulic gradient values ( $i_{ES_D}/h_D$ ) of fragment  $D$  when  $rR/T$  equals infinity. Fig. 4.9 shows the convergence of both form factors and  $i_{ES_D}/h_D$  values to the fragment  $C$  values while changing the  $rR/T$  ratio as 1, 1.5, 2, 5 and 10.

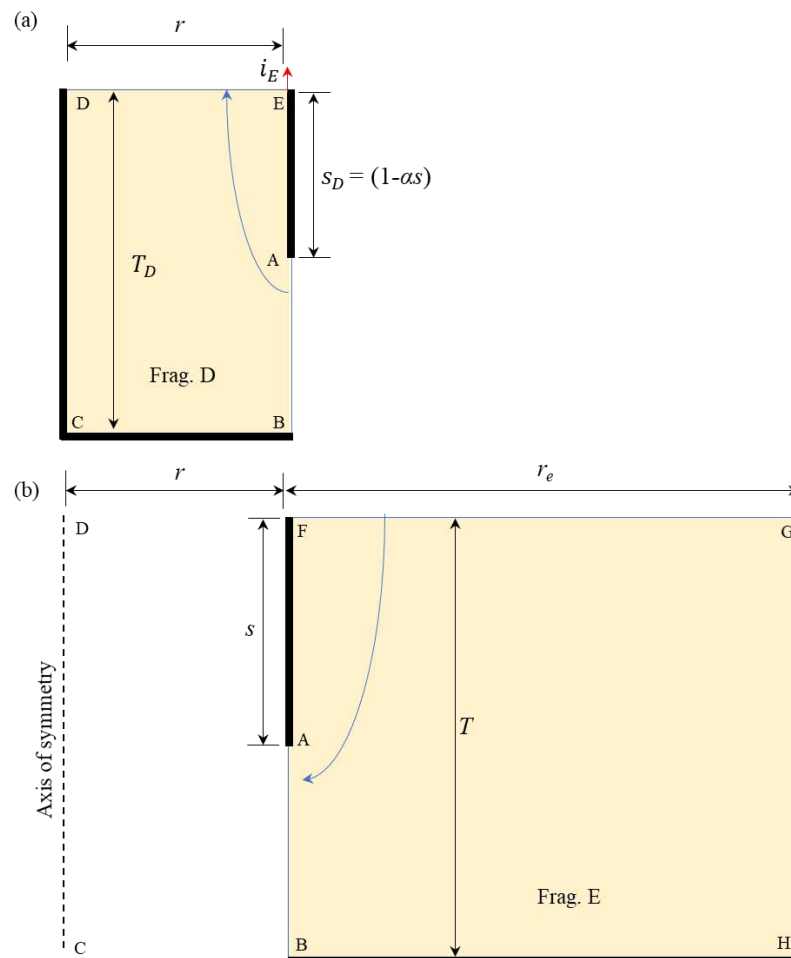


**Fig. 4.8** Numerical model geometry used for axisymmetric fragments:

(a) fragment  $D$ ; (b) fragment  $E$

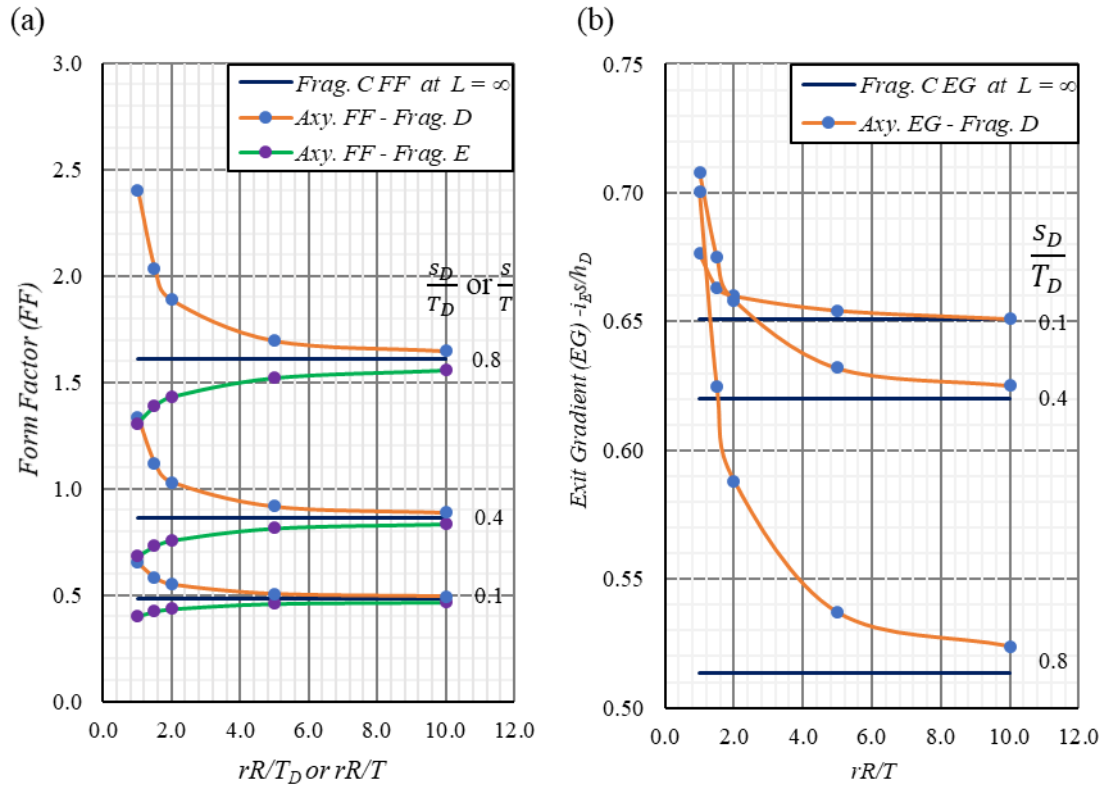


**Fig. 4.9** Convergence of axisymmetric form factor and dimensionless exit hydraulic gradient values to single sheet pile wall values: (a) form factors; (b) exit hydraulic gradient

Design charts for formfactor estimations of fragments D and E

Using the flow rate values obtained for both fragments, corresponding form factor values were calculated via Eq. 4.6 and are presented in the form of design charts shown in Fig. 4.10 and 4.11, for the fragment *D* and *E*, respectively (Appendix B1 shows the calculated form factor values of fragment *D* while appendix B2 shows the fragment *E* values). These charts can be used for determining the flow rate  $q$  per unit length along the perimeter of circular cofferdams. The effect of the soil anisotropy,  $R$  is also incorporated in these charts.

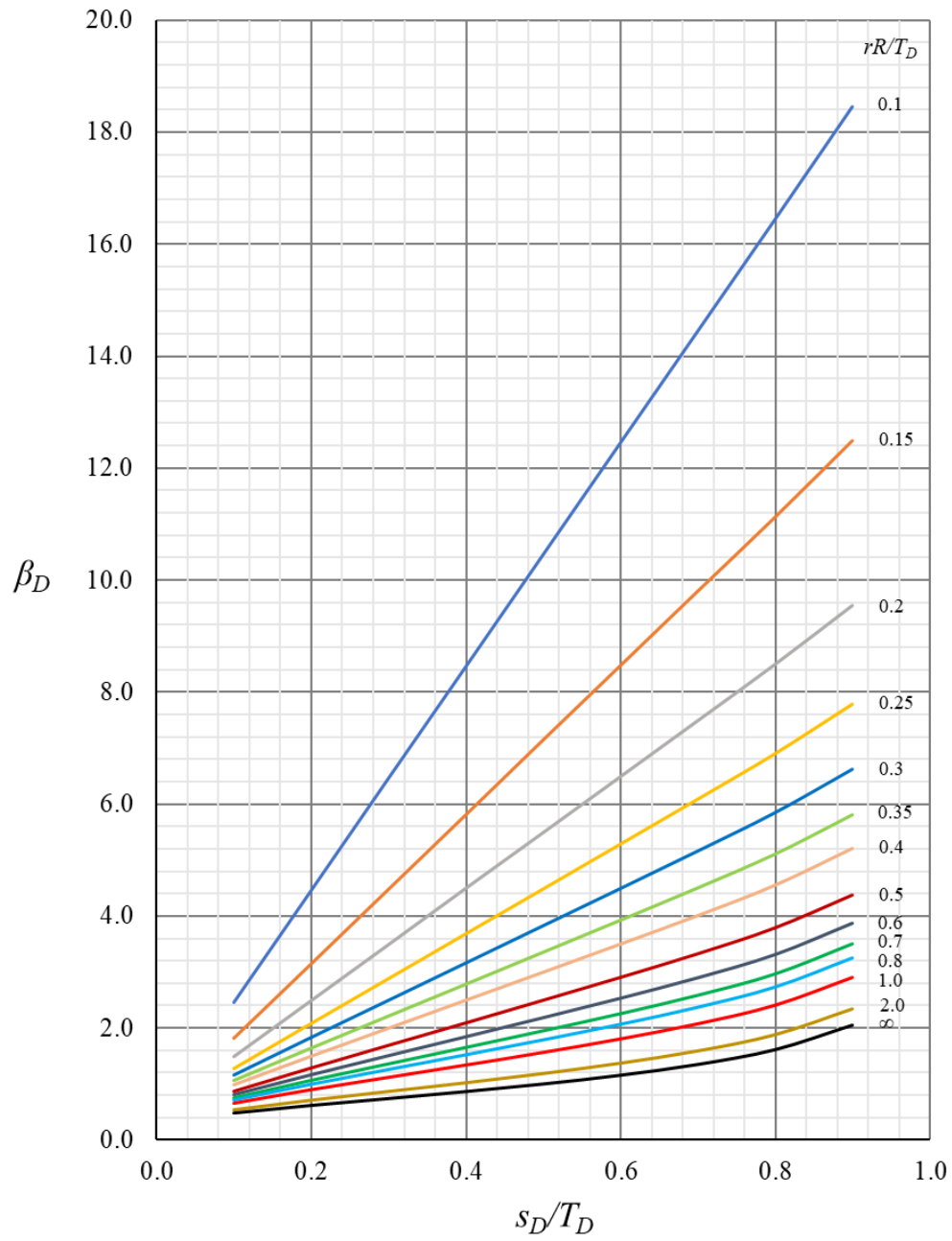


**Fig. 4.10** Form factor  $\beta_D$  values for fragment  $D$  (from finite element simulation)

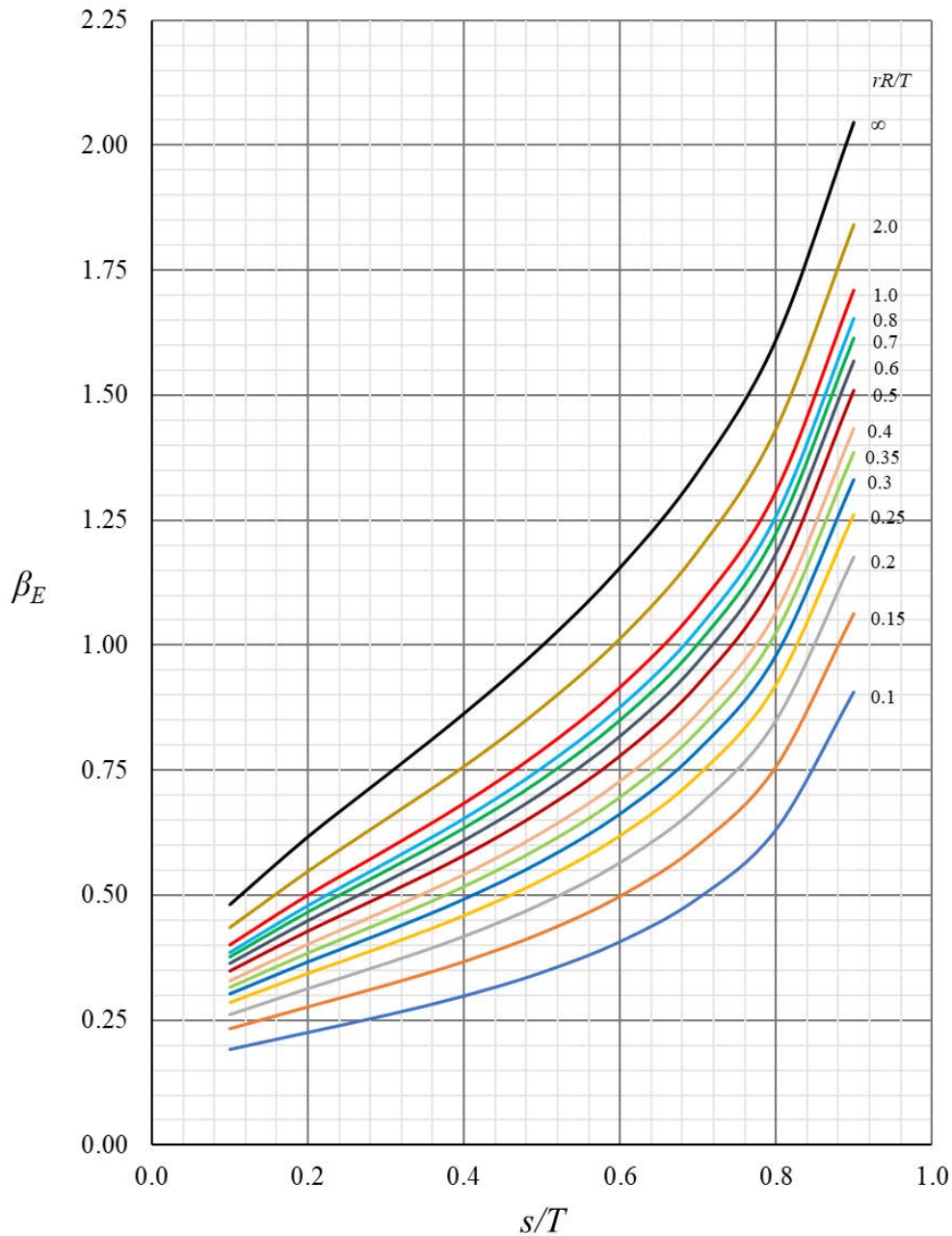


**Fig. 4.11** Form factor  $\beta_E$  values for fragment  $E$  (from finite element simulation)

Design chart for exit hydraulic gradient estimations of fragment  $D$

Calculated  $i_E$  values of fragment  $D$  were converted into the dimensionless form ( $i_E s_D / h_D$ ) and are presented in Fig. 4.12 (see Appendix B3 for the calculated normalized exit hydraulic gradient values of fragment  $D$ ). This chart can be used along with two form factor charts (Figs.

4.10 and 4.11) to determine the exit hydraulic gradient of any circular cofferdam geometry.

Here, too, soil anisotropy effect  $R$  can be incorporated directly.

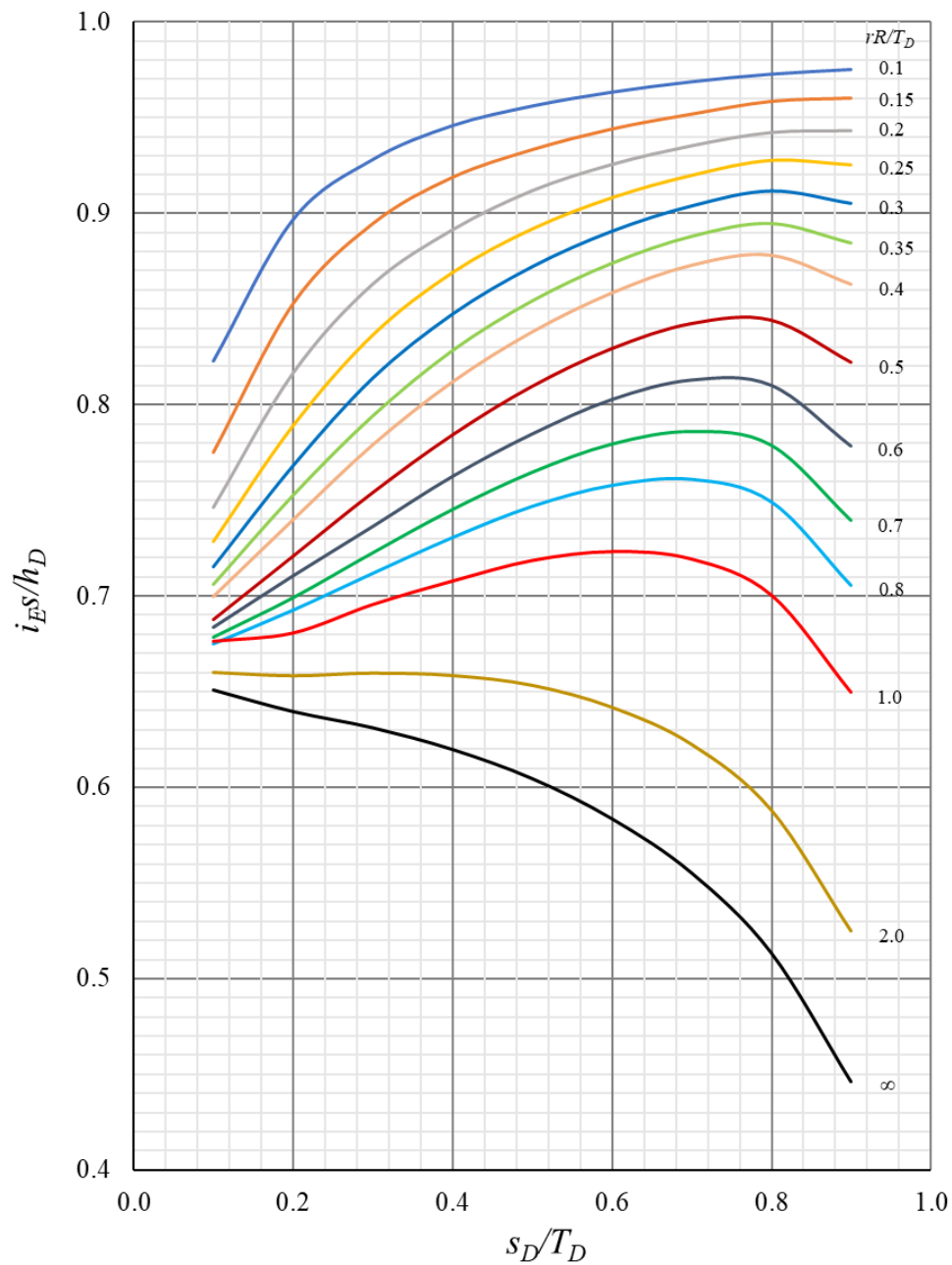


**Fig. 4.12** Exit gradient values for fragment  $D$  (from finite element simulation)

#### 4.6 Validation of MoF solutions for circular cofferdams

The flow rate  $q$  and exit hydraulic gradient  $i_E$  values predicted using the proposed axisymmetric MoF solutions were compared among the finite element solutions, analytical

solutions and experimental results reported in the literature. Further, a small-scale laboratory model was developed for analysing the circular cofferdams, and using that, series of tests were carried out. Then, these experimental results were compared against the solutions derived using the proposed MoF solutions. The finite element, analytical and experimental results used for the validations do not make any assumptions about the equipotential line at the tip of the sheet pile being vertical. Here, the term full numerical modelling (Full NM) is used to define finite element solutions as applied in chapter 3.

#### 4.6.1 Comparison against finite element solutions

Fig. 4.13 shows the comparison of normalized seepage quantity ( $q/kh$ ) and  $i_E$  obtained by the MoF solution with the corresponding finite element solutions (Full NM) for the series of geometries. Here, 108 geometries were studied changing the  $rR/T$  from 0.1 to 1 and  $s/T$  from 0.1 to 0.9 while keeping the soil as isotropic ( $R = 1$ ) and depth of excavation as zero ( $\alpha = 0$ ).

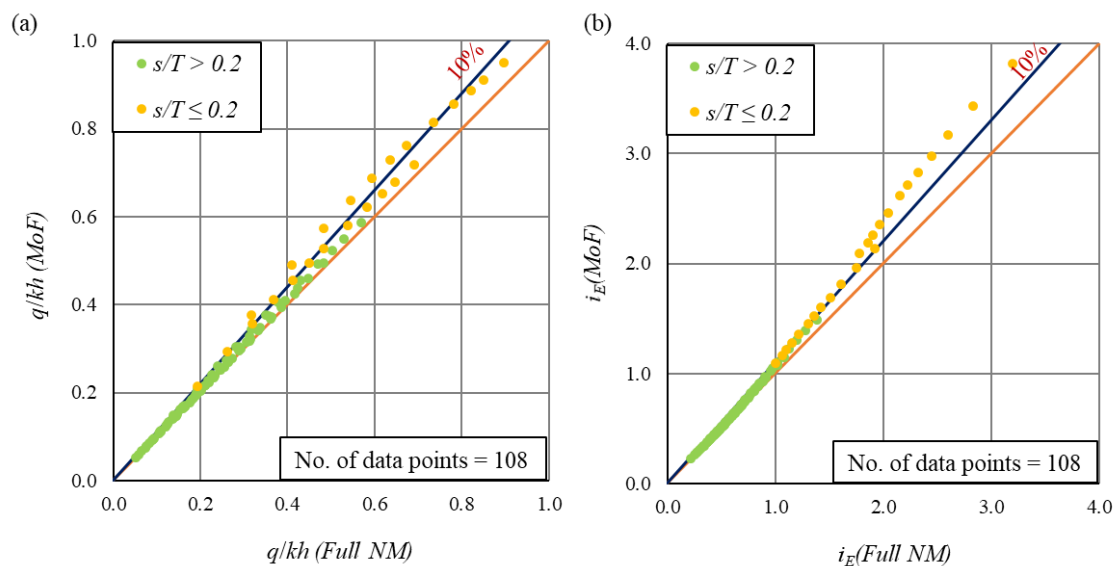


**Fig. 4.13** Comparison of predictions from axisymmetric MoF and full numerical model (Full NM) solutions when  $\alpha = 0$ : (a) seepage quantity; (b) exit hydraulic gradient

Both comparisons show strong relationship between the MoF solutions and the finite element solutions. Also, MoF solutions are always on the safe side, overestimating both  $q$  and  $i_E$  slightly, (i.e., they are conservative) and differ by less than 10% compared to the corresponding finite element solutions for most of the cases (i.e., 95 and 87 cases out of the 108 for  $q/kh$  and,  $i_E$  respectively). The few cases where the deviation is slightly larger (10-22%) correspond to the geometries having the less applicability in the practice ( $s/T \leq 0.2$ ).

In addition, Fig. 4.14 compares the  $q/kh$  and  $i_E$  at three excavation depths ( $\alpha = 0, 0.4$  and  $0.8$ ) predicted by MoF against the corresponding numerical simulation results for three different cofferdam radii of  $rR/T = 0.1, 0.4$  and  $0.8$  changing  $s/T$  from  $0.1$  to  $0.9$ . For all three cases ( $\alpha = 0, 0.4$  and  $0.8$ ), the relation between the MoF predictions and numerical solutions follows a similar trend, i.e., MoF predictions are always conservative, and the error decreases with increasing the  $s/T$  and  $rR/T$  values. In addition, for two cases where  $\alpha = 0$  and  $0.4$ , deviations of MoF solutions from the numerical results are less compared to that for the case of  $\alpha = 0.8$ . These observations are in line with the conclusion made with the Fig. 4.7 above (i.e., effect of the excavation depth on the validity of the assumption is a concern only when excavating to a considerably larger depth). However, the effect of violating this assumption is always on the conservative side (i.e., both the  $q/kh$  and  $i_E$  are overestimated).

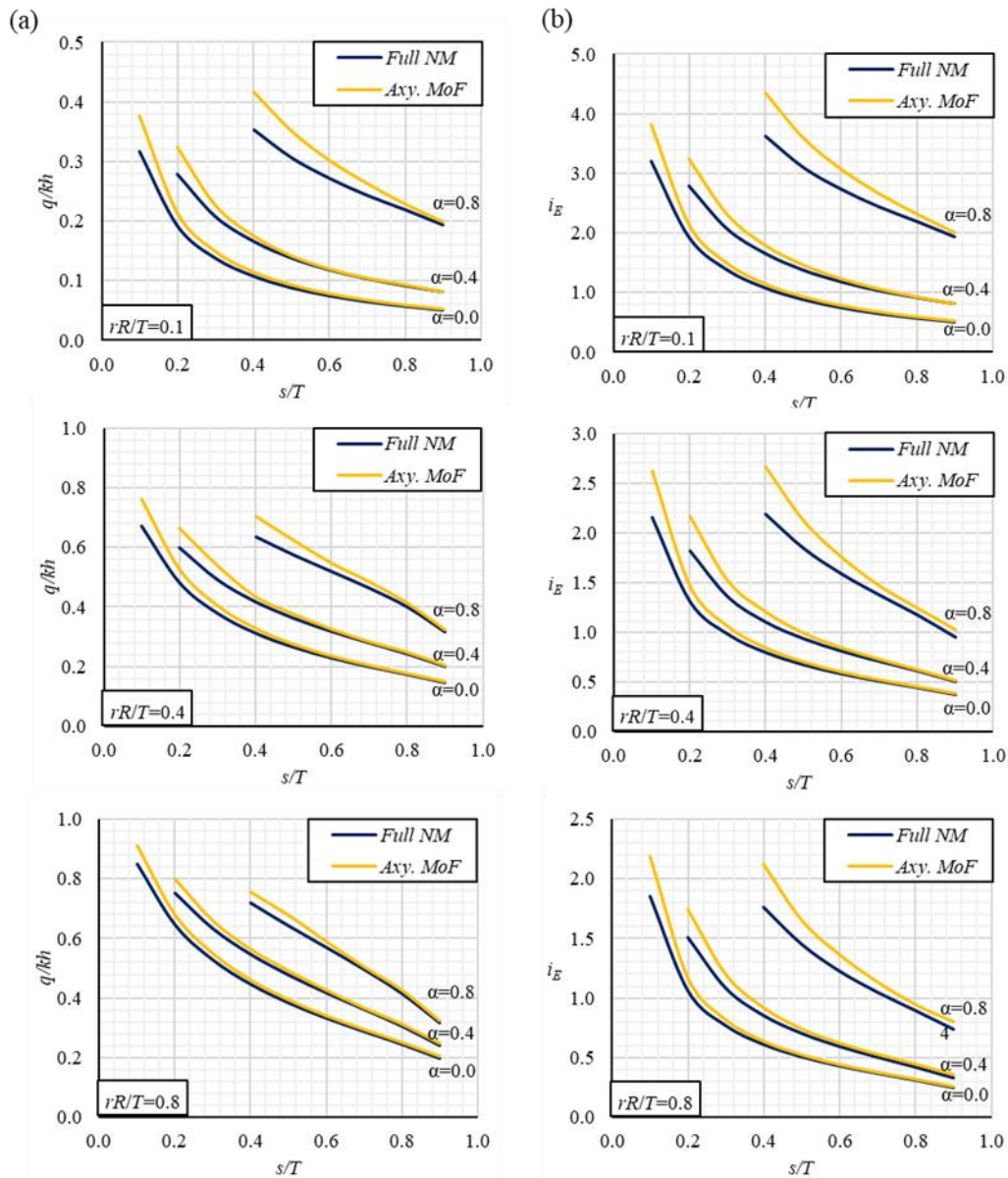


**Fig. 4.14** Effect of cofferdam geometry on the accuracy of axisymmetric MoF solutions:

(a) seepage quantity; (b) exit hydraulic gradient

#### 4.6.2 Comparison against analytical solutions

Normalised seepage quantities  $q/kh$  estimated by the proposed axisymmetric MoF method are compared against the analytical solutions by the Neveu (1972) for the isotropic condition ( $R=1$ ). The geometry range considered for the comparison is given in Table 4.3, and the comparison results are shown in Fig. 4.15.

**Table 4.3** Cofferdam geometries used for axisymmetric MoF comparisons against analytical solution by Neveu (1972)

$\alpha$	$s/T$	$rR/T$
0	0.2	0.10
	0.2	0.20
	0.2	0.40
	0.5	0.25
	0.5	0.50
	0.5	1.00
	0.8	0.40
	0.8	0.80
0.505	0.2	0.10
	0.2	0.20
	0.2	0.40
	0.5	0.25
	0.5	0.50
	0.5	1.00
	0.8	0.40
	0.8	0.80
0.808	0.5	0.25
	0.5	0.50
	0.5	1.00
	0.8	0.40
	0.8	0.80
	0.8	1.60

When the excavation depth is zero ( $\alpha = 0$ ), the maximum deviation is about 12% for low depth of cut-off wall ( $s = 0.2T$ ), and it is about 6% for other two cases ( $s = 0.5T$  and  $s = 0.8T$ ). For the excavation depth ( $\alpha$ ) is equal to 0.505, a slightly larger deviation of 19% is observed for  $s = 0.2T$ . This is due to further lowering of  $s_D/T_D$  ratio of the fragment  $D$  [i.e.  $s(1 - \alpha)/(T - \alpha s)$ ], and in this case it is 0.11. For the same excavation depth ( $\alpha = 0.505$ ), the maximum deviation is 8% for other two cases ( $s = 0.5T$  and  $s = 0.8T$ ). When  $\alpha$  is equal to

0.808, the maximum deviation is about 17% for  $s/T = 0.5$  and 0.8. Also, for all these situations, MoF predictions are conservative (i.e., they are overestimate). In summary, proposed MoF solutions are agreed well with the analytical solutions of Neveu (1972). Also, when increasing the excavation depth, the level of discrepancy increases; however, this deviation is on the conservative side, overestimating the seepage quantity. These observations are similar to the observation made with MoF and finite element solutions comparison above.

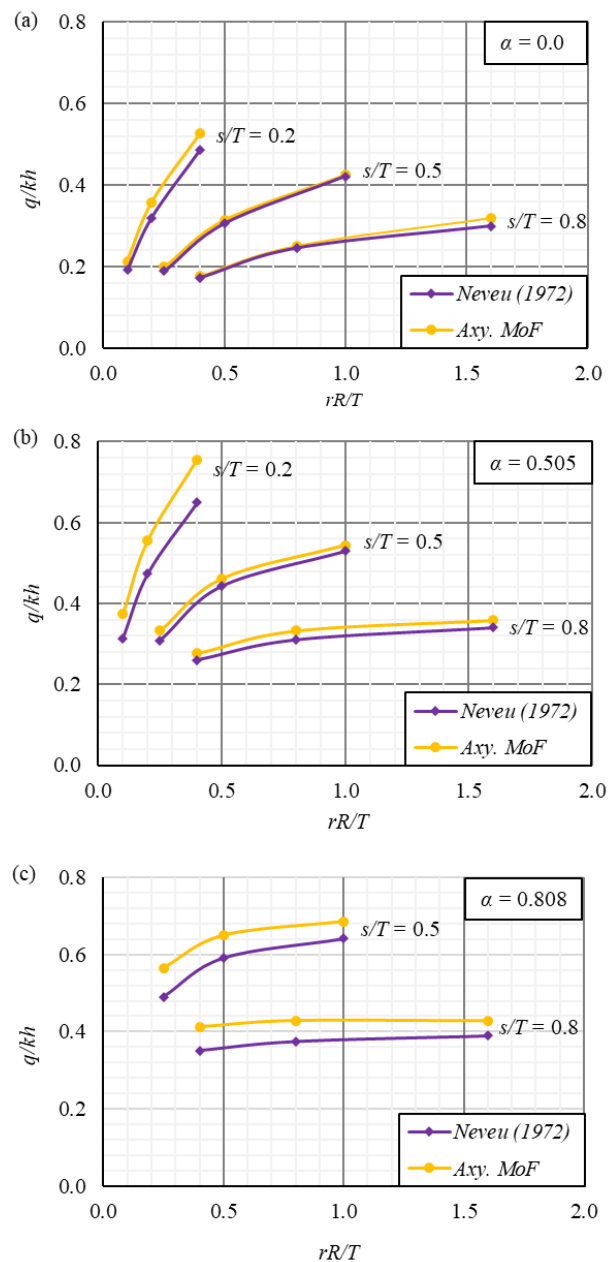


**Fig. 4.15** Comparison of seepage quantities estimated by proposed axisymmetric MoF solutions against analytical solutions by Neveu (1972): (a)  $\alpha=0$ ; (b)  $\alpha=0.505$ ; (c)  $\alpha=0.808$

### 4.6.3 Comparison against experimental results

In order to compare the proposed MoF solutions against the experimental results, an attempt is made to develop a small-scale laboratory model that can be used to study series of circular cofferdam geometries.

#### Soil sample used

Since cofferdams are widely applied in sandy soils, it was decided to use a sandy soil for all laboratory simulations. Also, it is important to select a sand type having particles sizes within a narrow range (poorly graded) since the permeability of these type of soils are less influenced by its packing density variation, and hence, less errors are encountered. So, grain size distributions tests were conducted for three sand samples as per the AS1289.3.6.1 to decide the most suitable sand type. Fig. 4.16 shows the grains size distribution graphs, and Table 4.4 gives the important grain sizes determined.

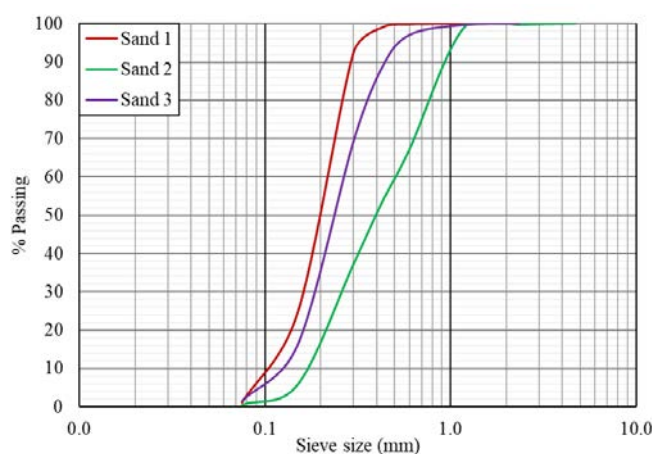


**Fig. 4.16** Grain size distributions for three sand samples

Considering the Fig. 4.16 and the index parameters given in Table 4.4, it is clear that all three samples are poorly graded. However, sand 1 has the most uniform particle size distribution, and hence, its permeability is the least affected one from the variation of packing density. So, sand 1 was selected for running the laboratory model, and hence, other physical properties

required were determined only for the sand 1. Series of tests were conducted as per the Australian standards listed in Table 4.5, and the determined physical properties are shown in Table 4.6.

**Table 4.4** Result of grain size distribution tests

Index property	Sample Name		
	Sand 1	Sand 2	Sand 3
$d_{10}$ (mm)	0.10	0.13	0.17
$d_{30}$ (mm)	0.16	0.18	0.26
$d_{50}$ (mm)	0.20	0.23	0.40
$d_{60}$ (mm)	0.22	0.26	0.50
$C_u$	2.20	2.00	2.94
$C_c$	1.16	0.96	0.80

**Table 4.5** Tests and the list of standards used for determining the physical properties of sand

Tests	Standard used
Grain size distribution	AS1289.3.6.1
Moisture content	AS1289.2.1.1
Specific gravity	AS 1289.3.5.1
Maximum and minimum dry density	AS1289.5.5.1

**Table 4.6** Physical properties of sand 1

properties	Sand 1
Moisture content (%)	0.34
Specific gravity $G_s$	2.67
Minimum dry density $\rho_{dmin}$ (g/cm <sup>3</sup> )	1.37
Maximum dry density $\rho_{dmax}$ (g/cm <sup>3</sup> )	1.59

Using the maximum and minimum dry density values (shown in Table 4.6), minimum and maximum void ratio values ( $e_{min}$  and  $e_{max}$ , respectively) were estimated as:

$$\rho_{dmax} = \frac{G_s \rho_w}{1 + e_{min}} \quad (4.8)$$

$$\rho_{dmax} = \frac{G_s \rho_w}{1 + e_{min}} \quad (4.9)$$

where,  $\rho_w$  is the density of the water. Before running the laboratory model for cofferdam seepage analysis, it was required to define the relationship between the soil permeability  $k$  and the relative density ( $D_r$ ) since knowing the permeability of the sand at a given relative density was essential. It was decided to run all the laboratory tests at  $D_r$  of 40% to minimize the error associated with changing the packing density of sand within the model. So, three constant head permeability tests (at  $D_r$  of 20%, 35% and 50%) were conducted as per the AS 1289.6.7.1 using the permeability test apparatus shown in Fig. 4.17. For permeability estimations, sand 1 was assumed as a homogeneous and isotropic soil. This is a reasonable assumption as discussed before in chapter 2 based on the study conducted by Hatanaka et al. (1997). However, permeability in the horizontal direction can be higher than that of the vertical direction slightly, limiting the maximum difference to the 70% as noted by Hatanaka et al. (1997). Therefore, it is expected that the actual sand permeability can be slightly higher than the calculated value which is based on the vertical flow through the constant head test set-up (see Fig. 4.17).

The diameter and the sample height of the permeameter used were 64 mm 700 mm, respectively. Then, it was essential to calculate the sand quantity (mass) required to fill the permeameter at a given relative density. For that, void ratio  $e$  at the required relative density was determined by:

$$D_r = \frac{e_{max} - e}{e_{max} - e_{min}} \quad (4.10)$$

Then, dry density of the sample at that particular relative density was calculated as:

$$\rho_d = \frac{G_s \rho_w}{1 + e} \quad (4.11)$$

Next, using the dry density values given by Eq. 4.11, soil masses required to fill the perimeter for three cases ( $D_r$  of 20%, 35% and 50%) were calculated. Then, calculated soil mass at each case was placed into the permeameter in seven equal layers (each 10 cm long), ensuring the uniform packing density. At relative densities of 35% and 50%, it was required to apply some compaction effort within the permeameter and which was achieved using a tamping rod on each layer. Then, three permeability values were determined for each case using the procedure described in Sec. 2.2.2 of chapter 2 and were plotted against the corresponding  $D_r$  values in a graph as shown in Fig. 4.18. Using that graph, the relationship between permeability and the  $D_r$  was developed as:

$$k = -0.0003D_r + 0.0238 \quad (4.12)$$

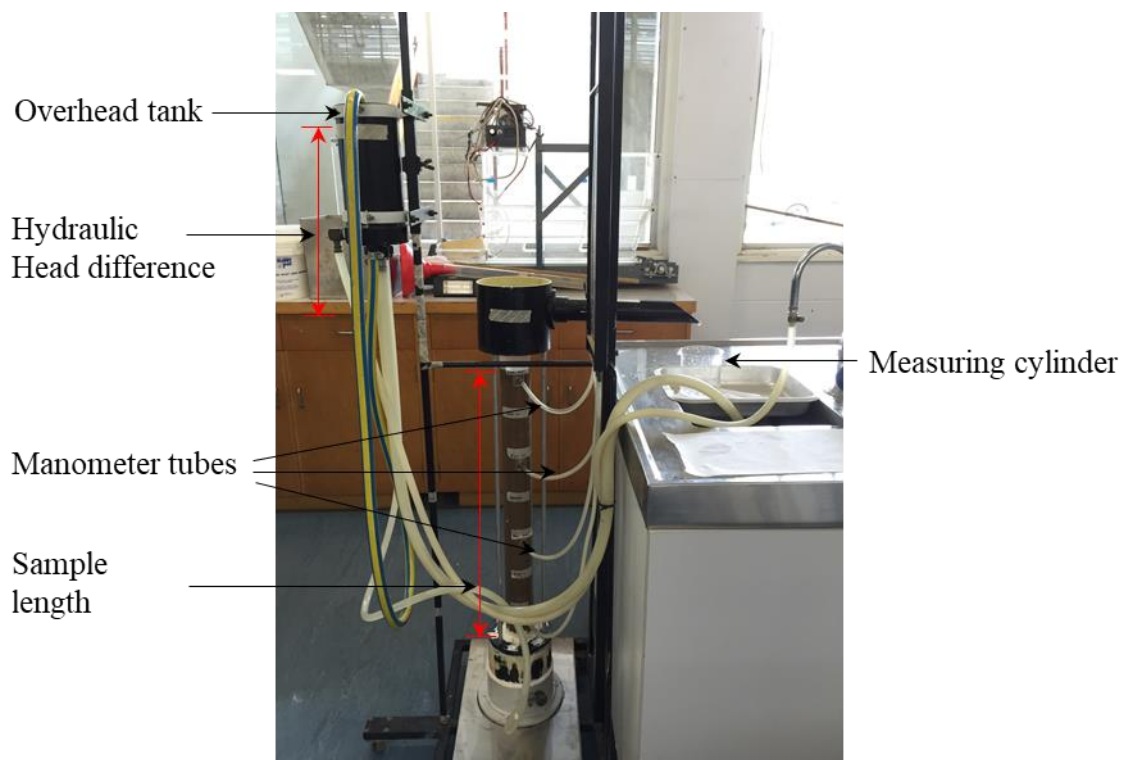


**Fig. 4.17** Constant head test set-up used for permeability values determination

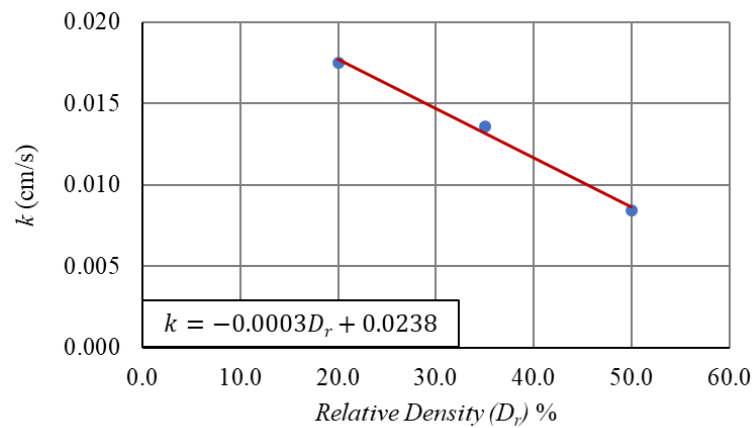


**Fig. 4.18** Relation between permeability and relative density ( $D_r$ )

#### Laboratory test set-up

Fig. 4.19a shows the schematic diagram of the laboratory model (to scale), and Fig. 4.19b is a photograph of the same test set-up used for simulating the series of circular cofferdam geometries. The definitions of the parameters  $r$ ,  $s$ ,  $T$  and  $\alpha$  shown in Fig.4.19a are same as the definitions given in Fig 4.1. The main components of the laboratory model apparatus are:

1. A model circular cofferdam which is made of Perspex tube and has been fixed at the center of the larger tank using the bracing system shown in Fig. 4.19b.
2. A larger tank made of plastic providing the boundary limits for seepage flow into the cofferdam
3. A Constant head set-up, which includes a drain tube attached to the cofferdam (inner Perspex tube) and an overflow tube attached to the larger plastic tank to provide a constant hydraulic head difference for seepage flow into the cofferdam.

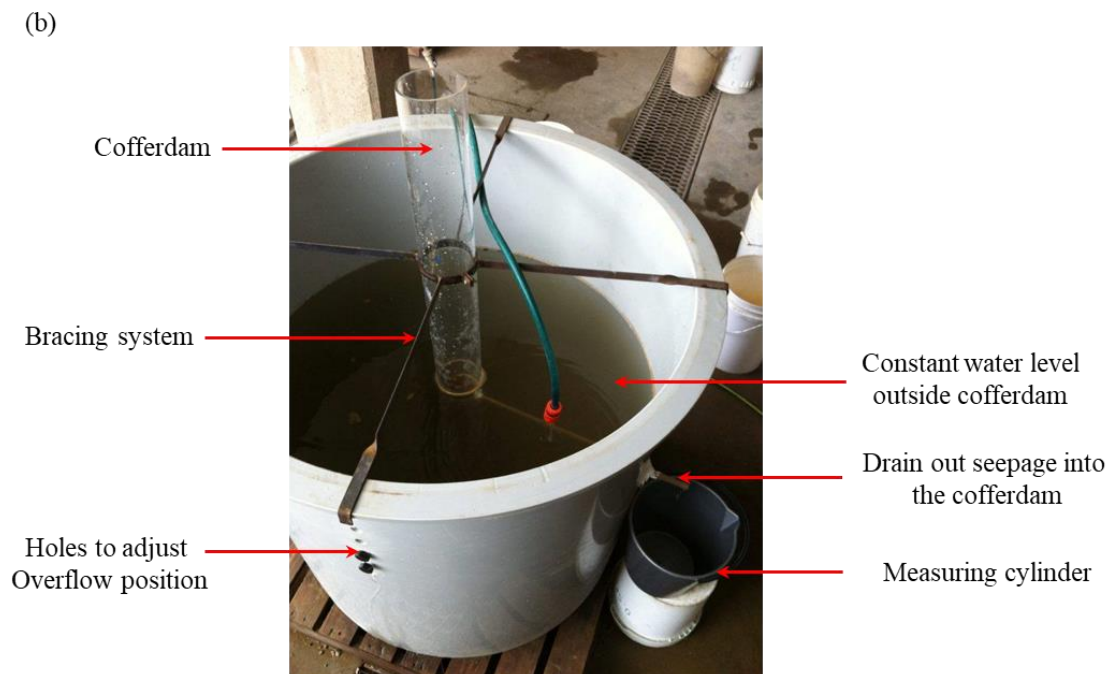
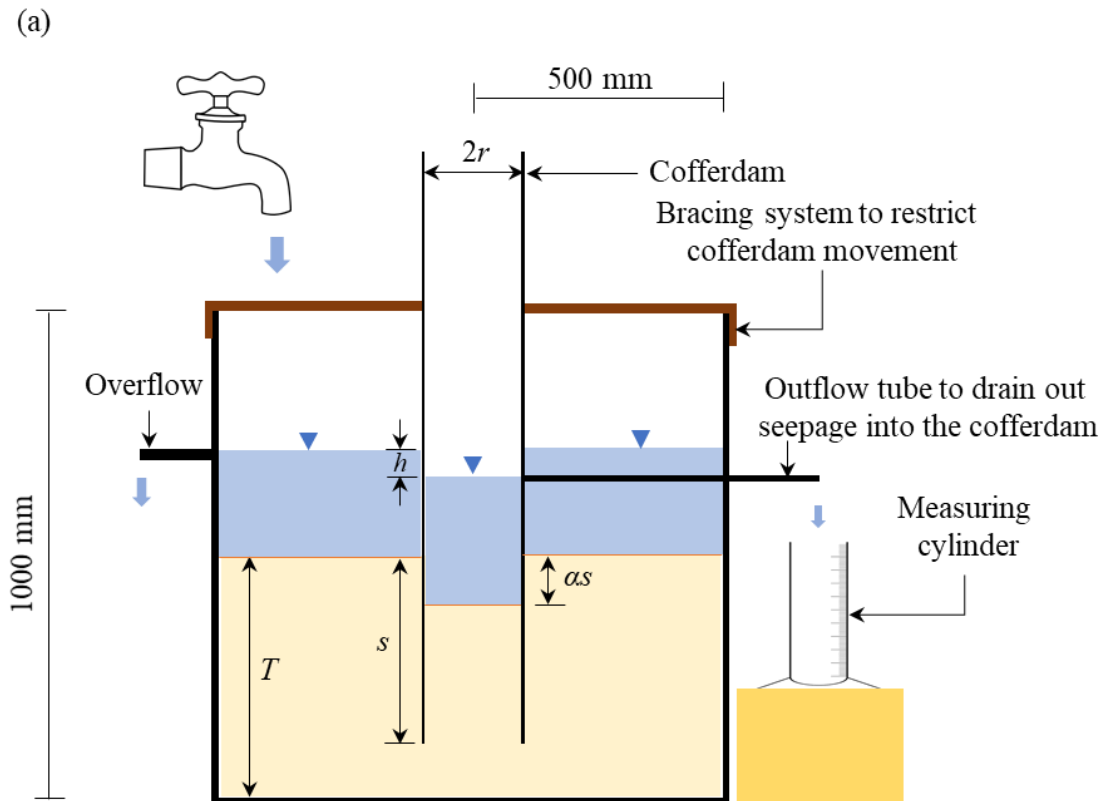


**Fig. 4.19** (a) The schematic diagram of the laboratory test set-up (to scale); (b) a photograph of the test set-up

Using the test set-up shown in Fig. 4.19b, series of tests were conducted under two groups depending on the cofferdam radius used. The first group of tests were based on a larger Perspex tube having the inner diameter of 194 mm (i.e., radius of the cofferdam is 97 mm) while the second group of tests were relevant to the small Perspex tube with the radius of 50 mm. The wall thicknesses of the two Perspex tubes were 3 mm and 5 mm for the larger and smaller tubes, respectively. The dimensions of the tubes (inner diameters and radii) were selected ensuring that they are not significantly affecting the flow. Fand and Thinakaran (1990) [vide Van Lopik et al. (2017)] noted that Pipe diameter to be 40+ times larger than  $d_{50}$ . In the two cases studied here, these ratios are 1000 and 500 for larger and smaller tubes, respectively. Further, the ratio between wall thickness and  $d_{50}$  is 15 for the larger tube while it is 25 for the smaller one. Therefore, it can be assumed that the flow within the inner Perspex tubes are not affected by their wall effects.

#### Laboratory tests methodology

Series of tests were conducted changing the cofferdam geometry ( $rR/T$ ,  $s/T$  and  $\alpha$ ) over a wider range. Noting that, anisotropy ratio  $R$  is equal to 1 in the laboratory simulations since the soil was assumed as isotropic. Table 4.7 shows the sequence of the series of tests conducted. For the first test, the geometry was selected as  $rR/T = 0.8$ ,  $s/T = 0.2$  and  $\alpha = .05$ . Since  $r = 97$  mm, the required soil height  $T$  (outside the cofferdam) was 121 mm and the depth of the cofferdam required to be embedded was 24 mm. Accordingly, the larger Perspex tube was attached firmly at the center of the large tank using the bracing system shown in Fig. 4.19b. Next sand quantity required to fill the volume of larger tank (outside the inner tube) was calculated at the  $D_r$  of 40% using the similar procedure discussed in Eqs. 4.8 - 4.11. Similarly, sand required for filling inner tube was also calculated at the same  $D_r$  value keeping the  $\alpha =$

0.5. Next, pre-determined sand quantities were filled in both inside and outside the cofferdam in several layers ensuring that the sample was placed into the tanks at  $D_r$  of 40%.

**Table 4.7** Sequence of the laboratory tests conducted

Test phase	Test no	$r$ (m)	$rR/T$	$s/T$	$\alpha$
1	1	0.097	0.80	0.20	0.50
	2	0.097	0.60	0.40	0.00
	3	0.097	0.60	0.40	0.00
	4	0.097	0.40	0.60	0.25
	5	0.097	0.40	0.60	0.25
	6	0.097	0.40	0.60	0.00
	7	0.097	0.40	0.60	0.00
	8	0.097	0.30	0.70	0.25
	9	0.097	0.30	0.70	0.25
	10	0.097	0.20	0.80	0.25
	11	0.097	0.20	0.80	0.00
2	12	0.050	0.60	0.40	0.00
	13	0.050	0.40	0.60	0.00
	14	0.050	0.30	0.70	0.00
	15	0.050	0.20	0.80	0.25
	16	0.050	0.20	0.80	0.00

Next water was allowed to enter into the larger tank using a tap. Then, overflow position was adjusted selecting the relevant hole (according to the hydraulic head difference required) among the 6 holes (drilled 5 cm apart vertically) on the wall of the larger tank (see Fig. 4.19b). Then, water started to flow into the cofferdam (inner tube) from the larger tank and was drained out by the outflow tube attached to the cofferdam. After reaching a steady flow condition, flow rate into the cofferdam was measured using the water drain out over 300 seconds through the outflow tube. Three trials were conducted for each geometry, and the flow rate was calculated as the average of three trials. After completing the first test, existing ponding water in both

inner and outer of the cofferdam was drained out completely using buckets and an electric pump. Next, the additional sand amount required to the test 2 geometry (i.e.,  $rR/T = 0.6$ ,  $s/T = 0.4$  and  $\alpha = 0$ ) was filled on top of the sand which was used for the pervious test. Noting that inner tube (model cofferdam) is fixed, and hence,  $rR/T$  value decreases and  $s/T$  value increases while filling the sand for the next test. Using the same procedure, 11 tests were carried out for the group 1 (using the larger Perspex tube). After completing the phase 1 tests, entire test set-up (bracing system, inner tube and sand) was dismantled and was cleaned. Then, tests of phase 2 were started using the small Perspex tube. The procedure applied for phase 2 tests was also similar to the one discussed above for phase 1. In phase 2, five tests were carried out representing the geometries shown in Table 4.7. Appendix B4 shows the results of laboratory simulations of circular cofferdams.

#### Comparison of the results

Measured flow rate for 16 tests were compared against the flow rate predictions using the proposed MoF solutions as shown in Fig. 4.20. Note that normalized flow rate values ( $q/kh$ ) were used for the comparison, and the permeability value required at  $D_r$  of 40% was estimated using Eq. 4.12. Table 4.8 shows the relative errors ( $RE$ ) calculated for each test. The definition used for the relative error calculations was:

$$RE = \frac{(q/kh_{MoF} - q/kh_{Exp})}{q/kh_{Exp}} \quad (4.13)$$

where  $q/kh_{MoF}$  and  $q/kh_{Exp}$  are the normalized flow rate calculated by MoF and experimental results, respectively.

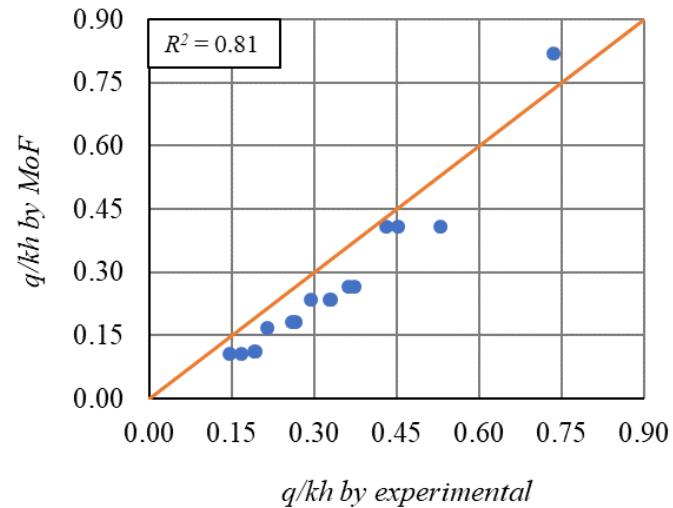


**Fig. 4.20** Comparison of seepage quantities estimated by proposed axisymmetric MoF solutions against experimental results

**Table 4.8** Relative errors between experimental results and MoF Predictions

Test phase	Test no	RE (%)
1	1	11%
	2	-10%
	3	-23%
	4	-26%
	5	-28%
	6	-28%
	7	-28%
	8	-30%
	9	-32%
	10	-41%
	11	-26%
2	12	-5%
	13	-19%
	14	-21%
	15	-41%
	16	-36%

In Fig. 4.20, MoF predictions were lower than the experimental values except for the first test, and the relative errors ranged between +11% and -41%. However, for 12 cases, relative errors

were less than 30% while it is 30-41% only for the 4 cases. Also, calculated  $R^2$  value for the experimental results corresponding to the 1:1 line was 0.81. These observations were not in consistent with the MoF comparisons against the numerical and analytical solutions discussed in Secs. 4.6.1 and 4.6.2 above. In those cases, MoF predictions were conservative, and the relative errors were within 10% in most of the cases. The two possible reasons for this variation of experimental results can be identified as follows.

1. Normalized flow rate values for experimental results  $q/kh_{EXP}$  were calculated assuming the soil permeability as isotropic. But, as noted earlier in this section, even for sands, permeability in horizontal direction can be higher up to the 70%, and hence, actual normalized flow rate values can be slightly lower than the calculated values assuming the soil as isotropic.
2. As noted before in test methodology section, all tests in a given phase were carried out in a continuous sequence. Therefore, completely unused sand was used only for the first test of each phase i.e., from the second test, only the additional sand amount required was filled on top of the sand which was used before for pervious tests. Therefore, there is a possibility of changing the soil permeability due to changing the soil structure with progressing the tests. This effect can be seen in increasing the relative error in both phases of tests (see Table 4.8) while progressing the tests (for instance, in Phase 1,  $RE$  started as +11% and changed up to -41% after 11 tests).

Considering the two possible reasons mentioned above, it can be accepted that MoF predictions are comparable with the experimental results. However, for further verifications, MoF predictions were compared against another set of experimental data based on the study conducted by Davidenkoff and Franke (1965). As discussed before in Sec. 4.2.1, their experimental investigation was based on the electrical analogy model, and hence, soil

permeability corresponds to the inverse of the resistance of conducting material. So, it is more uniform within the conducting material used and also the material remains the same between the tests. So, the two limitations mentioned above with the laboratory model (studied using sands) were not affecting the electrical analogy model results, and hence, MoF predictions using isotropic soil model are well comparable with the experimental values. Fig. 4.21 shows the comparison of these experimental results (based on electrical analogy model) against the corresponding MoF predictions. Here also relative errors were calculated using Eq. 4.13 and are shown in Table 4.9. It was found that MoF predictions are higher than the experimental values for all the cases and deviate less than 10% for most of the cases (10 cases out of 13). The three cases where the deviations are larger than 10% correspond to the geometries having lower  $s/T$  values (see Table 4.9). These observations are strongly agreed to the MoF comparison result obtained against numerical and analytical results discussed in Secs. 4.6.1 and 4.6.2, respectively. Further, calculated  $R^2$  value for the experimental results shown in Fig. 4.21 corresponding to the 1:1 line was 0.95. This also confirms the strong relationship between the experimental results and MoF predictions.

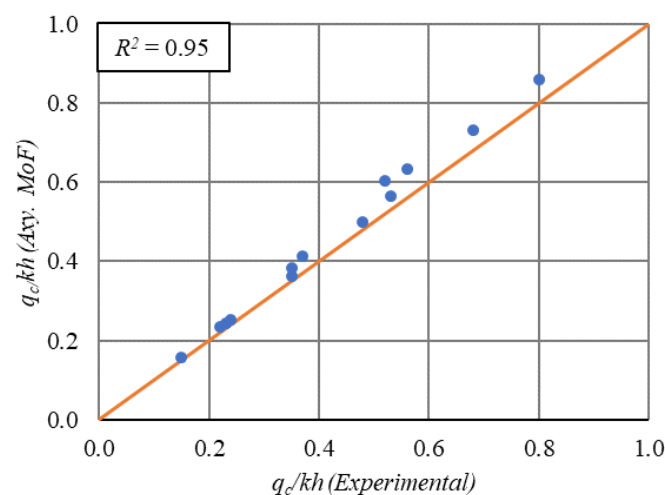


**Fig. 4.21** Comparison of seepage quantities estimated by proposed axisymmetric MoF solutions against experimental results by Davidenkoff and Franke (1965)

**Table 4.9** Relative errors between experimental results (using electrical analogy model) and

MoF Predictions			
$rR/T$	$s/T$	$\alpha$	$RE$
0.671	0.105	0.00	8%
	0.255	0.00	7%
	0.255	0.50	8%
	0.505	0.00	3%
	0.500	0.50	4%
	0.800	0.00	6%
0.336	0.127	0.00	13%
	0.252	0.00	12%
	0.250	0.50	16%
	0.502	0.00	6%
	0.500	0.50	10%
	0.802	0.00	5%
	0.802	0.50	5%

Considering all the MoF validation sections above, it can be concluded that MoF is a sufficiently accurate tool for quick estimations of  $q$  and  $i_E$  for the circular cofferdam problems. Similar to the MoF solutions discussed in double-walled case, even when the assumption is violated,  $q$  and  $i_E$  are conservatively overestimated by less than 10% for most practical situations ( $s/T > 0.2$ ) of circular cofferdams. Note that these model tests were only for comparing the flow rates. No attempt was made to measure the exit hydraulic gradient, which was validated by the other methods as shown in Sec. 4.6.1.

#### **4.7 Development of expressions for axisymmetric form factors and exit hydraulic gradient estimations**

The graphical nature of the developed design charts (4.10, 4.11 and 4.12) for selected  $s_D/T_D$ , and  $rR/T_D$  values for fragment type  $D$ , and  $s/T$  and  $rR/T$  values for fragment type  $E$  require more time in estimating the form factor values for some geometries. Therefore, an attempt is made to develop expressions for estimating the form factor values of both fragment types and

the normalized exit hydraulic gradient values of the fragment type  $D$ . These expressions enable the quick estimations of  $q$  and  $i_E$ , without going for the graphical solutions, and they can be implemented in a spreadsheet for a parametric study.

#### 4.7.1 Fragment $D$ form factor

The form factor values given in Fig. 4.10 show an approximately linear relationship to the  $s_D/T_D$  values for a given  $rR/T_D$  within the range of  $s_D/T_D = 0.1 - 0.9$  and  $rR/T_D = 0.1 - 1.0$ . Hence, the form factor ( $\beta_D$ ) can be expressed for the above range of  $s_D/T_D$  and  $rR/T_D$  as:

$$\beta_D = a(s_D/T_D) + b \quad (4.14)$$

where  $a$  and  $b$  are functions of  $rR/T_D$ . By plotting  $a$  and  $b$  against  $rR/T_D$  separately, the relationships of the  $a$  and  $b$  to the  $rR/T_D$  can be written as:

$$a = 2.4(rR/T_D)^{-0.9} \quad (4.15)$$

$$b = 0.5 - 0.2 (rR/T_D) \quad (4.16)$$

Substituting Eqs. 4.15 and 4.16 into the Eq. 4.14, fragment  $D$  form factor ( $\beta_D$ ) can be rewritten as:

$$\beta_D = 2.4 (rR/T_D)^{-0.9}(s_D/T_D) + 0.5 - 0.2 (rR/T_D) \quad (4.17)$$

for  $s_D/T_D = 0.1 - 0.9$  and  $rR/T_D = 0.1 - 1.0$

#### 4.7.2 Fragment $E$ form factor

The form factor values given in Fig. 4.11 show an approximately exponential relationship with  $s/T$  for a given  $rR/T$ . Hence an expression for the form factor ( $\beta_E$ ) is proposed for the same geometry range considered for the fragment  $D$  form factor expression development as:

$$\beta_E = c \exp[d(s/T)] \quad (4.18)$$

Here again,  $c$  and  $d$  are functions of  $rR/T$ , and were determined by plotting them against  $rR/T$ , separately as:

$$c = 0.086 \ln(rR/T) + 0.35 \quad (4.19)$$

$$d = 1.683(rR/T)^{-0.025} \quad (4.20)$$

Substituting Eqs. 4.19 and 4.20 into Eq. 4.18, fragment  $E$  form factor ( $\beta_E$ ) can be written as:

$$\beta_E = [0.086 \ln(rR/T) + 0.35] \{ \exp[1.683(rR/T)^{-0.025}(s/T)] \} \quad (4.21)$$

for  $s_D/T_D = 0.1 - 0.9$  and  $rR/T_D = 0.1 - 1.0$

#### 4.7.3 Fragment $D$ normalised exit hydraulic gradient

The normalised exit hydraulic gradient ( $i_E s_D/h_D$ ) values given in Fig. 4.12 can be related to  $s_D/T_D$  values for a given  $rR/T_D$  as:

$$i_E s_D/h_D = g(s_D/T_D)^j [1 - \exp(-s_D/T_D)] \quad (4.22)$$

where  $g$  and  $j$  are functions of  $rR/T_D$ . Hence, relationships of  $g$  and  $j$  to the  $rR/T_D$  were also determined by plotting them separately as:

$$g = 1.53 - 0.5 rR/T_D \quad (4.23)$$

For,  $rR/T_D < 0.25$

$$j = 0.27 rR/T_D - 0.78 \quad (4.24a)$$

For,  $rR/T_D \geq 0.25$

$$j = -0.15 rR/T_D - 0.67 \quad (4.24b)$$

Then  $i_E s_D/h_D$  can be expressed as:

For  $0.1 \leq rR/T_D < 0.25$ ;

$$i_E s_D/h_D = [1 - \exp(-s_D/T_D)] \left( 1.53 - 0.5 \frac{rR}{T_D} \right) (s_D/T_D)^{(0.27 rR/T_D - 0.78)} \quad (4.25a)$$

For  $0.25 \leq rR/T_D \leq 1$

$$i_E s_D/h_D = [1 - \exp(-s_D/T_D)] \left( 1.53 - 0.5 \frac{rR}{T_D} \right) (s_D/T_D)^{(-0.15 rR/T_D - 0.67)} \quad (4.25b)$$

The expressions proposed for the fragment  $D$  exit gradient estimations are also valid for the geometries where  $s_D/T_D = 0.1-0.9$  and  $rR/T_D = 0.1-1.0$ .

#### 4.7.4 Validation of the proposed expressions

Fig. 4.22 shows the comparison of flow rate and exit gradient predictions against the numerical simulation results. Similar to the comparison of the results observed for MoF chart assessments (see Fig. 4.14), proposed expressions overestimate the seepage quantity and exit gradient for low cut-off wall depths ( $s/T \leq 0.2$ ) with the range of difference in 10 - 20% in general. When  $s/T > 0.2$ , for most of the cofferdam geometries, proposed expressions slightly overestimate the seepage quantity and exit hydraulic gradient by less than 10% deviation compared to the finite element solutions. For very few cases, predictions by the proposed expression are underestimated; however, they differ only by less than 5% for both the seepage quantity and exit hydraulic gradient. Most importantly, these expressions enable implementing the proposed axisymmetric MoF solution in spreadsheet; hence, authors suggested these expressions for quick estimate of seepage quantity and exit gradient for any realistic circular cofferdam geometry where  $0.1 \leq s/T \leq 0.9$  and  $0.1 \leq rR/T \leq 1$ .

In conclusion, solutions given by the proposed expressions are sufficiently accurate for most of the circular cofferdam geometries encountered in practice. They are valuable in parametric studies or sensitivity analysis to study the effect of certain dimensions on the flow rate or exit hydraulic gradient. All three expressions proposed for the fragment  $D$  form factor, fragment  $E$  form factor and fragment  $D$  exit hydraulic gradient are valid only when the ratio  $rR/T$  is in between 0.1 to 1.0. However, this range covers most of the typical cofferdam geometries, and only small portion of the range mentioned in the charts (i.e.  $rR/T > 1$ ) cannot be computed using these expressions. Author suggests using the chart for these situations ( $rR/T > 1$ ).

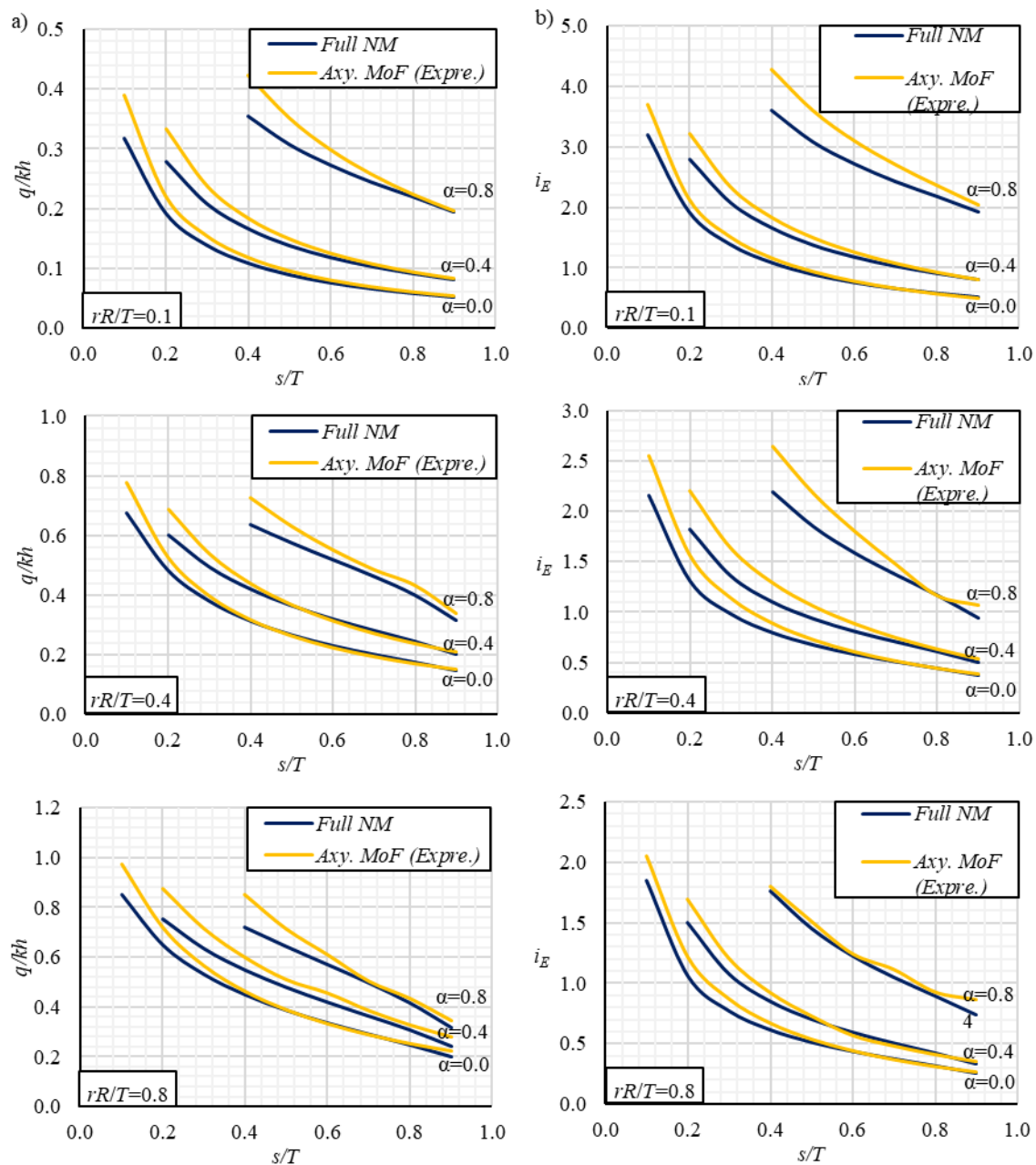


**Fig. 4.22** Comparison of proposed expressions solutions with full numerical model (NM) solutions: (a) seepage quantity; (b) exit hydraulic gradient

#### 4.8 Summary and conclusions

A simple method to solve seepage problems pertaining to the circular cofferdam has been presented. It is based on the Method of fragments, and the accuracy relies on the assumption that the equipotential line at the tip of the sheet pile is vertical, which divides the flow domain into two fragments ( $D$  and  $E$ ). An assessment is made in this chapter on the validity of this

assumption and the effects of any violation on the computed values of flow rate  $q$  and the exit hydraulic gradient  $i_E$ . It is shown that the equipotential surface is far from vertical at low cofferdam radius ( $rR/T$ ) and the low cut-off wall depth ( $s/T$ ) and becomes closer to the vertical with increasing  $rR/T$  and  $s/T$  where the accuracy of the MoF solution improves. However, it is observed that in spite of the assumption deviation, the flow rate and exit hydraulic gradient estimates from MoF are very good for most cofferdam geometries.

Three design charts have been developed; two for estimating the form factors for each of the axisymmetric fragments (defined as “ $D$ ” and “ $E$ ”), and one for the dimensionless exit hydraulic gradient of fragment  $D$ . These form factor and exit hydraulic gradient charts represent efficient means of obtaining both the quantity of seepage and the exit hydraulic gradient, and for virtually any circular cofferdam geometry of practical interest. The outcomes of the proposed MoF solutions were compared against the detailed numerical solutions, analytical work of Neveu (1972), and experimental results. It is shown that the proposed axisymmetric MoF is adequate for reasonable estimates of the flow rate and exit gradient provided  $s/T > 0.2$ , with relative errors less than 10%. When  $s/T \leq 0.2$ , MoF still provides conservative solutions, but their level of accuracy is low (relative errors are between 10 and 20%) when compared to the geometries with  $s/T > 0.2$ . Although, the situations where  $s/T \leq 0.2$  are of no practical significance, and hence, this should not be a deterrent for using MoF in engineering practice.

In addition, three simple expressions were proposed to estimate the form factors and exit hydraulic gradients. These expressions make it possible to implement the axisymmetric MoF through spreadsheets or carry out parametric studies. The geometry range of cofferdams which can be treated directly with the proposed expression are limited to  $0.1 \leq s/T \leq 0.9$  and  $0.1 \leq rR/T \leq 1$ , which covers most practical situations. For situations where  $rR/T > 1$ , the

design charts provide reasonable solutions. The expressions were also validated against the full numerical solution, and it shows that the values predicted by proposed expression are satisfactory for most geometries. The extreme situations where the deviations are considerable have little practical relevance ( $s/T \leq 0.2$ ); however, predictions by the expression are on the conservative side in these instances too.

---

## Chapter 5 Relationship between minimum creep length and maximum exit hydraulic gradient in double-walled and circular cofferdams

### 5.1 Introduction

As noted in Sec. 2.3.1, piping is the most common hydraulic failure mode for cofferdams. When the maximum exit hydraulic gradient  $i_E$  exceeds the critical hydraulic gradient  $i_C$ , piping failure initiates at the excavation base adjacent to the sheet pile wall. Then, it starts to erode the soil, progressing from downstream towards upstream, and hence, the length of the shortest seepage path from upstream to downstream (i.e., along the sheet pile wall) decreases. Therefore, average hydraulic gradient along the shortest seepage flow path is increased. Consequently, rate of soil erosion is also increased forming a free water channel from downstream towards upstream, and it leads to a complete and rapid structural failure in a short period of time with little advance warning. This phenomenon (piping failure) has been recorded around the world and is responsible for catastrophic situations (Bauer 1984; Tanaka et al. 1994; Tanaka et al. 2002; Cai and Ugai 2003; Tanaka 2003; Cai and Ugai 2004). Considering the severe consequences, a more conservative approach is applied using higher safety factors for designs against piping failure compared to the safety factors applied in other areas of geotechnical designs; for instance, safety factor for the slope stability assessment is around 1.3 (Griffiths et al. 1996).

### 5.2 Factor of safety applied against piping failure

Eq. 2.28 showed that factor of safety ( $F$ ) against piping failure can be defined as  $i_C/i_E$ . Also,  $i_C$  is a function of the specific gravity  $G_s$  and the void ratio  $e$  (see Eq. 2.29). In sandy soils,  $i_C$  varies between 0.83 to 1.11 for the typical values of void ratios (0.5 to 1) and specific gravity (around 2.65). However, if these information are not available, it is common to consider  $i_C$  as

one for granular soils since it is an average value (Reddi 2003). Further, U.S. Department of the Army (1989) guideline suggested to use  $i_c$  equals to 1. Therefore,  $i_c$  is considered as 1 throughout this chapter, too. Then Eq. 2.28 can be rewritten as:

$$F = \frac{1}{i_E} \quad (5.1)$$

Harr (1962) recommended that the factor of safety ( $F$ ) of 4 to 5 is adequate to consider for the piping failure assessment. Also U.S. Department of the Army (1989) suggested that  $i_E$  should not exceeds 0.3 to 0.4 for a safe structure against the piping failure. Hence,  $F$  values adopted by US Army Engineers Manual are in between 3.3 to 2.5 (using Eq. 5.1). In addition, Griffiths et al. (1996) have mentioned that it is required to have a larger  $F$  value of the order of 5 or 6 considering the possible damages by the piping failure and uncertainty of the soil properties. Further, recent text books (Chen and Liew 2002; Das and Sivakugan 2016) suggested  $F$  in the order of 3 to 5. Considering all,  $F$  values in the order of 3 to 5 are applied for the piping failure assessment of cofferdams in this chapter.

### 5.3 Line of creep method

This is a crude method and can be used to assess the safety of hydraulic structures against the piping failure. This method is proposed by Bligh (1910) and is a more convenient and simpler method compared to other solution methods (flow net, MoF and numerical simulation) discussed before. Even though this is a crude method, it has a value as the simplest and quickest tool to provide a first order estimate of whether the structure is safe or not against possible piping failure. However, most of the discussions reported in the literature on the application of this method are limited to concrete or masonry dam problems (Terzaghi et al. 1996; Das 2013).

This is an empirically derived method. Fig. 5.1 shows the application of this method for a dam structure where the shortest seepage path from upstream to downstream is shown by the horizontal and vertical arrows. This shortest seepage path is termed as the creep length  $C$ , and it can be written for the dam structure shown in Fig. 5.1 as:

$$C = \sum L_h + \sum L_v \quad (5.2)$$

where,  $\sum L_h$  and  $\sum L_v$  are the sum of horizontal and vertical distances, respectively. In this method, a dam was considered safe, when the average hydraulic gradient  $i_{avg} (= h/C)$  is less than a certain value, depending on the founding soil type. Further, Bligh (1910) defined a term, called creep ratio  $C_c$  as:

$$C_c = \frac{C}{h} \quad (5.3)$$

Next, he developed a guideline considering a data base of failed dams and dams that have not failed. In that guideline, a minimum value was recommended for  $C_c$ , and for a safe structure, calculated  $C_c$  by Eq. 5.3 should be greater than the minimum value given in the guideline.

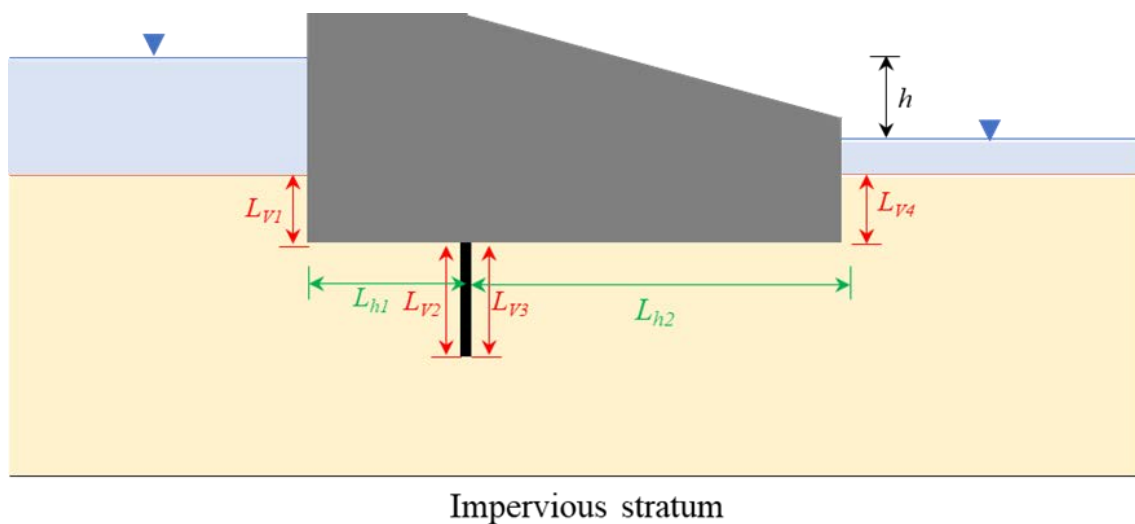


**Fig. 5.1** Line of creep method for a dam problem

Over time, it was understood that the vertical flow paths contribute more in reducing the average hydraulic gradient compared to the horizontal flow paths. The reason for that is the coefficient of permeability in the horizontal direction is always larger than that of the vertical direction. Further, head loss per unit vertical length along the creep line to that of the unit horizontal length is approximately equal to the ratio of  $k_H/k_V$  where  $k_H$  and  $k_V$  are the horizontal and vertical coefficients of permeability, respectively (Terzaghi et al. 1996). Lane (1935) considered the effect of permeability anisotropy and refined the line of creep method based on an extensive number of case histories in different soil conditions. In addition, he introduced the term known as weighted creep length  $L_w$ , and it was defined for  $k_H/k_V$  of 3 as:

$$L_w = \frac{\sum L_h}{3} + \sum L_v \quad (5.4)$$

Further, he suggested another term, weighted creep ratio  $C_w$  as:

$$C_w = \frac{L_w}{h} \quad (5.5)$$

For a safe structure against the piping failure, this ratio  $C_w$  has to be greater than the series of values he suggested (given in the Table 5.1) for the different soil types.

In summary, it is clear that, the line of creep method provides safety factor against piping failure just considering only the shortest seepage path (creep length  $C$ ). So, there is a perceived benefit in having a similar approximation for the cofferdam problems, since cofferdams are also among the frequently used hydraulic structures. Therefore, this chapter extends the line of creep method to cofferdam problems aiming to develop approximate solutions, to have a first order estimate of the safety factor with respect to piping failure for the double-walled and circular cofferdams.

Table 5.1. Lane's recommended values for weighted creep ratio  $C_w$ 

Soil type	$C_w$
Very fine sand and silt	8.5
Fine sand	7.0
Medium sand	6.0
Coarse sand	5.0
Fine gravel	4.0
Medium gravel	3.5
Coarse gravels and cobbles	3.0
Soft clay	2.5
Boulders with some cobbles	3.0
Medium clay	2.0
Hard clay	1.8
Very hard clay	1.6

#### 5.4 Line of creep method for double-walled cofferdams

For double-walled cofferdams, the shortest flow path is the flow line along the sheet pile wall from upstream to downstream, which is the creep length  $C$ . Fig. 5.2 shows the marked creep length for a double-walled cofferdam. The parameters  $L$ ,  $s$ ,  $T$ ,  $\alpha s$  and  $h$  are similar to those defined in Fig. 3.1 in chapter 3. Here, creep line contains only vertical flow paths; therefore, no adjustment is required involving the ratio of  $k_H/k_V$ , and hence, weighted creep length  $L_w$  should equal to the creep length  $C$ . So, creep length  $C$  and creep ratio  $C_c$  terms are used in this chapter for the cofferdam analysis instead of the weighted creep length and weighted creep ratio terms. Note that, the thickness of the sheet pile has been ignored in calculating the  $C$  value since it is very low compared to the vertical length values, and also, the effect of ignoring it on the conservative side. Accordingly, the  $C$  value for double-walled cofferdams can be defined as:

$$C = s + (1 - \alpha)s \quad (5.6)$$

Thus, the creep ratio  $C_c$  for double-walled cofferdams is given as:

$$C_c = \frac{C}{h} \quad (5.7)$$

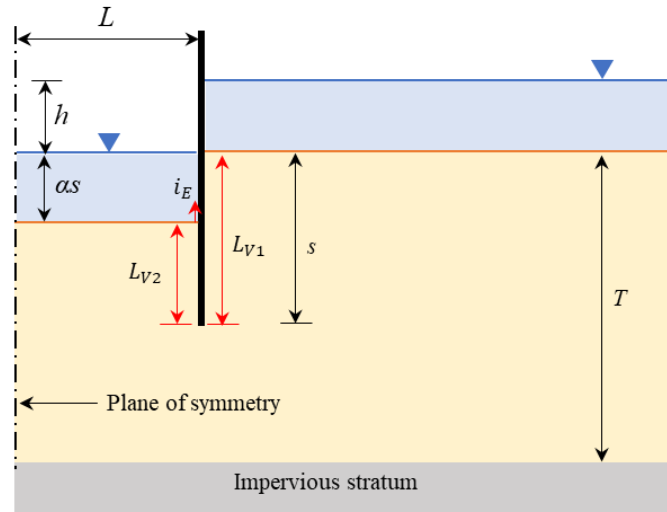


**Fig. 5.2** Creep length calculation for double-walled cofferdams

#### 5.4.1 Relationship between creep length and maximum exit hydraulic gradient of double-walled cofferdams

Maximum exit hydraulic gradient  $i_E$  and corresponding creep length  $C$  values were calculated for a range of double-walled cofferdam geometries using numerical simulations. The numerical model, parameters and the simulation procedure used are similar to the procedure described in Sec. 3.3.1 of chapter 3. Here 630 geometries were studied varying the  $LR/T$  as 0.1, 0.15, 0.2, 0.25, 0.3, 0.35, 0.4, 0.5, 0.6, 0.7, 0.8, 1, 1.5 and 2 while  $s/T$  was varied as 0.1, 0.2, 0.3, 0.4, 0.5, 0.6, 0.7, 0.8 and 0.9. Also, five excavation depth simulations were analysed for each geometry, considering  $\alpha$  as 0, 0.2, 0.4, 0.6 and 0.8. As noted in chapter 3, half-width of the cofferdam is termed as  $LR$  (multiply  $L$  by  $R$ ) considering the model capability of treating the soil anisotropic ( $R \neq 1$ ). Also, as discussed in chapter 3, the geometry with  $LR/T = 2$  is equivalent to the situation where cofferdam width is infinite (when the soil is isotropic). Further, geometries

where  $LR/T$  and  $s/T$  are less than 0.1, and  $\alpha$  is greater than 0.8 are not considered in this study, because they are having very little practical significance. Then, it was assumed that, the geometry range considered above is adequate to cover all cofferdam geometries of practical interest.

All the simulations were run keeping the soil as homogeneous and isotropic ( $R = \sqrt{k_V/k_H} = 1$ ). However, the range of the applicability of proposed solutions in this chapter is not limited to the isotropic condition. When the soil is homogeneous and anisotropic ( $R \neq 1$ ), corresponding solutions can be obtained by considering the cofferdam width  $L$  in the transformed section, i.e.,  $LR$  as discussed before. In addition, soil layer thickness  $T$ , and total head loss  $h$  were kept constant for all the runs, with values of 20 m and 2.5 m, respectively. Before developing the relation between  $i_E$  and  $C$ , a preliminary assessment was carried out to see the effect of  $LR/T$  on  $i_E$  by plotting the normalised values ( $i_E/h$ ) against  $LR/T$  for different  $s/T$  and  $\alpha$  values as shown in Fig. 5.3. It shows that the effect of  $LR/T$  on  $i_E/h$  is not significant when  $LR/T \geq 0.5$  compared to the case of  $0.1 \leq LR/T < 0.5$ . Therefore, creep length analysis was done separately for  $LR/T \geq 0.5$  and for  $0.1 \leq LR/T < 0.5$ . In total, 630 geometries were considered (as noted before), and the calculated  $i_E/h$  and  $C$  values are shown in appendix C1. The results of the creep length analysis for the two cases ( $LR/T \geq 0.5$  and for  $0.1 \leq LR/T < 0.5$ ) are shown in Fig. 5.4. In Fig. 5.4a, coefficient of determination ( $R^2$ ) is 0.85 while it is 0.9 for Fig. 5.4b implying that the  $i_E$  predictions are slightly more accurate for the case of  $LR/T \geq 0.5$ . However, having  $R^2$  value of 0.85 for the case of  $0.1 \leq LR/T < 0.5$  shows that the  $i_E$  predictions using the relationship given in Fig. 5.4a is also a reasonable one.

Therefore, relationships between  $i_E/h$  and the creep length  $C$  for the two cases are:

For  $0.1 \leq LR/T < 0.5$ ,

$$\frac{i_E}{h} = 0.89 C^{-0.89} \quad (5.8)$$

For  $LR/T \geq 0.5$ ,

$$\frac{i_E}{h} = 1.03 C^{-1.09} \quad (5.9)$$

Note that, for Eqs. 5.8 and 5.9 and rest of the equations described below for the double-walled cofferdams analysis, the values of  $h$  and  $C$  should be in meters.

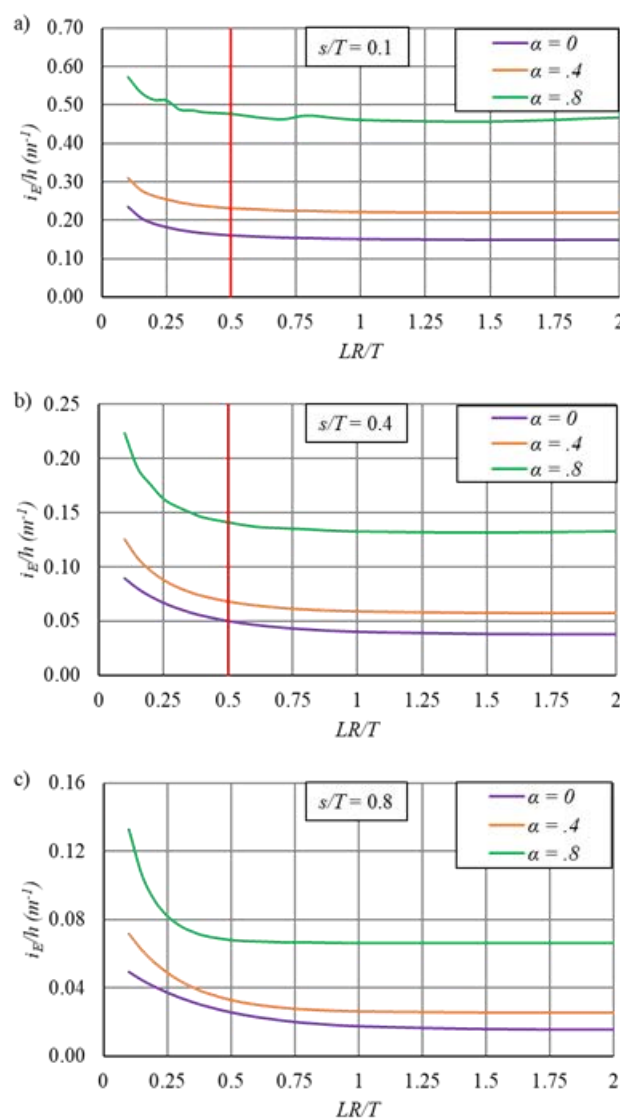


**Fig. 5.3** Changing the normalised  $i_E$  values with cofferdam width in double-walled

cofferdams: (a)  $s/T = 0.2$ ; (b)  $s/T = 0.4$ ; (c)  $s/T = 0.8$

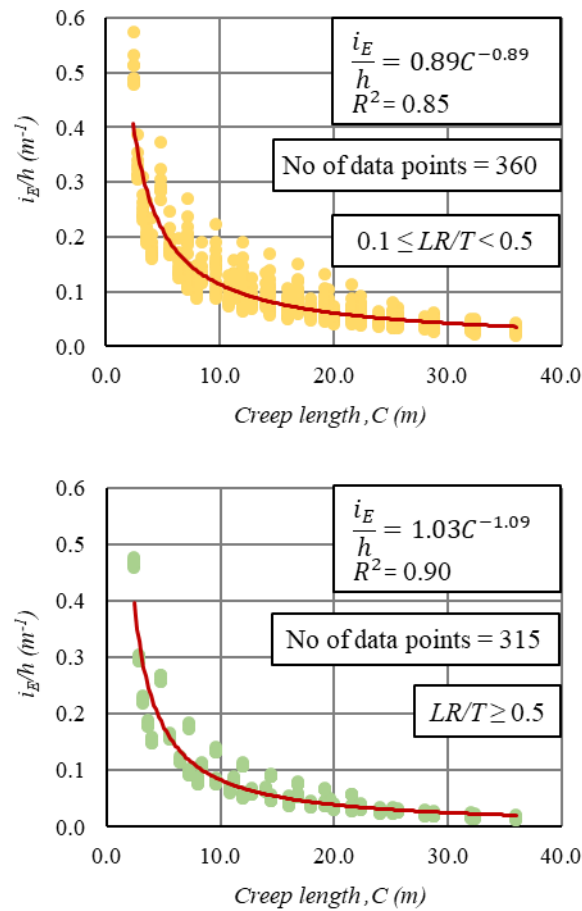


**Fig. 5.4** Normalised  $i_E$  vs creep ratio  $C_c$  relationship for double-walled cofferdams:

(a)  $0.1 \leq LR/T < 0.5$ ; (b)  $LR/T \geq 0.5$

Using Eq. 5.1, Eq. 5.8 can be rewritten as:

$$\frac{1}{Fh} = 0.89C^{-0.89} \quad (5.10)$$

Then, the minimum value for  $C$  required at a given  $F$  can be derived as:

$$C = 0.88(Fh)^{1.12} \quad (5.11)$$

Similarly, the minimum  $C$  value when  $LR/T \geq 0.5$  can be defined as:

$$C = 1.03(Fh)^{0.92} \quad (5.12)$$

For a double-walled cofferdam with a specified  $F$  value and a known head difference  $h$ , the required minimum  $C$  value against piping failure can be determined from Eqs. 5.11 or 5.12.

Alternatively, for a given geometry, and hence, for the known  $C$  value, the safety factor  $F$

against piping failure can be determined at a given  $h$  from the same two equations. While Eqs. 5.8 and 5.9 (or 5.11 and 5.12) can be used for reasonable estimates of the  $F$  or  $C$ , there is some scatter coming from the less sensitive parameters ( $LR/T$ ,  $s/T$  and  $\alpha_s$ ) that were not considered herein. Therefore, for a given  $C$ , it is desirable to know the possible range of the  $i_E$ . An attempt is made to establish the upper and lower bound values for  $i_E$  based on the simulations carried out on 630 geometries.

#### 5.4.2 Upper and lower bound curves for double-walled cofferdams

Upper and lower bound curves were estimated considering two separate cases as defined in previous section, i.e.,  $0.1 \leq LR/T < 0.5$  and  $LR/T \geq 0.5$ . For the case 1 ( $0.1 \leq LR/T < 0.5$ ), upper bound curve was estimated by fitting the data for the geometry of  $LR/T = 0.1$ , since this is the lowest  $LR/T$  value used in this analysis while  $LR/T = 0.5$  was considered for the lower bound curve estimation. Fig. 5.5 shows the best-fit lines, and the upper and lower bound curves estimated. The steps adopted for upper and lower bound curves estimation for the case 1 are outlined below.

##### a. Upper bound curve

1. All  $i_E/h$  values of  $LR/T = 0.1$  were plotted against the  $C$  values.
2. Best-fit line was estimated as  $\frac{i_E}{h} = 0.98C^{-0.80}$  (see Fig. 5.5a). Since this is the average line of the data series, the upper bound line should also be in the form of  $\frac{i_E}{h} = aC^{-0.80}$ , where  $a$  is a constant and should be larger than 0.98.
3. Using the MS Excel program, a value for the constant  $a$  was obtained through several trials satisfying the two conditions given below.
  - I. All  $i_E/h$  values of  $LR/T = 0.1$  at any given  $C$  value are smaller than to the corresponding value predicted by the proposed upper boundary line.

- II. The point where the upper bound curve and actual data point exist at their closest, the deviation of  $i_E/h$  value predicted by the upper bound equation from the actual value was limited to less than 1%.

Using above steps, the best value obtained for constant  $a$  was 1.44. The best-fit line and upper bound curve are shown in Fig. 5.5a.

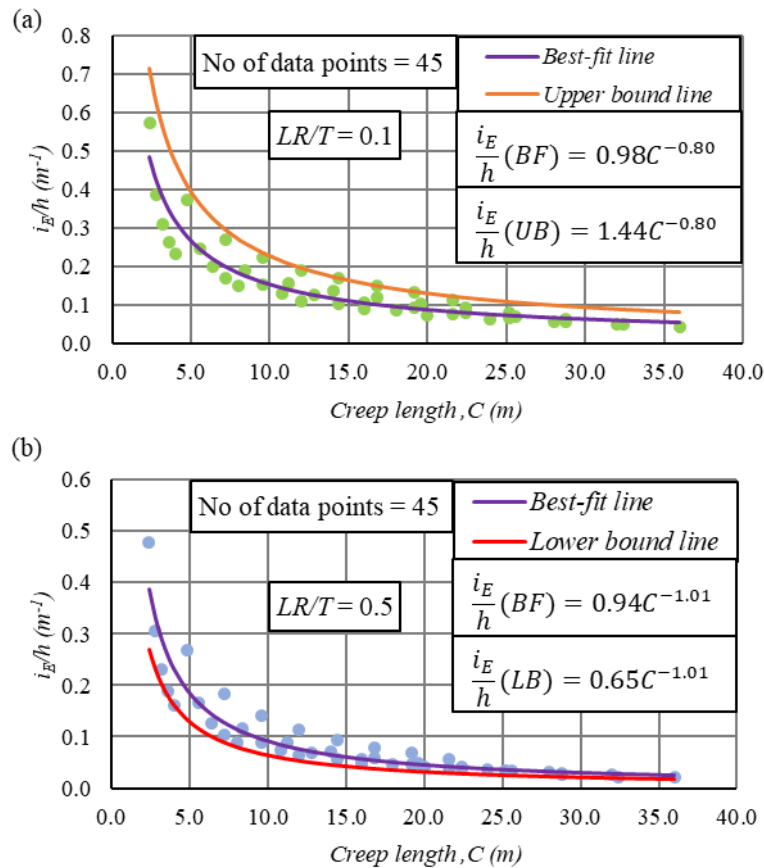


**Fig. 5.5** Boundary curves for  $0.1 \leq LR/T < 0.5$ :

(a) Upper bound curve; (b) Lower bound curve

b. Lower bound curve

1. All  $i_E/h$  values of  $LR/T = 0.5$  were plotted against the  $C$  values.
2. Best-fit line was estimated as  $\frac{i_E}{h} = 0.94C^{-1.01}$  (see Fig. 5.5b). As discussed before, equation of the lower bound line should also be in the form of  $\frac{i_E}{h} = bC^{-1.01}$ , and hence, the constant  $b$  should be smaller than 0.94.

3. Here also, through the several trials using the MS Excel program, constant  $b$  was determined satisfying the two conditions given below.

- I. All  $i_E/h$  values of  $LR/T = 0.5$  at any given creep length are larger than to the corresponding value predicted by the proposed lower bound line.
- II. The point where the lower bound curve and actual data point exist at their closest, the deviation of  $i_E/h$  value predicted by the lower bound equation from the actual value was limited to less than 1%.

Using above steps, constant  $b$  was determined as 0.65, and Fig. 5.5b shows the best-fit line and lower bound curve.

Then, two equations of lower and upper bound curves for the case 1 ( $0.1 \leq LR/T < 0.5$ ) are summarised below.

The lower bound is as:

$$\frac{i_E}{h} = 0.65C^{-1.01} \quad (5.13)$$

The upper bound curve is given by:

$$\frac{i_E}{h} = 1.44C^{-0.80} \quad (5.14)$$

Also Fig. 5.6a shows that all the  $i_E/h$  points (360 points), corresponding to the extensive range of geometry ( $0.1 \leq LR/T < 0.5$ ,  $s/T = 0.1$  to  $0.9$  and  $\alpha = 0$  to  $0.8$ ) are covered by these two curves.

For the case 2 ( $LR/T \geq 0.5$ ) also, same steps outlined above were applied for determining the boundary curves. Upper bound curve was estimated by fitting the  $i_E/h$  values of  $LR/T = 0.5$

while  $LR/T = \infty$  was applied for the lower bound curve estimations. The two curves derived for the case 2 are given below. The equation for the lower bound curve is as:

$$\frac{i_E}{h} = 0.73C^{-1.15} \quad (5.15)$$

The upper bound curve is given by:

$$\frac{i_E}{h} = 1.41C^{-1.01} \quad (5.16)$$

Fig. 5.6b shows all the  $i_E/h$  relevant to the case 2 ( $LR/T \geq 0.5$ ,  $s/T = 0.1$  to  $0.9$  and  $\alpha = 0$  to  $0.8$ ) are confined to the zone defined by these two curves (Eqs. 5.15 and 5.16).

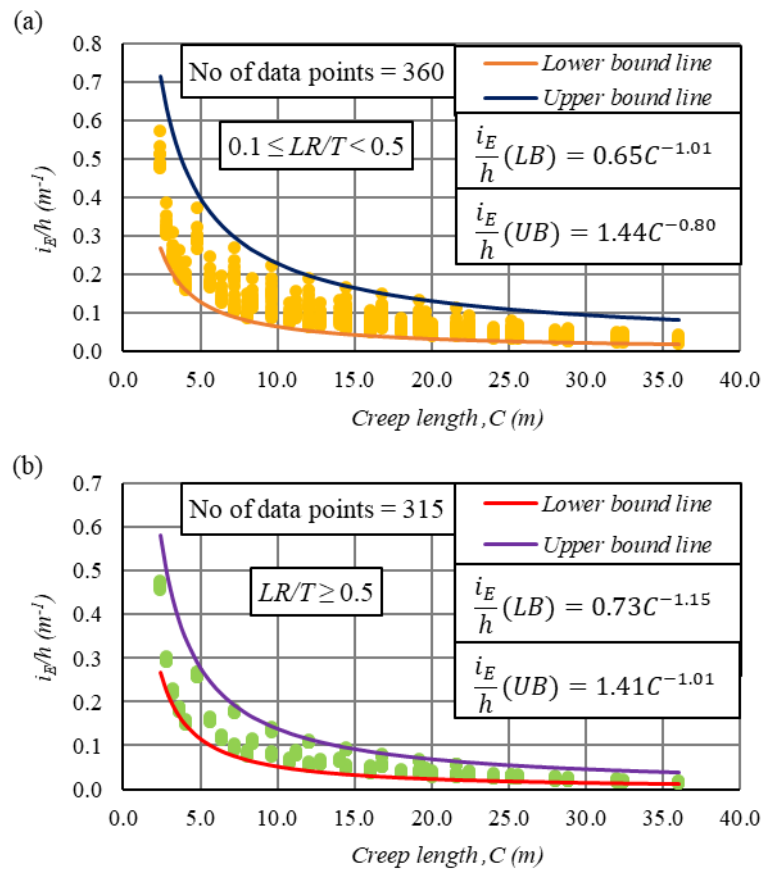


**Fig. 5.6** Both upper and lower bound curves for normalised  $i_E$  of double-walled cofferdams:

(a)  $0.1 \leq LR/T < 0.5$ ; (b)  $LR/T \geq 0.5$

### 5.4.3 Validation of the proposed solutions for double-walled cofferdams

For the validation, extensive number of cases (630) in a wider range of geometry were analysed through the steps given below.

1. A factor of safety  $F = 4$  is considered, implying maximum allowable exit gradient  $i_E$  of 0.25 (see Eq. 5.1).
2. Minimum creep ratio  $C_c$  values were calculated for the two cases ( $0.1 \leq LR/T < 0.5$  and  $LR/T \geq 0.5$ ) using the  $C$  values given by Eqs. 5.11 and 5.12, respectively at a total head loss of 2.5 m. For  $0.1 \leq LR/T < 0.5$ ,  $C_c$  value calculated was 4.6 while it was 3.4 for  $LR/T \geq 0.5$ .
3. Then  $i_E$  values calculated by the numerical simulation of series of cofferdam geometries were plotted against the corresponding  $C_c$  values for the two cases separately as shown in Fig. 5.7. The red vertical lines drawn at the minimum  $C_c$  values (4.6 and 3.4) calculated in point 2 above and the blue horizontal line at  $i_E = 0.25$  divides the plot area of each graph into four zones (Z1, Z2, Z3, and Z4).

Zone Z1 represents the cases where the creep ratio  $C_c$  is insufficient, and hence, unacceptably high  $i_E$  are likely. Zone Z4 represents the cases where the  $C_c$  is adequate to ensure the  $i_E$  is lower than 0.25, confirming  $F > 4$ . Zone Z2 includes  $C_c$  values which are less than the minimum required value, and  $i_E$  values which are within the maximum allowable limit (i.e., safe against piping). Therefore, ideally no points should lie within zone Z2 since the geometries where  $C_c$  values are smaller than the minimum required should be unsafe with  $i_E$  greater than 0.25. Similarly, in Zone Z3 too, no points should lie if the model works perfectly because all the geometries with larger  $C_c$  than the minimum required are safe, and hence, all the  $i_E$  values should be lower than to the maximum allowable value of 0.25.

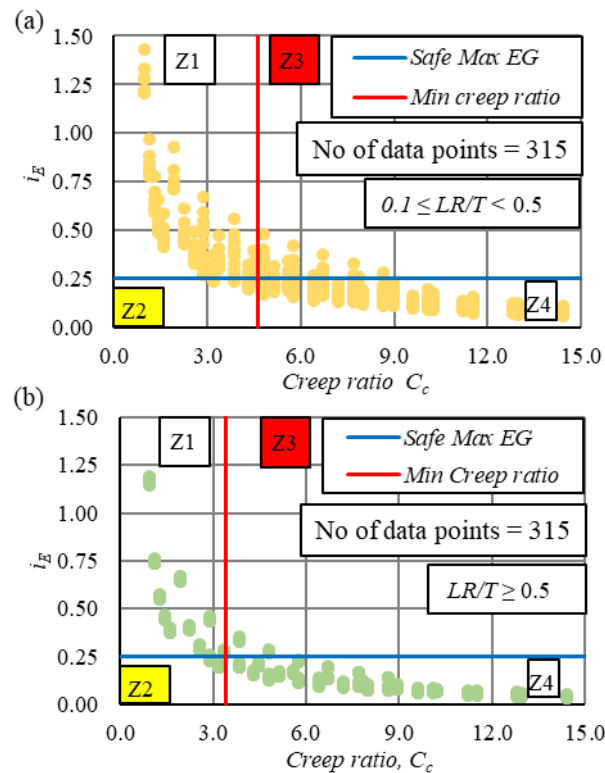


**Fig. 5.7** Validity assessment for double-walled cofferdams:

(a)  $0.1 \leq LR/T < 0.5$  ;(b)  $LR/T \geq 0.5$

Validation results for the case of  $0.1 \leq LR/T < 0.5$  (see Fig. 5.7a) shows that, out of the 315 cases considered, 275 cases fell within zones Z1 and Z4, with 10 and 30 falling in Z2 and Z3, respectively. For the cases with  $LR/T \geq 0.5$  (see Fig. 5.7b), 288 fell within zones Z1 and Z4, with 13 and 14 reporting in Z2 or Z3. As mentioned before, ideally no points should lie within zones Z2 and Z3, but here few points are reported in zones Z2 and Z3 for both Figs. 5.7a and 5.7b cases implying that the model predictions are wrong for these cases. That is due to this study has considered only the most critical parameter (i.e., creep length) for the solutions development and has ignored the effect of ignoring other less sensitive parameters such as excavation depth  $a_s$ , cofferdam width  $LR$ , and sheet pile embedded depth  $s$  on maximum exit hydraulic gradient.

Note that, effects of reporting some  $i_E$  points in zone Z2 which are slightly lower than 0.25 are onto the conservative side; however, effects of points reported in zone Z3 are unsafe. Similar assessments were conducted for the other two  $F$  values (3 and 5) considered in this study, and the results summary is shown in Table 5.2. It shows that, proposed model predictions are reasonably good since 87% or more of the data are within the expected zones (zone Z1 and Z4) for all three  $F$  values. Less than 10% predictions are on the unsafe side (Zone Z3). Considering all, it can be concluded that proposed model provides sufficiently accurate predictions for cofferdam stability against piping failure just by considering their creep length  $C$  values.

**Table 5.2** Summary of the validity assessment for double-walled cofferdams

$F$	$h$ (m)	Allowable max. $i_E$	$LR/T$	Min. $C_c$	Number of points in zones			Total No. points
					1&4	2	3	
3	2.5	0.33	< 0.5	3.4	282	15	18	315
			$\geq 0.5$	2.6	297	7	11	315
4	2.5	0.25	< 0.5	4.6	275	10	30	315
			$\geq 0.5$	3.4	288	13	14	315
5	2.5	0.2	< 0.5	6.0	277	11	27	315
			$\geq 0.5$	4.2	291	6	18	315

### 5.5 Line of creep method for circular cofferdams

For circular cofferdams also, the shortest flow path (creep length  $C$ ) is exactly same as that discussed for the double-walled case (given in Eq. 5.6) since both cofferdam types are similar in the sectional view (see Figs. 3.1 and 4.1). Therefore, Eqs. 5.6 and 5.7 can be used to estimate the  $C$  and  $C_c$  values, respectively for circular cofferdams, too. Also, for the creep length analysis, the procedure followed here was similar to that described above for double-walled cofferdams analysis. Noting that, cofferdam radius is termed as  $rR$  in the more general form as discussed in chapter 4, allowing for the permeability anisotropy.

### 5.5.1 Relationship between creep length and maximum exit hydraulic gradient of circular cofferdams

Maximum exit hydraulic gradient  $i_E$  and corresponding creep length  $C$  values were calculated for a range of circular cofferdam geometries using numerical simulations. The numerical model geometry, parameters and the simulation procedure applied are exact to the procedure given in Sec. 4.2 of chapter 4. The ranges of the  $s/T$  and  $\alpha$  varied were similar to the range considered for the double-walled case discussed in Sec. 5.4.1. Total number of cofferdam geometries studied were 675 varying  $rR/T$  as 0.1, 0.15, 0.2, 0.25, 0.3, 0.35, 0.4, 0.5, 0.6, 0.7, 0.8, 1.0, 1.5, 2 and  $\infty$ . When cofferdam radius  $r$  tends to infinity,  $i_E$  values were calculated using the double-walled cofferdam model of infinite width (single sheet pile wall) as discussed in Sec. 3.3.2 of chapter 3.

Before developing the relation of  $i_E$  and  $C$ , a preliminary assessment was carried out to see the effect of  $rR/T$  on  $i_E$  as discussed for the double-walled case. From Fig. 5.8, it is evident that when  $rR/T \geq 0.5$ , its influence on  $i_E/h$  is insignificant compared that for the case of  $0.1 \leq rR/T < 0.5$ . Therefore, similar to the double-walled case, the creep length analysis was carried out separately for  $0.1 \leq rR/T < 0.5$  and  $rR/T \geq 0.5$ . Appendix C2 shows the calculated  $i_E/h$  values and corresponding creep length values for the 675 cases considered. The results of the analysis are shown in Fig. 5.9. It shows that, coefficient of determination ( $R^2$ ) is slightly lower for the case of  $0.1 \leq rR/T < 0.5$  (see Fig. 5.9a) compared to that for the  $rR/T \geq 0.5$  shown in Fig. 5.9b, confirming that the prediction are slightly more accurate with  $rR/T \geq 0.5$ . However, having  $R^2$  value of 0.82 for the case of  $0.1 \leq rR/T < 0.5$  while it is 0.84 for  $rR/T \geq 0.5$  ensure that both relationships are reasonable to estimate the  $i_E$  values only considering single parameter, i.e., creep length  $C$ .

Then, Fig. 5.9 was used for defining the relationships of  $i_E/h$  to the  $C$  in two cases as follows.

For  $0.1 \leq rR/T < 0.5$ ,

$$\frac{i_E}{h} = 1.17C^{-0.85} \quad (5.17)$$

For  $rR/T \geq 0.5$ ,

$$\frac{i_E}{h} = 1.05C^{-1.0} \quad (5.18)$$

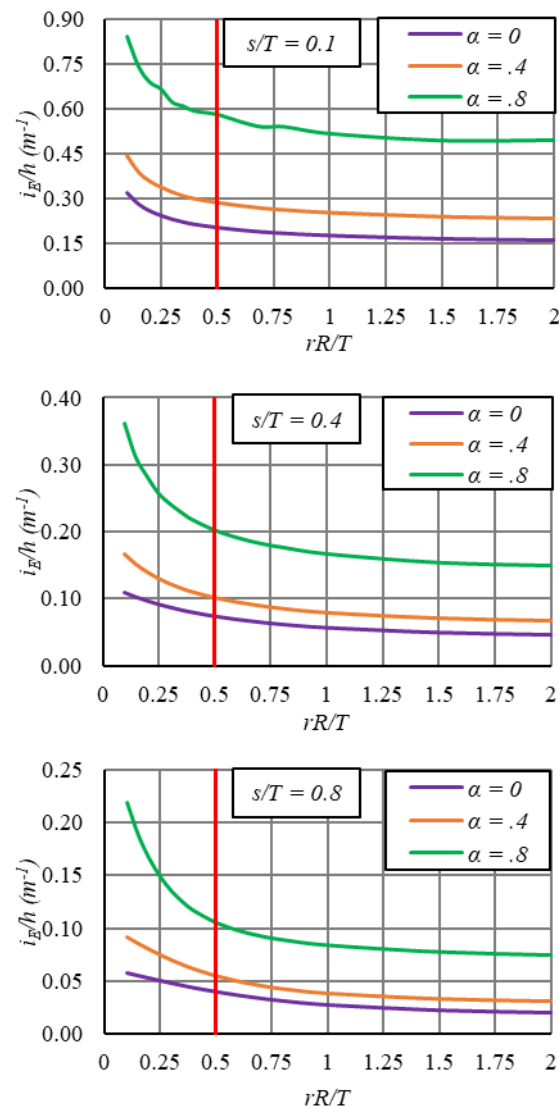


**Fig. 5.8** Changing the normalised  $i_E$  values with cofferdam width in circular cofferdams:

(a)  $s/T = 0.2$ ; (b)  $s/T = 0.4$ ; (c)  $s/T = 0.8$

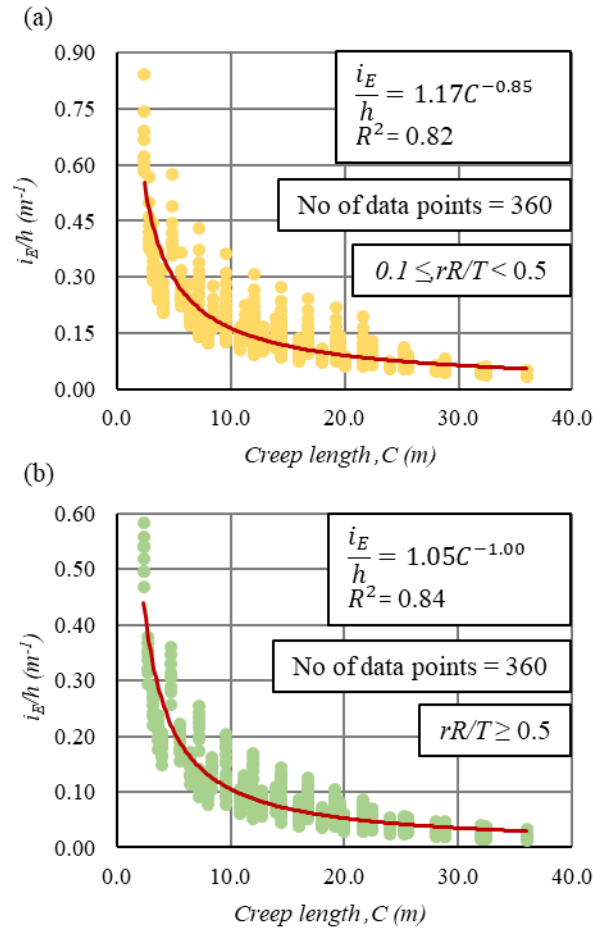


**Fig. 5.9** Normalised  $i_E$  vs creep ratio  $C_c$  relationship for circular cofferdams:

(a)  $0.1 \leq rR/T < 0.5$ ; (b)  $rR/T \geq 0.5$

Also noted that, for all the equations proposed for circular cofferdams also, values of  $h$  and  $C$  should be in meters. Similar to the Eqs.5.11 and 5.12 developed for the double-walled cofferdams, minimum  $C$  value required at a given  $F$  for circular cofferdams can be defined using Eqs. 5.17 and 5.18 as:

For  $0.1 \leq rR/T < 0.5$ ,

$$C = 1.20(Fh)^{1.18} \quad (5.19)$$

For  $rR/T \geq 0.5$ ,

$$C = 1.05Fh \quad (5.20)$$

## 5.5.2 Boundary curves for circular cofferdams

Here also, lower and upper boundary curves were defined considering the two cases ( $0.1 \leq rR/T < 0.5$  and  $rR/T \geq 0.5$ ), separately as shown in Fig. 5.10. The procedure adopted here was similar to the procedure discussed for the double-walled cofferdams problems in Sec. 5.4.2.

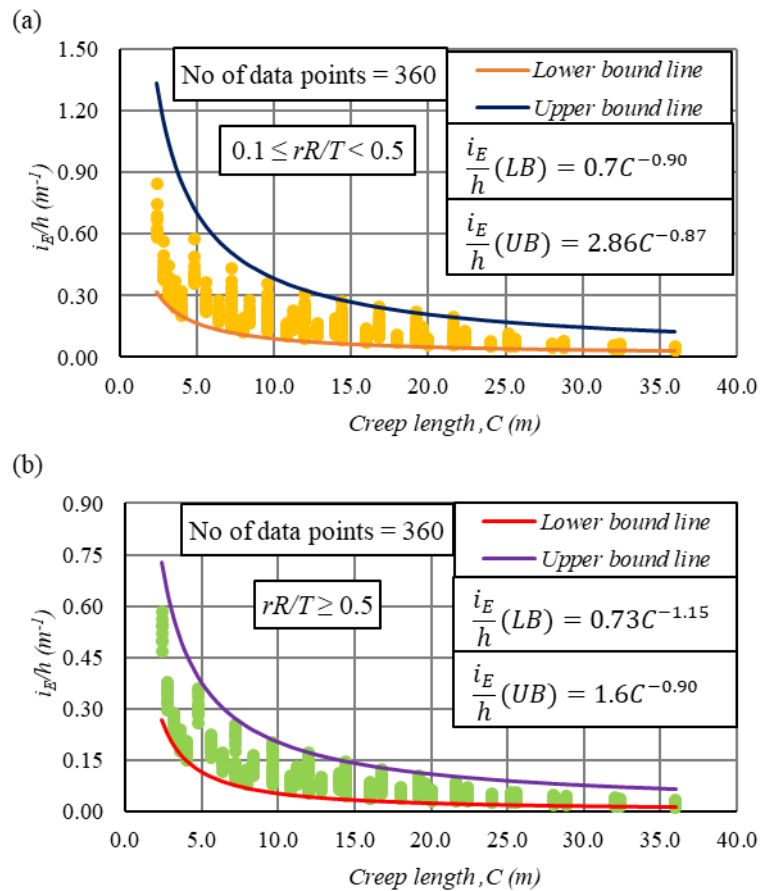


**Fig. 5.10** Both upper and lower bound curves for normalised  $i_E$  of circular cofferdams:

(a)  $0.1 \leq rR/T < 0.5$ ; (b)  $rR/T \geq 0.5$

For  $0.1 \leq rR/T < 0.5$ , equations for these curves are as follows. The lower bound curve is as:

$$\frac{i_E}{h} = 0.70C^{-0.90} \quad (5.21)$$

The upper bound curve is given by:

$$\frac{i_E}{h} = 2.86C^{-0.87} \quad (5.22)$$

For  $rR/T \geq 0.5$ , lower bound curve is defined as:

$$\frac{i_E}{h} = 0.73C^{-1.15} \quad (5.23)$$

The upper bound curve is given by:

$$\frac{i_E}{h} = 1.6C^{-0.90} \quad (5.24)$$

### 5.5.3 Validation of the proposed solutions for circular cofferdams

Here, 675 cases (315 for  $0.1 \leq rR/T < 0.5$  and 360 for  $rR/T \geq 0.5$ ) were analysed through the same procedure discussed for double-walled validation in Sec. 5.4.3. Fig. 5.11 shows the validation results for the factor of safety  $F = 4$  and the total head loss of 2.5 m. Most of the geometries (273/315 in Fig. 5.11a and 323/360 in Fig. 5.11b) were reported in the zones Z1 and Z4 making the model predictions are correct. However, few points reported in the zone Z2 (15 for  $0.1 \leq rR/T < 0.5$  and 8 for  $rR/T \geq 0.5$ ), giving wrong predictions, but they are conservative. Further, 27 and 29 data points in Fig. 5.11a and 5.11b, respectively fell into the zone Z3 giving wrong and unsafe predictions. However, most of the points located in the zone Z3 are closer to the maximum allowable exit gradient; hence, their actual  $F$  values are not far from the required minimum. A similar analysis was conducted for three  $F$  values (3, 4, and 5), and the results are shown in Table 5.3. In summary, more than 85% of the prediction are within zone Z1 and Z4 while less than 11% predictions are on the unsafe side for all three  $F$  values considered.

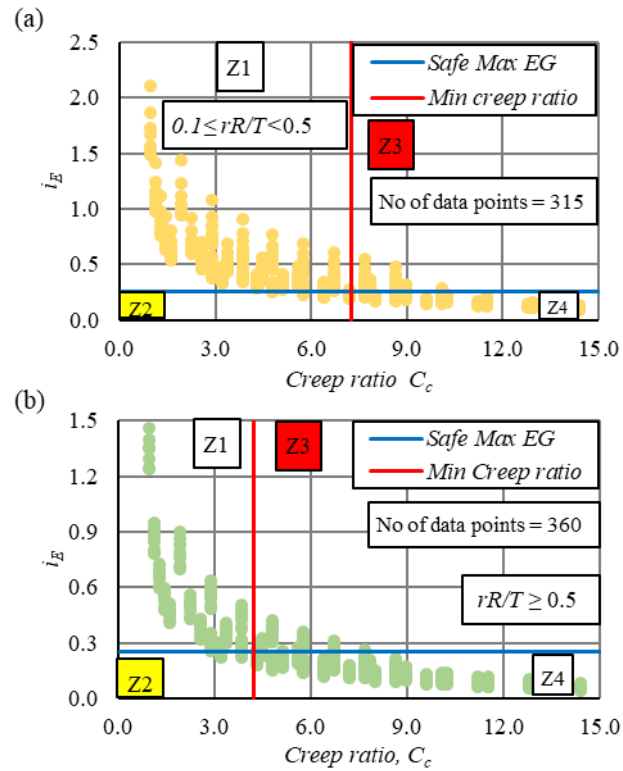


**Fig. 5.11** Validity assessment for circular cofferdams:

(a)  $0.1 \leq rR/T < 0.5$ ; (b)  $rR/T \geq 0.5$

**Table 5.3** Summary of the validity assessment for circular cofferdams

$F$	$h$ (m)	Allowable max. $i_E$	$rR/T$	Min. $C_c$	Number of points in zones			Total No. points
					1&4	2	3	
3	2.5	0.33	$< 0.5$	5.2	268	15	32	315
			$\geq 0.5$	3.2	332	9	19	360
4	2.5	0.25	$< 0.5$	7.3	273	15	27	315
			$\geq 0.5$	4.2	323	8	29	360
5	2.5	0.2	$< 0.5$	9.5	294	14	7	315
			$\geq 0.5$	5.3	312	15	33	360

### 5.6 Approximate creep ratios for cofferdams

Creep ratio  $C_c$  is a practical parameter that can be used in the preliminary designs for assessing the safety against piping failure. It is the additional creep length required per unit increase in

the total head (see Eq.5.7). The  $C_c$  recommended by Bligh (1910) and Lane (1935) were based on an extensive database of more than 200 case histories, where they also considered the soil type. The study reported herein is based on the series of finite element simulations for a homogeneous soil medium; therefore,  $i_E$  value is independent from the soil type and is a function only of the cofferdam geometry and total head difference. In addition, cofferdams are widely applied for sandy soils, and hence, creep ratio values proposed in this study are mainly for sandy soils with critical hydraulic gradient  $i_c$  approximately equals to unity, implying  $i_E$  is the reciprocal of the factor of safety  $F$  against piping. So, soil type is not distinguished in this study, and the estimated  $C_c$  for cofferdams are shown in Table 5.4 at three  $F$  values (3, 4 and 5) and three total head loss  $h$  values of 2.5 m, 5 m and 10 m.

For circular cofferdams with  $rR/T \geq 0.5$ , from Eq. (5.20) it can be seen that the creep ratio  $C_c$  is independent of  $h$ . For all other cases, the  $C_c$  is no more a constant; it varies, but only slightly with  $h$ . When the  $F$  equals to 4,  $C_c$  values of double-walled cofferdams ranged between 4.6 to 5.5 for  $h$  values varying from 2.5 m to 10 m for the case of  $0.1 \leq LR/T < 0.5$ , with an average value of 5.1 (see Table 5.4). Also, average  $C_c$  value for the case of  $LR/T \geq 0.5$  is 3.2. Similarly, when the  $F$  equals to 4, average  $C_c$  values while changing the  $h$  values from 2.5m to 10m for the circular cofferdams are 8.3 and 4.2 for the cases of  $0.1 \leq rR/T < 0.5$  and  $rR/T \geq 0.5$ , respectively. It can be seen from Table 5.4 that the  $C_c$  is influenced slightly by the head  $h$  and thus, varies in a narrow range. Therefore, it is suggested to use appropriate value for  $h$  in Eqs. 5.11, and 5.12 for doubled walled cofferdams and Eqs. 5.20 and 5.21 for circular cofferdams for computing the minimum required creep length  $C$  values.

As mentioned before,  $C_c$  values obtained in this study are valid only for the sandy soils and depend on the  $F$  and  $h$  values. However, weighted creep ratio values  $C_w$  proposed by Lane

(1935) are empirical values, and there is no relationship showing  $F$  values to the creep ratios. They predict whether structure is safe or not against piping. Therefore, proposed  $C_c$  values in this study cannot compare directly with the values given by Lane (1935). For the three  $F$  values (3, 4 and 5) considered in this study,  $C_c$  values ranged between 2.4 to 7 for the double-walled cofferdams while it varies from 3.2 to 12.1 for the circular cofferdams. The  $C_c$  values proposed by Lane (1935) for coarse to fine sand vary from 5 to 7 (see Table 1) and are still in comparable range with estimated  $C_c$  values for the double-walled cofferdams in this study.  $C_c$  values for the circular cofferdams are based on the three dimensional flow into the excavation, and hence, they are not comparable to the historical data because Lane (1935) values have been derived considering the two dimensional flow condition.

**Table 5.4** Summary of the estimated creep ratio  $C_c$  values for cofferdams

$F$	$LR/T$ or $rR/T$	$h$ (m)	Min. $C$ (m)		Creep ratio $C_c$ ( $C/h$ )	
			Double-walled	Circular	Double-walled	Circular
3	< 0.5	2.5	8.4	12.9	3.4	5.2
		5	18.3	29.3	3.7	5.9
		10	39.7	66.4	4.0	6.6
	$\geq 0.5$	2.5	6.6	7.9	2.6	3.2
		5	12.4	15.8	2.5	3.2
		10	23.5	31.5	2.4	3.2
4	< 0.5	2.5	11.6	18.2	4.6	7.3
		5	25.2	41.2	5.0	8.2
		10	54.8	93.2	5.5	9.3
	$\geq 0.5$	2.5	8.6	10.5	3.4	4.2
		5	16.2	21.0	3.2	4.2
		10	30.7	42.0	3.1	4.2
5	< 0.5	2.5	14.9	23.6	6.0	9.5
		5	32.4	53.5	6.5	10.7
		10	70.4	121.3	7.0	12.1
	$\geq 0.5$	2.5	10.5	13.1	4.2	5.3
		5	19.9	26.3	4.0	5.3
		10	37.7	52.5	3.8	5.3

### 5.7 Summary and conclusions

A simple method for evaluating the cofferdam safety against possible piping failure is presented. Both doubled-walled and circular cofferdams founded on a homogeneous granular soil where the depth of soil layer is finite were studied separately. The proposed solutions can be applied in both isotropic and anisotropic soil conditions. Using them, a first-order estimate of the required creep length  $C$  to limit the maximum exit hydraulic gradient  $i_E$  to a specific value can be determined. Alternatively, for a given configuration of the cofferdam, maximum possible  $i_E$  can also be estimated thus defining the factor of safety against piping. The values reported include the mean, and the upper and lower bounds. The equations and curves are summarised in Fig. 5.12. Eqs. 5.15 and 5.23, defining the lower bound curves, are the same for the double-walled and circular cofferdams. All eleven equations are of the form of:

$$\frac{i_E}{h} = aC^b \quad (5.25)$$

where,  $a$  and  $b$  are constants.

The solutions proposed in this chapter have considered only the shortest seepage path (creep length  $C$ ) value for estimating the piping potential at a given total head value of cofferdams. However, it is noted that,  $i_E$  is also a function of width and radius of the double-walled and circular cofferdams, respectively. The effect of ignoring the cofferdam width/radius on the proposed solutions have been minimised by considering the geometries in two separate groups as,  $0.1 \leq \left(\frac{LR}{T} \text{ or } \frac{rR}{T}\right) < 0.5$  and  $\left(\frac{LR}{T} \text{ or } \frac{rR}{T}\right) \geq 0.5$ .

The proposed equations were validated using series of finite element simulations. These equations can be valuable tools for back-of-the-envelope calculations in the preliminary analysis while selecting the dimensions in a cofferdam.

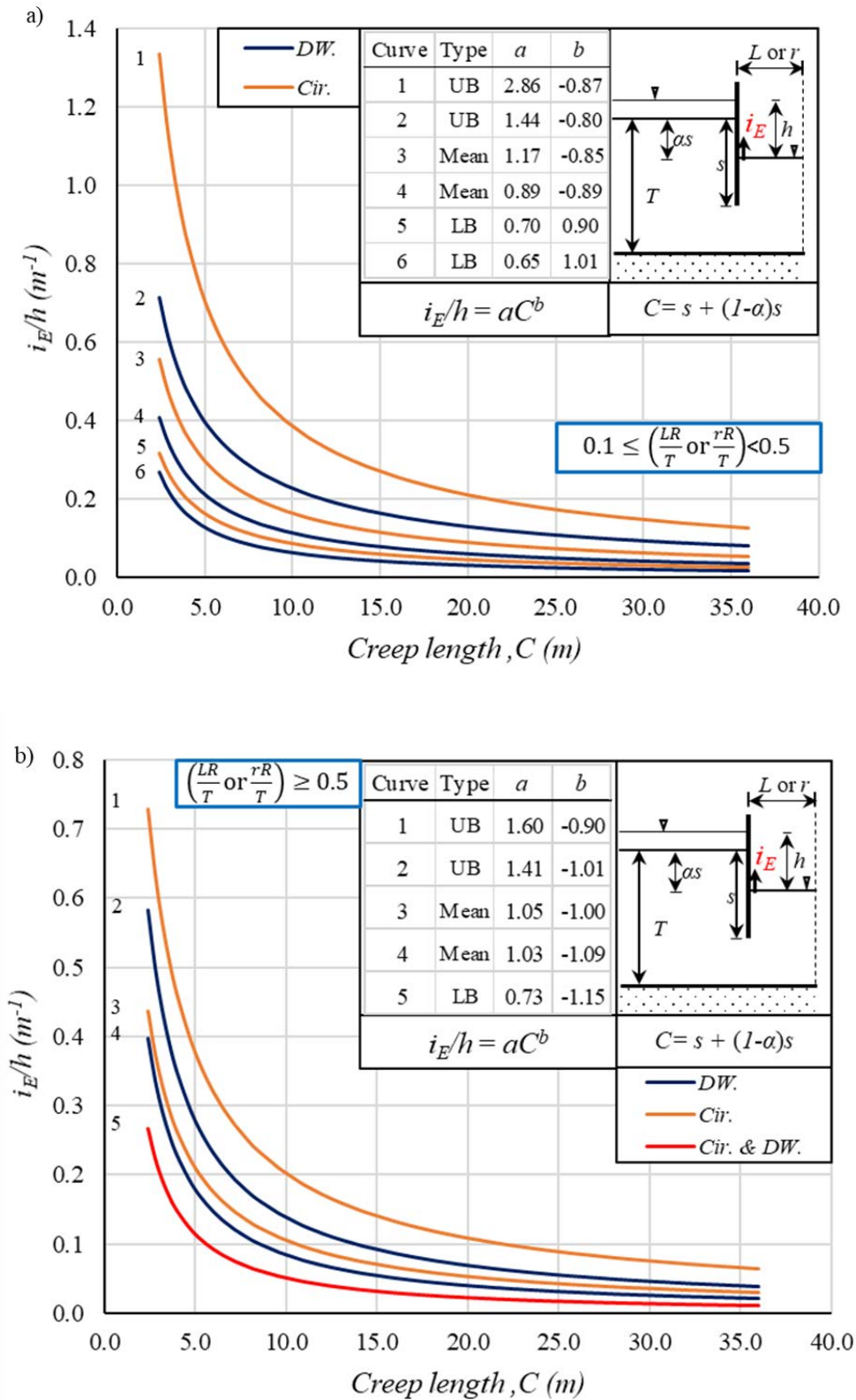


**Fig. 5.12** Summary of the equations and curves for the double-walled (DW) and circular

(Cir.) cofferdams: (a)  $0.1 \leq \left(\frac{LR}{T} \text{ or } \frac{rR}{T}\right) < 0.5$ ; (b)  $\left(\frac{LR}{T} \text{ or } \frac{rR}{T}\right) \geq 0.5$

---

## Chapter 6 Simple solutions for square and rectangular cofferdam seepage problems

### 6.1 Introduction

Square or rectangular shape enclosures are among the commonly seen cofferdam shapes. They are encountered with excavations for building foundations, small bridges or river pier foundations. In these cofferdams, flow into the excavation is three-dimensional, and hence, flow paths in all directions give higher flow rate and exit hydraulic gradient values than what is predicted using a 2D analysis, assuming a double-walled cofferdam. Therefore, 2D approximation considering the situation as a double-walled cofferdam can jeopardize the safety. Hence, 3D numerical simulation using a finite element or finite difference computer package has a place as the most accurate seepage solution method for square or rectangular cofferdams. But it requires an expensive 3D simulation package, and hence, approximate solution methods are applied as a tool for preliminary estimates of seepage solutions for square and rectangular cofferdams.

### 6.2 Seepage solutions for square cofferdams

There are two approximate solution methods practiced in industry for estimating the flow rate and exit hydraulic gradient values for square cofferdams.

1. Axisymmetric approximation, considering square cofferdam is equivalent to the corresponding circular one of the same width (i.e.,  $B = r$ ) (Tanaka and Yokoyama 2005; Bouchelghoum and Benmebarek 2011).
2. Predicting flow rate and exit hydraulic gradient values of square cofferdams applying correction factors to the corresponding values of double-walled cofferdams as proposed by Becker and Moore (2006) in the Canadian Foundation Engineering Manual (CFEM 2006).

In the first part of this chapter, accuracy of these two approaches are assessed using the flow rate and exit hydraulic gradient values calculated through the 3D simulations of series of square cofferdam geometries.

### 6.2.1 Numerical simulations of square cofferdams

The 3D finite element program *RS3 2.0* developed by the Rocscience was used for the numerical simulations. The geometry of the numerical model applied for the square cofferdam is shown in Fig. 6.1a. Here, only one of the four quadrants was analysed considering the symmetry. The definitions of the parameters ( $h$ ,  $B$ ,  $s$ ,  $T$ ) and the boundary conditions applied are similar to those defined in Fig. 2.15 of chapter 2.  $B_e$  is the safe distance from the sheet pile wall to the model's boundary, and  $\alpha s$  is the excavation depth where  $0 \leq \alpha < 1$ . In square cofferdams, two important exit hydraulic gradient values were considered, namely,  $i_{EC}$  and  $i_{EM}$ .  $i_{EC}$  is the exit hydraulic gradient at the corner of the cofferdam where two sheet pile walls meet while  $i_{EM}$  gives exit hydraulic gradient at the mid-point of the sheet pile wall (see Fig.6.1a). For all the simulations, a homogeneous and isotropic soil model was applied. Also, soil permeability  $k$  and total head loss  $h$  were kept constant as  $10^{-5}$  m/s and 10m, respectively for all the models. Simulations were carried out as flow only problems for a completely saturated soil, and a graded mesh with ten-noded tetrahedral elements was used for 3D meshing. The mesh used is shown in Fig. 6.1b.

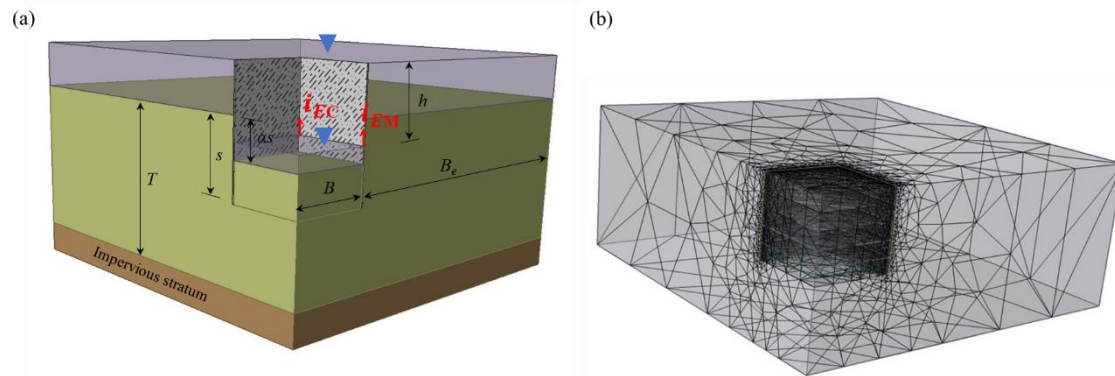


**Fig. 6.1** Numerical model used for square cofferdams: (a) model geometry; (b) 3D mesh

### Numerical model validation

Before using the 3D model for seepage analysis, it was calibrated against the results of the extensive experimental study conducted by the Davidenkoff and Franke (1965) using the electrical analogy model. For the validation, flow rate and exit hydraulic gradient ( $i_{EC}$  and  $i_{EM}$ ) values calculated using 3D simulations were compared against the experimental results for the series of square cofferdam geometries shown in Table 6.1. For the flow rate comparison, dimensionless form ( $q_s/kh$ ) was considered while normalised forms ( $i_{EC\ Avg.}/h$  and  $i_{EM\ Avg.}/h$ ) were analysed for the exit hydraulic gradients validations. Here,  $q_s$  gives flow rate per meter perimeter length of the square cofferdam. Note that,  $i_{EC\ Avg.}$  and  $i_{EM\ Avg.}$  values used for the comparison are the average exit hydraulic gradient values and were calculated using the same procedure discussed in Sec. 4.2.1 of chapter 4 for circular cofferdams. As noted in Chapter 4, these are average values of the hydraulic gradients within the sheet pile enclosure, from the sheet pile tip to the floor of the excavation. Fig. 6.2 shows the comparison results. Flow rate and exit hydraulic gradient values calculated using numerical simulations are well agreed to the corresponding experimental results. In the flow rate estimations, numerical simulation results deviate less than 10% from the experimental values while all the average exit hydraulic gradient values (at mid and corner points) are within  $\pm 5\%$ .

**Table 6.1** Cofferdam geometries used for validating the 3D numerical model for square

cofferdam

$B/T$	$s/T$	$\alpha$
0.34	0.12	0.06
	0.11	0.45
	0.22	0.03
	0.21	0.47
	0.42	0.02
	0.41	0.49
0.67	0.14	0.14
	0.13	0.46
	0.24	0.06
	0.22	0.45
	0.44	0.03
	0.43	0.47
	0.84	0.02
0.83	0.49	
1.34	0.28	0.15
	0.26	0.47
	0.47	0.07
	0.45	0.46
	0.87	0.04
	0.85	0.48
3.36	0.70	0.15
	0.66	0.47
	0.94	0.10
	0.88	0.47

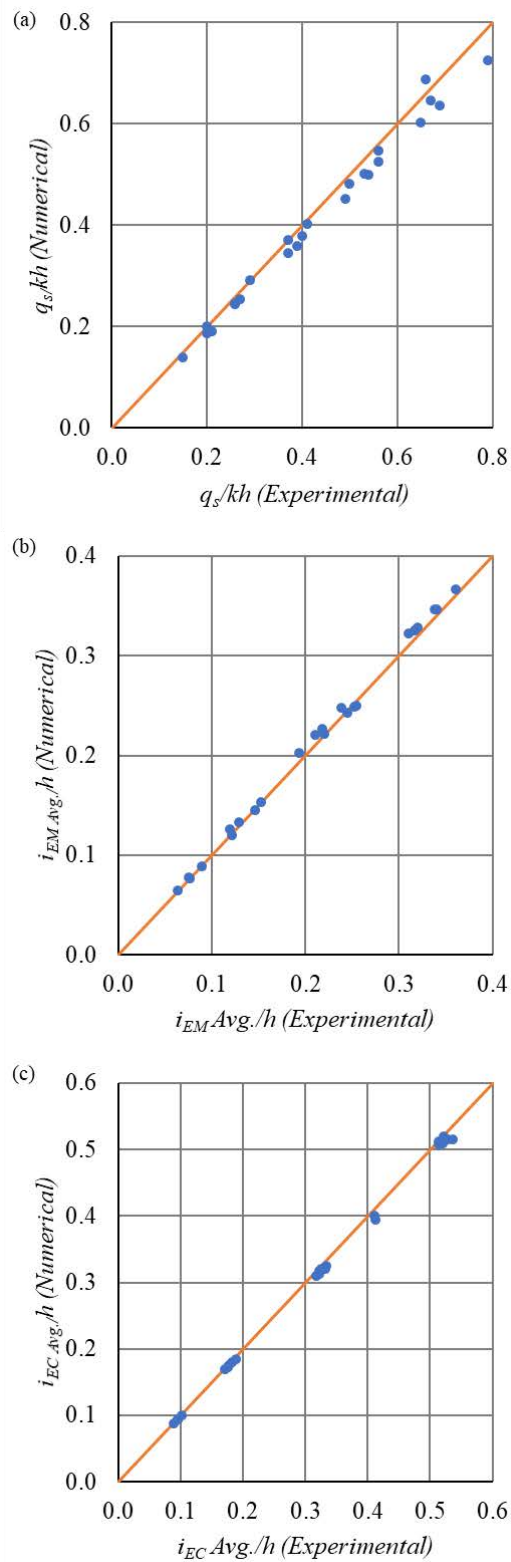


**Fig. 6.2** Square cofferdam model validation: (a) flow rate; (b) average exit hydraulic gradient at middle of a side  $i_{EM Avg.}/h$ ; (c) average exit hydraulic gradient at corner  $i_{EC Avg.}/h$

In terms of the degree of accuracy of the experimental results, Davidenkoff and Franke (1965) stated that their results can be within the  $\pm 5\%$  considering the errors in electrical measuring instruments and the influence of electrolysis and diffusion of the model. Further, they have mentioned that solving square cofferdam problems using the electric analogy is difficult compared to the circular cofferdams. This is due to the difficulty of the experimental model of square cofferdam since it requires to ensure that the model simulates the total head value at tip of the sheet pile increases from mid of the wall to the corner (approximately linear). However, this can simply simulate in circular cofferdam model since total head values at tip of the sheet pile along the cofferdam perimeter remains constant. Therefore, it is expected that the accuracy of experimental results is slightly low with square cofferdams (especially for flow rate estimation) compared to that for the circular cofferdams. This is observed in our comparison analysis also since the numerical estimations of the flow rate for the circular cofferdams deviate within  $\pm 5\%$  as shown in chapter 4 (see. Fig. 4.2) while this is within  $\pm 10\%$  for the square cofferdams. Consequently, it can be concluded that the 3D model proposed above for simulating the square cofferdams is within the sufficient accuracy for analysing the seepage beneath the square cofferdams.

### Sensitivity analysis

Next, a sensitivity analysis was conducted to determine the safe distance from sheet pile wall to the model's boundary ( $B_e$ ) ensuring that its effect on the seepage results is insignificant. Fig. 6.3 shows the sensitivity analysis results conducted for nine geometries considering three  $B/T$  values of 0.2, 0.5 and 0.8 at  $s/T = 0.5$ . For each  $B/T$ , three excavation depth values were also considered ( $\alpha = 0, 0.4$  and  $0.8$ ) since these combinations give representative results for all cases. Next, for each geometry, the distance  $B_e$  was varied by increasing the  $(B + B_e)/B$  ratio from 2 to 6. The safe distance for  $B_e$  was selected in the way that percentage increment of flow rate

$q_s$  and exit gradient values ( $i_{EM}$  and  $i_{EC}$ ) when the geometry changing from one-step of  $(B + B_e)/B$  to the next step is around 1% or lower. Analysis showed that it is negligible the increments of values when  $(B + B_e)/B$  ratio changing from 5 to 6 for all the cases (see Fig. 6.3a for  $q_s$ , 6.3b for  $i_{EM}$  and 6.3c for  $i_{EC}$ ). Therefore,  $B_e$  was selected when the ratio  $(B + B_e)/B$  equals or greater than 5, and hence, the distance  $B_e$  should be equal or larger than  $4B$ . Then, proposed 3D numerical model was used to assess the accuracy of the two approximate solutions methods discussed in Sec. 6.2.

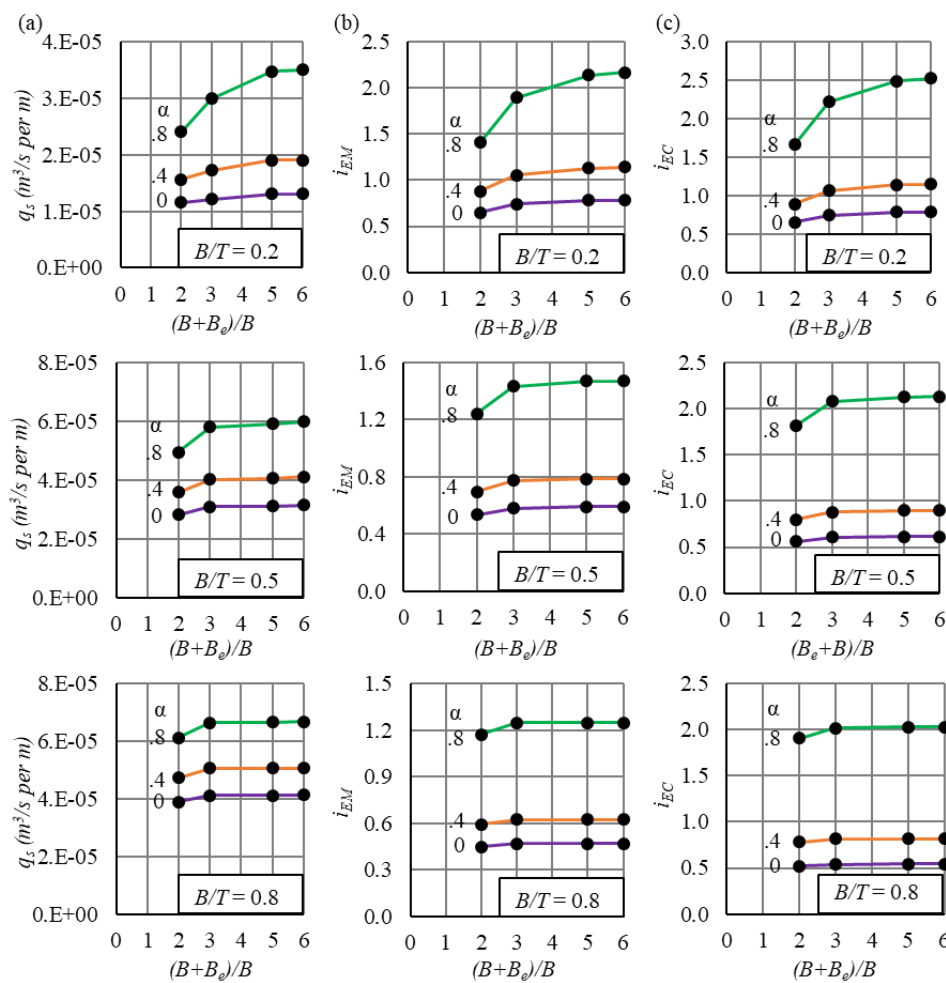


**Fig. 6.3** Sensitivity analysis results for square cofferdams: (a) flow rate; (b) exit hydraulic gradient at mid-point  $i_{EM}$ ; (c) exit hydraulic gradient at corner  $i_{EC}$

### 6.2.2 Accuracy assessment of current approximate seepage solution methods for square cofferdams

For the assessment of two approximate solution methods mentioned in Sec. 6.2, series of square cofferdam geometries (45 cases) were studied considering three  $B/T$  values, three  $s/T$  values and five excavation depths ( $\alpha = 0, 0.2, 0.4, 0.6$  and  $0.8$ ). The range of geometries studied is shown in Table 6.2. For each geometry, actual flow rate  $q_s$  and exit gradient values ( $i_{EC}$  and  $i_{EM}$ ) calculated using 3D simulations were compared among the estimated values by the two methods mentioned in Sec. 6.2. All 3D simulations were carried out considering the offshore cofferdam model (Fig. 6.1a) since the results are valid and conservative for onshore cases also, as pointed in chapters 3 and 4. In each case,  $q_s$ ,  $i_{EC}$  and  $i_{EM}$  values were calculated. Next, for each square geometry studied, corresponding double-walled (Cartesian flow) and circular cofferdams (axisymmetric flow) were analysed (i.e.,  $r = B$  for the circular cofferdam and  $L = B$  for the double-walled one) using the 2D numerical simulation procedures discussed in chapter 3 and 4, respectively. For each of the circular and double-walled cofferdam, flow rate ( $q_c$  and  $q_d$ ) and maximum exit hydraulic gradient  $i_E$  values were calculated. Here,  $q_c$  is the flow rate of circular cofferdam per meter length of the perimeter while  $q_d$  is the flow rate per meter length of half the section of double-walled cofferdam.

#### Accuracy assessment for flow rate estimation

For the assessment also, 45 cases shown in Table 6.2 were considered. Then, flow rate values of square cofferdams  $q_s$  calculated using numerical simulations were plotted against the corresponding flow rate values of  $q_c$  and  $q_d$ , separately as shown in Fig. 6.4. For the square cases, cofferdam perimeter equals to the  $8B$  while this is  $2\pi r$  for the circular cofferdams. Both  $q_c$  and  $q_d$  show strong linear relationships to the  $q_s$ .

**Table 6.2** Geometry range used for square cofferdam analysis

$B/T$	$s/T$	$\alpha$
	0.20	0,0.2,0.4,0.6,0.8
0.20	0.50	0,0.2,0.4,0.6,0.8
	0.80	0,0.2,0.4,0.6,0.8
	0.20	0,0.2,0.4,0.6,0.8
0.50	0.50	0,0.2,0.4,0.6,0.8
	0.80	0,0.2,0.4,0.6,0.8
	0.20	0,0.2,0.4,0.6,0.8
0.80	0.50	0,0.2,0.4,0.6,0.8
	0.80	0,0.2,0.4,0.6,0.8

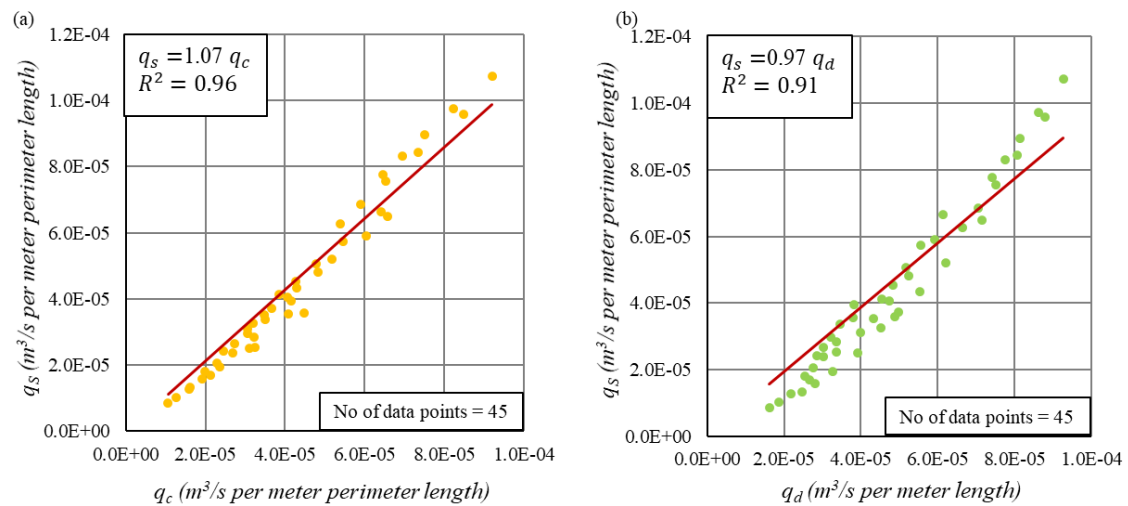


**Fig. 6.4** Relationships between 2D flow rates ( $q_c$  and  $q_d$ ) to the 3D flow rate  $q_s$  into square cofferdam: (a) axisymmetric flow; (b) Cartesian flow

From Fig.6.4a,

$$q_s = 1.07q_c \quad (6.1)$$

Then, total flow rate  $Q_s$  into the square cofferdam can be estimated multiplying  $q_s$  by the perimeter and hence:

$$Q_s = 1.07q_c 8B = 8.56q_c B \quad (6.2)$$

For square cofferdam approximated as an equivalent circular cofferdam of the same width (i.e.,  $r = B$ ), the total flow into the excavation  $Q_s$  is given by:

$$Q_s = q_c 2\pi B = 6.28q_c B \quad (6.3)$$

Therefore, from Eqs. 6.2 and 6.3, it can be seen that treating a square cofferdam as an equivalent circular cofferdam underestimates the flow rate by 27%.

Similarly, from Figure 6.4b,  $Q_s$  can be estimated using the flow rate values of double-walled cofferdams  $q_d$  as:

$$Q_s = 0.97q_d 8B = 7.7q_d B \quad (6.4)$$

Next, the expression proposed in the CFEM (2006) for predicting the flow rate into the square cofferdam using double-walled figures was compared against the  $q_s - q_d$  relation found in this study (Eq. 6.4). Considering the half width of the square cofferdam as  $B$ , the expression in the CFEM (2006) can be presented as:

$$Q_s = 0.7 \left[ \frac{kh}{\Phi_A + \Phi_C} \right] 8B \quad (6.5)$$

The term  $\left[ \frac{kh}{\Phi_A + \Phi_C} \right]$  provides the flow rate per meter length into the half section of double-walled cofferdam using the method of fragments (MoF) where  $\Phi_A$  and  $\Phi_C$  are the form factors of the fragments  $A$  and  $C$  (see Fig. 3.1 and Eq. 3.1). Chapter 3 found a very good similarity between numerical model simulation results and MoF solutions for series of double-walled cofferdam geometries. Therefore, the term  $\left[ \frac{kh}{\Phi_A + \Phi_C} \right]$  in Eq. 6.5 can be replaced by the numerical simulation result  $q_d$  for the double-walled cofferdams, and hence the CFEM (2006) expression becomes:

$$Q_s = 0.7q_d 8B = 5.6q_d B \quad (6.6)$$

Comparing Eqs. 6.4 and 6.6, it is clear that CFEM (2006) predictions are significantly lower than the predictions by the  $q_s - q_d$  expression (Eq. 6.4) developed in this study. To compare these two equations further (to see their deviation from the actual flow rate), predictions by Eqs. 6.4 and 6.6 are plotted against the actual total flow rate  $Q_s$  (determined from the 3D numerical model), in a same graph as shown in Fig. 6.5. It shows that, most predictions by Eq. 6.6 are underestimates, i.e., 37/45 (82%) with maximum deviation of 40%. Also, only 12 points remain within the range of  $\pm 15\%$  while 8 points are overestimated limiting the maximum deviation to 32%. However, for Eq. 6.4, 25 points (56%) remain within  $\pm 15\%$  while maximum underestimation limits to 16%. Here 19 points are overestimated extending maximum deviation up to 83%. Note that, the few cases where overestimations are largest (i.e.  $> 50\%$ ) for the cases having less significance in practice ( $s/T < 0.2$ ).

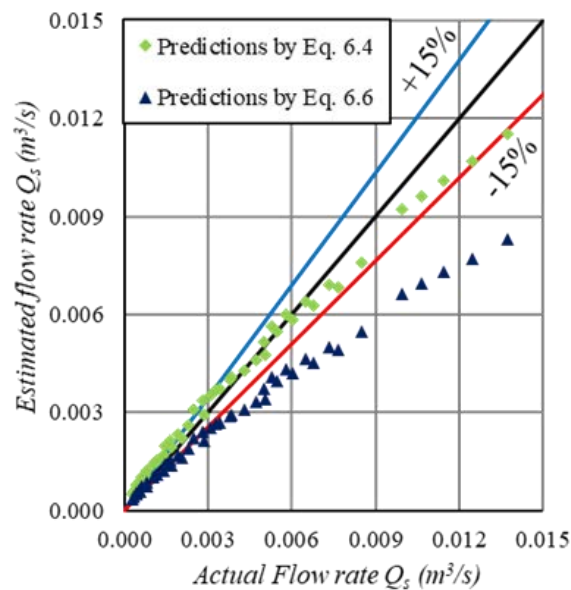


**Fig. 6.5** Deviation of the flow rate predictions of square cofferdam by Eq. 6 and Eq. 8 from the actual flow rate

Considering all, it can be concluded that Eq. 6.4 predicts the flow rate better compared to the expression proposed in the CFEM (2006). Also, CFEM (2006) uses  $\Phi_A$  and  $\Phi_C$  (referred to as  $\Phi_1$  and  $\Phi_2$ ) without explicitly saying that they are the form factors used in MoF. Fig. 6.6 shows the geometry of double-walled cofferdam and the form factor chart used in CFEM (2006). It suggests computing these form factors from this chart by treating the two fragments (fragments  $A$  and  $C$  discussed in chapter 3) similar to the fragment  $C$ , but they are not similar. Fragment  $C$  has a width of  $L$  while fragment  $A$  extends to infinity horizontally (see Fig. 3.1). Since form factor is a measure of the resistance to the flow based on the geometrical constraints (i.e., flow boundaries), not considering the infinite lateral extent of the fragment  $A$  overestimates  $\Phi_A$  and hence, underestimates the flow rate. Also fragment  $A$  form factors are only a function of the  $s/T$ , as pointed in Sec. 3.4.2 of chapter 3. However, *CFEM can still be used to estimate  $\Phi_A$  using the same chart but based on  $d_1/T_1$  and  $T_2/b = 0$* . Note that,  $d_1/T_1$  and  $d_2/T_2$  ratios used in CFEM (see Fig. 6.6) are the same ratios defined as  $s/T$  and  $s_C/T_C$  in chapter 3 while  $b$  represents the half-width of cofferdam which is defined as  $L$  in this dissertation.

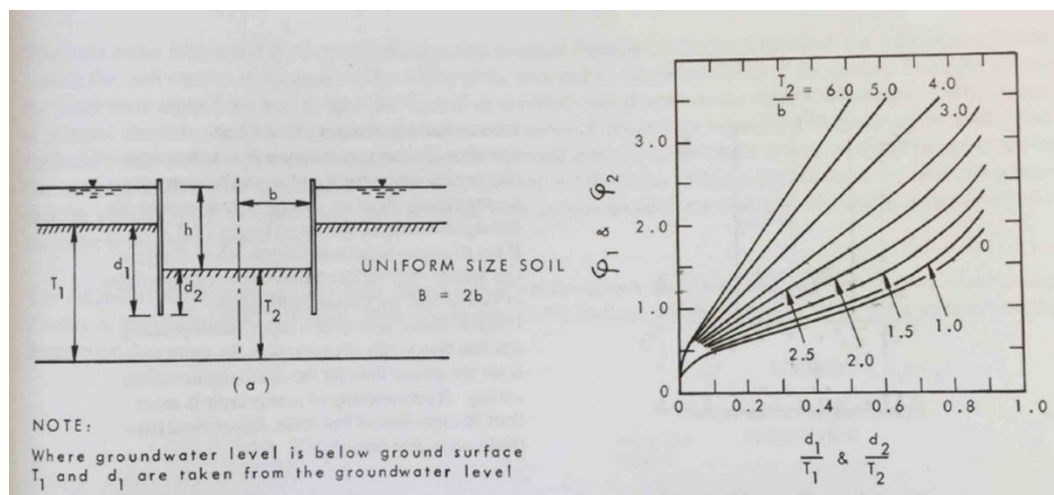


**Fig. 6.6** Double-walled cofferdam geometry and form factors chart used in CFEM (2006)

[adopted from (CFEM 2006)]

Accuracy assessment for exit hydraulic gradients estimations

For the assessment,  $i_{EM}$  and  $i_{EC}$  values calculated by 3D numerical simulation were plotted against the  $i_E$  values (obtained using 2D numerical simulations) of corresponding circular and double-walled cofferdams in Fig. 6.7. Fig. 6.7a shows the relation based on the  $i_E$  values of circular cofferdams where the left one is for the  $i_{EM}$  and right one is for the  $i_{EC}$ . The corresponding results based on the  $i_E$  values of double-walled cofferdams are shown in the Fig. 6.7b. Here also, both circular and double-walled  $i_E$  values show strong linear relationship with both  $i_{EM}$  and  $i_{EC}$ .

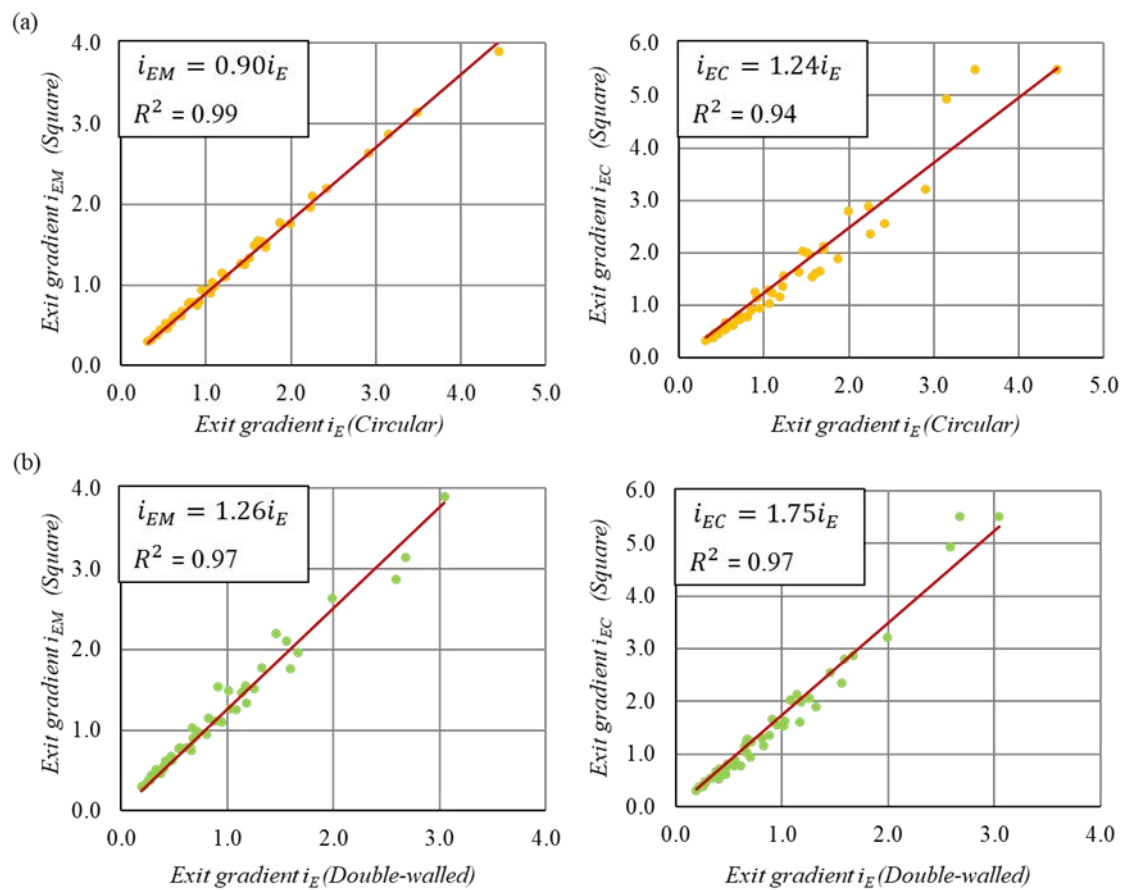


**Fig. 6.7** Relationships between 2D exit hydraulic gradient  $i_E$  values and  $i_{EM}$  and  $i_{EC}$  values of square cofferdams: (a) circular cofferdam; (b) double-walled cofferdam

From Fig. 6.7a,

$$i_{EM} = 0.9i_E \quad (6.7)$$

$$i_{EC} = 1.24i_E \quad (6.8)$$

Then, it is observed that treating a square cofferdam as an equivalent circular cofferdam overestimates  $i_{EM}$  by 11% (see Eq. 6.7); however, it underestimates  $i_{EC}$  by 19% (see Eq. 6.8). Therefore, approximate solution 1 discussed in Sec. 6.2 (replacing a square cofferdam by the equivalent circular one) is not recommended.

From Fig. 6.9b,

$$i_{EM} = 1.26i_E \quad (6.9)$$

$$i_{EC} = 1.75i_E \quad (6.10)$$

CFEM (2006) provides Eqs. 6.11 and 6.12 for determining  $i_{EM}$  and  $i_{EC}$ , respectively, and they are in very good agreement with Eqs. 6.9 and 6.10.

$$i_{EM} = 1.3i_E \quad (6.11)$$

$$i_{EC} = 1.7i_E \quad (6.12)$$

However,  $i_{EM}$  and  $i_{EC}$  values given in CFEM are the average values of the hydraulic gradients at the mid-point and corner. These values are averaged over the entire embedment depth  $\alpha(1 - s)$  within the cofferdam enclosure. The values computed from Eqs. 6.9 and 6.10 are determined exactly at the point of exit and hence the true exit hydraulic gradients. The average values computed over the embedment depth can be expected to be less.

Next a detailed analysis was carried out to assess the accuracy of Eqs. 6.7 - 6.10 comparing the predictions by above equations to the actual values obtained by 3D simulation for the square cofferdam geometries shown in Table 6.2. Fig. 6.8a shows the comparisons based on the circular cofferdam relations (Eqs. 6.7 and 6.8) while Fig. 6.8b is for the double-walled cofferdam case (Eqs. 6.9 and 6.10). For the  $i_{EM}$  estimation, predictions using  $i_E$  of circular

cofferdam (Fig. 6.8a left) is more accurate than the double-walled one (Fig. 6.8b left). In Fig. 6.8a left, all the predictions are within  $\pm 10\%$  while only 27 out of 45 predictions by Eq. 6.9 (Fig. 6.8b left) are within  $\pm 10\%$ . In addition, 14 predictions by Eq. 6.9 are on the unsafe side with the deviation exceeding 10%, and the maximum deviation being 25%. Therefore, Eq. 6.7 is better than Eq. 6.9 for estimating  $i_{EM}$ .

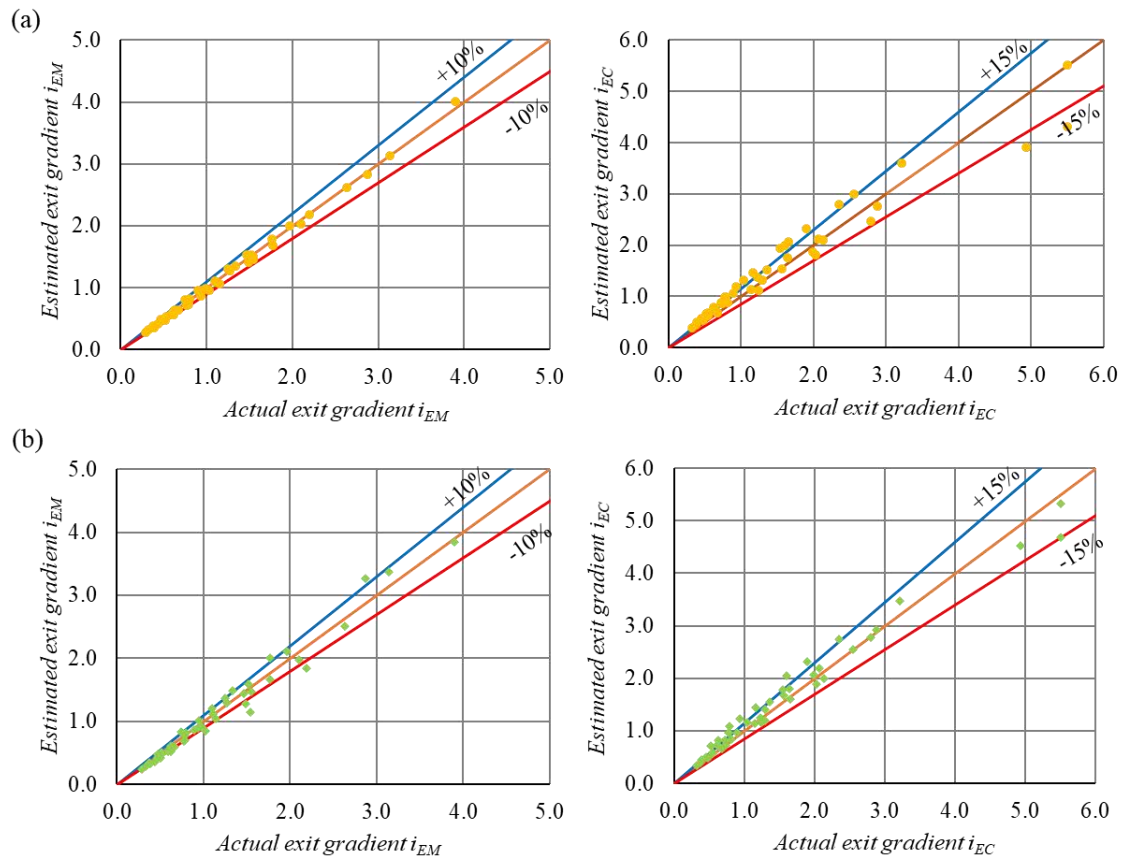


**Fig. 6.8** Comparison of the exit gradient predictions using 2D flow patterns: (a) circular cofferdam; (b) double-walled cofferdam

In the  $i_{EC}$  estimations, most of the predictions by both Eqs. 6.8 and 6.10 are on the conservative side, i.e., 36/45 and 35/45 predictions from Eq. 6.8 and Eq. 6.10, respectively, overestimating the  $i_{EC}$ . However, most of the predictions (30/45) by the Eq. 6.10 are within the  $\pm 15\%$  while it is only (20/45) for the Eq. 6.8. Also, maximum deviation to the unsafe side is 22% by the Eq. 6.8, but this is within 15% for Eq. 6.10 predictions. In contrast, maximum overestimate prediction by the Eq. 6.8 is 28% while it is 37% with the Eq. 6.10. Therefore, between the two

methods (Eqs 6.8 and 6.10), one is not significantly better than the other. Also, in Fig. 6.8 or from the Eqs. 6.7 - 6.10, it is observed that  $i_{EC}$  and  $i_{EM}$  are related as:

$$\frac{i_{EC}}{i_{EM}} = 1.38 \quad (6.13)$$

This relation is useful since one exit hydraulic gradient can be determined from the other for square cofferdams.

Considering all, it can be concluded that existing approximate solution methods (mentioned in Sec. 6.2) tend to underestimate the seepage solutions of square cofferdams and hence, are not accurate enough for the preliminary estimations. Therefore, following solutions are proposed using the above analysis.

### 6.2.3 Proposed solution method for square cofferdams

#### Flow rate estimation

From, Fig. 6.4, it is clear that, the  $q_s - q_c$  relation is stronger than the  $q_s - q_d$  relation, with slightly higher coefficient of determination ( $R^2$ ). For a detailed assessment of the accuracy of the two relations ( $q_s - q_c$  and  $q_s - q_d$ ), total flow into the square cofferdam  $Q_s$  computed using Eqs. 6.2 and 6.4 were compared in Fig. 6.9 with the actual values determined from the 3D numerical simulations. For this comparison also, same 45 geometries shown in Table 6.2 were considered. In Fig. 6.9a, 30 points out of the 45 (67%) are within the  $\pm 15\%$  while it is 25 (56%) in the Fig 6.9b. In addition, maximum underestimation of the flow rate is 11% for the Eq. 6.2 (Fig. 6.9a) while this is 16% for the Eq. 6.4 (Fig. 6.9b). Further, maximum overestimation is by 37% for Eq. 6.2 with only 8 cases greater than the 30%. In Fig.6.9b (for Eq. 6.4), maximum overestimation was 83% with 8 cases exceeding 50%. Therefore, it can be

concluded that deriving the flow rates for a square cofferdam based on circular cofferdam (Eq. 6.2) is better than those derived from the double-walled cofferdam (Eq. 6.4).

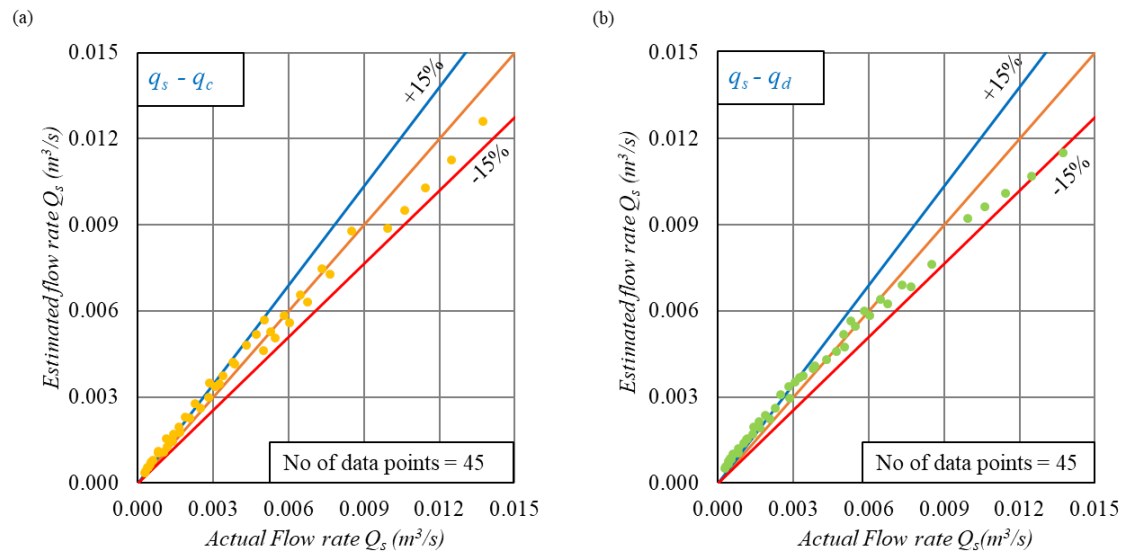


**Fig.6.9** Comparison of the flow rate predictions for square cofferdams using 2D flow patterns: (a) circular cofferdam; (b) double-walled cofferdam

#### Exit hydraulic gradients estimation

As noted in Fig. 6.8, Eq. 6.7 is more accurate for estimating the exit gradient  $i_{EM}$  at the mid-point of the square cofferdam, and numerical simulation or method of fragment (MoF) solutions given in chapter 4 can be used for finding the corresponding  $i_E$  value of circular cofferdam. In predicting the  $i_{EC}$  both double-walled based or circular based relationships (Eqs.6.8 or 6.10) can be used, depending on which of the 2D exit gradient values is available. Alternatively,  $i_{EC}$  can be determined as  $1.38 i_{EM}$  (see Eq. 6.13). For both cases, 2D numerical simulation or MoF solutions provide the necessary value for the equivalent circular or double walled cofferdam.

Further, flow patterns into the square, circular and double-walled cofferdams were compared studying the equipotential lines behaviour for a series of geometry. Fig. 6.10a shows the distribution of equipotential lines at  $h/10$  intervals of square cofferdams at three cofferdam

widths ( $B/T = 0.2, 0.5$  and  $0.8$ ) for the  $s/T = 0.5$  and  $\alpha = 0.4$ . Fig. 6.10b shows the equipotential lines distribution for the corresponding circular cofferdams (i.e.,  $B = r$ ) while Fig. 6.10c gives corresponding distributions for double-walled cofferdams (i.e.,  $B = L$ ). It shows that there is good similarity between flow patterns into the circular and square cofferdams than between square and double-walled cofferdams. That is due to both flow patterns into the circular and square cofferdams are 3D while it is 2D in double-walled case. Therefore, it is confirmed that applying a correction factor to the seepage solutions of circular cofferdams (Eqs. 6.2, 6.7 and 6.8) can be used to predict more accurate seepage solutions for square cofferdams than the predictions given by correction factors applied to double-walled (2D) figures (Eq. 6.4, 6.9).

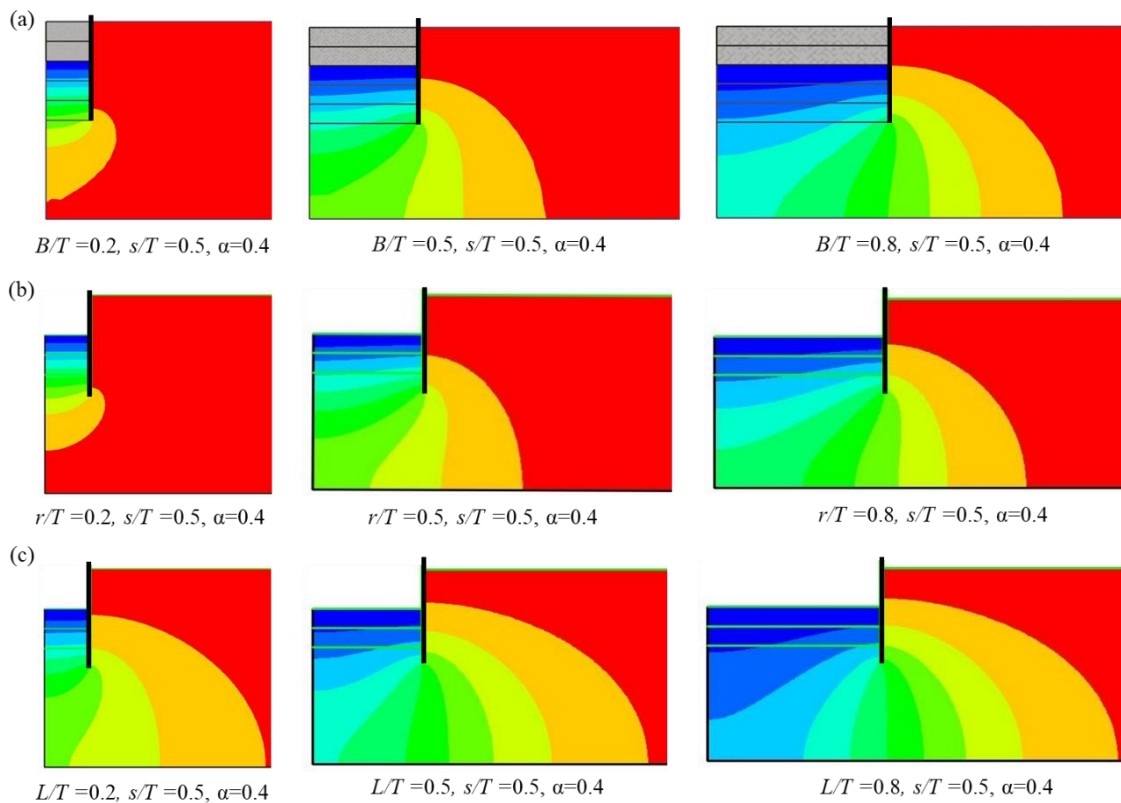


**Fig. 6.10** Equipotential lines distributions: (a) square cofferdams; (b) circular cofferdams; (c) double-walled cofferdams

In Summary, it can be concluded that the flow rate into a square cofferdam is better predicted using  $q_c$  computed for a circular cofferdam of the same width by Eq. 6.2 than  $q_d$  computed for

the corresponding double-walled cofferdam using Eq. 6.4 or 6.6. The  $q_c$  for the circular cofferdam can be determined through the 2D simulation as the axisymmetric problem or more easily, via the method of fragment (MoF) solution proposed in chapter 4. However, current industry practice, (i.e., replacing the square cofferdam by an equivalent circular one without applying the correction factor) is discouraged since flow into a circular cofferdam is about 27% less than the flow into a square cofferdam of the same width (see Eqs. 6.2 and 6.3).

### 6.3 Seepage solution for rectangular cofferdams

As discussed previously, the only accurate solution method available for rectangular cofferdams is the 3D numerical simulation. However, due to the cost and advanced resource requirement for 3D simulation, these problems are solved as 2D problems in Cartesian coordinate system (i.e., as double-walled cofferdams). Nevertheless, this approximation is unsafe especially when the cofferdam length is not considerably larger than its width since the actual flow into the cofferdam is in three-dimensional in these situations. This can significantly underestimate the exit hydraulic gradient and the flow rate values. Therefore, a thorough analysis was performed in this section to identify a safe length to width ratio at which 2D approximation is reasonable (neglecting the effects of two shorter sides) and also to develop accurate solution method when the length to width ratio is low (i.e., it is required to consider 3D flow effect into the cofferdam) for rectangular cofferdams.

#### 6.3.1 Numerical simulations of rectangular cofferdams

Fig. 6.11 shows the numerical model used for rectangular cofferdam analysis using the 3D finite element program (*RS3 2.0*) developed by Rocscience. Here also, only a quadrant was analysed, taking the advantage of symmetry. The boundary conditions and the parameters  $h$ ,  $s$ ,  $\alpha$  and  $T$  are defined in the same way discussed for the square cofferdam modelling (see Fig.

6.1a left). Here  $B$  is the half-width of the shorter side of the cofferdam while  $l$  represents the half-length of the longer side. Therefore, the ratio  $l/B$  equals to the length/width ratio of cofferdam.  $B_e$  and  $l_e$  are the distances from the sheet pile wall to the model's boundaries of shorter and longer side, respectively.

All the numerical runs were carried out as flow only problems, and a graded mesh was applied with ten-noded tetrahedral elements for meshing. The distances  $B_e$  and  $l_e$  were selected through a sensitivity analysis in a similar way discussed for the square cofferdam analysis, i.e., further increasing of  $B_e$  and  $l_e$  beyond the selected values increase the flow rate and exit hydraulic gradient values only by 1% or lower. Analysis showed that it is negligible the increments of values when  $(B + B_e)/B$  and  $(l + l_e)/l$  ratios changing from 5 to 6 for all the geometries. Therefore, the distances  $B_e$  and  $l_e$  were selected as equal or larger than  $4B$  and  $4l$ , respectively. In all the simulations, values of  $T$  and  $h$  were kept constant, with 20 m and 10 m, respectively. The soil was treated as completely saturated and isotropic ( $R = 1$ ) with permeability of  $10^{-5}$  m/s.

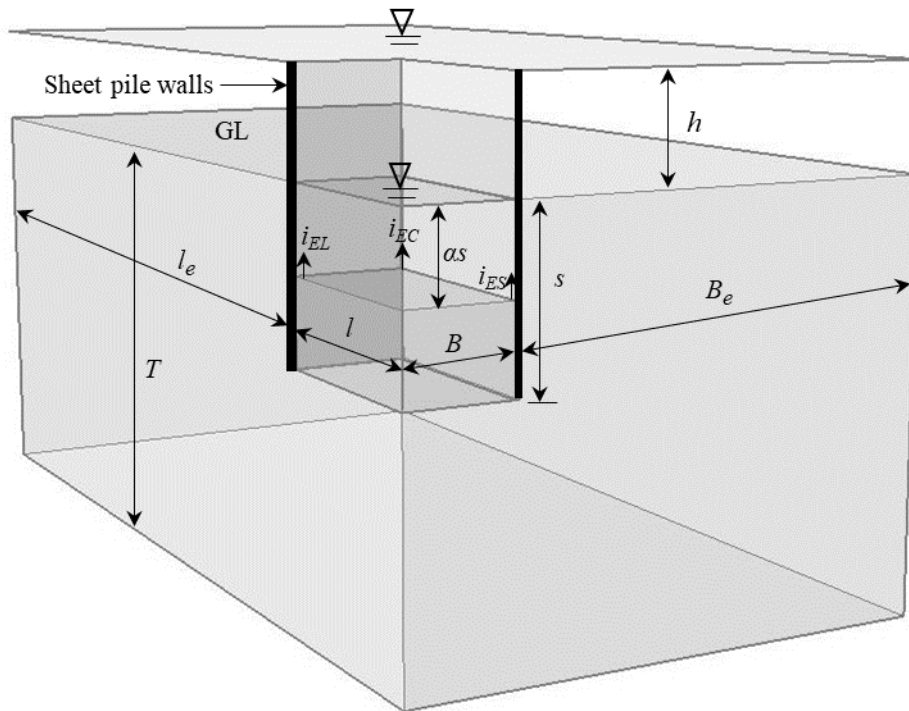


**Fig. 6.11** Numerical model geometry used for rectangular cofferdams

### 6.3.2 Accuracy assessment of double-walled approximation to the seepage solutions for rectangular cofferdams

For the analysis, seven  $l/B$  ratios were considered as 1, 1.5, 2, 3, 5, 10 and 20, assuming that the geometries where  $l/B$  ratio greater than 20 are rarely seen. For each  $l/B$  ratio, 45 geometries were analysed, considering three  $B/T$  values (0.2, 0.5 and 0.8), three  $s/T$  values (0.2, 0.5 and 0.8) and five excavation depths  $\alpha s$  (for  $\alpha$  0, 0.2, 0.4, 0.6 and 0.8), similar to the way that the square cofferdams were analysed. In each case, flow rate and the three exit hydraulic gradient values adjacent to the sheet pile walls ( $i_{EC}$ ,  $i_{ES}$  and  $i_{EL}$ ) were calculated.  $i_{EC}$  is the exit hydraulic gradient at the corner of the rectangular cofferdam while  $i_{ES}$  and  $i_{EL}$  give exit hydraulic gradients at the mid-points of the shorter side and longer side, respectively (see Fig. 6.11). Next, for each rectangular geometry, flow rate  $q_d$  (per meter length of perimeter of

half the section) and exit hydraulic gradient  $i_E$  of the corresponding double-walled cofferdam were calculated.

#### Accuracy assessment for flow rate estimation

For the assessment, 315 geometries were considered with 45 for each of the seven  $l/B$  ratios. Then calculated flow rate for the rectangular cofferdams using the 3D simulation was divided by relevant  $l$  value (neglecting the flow across the shorter side) to find the flow rate per meter length along the longer side  $q_r$  for each model, considering the double-walled approximation. Then, for each the  $l/B$  ratio,  $q_r$  values were plotted against the corresponding flow rate of the double-walled cofferdams  $q_d$ , in separate graphs. The graph for  $l/B = 3.0$  is shown in Fig. 6.12. Appendix D1 shows the graphs for rest of the  $l/B$  ratios considered in this dissertation. Fig. 6.12 shows strong linear relationship between  $q_r$  and  $q_d$  in the form of  $q_r = a q_d$ . Also, it shows that, approximating a rectangular cofferdam having the  $l/B$  ratio of 3 to the corresponding double-walled cofferdam tends to underestimate the flow rate by 32%. The multipliers calculated for other  $l/B$  values are given in Table 6.3.

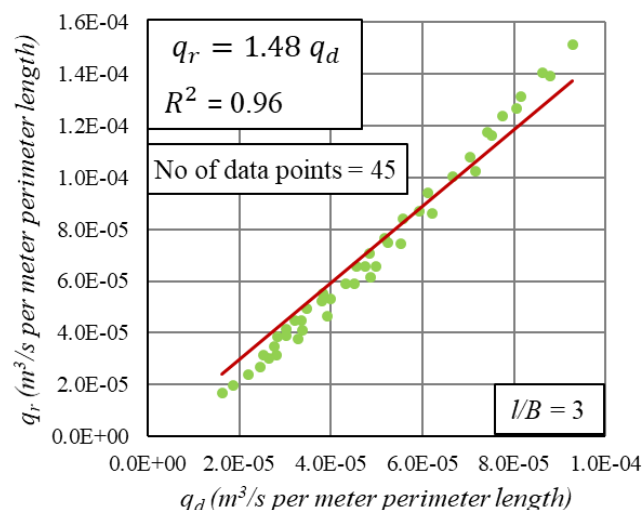


**Fig. 6.12** Relationship between double-walled flow rate to the 3D flow rate into rectangular cofferdam at  $l/B = 3$

**Table 6.3** Summary of the flow rate analysis of rectangular cofferdam

$l/B$	$a$	$R^2$
1	1.94	0.92
1.5	1.71	0.94
2	1.61	0.95
3	1.48	0.96
5	1.37	0.97
10	1.29	0.97
20	1.25	0.97

Results in the Table 6.3 show that even for  $l/B$  as high as 20, assuming  $l/B$  as infinite (approximating the rectangular cofferdam to the double-walled one) tends to underestimate the flow rate by about 20%, requiring a multiplication factor  $a$  of 1.25. Note that, derived  $a$  value here is the average value for  $l/B = 20$  covering a wider range of geometries, i.e., three  $B/T$  values (0.2, 0.5 and 0.8), three  $s/T$  values (0.2, 0.5 and 0.8) and five excavation depths  $\alpha s$  (for  $\alpha$  0, 0.2, 0.4, 0.6 and 0.8). Therefore, the ratio  $l/B$ , at which, the shorter side can be neglected, and the problem can be treated as a double-walled, depends on  $B/T$ ,  $s/T$  and  $\alpha$ . However, it is not possible to arrive at a single limiting value of  $l/B$  within the range considered in this study ( $l/B \leq 20$ ) beyond which such approximation holds in terms of flow rate estimation.

#### Accuracy assessment for exit hydraulic gradients estimation

The 45 geometries shown in Table 6.2 were considered again at the same  $l/B$  ratios (1, 1.5, 2, 3, 5, 10 and 20) discussed above making a total of 315 geometries to assess the accuracy of exit hydraulic gradient predictions. For each geometry, three exit gradient values mentioned previously ( $i_{EC}$ ,  $i_{ES}$  and  $i_{EL}$ ) were determined using the 3D simulation. Next, for each  $l/B$  ratio, these three exit gradient values were plotted in three separate graphs against the exit hydraulic

gradient  $i_E$  values of corresponding double-walled cofferdams. The graph for  $i_{EC}$  at  $l/B = 3$  is shown in Fig. 6.13, and here,  $i_{EC}$  relates strongly to the corresponding  $i_E$  of the double-walled cofferdam in the form of  $i_{EC} = bi_E$ . All three exit hydraulic gradient values ( $i_{EL}$ ,  $i_{ES}$  and  $i_{EC}$ ) for each case of  $l/B$  showed similarly strong relation to the  $i_E$  of double-walled cofferdams. Appendices D2 and D3 show the plotted graphs for  $i_{EL}$  and  $i_{ES}$  for all the  $l/B$  ratios while appendix D4 shows the graphs of rest of the  $l/B$  ratios (except  $l/B = 3$ ) for  $i_{EC}$ . The summary of the analysis is given in Table 6.4.

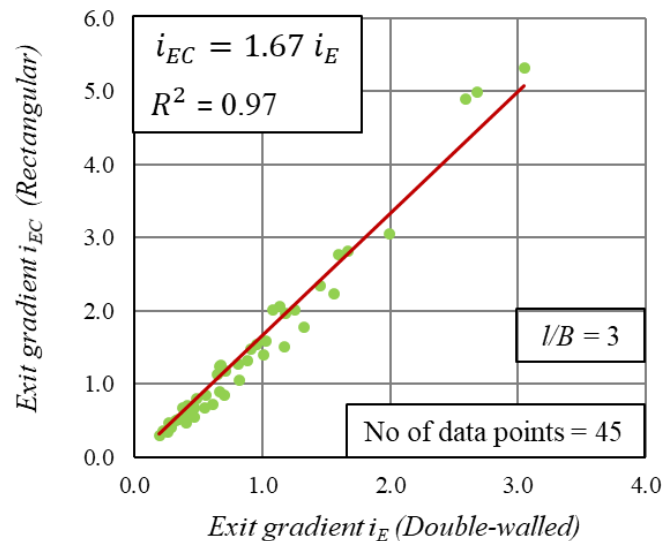


**Fig. 6.13** Relationship between double-walled exit gradient to the actual exit gradient values of rectangular cofferdams at  $l/B = 3$

The results show that the highest exit gradient values are reported for the corner ( $i_{EC}$ ) where the seepage forces concentrate more strongly compared to the mid sections of the two sides. Also, the second largest exit hydraulic gradient is reported for  $i_{ES}$  i.e., at the mid-point of the shorter side while  $i_{EL}$  is the lowest. This is due to the higher concentration of streamlines at the shorter side compared to that for the longer side. So,  $i_{EC}$  and  $i_{ES}$  are the two important exit gradient values in terms of piping failure assessment.

For  $l/B \geq 3$ ,  $b$  remains constant for all three locations, implying that the  $i_{EC}$ ,  $i_{ES}$  and  $i_{EL}$  values remain constants too. Also, for the  $i_{EC}$  and  $i_{ES}$  estimations, the two critical locations, there is only a slight reduction in  $b$  value when  $l/B$  changes from 1 to 3. Therefore, even for  $l/B$  values as high as 20, the two critical exit hydraulic gradients  $i_{EC}$  and  $i_{ES}$  are significantly higher than what is derived from a 2D approximation, (neglecting the effects of shorter sides), and hence, assuming as a double-walled cofferdam is not recommended for exit hydraulic gradients estimation for any values of  $l/B$  in terms of  $i_{EC}$  and  $i_{ES}$ .

**Table 6.4** Summary of the exit gradient estimation relations for rectangular cofferdam

$l/B$	$i_{EL}$		$i_{ES}$		$i_{EC}$	
	$b$	$R^2$	$b$	$R^2$	$b$	$R^2$
1	1.26	0.97	1.26	0.97	1.75	0.97
1.5	1.15	0.98	1.22	0.98	1.69	0.97
2	1.10	0.99	1.21	0.98	1.68	0.97
3	1.05	0.99	1.19	0.98	1.67	0.97
5	1.02	0.99	1.19	0.98	1.66	0.97
10	1.00	0.99	1.19	0.98	1.66	0.97
20	1.00	0.99	1.19	0.98	1.66	0.97

### 6.3.3 Proposed solution method for rectangular cofferdams

#### Flow rate estimation

The variation of  $a$  against  $l/B$  is shown in Fig. 6.14, and using that, the relationship between  $a$  and  $l/B$  can be defined as:

$$a = 1.81(l/B)^{-0.14} \quad (6.14)$$

Accordingly, total flow rate into the rectangular cofferdam  $Q_r$  when  $0 < l/B \leq 20$  can be estimated as:

$$Q_r = a q_d 4l = 4a q_d l \quad (6.15)$$

As noted before, it is uncommon to see a rectangular cofferdams with  $l/B$  ratio greater than 20; however, authors suggest using  $a = 1.19$  predicted by Eq. 6.14 at  $l/B = 20$  for any geometries having a larger  $l/B$  ratio than 20.

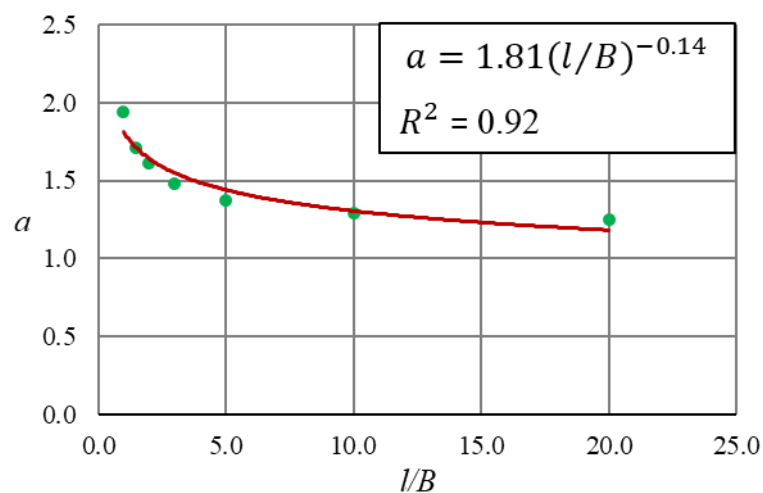


**Fig. 6.14** Relationship of  $a$  value to the  $l/B$  ratio

The proposed solution method (Eq. 6.15) was validated at  $l/B = 3$  covering a wider geometry range for  $B/T$ ,  $s/T$  and  $\alpha$  (45 cases shown in Table 6.2) through the steps mentioned below.

1. Estimated  $a$  value at  $l/B = 3$  from Eq. 6.14, and it was 1.55.
2. Predicted the total flow rate  $Q_r$  from the Eq. 6.15 and compared the predictions against the actual flow rate estimated by the 3D simulation for all 45 cases. The comparison result is shown in the Fig. 6.15.

In Fig. 6.15, most of the predictions (28/45) are within  $\pm 15\%$  limiting the maximum underestimation is less than 5%. Also, for the 9 cases, where the flowrate is overestimated by 25% or more the geometries correspond to cases having very little significance in practice

where  $B/T = 0.2$  and  $s/T$  values equal to 0.5 and 0.8. Overall, proposed Eq. 6.15 provides reasonable estimates of flow rate, and the few predictions where deviations are large are on the conservative side.

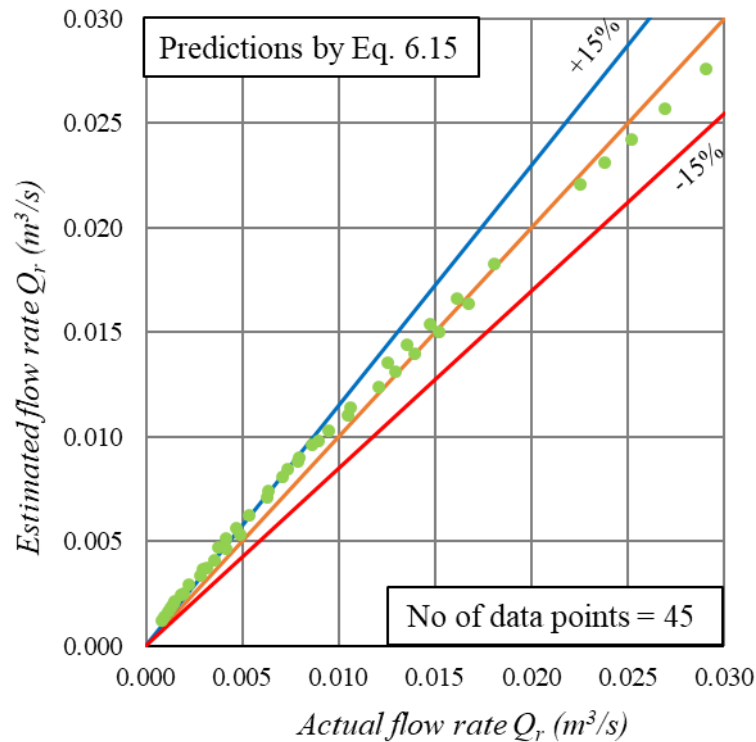


**Fig. 6.15** Comparison of the flow rate predictions for rectangular cofferdam at  $l/B = 3$

#### Exit hydraulic gradients estimation

Using the results shown in Table 6.4,  $b$  can be conservatively taken as 1.75 and 1.26 for  $i_{EC}$  and  $i_{ES}$  estimations, respectively for all  $l/B$  values. Accordingly, following equations are proposed for  $i_{EC}$  and  $i_{ES}$  for all rectangular cofferdams:

$$i_{EC} = 1.75i_E \quad (6.16)$$

$$i_{ES} = 1.26i_E \quad (6.17)$$

However, the change of  $b$  for  $i_{EL}$  estimation is considerable compared to the  $i_{EC}$  and  $i_{ES}$  estimations. Then, a graph was plotted for estimating the  $b$  value for the  $0 < l/B \leq 3$  as shown in Fig. 6.16.

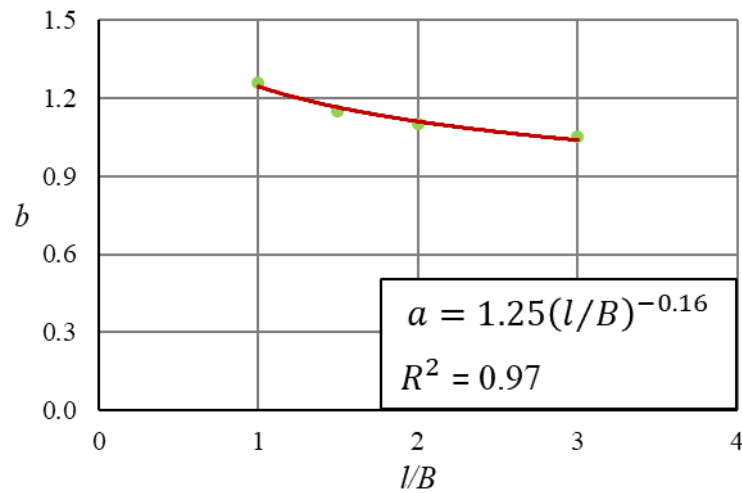


**Fig. 6.16** Relationship of  $b$  value to the  $l/B$  ratio on  $i_{EL}$  estimation

The relation of  $b$  to the  $l/B$  is given as:

$$b = 1.25(l/B)^{-0.16} \quad (6.18)$$

Accordingly,  $i_{EL}$  can be estimated when  $0 < l/B \leq 3$  as:

$$i_{EL} = bi_E \quad (6.19)$$

When the  $l/B$  ratio is greater than 3, it is suggested to conservatively use same  $b$  value when  $l/B$  is at 3. Also, at  $l/B = 3$ ,  $b \approx 1$  and hence, a rectangular cofferdam can be analysed as corresponding double-walled one, but only for estimating the  $i_{EL}$  for  $l/B \geq 3$ . As noted before, engineer should be more interested in  $i_{EC}$  and  $i_{ES}$  since any potential piping may occur at the corner or at the middle of short side where exit hydraulic gradient are highest. So, there is no significance of approximating a rectangular cofferdam to the corresponding double-walled one only for estimating the  $i_{EL}$ .

The proposed solutions for the exit hydraulic gradient estimations of rectangular cofferdams [Eqs. 6.16, 6.17, and 6.19] were also validated considering the same 45 geometries used before for flow rate estimation validation at  $l/B = 3$ . Here,  $i_{EC}$ ,  $i_{ES}$  and  $i_{EL}$  were estimated using Eqs. 6.16, 6.17 and 6.19, respectively and then were compared against the actual values calculated by 3D simulations. Fig. 6.17 shows the validation results. In the  $i_{EC}$  estimation, 29 cases predicted by the proposed Eq. 6.16 are within  $\pm 15\%$  while maximum underestimation is limited to 7% (Fig. 6.17a). Also 12 cases overestimated  $i_{EC}$  by more than 25%, but most of them are for the geometries with no significance in practical applications, i.e.,  $B/T = 0.2$ . For the  $i_{ES}$  estimations, 43/45 predictions are within  $\pm 15\%$  (see Fig. 6.17b) while all the prediction for  $i_{EL}$  (by Eq. 6.19) are within  $\pm 10\%$  (Fig. 6.17c). Therefore, it is concluded that proposed Eqs. 6.16, 6.17 and 6.19 predict exit hydraulic gradient values for the rectangular cofferdams in good level of accuracy, and the few cases where the deviations are significant are always on the safe side.

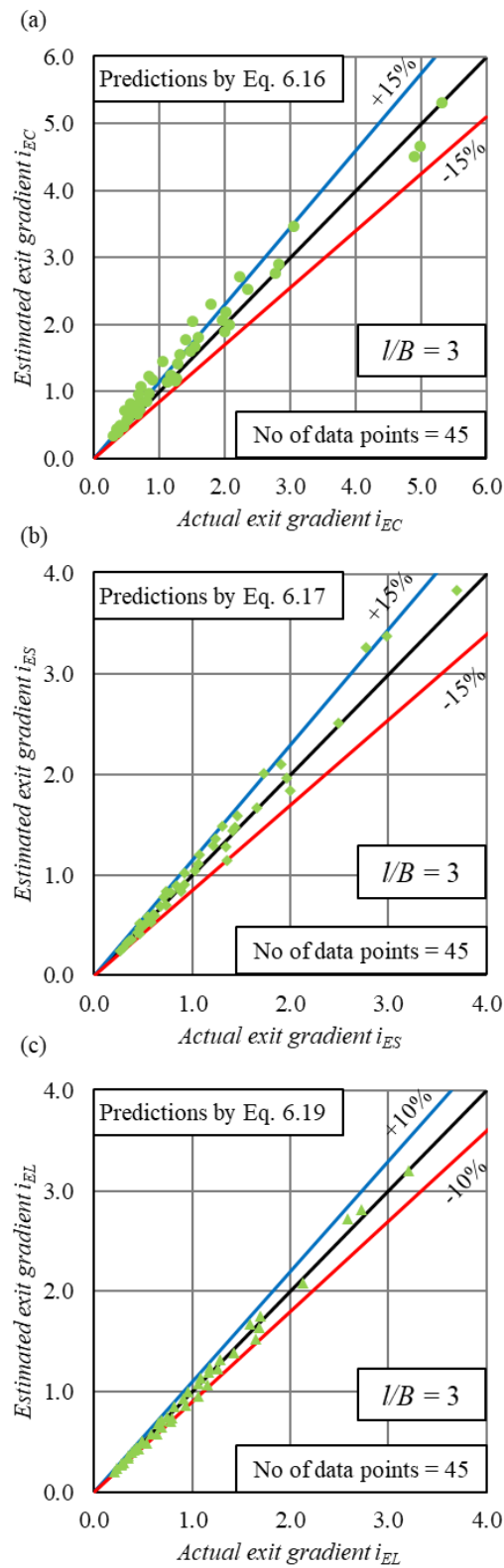


**Fig. 6.17** Comparison of the exit hydraulic gradient predictions for rectangular cofferdams:

(a)  $i_{EC}$ ; (b)  $i_{ES}$ ; (c)  $i_{EL}$

#### 6.4 Summary and conclusions

Simple solutions for estimating the flow rates and exit hydraulic gradients of square and rectangular cofferdams are presented. Both square and rectangular cases were studied separately. The proposed expressions for flow rate estimations are in the form of:

$$Q_{3D} = a q_{2D} C \quad (6.20)$$

where  $Q_{3D}$  is the total flow rate into the square or rectangular cofferdam,  $a$  is a constant, and  $C$  is the perimeter length of the square cofferdams while it is the length of the two longer sides for rectangular cofferdams.  $q_{2D}$  is the flow rate per meter length along the perimeter of the circular or double-walled cofferdam. When estimating the flow rate for a square cofferdam, it is suggested to use  $q_{2D}$  from the circular cofferdam, with  $a = 1.07$  (see Eq. 6.2). For a rectangular cofferdam,  $q_{2D}$  values should be determined from the corresponding double-walled cofferdam where  $a$  varies between 1.19 and 1.81 depending on the  $l/B$  ratio (see Eq. 6.14). Also, it is not safe to consider a rectangular cofferdam as equivalent to the double-walled one even with  $l/B$  ratio as high as 20 in terms of flow rate estimation.

In both square and rectangular cofferdams, it is shown that the exit hydraulic gradient is the maximum at the corner. Expressions for the exit hydraulic gradient at the corner  $i_{EC}$  and mid-points of the two sides within the excavation are proposed (in rectangular cofferdams, one for short side  $i_{ES}$  and one for the long side  $i_{EL}$ ). All three exit gradients are of the form

$$i_{3D} = b i_{2D} \quad (6.21)$$

where  $i_{3D}$  is the exit hydraulic gradient for the square or rectangular cofferdam,  $b$  is a constant, and  $i_{2D}$  is the exit hydraulic gradient of the circular cofferdam for the square cases while it is for the double-walled cofferdam for the rectangular cases. In square cofferdams,  $b = 1.24$  for the corner and  $b = 0.90$  for the mid-point of any side. In rectangular cofferdams,  $b = 1.75$  for

the corner and 1.26 for the mid-point of the short side, and these are independent of the  $l/B$  ratio, and hence, there is no maximum value for  $l/B$  beyond which the problem can be assumed as double-walled cofferdam. For the mid-point of the long side in rectangular cofferdams,  $b$  varies between 1.05 and 1.25 depending on  $l/B$  (see Eq. 6.18). However, when the  $l/B \geq 3$ , a rectangular cofferdam can be considered as a double-walled one, but only for estimating the exit hydraulic gradient value at the mid-point of the long side  $i_{EL}$ .

The proposed expressions were validated using series of finite element simulations and are very valuable for accurately estimating the flow rate and exit hydraulic gradient values when the flow pattern is in three-dimensional as in square or rectangular cofferdams. The solutions proposed in this chapter are applicable for the situation where the soil medium is isotropic and homogeneous, i.e., uniform soil thickness along the depth. However, when the soil medium is anisotropic and homogeneous, proposed solutions are still applicable with a reasonable accuracy since the MoF provides the facility to incorporate anisotropic condition in determining the form factors for both double-walled and circular cofferdam cases. For that, it requires to calculate relevant 2D solutions using the MoF first, and then, proposed equations for the square or rectangular cofferdams can be used for finding the appropriate 3D solutions. The solutions proposed herein can be very useful as a design tool in providing reasonable estimates of the flow rate and exit hydraulic gradients, especially in preliminary assessments and for carrying out parametric studies, before going for a detailed analysis.

## Chapter 7 Summary, Conclusions and Recommendations

This chapter presents a summary of the dissertation, conclusions and recommendations for possible future research.

### 7.1 Summary

The aim of the dissertation was to develop simple seepage solutions for double-walled, circular, square and rectangular cofferdams using a simple solution method known as Method of fragments (MoF).

Cofferdams are widely used as temporary water cut-off structures into the excavations in construction sites. Through a review of literature, it was found that flow rate and maximum exit hydraulic gradient are two of the main design parameters required for any shape of cofferdam, and, piping is the most common hydraulic failure mode. Further it showed that flow into double-walled cofferdams can be analysed using a two-dimensional (2D) flow model in the Cartesian plane while it is required to consider three-dimensional (3D) flow models for circular, square and rectangular cofferdams. However, for circular cofferdams, 2D flow model can still be applied considering the problem in a radial plane (i.e., axisymmetric analysis). Literature review showed that MoF provides simple and quick seepage solutions for double-walled cofferdams while numerical simulations remains as the only accurate solution method for circular, square and rectangular cofferdams.

Griffiths (1984) developed MoF solutions for double-walled cofferdams, and in this method, half the flow domain of double-walled cofferdam is divided into two fragments namely, fragments *A* and *C*, using an assumed vertical equipotential line at tip of the sheet pile. Then, flow rate and maximum exit hydraulic gradient values are estimated using dimensionless

parameters known as form factors defined for each of the fragment. These form factors are functions only of the fragment geometry, and hence, MoF provides simple solutions. However, the accuracy of the MoF solutions depends on the validity of the assumption that the equipotential line at the tip of the sheet pile is vertical. Therefore, assessing the validity of MoF solutions for double-walled cofferdams is crucial to improve the applicability of MoF. Further, there is a perceived benefit of having a similar solution method for circular, square and rectangular cofferdam problems. Therefore, this research was divided into four parts based on cofferdam shapes studied for the development of seepage solutions.

The first part of the research evaluated the accuracy of the MoF solutions for double-walled cofferdams assessing the validity of the assumption (equipotential lines behaviour), and the effects of assumption deviation on the seepage solutions. For that, series of cofferdam geometries were simulated using the finite element software *RS2 9.0* developed by Rocscience, and then, equipotential line behavior was studied. Next, numerical results were compared with the corresponding MoF solutions to see the effects of assumption deviation on the seepage solutions. It was found that, the assumption deviates considerably (i.e., equipotential lines are far from vertical) especially for low values of cofferdam width ( $LR/T$ ) and sheet pile embedded depth ( $s/T$ ); however, equipotential lines become closer to the vertical when increasing the  $LR/T$  and  $s/T$  making the assumption to a reasonable one. In addition, excavation depth  $\alpha s$  has not significantly affected the equipotential line behaviour for moderate excavation depths (i.e.,  $\alpha s \leq 0.4$ ). Also, the effects of deviating the assumption were always on the conservative side providing higher flow rate and exit hydraulic gradient values. Therefore, MoF is a sufficiently accurate tool for estimating the seepage solutions for double-walled cofferdams. Next, MoF solutions were simplified further, defining three simple analytical expressions to estimate the form factors of the two fragments  $A$  and  $C$  and the dimensionless exit gradient

values of fragment  $C$  eliminating the use of MoF chart solutions. These expressions enable MoF be implemented through spreadsheets, and hence, are very useful for carrying out parametric studies for quick determination of the flow rate and the maximum exit hydraulic gradient values.

In the second part of the research, a new solution method was developed to solve seepage problems pertaining to the circular cofferdams introducing an axisymmetric MoF solution method. Thus, two new axisymmetric fragment types (defined as fragments  $D$  and  $E$ ) were developed considering the flow domain of a radial plane using an assumed vertical equipotential surface along the perimeter of the circular cofferdam. Hence, the accuracy of the axisymmetric MoF solutions depends on the assumption that the equipotential line at the tip of the sheet pile is vertical making a cylindrical equipotential surface along the perimeter of the cofferdam. So, the accuracy of the assumption on vertical equipotential surface was assessed studying the series of cofferdam geometries simulated using finite element software *RS2 9.0*. At this point, the analysis type was axisymmetric. It was observed that the accuracy of the assumption decreases when decreasing the values of cofferdam radius ( $rR/T$ ) and sheet pile embedded depth ( $s/T$ ) and increases while increasing the  $rR/T$  and  $s/T$ . Here also, effect of excavation depth  $\alpha s$  is not a concern for moderate excavations (i.e.,  $\alpha s \leq 0.4$ ).

Next, three designed charts were developed including two for the axisymmetric form factor estimations of fragments  $D$  and  $E$  and one for the dimensionless exit hydraulic gradient estimations of fragment  $D$  using the series of numerical simulations of the two fragment geometries. The outcomes of the proposed axisymmetric MoF solutions were compared against the detailed numerical solutions, analytical work of Neveu (1972), and experimental results, and it was found that the axisymmetric MoF solution method is adequate for reasonable

estimates of the flow rate and exit hydraulic gradient of circular cofferdams. Then, axisymmetric MoF solution was simplified further developing three simple analytical expressions to estimate the form factors and exit hydraulic gradients. These expressions enable the axisymmetric MoF be implemented through spreadsheets, and hence, provide quicker determination of seepage solutions. This is very useful particularly for carrying out parametric studies.

Third part of the research involved developing a first-order solution method to evaluate the safety against a possible piping failure for doubled-walled and circular cofferdams. The solutions provided the required shortest seepage path (creep length  $C$ ) to limit the maximum exit hydraulic gradient to a specific value ensuring the safety against the piping failure. Alternatively, for a given configuration of the cofferdam, exit hydraulic gradient can also be estimated thus defining the factor of safety against piping. The exit hydraulic gradient values proposed include the mean, upper and lower bounds.

In the final part of the research, simple solutions were developed for estimating the flow rates and exit hydraulic gradient values of square and rectangular cofferdams. Proposed solutions for square cofferdams involved applying correction factors to the seepage solutions of corresponding circular cofferdams while the solutions for rectangular cofferdams applied correction factors to the corresponding solutions of double-walled cofferdams. These correction factors were developed relating the actual seepage solutions for the series of square and rectangular cofferdam calculated using the 3D numerical simulations (by *RS3 2.0* developed by Rocscience) to the corresponding solutions derived for circular and double walled cofferdams using the *RS2 9.0*. The solutions proposed for square and rectangular cofferdams can be very useful as a design tool in providing accurate estimates of the flow rate

and exit hydraulic gradients, especially in preliminary assessments and for carrying out parametric studies, before going for a detailed analysis.

## 7.2 Conclusions

The main conclusions of the study are divided into four sections depending on the solution methods proposed for various cofferdam shapes in this dissertation.

### 7.2.1 Method of Fragments (MoF) solutions for double-walled and circular cofferdams

- MoF solutions provide efficient means of obtaining both the quantity of seepage and the exit hydraulic gradient for virtually any double-walled or circular cofferdam geometry of practical interest.
- MoF solutions can be applied for cofferdams founded on a homogeneous soil medium in both isotropic and anisotropic soil conditions where the depth of soil layer is finite, and the thickness of soil layer is uniform.
- When the founding soil consists of two layers, MoF solutions can still be applied for double-walled cofferdams in conjunction with the solution method proposed by Polubarinova-Kochina (1962) for a two layered system.
- MoF predictions are also always on the conservative side, and relative errors are within 10% for most of the cases provided  $s/T > 0.2$ . When  $s/T \leq 0.2$ , MoF still provides conservative solutions, but their level of accuracy is low (relative errors are between 10 and 20%). However, these geometries are corresponding to the cases having low sheet pile embedded depth ( $s/T \leq 0.2$ ), and hence, are of no practical significance. Therefore, this should not be a deterrent for using the MoF solutions in engineering practice.

- Predictions given by the developed analytical expressions for form factors and normalised exit hydraulic gradient estimations have the same level of accuracy to the predictions given by MoF chart solutions; therefore, these expressions can be used to find full seepage solutions for any geometry of the double-walled or circular cofferdam without using the numerical modelling or MoF chart solutions.

### 7.2.2 Creep length solutions for piping failure assessment of double-walled and circular cofferdams

- The proposed creep length solution methods can be applied for double-walled and circular cofferdams founded on a homogeneous soil medium in both isotropic and anisotropic conditions where the soil layer is finite and uniform in thickness.
- These solutions provide reasonable first estimate for a possible piping failure in both double-walled and circular cofferdam cases by just considering only the shortest seepage path (creep length).
- The proposed equations can be valuable tools for back-of-the-envelope calculations in the preliminary analysis while selecting the dimensions in a cofferdam.

### 7.2.3 Approximate seepage solutions for square cofferdams

- Currently used approximate solution methods for square cofferdams tend to underestimate the flow rate and exit hydraulic gradient values considerably.
- The relation of the flow patterns into the circular and square cofferdams is stronger than that between the square and double-walled cofferdams. Therefore, applying a correction factor to the seepage solutions of circular cofferdams provides more accurate seepage solutions for square cofferdams than the predictions given by correction factors applied to the seepage solutions of double-walled cofferdams.

- Exit hydraulic gradient values are highest for the corner  $i_{EC}$  where the seepage forces concentrate more intensely while it is lowest at the mid sections of the two sides  $i_{EM}$ .
- Solution given in CFEM (2006) for estimating the flow rate and exit hydraulic gradient can be improved with the new solutions developed in this study.
- The ratio  $\frac{i_{EC}}{i_{EM}} = 1.38$ , and hence, one exit hydraulic gradient can be determined from the other for square cofferdams.

#### 7.2.4 Approximate seepage solutions for rectangular cofferdams

- It is unsafe to assume a rectangular cofferdam as a double-walled cofferdam even for length to width ratio ( $l/B$ ) as high as 20 since it underestimates both flow rate and exit hydraulic gradient values.
- Highest exit gradient values are reported for the corner ( $i_{EC}$ ) while the second largest exit hydraulic gradient  $i_{ES}$  is reported at the mid-point of the shorter side while exit hydraulic gradient at the mid-point of the longer side  $i_{EL}$  is the lowest.
- There is only a slight reduction of exit hydraulic gradient at the two critical locations ( $i_{EC}$  and  $i_{ES}$ ) when increasing the  $l/B$  ratio. Therefore, even for  $l/B$  values as high as 20, the two critical exit hydraulic gradients  $i_{EC}$  and  $i_{ES}$  are significantly higher than what is derived from a 2D approximation (considering as double-walled cofferdam), and hence, it is not safe to consider a rectangular cofferdam to the corresponding double-walled cofferdam at any value of  $l/B$  ratio.

### 7.3 Recommendation for future research

Even though this dissertation has provided seepage solutions covering most of the cofferdam geometries encountered in practice, still there are some potential research areas that can be

---

considered for the future. They are summarised below in the sequence of the cofferdam shapes discussed in this dissertation.

### 7.3.1 Method of Fragments (MoF) solutions for double-walled cofferdams

As noted before, MoF solutions can be applied for double-walled cofferdams founded on a soil medium having a range of soil conditions, i.e., both isotropic and anisotropic soils in a homogeneous soil medium, and two layered soil system. However, in some cases, founding soil may consist of three or more soil layers, and hence, it is beneficial to extend the MoF solutions to investigate the cases having multiple soil layers (three or more). Also, as noted in chapter 2, cofferdams are widely applied in granular soils; however, a thin layer of clay can be encountered within the granular media, and also, the founding soil medium may not be uniform in thickness. Therefore, MoF solutions could also be extended to address these two issues.

### 7.3.2 Method of Fragments (MoF) solutions for circular cofferdams

The axisymmetric MoF solutions can also be applied for cofferdams founded on a soil medium having similar conditions discussed above for double-walled cofferdams. However, when the founding soil consists of two soil layers, analytical solution method proposed by Polubarinova-Kochina (1962) cannot be incorporated with axisymmetric MoF since it is only applicable for flow scenarios in the 2D Cartesian plane. So, future studies are required to extend the axisymmetric MoF solutions for multi-layered system including two or more layers. Also, as pointed for double-walled cofferdam, it is beneficial to focus future research to extend the axisymmetric MoF method to address the situations where the founding soil medium contains a thin layer of clay and is not uniform in thickness.

### 7.3.3 Creep length solutions for piping failure assessment of double-walled and circular cofferdams

Creep length solutions developed in this dissertation are applicable for double-walled and circular cofferdams founded on a homogeneous granular soil medium; therefore, exit hydraulic gradient values are independent from the soil permeability and hence, are independent from the soil type. Also proposed solutions have considered only the most critical parameter (i.e., creep length) for the solutions development; however, it was noted that exit hydraulic gradient values are influenced slightly by two other less sensitive parameters (excavation depth and sheet pile embedded depth). Therefore, future research could be conducted focussing to incorporate the effect of soil type and the effect of less sensitive parameters on to the creep length solution method proposed in this study.

### 7.3.4 Seepage solutions for square and rectangular cofferdams

The proposed solutions for square and rectangular cofferdams are directly applicable for an isotropic and homogeneous soil medium. However, homogeneous and anisotropic cases can also be treated using the same correction factors since required corresponding 2D solution provides the facility of incorporating the anisotropic effect. However, it may be useful to investigate the accuracy of the correction factors proposed in this study (for the isotropic soils) when the founding soil medium is homogeneous and anisotropic. Also, proposed solutions for rectangular cofferdams can also be used to estimate the seepage solutions for elliptical cofferdams, but it is a very approximate prediction. Therefore, future research can be directed to develop more accurate correction factors for the cofferdams where the shapes are elliptical and also, more irregular.

#### **7.4 Final comments**

Throughout this dissertation, seepage solutions for most of the cofferdam shapes encountered in practice have been simplified significantly without losing much of the accuracy. Also proposed solutions can address the soil conditions considered in practice generally for most of the preliminary and parametric studies and hence, are very useful as practical tools to quick estimate of seepage solutions.

---

## References

- AS 1289.6. 7.1 (2001). "Methods of testing soils for engineering purposes—soil strength and consolidation tests—determination of permeability of a soil—constant head method for a remoulded specimen." Standards Australia, Sydney.
- AS 1289.6. 7.2 (2001). "Soil strength and consolidation tests—determination of permeability of a soil-falling head method for a remoulded specimen ", Standards Australia, Sydney.
- ASTM D2434-68 (2006). "Standard test method for permeability of granular soils (constant head)." ASTM International, West Conshohocken, PA.
- ASTM D5856-95 (2007). "Standard test method for measurement of hydraulic conductivity of porous material using a rigid-wall, compaction-mold permeameter." ASTM International, West Conshohocken, PA.
- Banerjee, S. (1993). "Design Charts for double walled cofferdams." *Journal of Geotechnical Engineering ASCE*, 119(2), 214-222.
- Banerjee, S., and Muleshkov, A. (1992). "Analytical solution of steady seepage into double-walled cofferdams." *Journal of Engineering Mechanics*, 118(3), 525-539.
- Bauer, G. (1984). "Dewatering, hydraulic failure and subsequent analysis of a sheeted excavation." *Proc. of Int. Conf. on Case Histories in Geotechnical Eng*, 1415-1421.
- Bear, J. (1972). *Dynamics of Fluids in Porous Media*, Dover Publications, New York.
- Becker, D. E., and Moore, I. D. (eds.) (2006). *Canadian foundation engineering manual*, 4<sup>th</sup> Ed., Canadian Geotechnical Society, Richmond, BC, Canada.
- Benmebarek, N., Benmebarek, S., Kastner, R., and Soubra, A.-H. (2006). "Passive and active earth pressures in the presence of groundwater flow." *Geotechnique*, 56(3), 149-158.
- Bligh, W. (1910). "Dams, barrages and weirs on porous foundations." *Engineering News*, 64(26), 708-710.

- Bouchelghoum, F., and Benmebarek, N. (2011). "Critical hydraulic head loss assessment for a circular sheet pile wall under axisymmetric seepage conditions." *Studia Geotechnica et Mechanica*, 33(4)(4), 3-23.
- Cai, F., and Ugai, K. (2003). "Three-dimensional numerical investigation of piping for excavations in cohesionless soils." *Proc., Groundwater Engineering-Recent Advances: Proceedings of the International Symposium*, Okayama, Japan, May 2003, CRC Press, 145.
- Cai, F., and Ugai, K. (2004). "Seepage analysis of two case histories of piping induced by excavations in cohesionless soils." *The First Inter. Conf. on Construction IT*, Beijing, China.
- Carman, P. C. (1937). "Fluid flow through granular beds." *Trans. Inst. Chem. Eng.*, 15, 150-166.
- Carrier III, W. D. (2003). "Goodbye, hazen; hello, kozeny-carman." *J. Geotech. Geoenviron. Eng.*, 129(11), 1054-1056.
- Casagrande, A. (1937). "Seepage through dams." *Journal of the New England Water Works Association*, LI(2), 56-58.
- Cedergren, H. R. (1977). *Seepage, drainage, and flow nets*, John Wiley & Sons.
- Chapuis, R. P. (2004). "Predicting the saturated hydraulic conductivity of sand and gravel using effective diameter and void ratio." *Can. Geotech. J.*, 41(5), 787-795.
- Chauveteau, G., and Thirriot, C. (1967). "Régimes d'écoulement en milieu poreux et limite de la loi de Darcy." *La Houille Blanche*(2), 141-148.
- Chen, W. F., and Liew, J. R. (2002). *The civil engineering handbook*, Crc Press, New York.
- Chien, C. H. (1952). "Relaxation technique for three-dimensional flow net." *Eos, Transactions American Geophysical Union*, 33(1), 123-125.

- 
- Coduto, D. P. (1999). *Geotechnical engineering: principles and practices*, Prentice Hall, New Jersey.
- Craig, R. F. (2004). *Craig's soil mechanics*, London.
- Darcy, H. (1856). *Les fontaines publiques de la ville de Dijon: exposition et application*, Victor Dalmont, Paris.
- Das, B. M. (2013). *Advanced soil mechanics*, CRC Press, New York.
- Das, B. M., and Sivakugan, N. (2016). *Fundamentals of geotechnical engineering*, Cengage Learning, Boston.
- Davidenkoff, R., and Franke, O. L. (1965). "Untersuchung der räumlichen Sickerströmung in eine umspundete Baugrube in offenen Gewässern." *Tidewellenberechnung nach dem Universalprogramm der BAW(22)*, 65-75.
- Ergun, S. (1952). "Fluid flow through packed columns." *Chem. Eng. Prog.*, 48, 89-94.
- Fand, R., and Thinakaran, R. (1990). "The influence of the wall on flow through pipes packed with spheres." *Journal of Fluids engineering*, 112(1), 84-88.
- Forchheimer, P. (1901). "Wasserbewegung durch boden." *Z. Ver. Deutsch, Ing.*, 45, 1782-1788.
- Fox, E., and McNamee, J. (1948). "XXV. The two-dimensional potential problem of seepage into a cofferdam." *The London, Edinburgh, and Dublin Philosophical Magazine and Journal of Science*, 39(290), 165-203.
- Geertsma, J. (1974). "Estimating the coefficient of inertial resistance in fluid flow through porous media." *Society of Petroleum Engineers Journal*, 14(05), 445-450.
- Griffiths, D., Fenton, G. A., and Paice, G. (1996). "Reliability-Based Exit Gradient Design of Water Retaining Structures." *Uncertainty in the Geologic Environment: from Theory to Practice*, ASCE, 518-534.

- Griffiths, D. V. (1984). "Rationalized charts for the method of fragments applied to confined seepage." *Geotechnique*, 34(2), 229-238.
- Griffiths, D. V. (1994). "Seepage beneath unsymmetric cofferdams." *Geotechnique*, 44(2), 297-305.
- Griffiths, D. V., and Li, C. O. (1986). "Finite element assesement of the method of fragments for problems of confined seepage." *VI International conference on Finite elements in water resources* Portugal.
- Harr, M. E. (1962). *Groundwater and seepage*, McGraw-Hill, New York.
- Harr, M. E. (1977). *Mechanics of particulate media*, McGraw-Hill, New York.
- Harr, M. E., and Deen, R. C. (1961). "Analysis of seepage problems." *Journal of the Soil Mechanics and Foundations Division*, 87(5), 91-110.
- Harza, L. (1935). "Uplift and seepage under dams on sand." *Trans. ASCE*, 100(1), 1352-1385.
- Hassanizadeh, S. M., and Gray, W. G. (1987). "High velocity flow in porous media." *Transp. Porous Media*, 2(6), 521-531.
- Hatanaka, M., Uchida, A., and Takehara, N. (1997). "Permeability characteristics of high-quality undisturbed sands measured in a triaxial cell." *Soils Found.*, 37(3), 129-135.
- Hatanaka, M., Uchida, A., Taya, Y., Takehara, N., Hagsisawa, T., Sakou, N., and Ogawa, S. (2001). "Permeability characteristics of high-quality undisturbed gravelly soils measured in laboratory tests." *Soils Found.*, 41(3), 45-55.
- Hazen, A. (1930). *Water supply*, Wiley, New York.
- Holtz, R. D., and Kovacs, W. D. (1981). *An introduction to geotechnical engineering*, prentice-Hall, Inc., Englewood Cliffs, , New Jersey, USA.
- Kadlec, R., and Knight, R. (1996). *Treatment wetlands*, CRC Press, London.
- Kaiser, P., and Hewitt, K. (1982). "The effect of groundwater flow on the stability and design of retained excavations." *Can. Geotech. J.*, 19(2), 139-153.

- Kavvadas, M., Giolas, A., and Papacharalambous, G. (1992). "Drainage of supported excavations." *Geotechnical & Geological Engineering*, 10(2), 141-157.
- King, G., and Cockroft, J. (1972). "The geometric design of long cofferdams." *Geotechnique*, 22(4), 619-633.
- Koltuk, S., and Azzam, R. (2016). "Design Charts for Circular-Shaped Sheeted Excavation Pits against Seepage Failure by Heave." *Periodica Polytechnica Civil Engineering*, 60(3), 421-426.
- Koltuk, S., Fernandez-Steeger, T. M., and Azzam, R. (2015). "A numerical study on the seepage failure by heave in sheeted excavation pits." *Geomechanics and Engineering*, 9(4), 513-530.
- Koltuk, S., and Iyisan, R. (2013). "Numerical analysis of groundwater flow through a rectangular cofferdam." *Electronic Journal of Geotechnical Engineering (EJGE)*, 18.
- Kovacs, G. (1981). *Seepage hydraulics*, Elsevier Scientific Publishing Company, Amsterdam.
- Kozeny, J. (1927). "Uber die kapillare Leitung des Wassers im Boden " *Wien Akad. Wiss*, 136 (2a), 271.
- Lane, E. W. (1935). "Security from under-seepage-masonry dams on earth foundations." *Trans. ASCE*, 60(4), 929-966.
- Lefas, I., and Georgiannou, V. (2001). "Analysis of a cofferdam support and design implications." *Computers & Structures*, 79(26), 2461-2469.
- Li, Z., Wan, J., Huang, K., Chang, W., and He, Y. (2017). "Effects of particle diameter on flow characteristics in sand columns." *International Journal of Heat and Mass Transfer*, 104, 533-536.
- Lindquist, E. (1933). "On the flow of water through porous soil." *Premier Congres des grands barrages (Stockholm)*Stockj olm, 81-101.

- Ma, H., and Ruth, D. (1993). "The microscopic analysis of high Forchheimer number flow in porous media." *Transp. Porous Media*, 13(2), 139-160.
- Macdonald, I., El-Sayed, M., Mow, K., and Dullien, F. (1979). "Flow through porous media—the Ergun equation revisited." *Industrial & Engineering Chemistry Fundamentals*, 18(3), 199-208.
- Marsland, A. (1953). "Model experiments to study the influence of seepage on the stability of a sheeted excavation in sand." *Geotechnique*, 3(6), 223-241.
- McNamee, J. (1949). "Seepage into a Sheeted Excavation." *Geotechnique*, 1(4), 229-241.
- Merry, S., and Du, R. (2014). "Plane Strain versus Axisymmetric Modeling of Convex Levees." *J. Geotech. Geoenviron. Eng.*, 141(4), 04014121.
- Miura, K., Supachawarote, C., and Ikeda, K. (2000). "Estimation of 3D seepage force inside cofferdam regarding boiling type of failure." *Geotech—Year 2000* Bangkok, Thailand, 371-380.
- Moutsopoulos, K. N., Papaspyros, I. N., and Tsihrintzis, V. A. (2009). "Experimental investigation of inertial flow processes in porous media." *Journal of hydrology*, 374(3-4), 242-254.
- Muskat, M. (1938). "The flow of homogeneous fluids through porous media." *Soil Science*, 46(2), 169.
- Muskat, M., and Wyckoff, R. D. (1937). *Flow of homogeneous fluids through porous media*, McGraw-Hill, New York.
- Neveu, G. (1972). "Axisymmetrical seepage flow through a circular sheet pile cofferdam." M.Eng. thesis, McGill Univ., Montreal.
- Parashar, S., Mitchell, R., Hee, M. W., Sanmugathan, D., and Nicholson, G. (2007). "Performance monitoring of deep shafts at Changi WRP project, Singapore." *7th FMGM 2007: Field Measurements in Geomechanics*, 1-12.

- Pavlovsky, N. (1922). *The theory of movement of ground water under hydraulic structures and its main applications*, Pertograd, USSR.
- Pavlovsky, N. N. (1956). *Collected Works*, Doklady Akademii Nauk USSR, Leningrad, USSR.
- Polubarinova-Kochina, P. Y. (1962). *Theory of Groundwater Movement, translated from Russian by JM Roger de Wiest, Princeton U.*
- Powers, J. P. (1992). *Construction dewatering: new methods and applications*, John Wiley & Sons.
- Rao, S. (1999). *The Finite Element Method in Engineering*, Butterworths-Heinemann, Boston.
- Reddi, L. N. (2003). *Seepage in soils: principles and applications*, John Wiley & Sons, New Jersey.
- Reynolds, O. (1883). "XXIX. An experimental investigation of the circumstances which determine whether the motion of water shall be direct or sinuous, and of the law of resistance in parallel channels." *Philosophical Transactions of the Royal Society of London*, 174, 935-982.
- Rott, N. (1990). "Note on the history of the Reynolds number." *Annual review of fluid mechanics*, 22(1), 1-12.
- RS2 V9.011 [Computer software]. Rocscience, Toronto.
- RS3 2.0 [Computer software]. Rocscience, Toronto.
- Salahi, M.-B., Sedghi-Asl, M., and Parvizi, M. (2015). "Nonlinear flow through a packed-column experiment." *Journal of Hydrologic Engineering*, 20(9), 04015003.
- Scheidegger, A. (1958). *The physics of flow through porous media*, University Of Toronto Press: London.
- Schneebeli, G. (1955). "Expériences sur la limite de validité de la loi de Darcy et l'apparition de la turbulence dans un écoulement de filtration." *La Houille Blanche*(2), 141-149.

- 
- Sedghi-Asl, M., Rahimi, H., and Salehi, R. (2014). "Non-Darcy flow of water through a packed column test." *Transp. Porous Media*, 101(2), 215-227.
- Seelheim, F. (1880). "Methoden zur Bestimmung der Durchlässigkeit des Bodens." *Zeitschrift für analytische Chemie*, 19(1), 387-418.
- Seguin, D., Montillet, A., Comiti, J., and Huet, F. (1998). "Experimental characterization of flow regimes in various porous media—II: Transition to turbulent regime." *Chemical engineering science*, 53(22), 3897-3909.
- Sidiropoulou, M. G., Moutsopoulos, K. N., and Tsihrintzis, V. A. (2007). "Determination of Forchheimer equation coefficients a and b." *Hydrological Processes: An International Journal*, 21(4), 534-554.
- Sivakugan, N., and Alaghbari, M. Y. S. (1993). "Method of fragments - quick solutions to seepage problems." *Proc., Environmental Management : Geo-Water and Engineering Aspects*, A A Balkema, Amsterdam, Netherlands, Amsterdam, Netherlands, 491-496.
- Sivakugan, N., and Das, B. M. (2009). *Geotechnical engineering: a practical problem solving approach*, J. Ross Publishing, Fort Lauderdale.
- Sivakugan, N., and Rankine, K. (2012). "Three-Dimensional Method of Fragments to Study Drainage through Hydraulic Fill Stopes." *Int. J. Geomech.*, 12(5), 612-615.
- Sivakugan, N., Rankine, K., Lovisa, J., and Hall, W. (2013). "Flow rate computations in hydraulic fill mine stopes." *Indian Geotechnical Journal*, 43(3), 195-202.
- Sommerfeld, A. (1908). "Ein beitrag zur hydrodynamischen erkläerung der turbulenten fluessigkeitsbewegungen." *Atti del*, 4, 116-124.
- Soubra, A.-H., Kastner, R., and Benmansour, A. (1999). "Passive earth pressures in the presence of hydraulic gradients." *Géotechnique, The Institution of Civil Engineers*, 49(3), 319-330.

- Stokes, G. G. (1851). *On the effect of the internal friction of fluids on the motion of pendulums*, Pitt Press, Cambridge.
- Tan, Y., and Wang, D. (2015). "Structural behaviors of large underground earth-retaining systems in Shanghai. I: Unpropped circular diaphragm wall." *Journal of Performance of Constructed Facilities*, 29(2), 04014058.
- Tanaka, T. (2003). "Blow-out of soil particles during construction of a caisson type pile." *Proc., Proceedings of the International Symposium on Groundwater Problems related to Geo-Environment*, Okayama.
- Tanaka, T., Hayashi, K., and Yamada, M. (2000). "Seepage failure of soil in an axisymmetric condition." *Proceedings of the Geotech-Year 2000, Developments in Geotechnical Engineering*, 27-30.
- Tanaka, T., Hori, H., and Inoue, K. (2002). "Boiling occurred within a braced cofferdam due to two dimensionally concentrated seepage flow." *Proc., 3rd international symposium, geotechnical aspects of underground construction in soft ground*, 33-38.
- Tanaka, T., Kusumi, S., and Inoue, K. (2013). "Effects of plane shapes of a cofferdam on 3D seepage failure stability and axisymmetric approximation." *Proc., Proceedings of the 18th International Conference on Soil Mechanics and Geotechnical Engineering*, 02-05.
- Tanaka, T., Toyokuni, E., and Ozaki, E. (1994). "A case study on piping during excavation for bridge abutments." *International Symposium on Underground Construction in Soft Ground*, A. A. Balkema, Rotterdam, , New Delhi, India, pp. 159-162.
- Tanaka, T., and Yokoyama, T. (2005) "Effects of jet grouting under sheet piles on seepage failure stability of soil." *Proc., Procs. of the 5th International Symposium on Geotechnical Aspects of Underground Construction in Soft Ground (IS-Amsterdam 2005)*, 923-929.

- Terzaghi, K. (1943). *Theoretical soil mechanics*, Wiley.
- Terzaghi, K., Peck, R. B., and Mesri, G. (1996). *Soil mechanics in engineering practice*, John Wiley & Sons, New York.
- Underwood, C. A., and Weber, B. A. (2011). "The Use of Reliability Analyses in the Design of Deep Excavations in Soft Clay, Fargo, North Dakota, USA." *Geo-Frontiers 2011: Advances in Geotechnical Engineering*, 3321-3331.
- U.S. Department of Army, Engineer Manual (1989). *Design of sheet pile cellular structures*, US Government Printing Office, Washington, DC.
- U.S. Department of Navy, Naval Facilities Engineering Command (1974). *Design manual: Soil mechanics, foundations, and earth structures*. NAVFAC, US Government Printing Office, Washington, DC.
- U.S. Department of Navy, Naval Facilities Engineering Command (1982). *Soil mechanics*, NAVFAC DM-7.1, US Government Printing Office, Washington, DC.
- Van Lopik, J. H., Snoeijers, R., van Dooren, T. C., Raof, A., and Schotting, R. J. (2017). "The effect of grain size distribution on nonlinear flow behavior in sandy porous media." *Transp. Porous Media*, 120(1), 37-66.
- Venkataraman, P., and Rao, P. R. M. (1998). "Darcian, transitional, and turbulent flow through porous media." *Journal of hydraulic engineering*, 124(8), 840-846.
- Verruijt, A. (1970). *Theory of Groundwater Flow*, Macmillan and Co Ltd, London.
- Ward, J. (1964). "Turbulent flow in porous media." *Journal of the Hydraulics Division*, 90(5), 1-12.
- Witt, K. J., and Brauns, J. (1983). "Permeability-anisotropy due to particle-shape." *J. Geotech. Eng.-ASCE*, 109(9), 1181-1187.

## Appendix A1

### Comparison of Griffiths (1984) fragment $C$ form factor values with the derived values in this desertion

**Table A1.1** Griffiths (1984) fragment  $C$  form factor  $\Phi_C$  values

$s_C/T_C$	$LR/T_C$										
	0.10	0.15	0.20	0.25	0.30	0.35	0.40	0.50	0.60	0.80	1.00
0.1	1.450	1.090	0.920	0.830	0.760	0.700	0.660	0.610	0.570	0.530	0.510
0.2	2.460	1.760	1.430	1.240	1.100	1.000	0.930	0.830	0.760	0.690	0.650
0.3	3.460	2.430	1.930	1.630	1.430	1.290	1.180	1.040	0.940	0.840	0.790
0.4	4.440	3.100	2.430	2.030	1.780	1.580	1.440	1.250	1.140	0.990	0.920
0.5		3.760	2.940	2.440	2.100	1.870	1.690	1.470	1.320	1.160	1.070
0.6		4.440	3.440	2.830	2.450	2.170	1.960	1.690	1.520	1.340	1.240
0.7			3.950	3.240	2.790	2.470	2.230	1.920	1.744	1.530	1.440
0.8			4.440	3.670	3.180	2.820	2.570	2.230	2.030	1.800	1.710
0.9				4.200	3.650	3.300	3.000	2.680	2.500	2.230	2.120

**Table A1.2** Developed fragment  $C$  form factors  $\Phi_C$  values using finite element simulations

$s_C/T_C$	$LR/T_C$										
	0.10	0.15	0.20	0.25	0.30	0.35	0.40	0.50	0.60	0.80	1.00
0.1	1.424	1.095	0.929	0.828	0.758	0.708	0.669	0.613	0.576	0.532	0.509
0.2	2.425	1.764	1.433	1.234	1.101	1.006	0.935	0.835	0.770	0.695	0.658
0.3	3.425	2.430	1.933	1.635	1.436	1.295	1.189	1.044	0.951	0.846	0.795
0.4	4.425	3.097	2.433	2.035	1.771	1.583	1.443	1.252	1.132	0.997	0.932
0.5	5.426	3.764	2.933	2.436	2.106	1.873	1.700	1.466	1.319	1.157	1.080
0.6	6.427	4.431	3.435	2.839	2.446	2.169	1.965	1.691	1.521	1.335	1.247
0.7	7.427	5.099	3.940	3.250	2.797	2.481	2.250	1.942	1.752	1.546	1.448
0.8	8.428	5.774	4.461	3.689	3.185	2.837	2.584	2.249	2.044	1.823	1.719
0.9	9.452	6.513	5.079	4.243	3.705	3.336	3.068	2.716	2.502	2.271	2.163

## Appendix A2

### Comparison of Griffiths (1984) fragment $C$ normalised exit hydraulic gradient values with the derived values in this desertion

**Table A2.1** Griffiths (1984) fragment  $C$  normalised exit hydraulic gradient  $i_{Es_C}/h_C$  values

$s_C/T_C$	$LR/T_C$										
	0.10	0.15	0.20	0.25	0.30	0.35	0.40	0.50	0.60	0.80	1.00
0.1	0.733	0.695	0.675	0.665	0.660	0.655	0.654	0.650	0.647	0.645	0.644
0.2	0.826	0.766	0.728	0.704	0.687	0.677	0.669	0.660	0.652	0.644	0.642
0.3	0.876	0.823	0.782	0.748	0.725	0.709	0.692	0.676	0.663	0.647	0.639
0.4	0.904	0.860	0.824	0.790	0.764	0.742	0.723	0.696	0.678	0.650	0.636
0.5	0.923	0.885	0.853	0.823	0.795	0.771	0.750	0.716	0.690	0.651	0.630
0.6	0.937	0.902	0.873	0.847	0.818	0.793	0.770	0.730	0.695	0.646	0.617
0.7	0.946	0.917	0.888	0.861	0.833	0.807	0.780	0.734	0.690	0.632	0.597
0.8	0.952	0.925	0.896	0.869	0.839	0.808	0.774	0.720	0.671	0.602	0.561
0.9	0.954	0.923	0.887	0.850	0.810	0.772	0.735	0.670	0.612	0.535	0.493

**Table A2.2** Developed fragment  $C$  normalised exit hydraulic gradient  $i_{Es_C}/h_C$  values using finite element simulations

$s_C/T_C$	$LR/T_C$										
	0.10	0.15	0.20	0.25	0.30	0.35	0.40	0.50	0.60	0.80	1.00
0.1	0.732	0.694	0.674	0.667	0.661	0.655	0.656	0.653	0.649	0.647	0.646
0.2	0.826	0.768	0.729	0.705	0.689	0.678	0.670	0.660	0.653	0.645	0.642
0.3	0.876	0.824	0.783	0.751	0.728	0.710	0.696	0.677	0.664	0.647	0.639
0.4	0.904	0.861	0.823	0.791	0.765	0.743	0.725	0.697	0.676	0.650	0.634
0.5	0.921	0.885	0.852	0.822	0.795	0.772	0.751	0.715	0.688	0.650	0.628
0.6	0.934	0.902	0.873	0.846	0.819	0.794	0.771	0.729	0.694	0.645	0.616
0.7	0.943	0.915	0.889	0.862	0.835	0.808	0.782	0.733	0.691	0.631	0.596
0.8	0.949	0.924	0.897	0.868	0.838	0.807	0.776	0.719	0.671	0.600	0.559
0.9	0.952	0.921	0.886	0.849	0.810	0.771	0.735	0.668	0.613	0.537	0.494

## Appendix A3

### Comparison of Griffiths (1984) fragment A form factor values with the derived values in this desertion

**Table A3.1** Griffiths (1984) fragment A form factor  $\Phi_A$  values when  $b = 0$

$s/T$	$\Phi_A$
0.1	0.480
0.2	0.610
0.3	0.710
0.4	0.840
0.5	0.990
0.6	1.150
0.7	1.350
0.8	1.620
0.9	2.050

**Table A3.2** Derived fragment C form factor  $\Phi_C$  values when  $L = 2T_C$  using finite element simulations

$s/T$	$\Phi_C$
0.1	0.483
0.2	0.618
0.3	0.741
0.4	0.866
0.5	1.000
0.6	1.154
0.7	1.349
0.8	1.612
0.9	2.050

## Appendix B1

### Developed axisymmetric form factor values of fragment $D$

**Table B1.1** Developed fragment  $D$  form factors  $\beta_D$  values using finite element simulations

$s_D/T_D$	$rR/T_D$													
	0.10	0.15	0.20	0.25	0.30	0.35	0.40	0.50	0.60	0.70	0.80	1.00	2.00	$\infty$
0.1	2.462	1.811	1.482	1.284	1.151	1.056	0.982	0.878	0.805	0.752	0.712	0.652	0.549	0.482
0.2	4.462	3.140	2.482	2.089	1.825	1.636	1.494	1.295	1.159	1.065	0.993	0.895	0.721	0.618
0.3	6.465	4.473	3.482	2.888	2.490	2.209	1.996	1.699	1.501	1.361	1.257	1.115	0.876	0.740
0.4	8.459	5.806	4.488	3.688	3.158	2.780	2.496	2.101	1.839	1.654	1.518	1.336	1.031	0.864
0.5	10.459	7.145	5.482	4.488	3.826	3.352	2.998	2.504	2.180	1.951	1.784	1.561	1.196	0.999
0.6	12.457	8.476	6.482	5.288	4.492	3.925	3.501	2.913	2.527	2.257	2.063	1.803	1.380	1.155
0.7	14.452	9.807	7.482	6.089	5.163	4.504	4.011	3.335	2.893	2.587	2.366	2.074	1.599	1.347
0.8	16.448	11.130	8.488	6.900	5.849	5.109	4.556	3.798	3.307	2.969	2.727	2.405	1.888	1.610
0.9	18.460	12.499	9.540	7.783	6.627	5.813	5.214	4.383	3.868	3.508	3.246	2.902	2.348	2.045

## Appendix B2

### Developed axisymmetric form factor values of fragment $E$

**Table B2.1** Developed fragment  $E$  form factors  $\beta_E$  values using finite element simulations

$s/T$	$rR/T$													
	0.10	0.15	0.20	0.25	0.30	0.35	0.40	0.50	0.60	0.70	0.80	1.00	2.00	$\infty$
0.1	0.192	0.232	0.262	0.285	0.303	0.317	0.329	0.349	0.364	0.376	0.385	0.400	0.436	0.482
0.2	0.226	0.276	0.314	0.343	0.367	0.385	0.402	0.429	0.449	0.466	0.479	0.500	0.548	0.618
0.3	0.260	0.319	0.364	0.399	0.427	0.450	0.470	0.502	0.528	0.548	0.564	0.590	0.652	0.740
0.4	0.298	0.367	0.418	0.459	0.492	0.518	0.542	0.580	0.610	0.633	0.653	0.683	0.757	0.864
0.5	0.346	0.424	0.483	0.530	0.568	0.598	0.626	0.670	0.704	0.731	0.754	0.789	0.875	0.999
0.6	0.407	0.497	0.565	0.619	0.662	0.697	0.728	0.779	0.818	0.849	0.875	0.915	1.013	1.155
0.7	0.494	0.599	0.677	0.739	0.790	0.829	0.865	0.922	0.966	1.002	1.031	1.077	1.188	1.347
0.8	0.630	0.756	0.849	0.921	0.979	1.026	1.066	1.132	1.183	1.223	1.256	1.307	1.432	1.610
0.9	0.905	1.063	1.175	1.262	1.331	1.387	1.434	1.510	1.568	1.615	1.652	1.710	1.841	2.045

## Appendix B3

### Developed normalised exit gradient values of fragment $D$

**Table B3.1** Developed fragment  $D$  normalised exit gradient  $i_{E s_D}/h_D$  values using finite element simulations

$s_D/T_D$	$i_{E s_D}/h_D$													
	0.10	0.15	0.20	0.25	0.30	0.35	0.40	0.50	0.60	0.70	0.80	1.00	2.00	$\infty$
0.1	0.823	0.775	0.746	0.728	0.715	0.706	0.700	0.688	0.684	0.679	0.675	0.676	0.660	0.651
0.2	0.897	0.853	0.817	0.789	0.768	0.753	0.740	0.721	0.711	0.699	0.693	0.681	0.658	0.640
0.3	0.928	0.894	0.863	0.836	0.814	0.794	0.779	0.754	0.737	0.723	0.712	0.696	0.660	0.631
0.4	0.946	0.919	0.892	0.869	0.847	0.828	0.812	0.784	0.763	0.745	0.731	0.708	0.658	0.620
0.5	0.956	0.933	0.912	0.892	0.872	0.854	0.838	0.810	0.785	0.765	0.747	0.719	0.653	0.605
0.6	0.963	0.944	0.926	0.908	0.891	0.874	0.858	0.829	0.803	0.779	0.758	0.723	0.642	0.584
0.7	0.969	0.952	0.935	0.920	0.904	0.888	0.873	0.842	0.813	0.786	0.761	0.719	0.622	0.555
0.8	0.973	0.958	0.942	0.927	0.912	0.895	0.878	0.844	0.810	0.779	0.749	0.701	0.588	0.514
0.9	0.975	0.960	0.943	0.925	0.905	0.885	0.863	0.822	0.779	0.740	0.706	0.650	0.525	0.446

## Appendix B4

### Laboratory simulation results of circular cofferdam

**Table B4.1** Laboratory simulation results of circular cofferdam

r (mm)	$rR/T$	$s/T$	$\alpha$	$h$ (mm)	Flow rate (m <sup>3</sup> /s)			
					Trial 1	Trial 2	Trial 3	Average
97	0.80	0.20	0.50	57.0	3.03E-06	3.01E-06	3.01E-06	3.02E-06
97	0.60	0.40	0.00	57.0	1.84E-06	1.87E-06	1.86E-06	1.86E-06
97	0.60	0.40	0.00	107.0	4.06E-06	4.09E-06	4.11E-06	4.09E-06
97	0.40	0.60	0.25	57.0	1.50E-06	1.47E-06	1.50E-06	1.49E-06
97	0.40	0.60	0.25	107.0	2.88E-06	2.87E-06	2.87E-06	2.88E-06
97	0.40	0.60	0.00	57.0	1.36E-06	1.36E-06	1.34E-06	1.35E-06
97	0.40	0.60	0.00	107.0	2.54E-06	2.51E-06	2.52E-06	2.52E-06
97	0.30	0.70	0.25	57.0	1.07E-06	1.04E-06	1.07E-06	1.06E-06
97	0.30	0.70	0.25	107.0	2.04E-06	2.04E-06	2.04E-06	2.04E-06
97	0.20	0.80	0.25	57.0	7.72E-07	8.00E-07	7.82E-07	7.85E-07
97	0.20	0.80	0.00	57.0	6.05E-07	5.90E-07	5.95E-07	5.97E-07
50	0.60	0.40	0.00	54.0	8.62E-07	8.60E-07	8.65E-07	8.63E-07
50	0.40	0.60	0.00	54.0	5.92E-07	5.86E-07	5.85E-07	5.88E-07
50	0.30	0.70	0.00	54.0	4.38E-07	4.26E-07	4.21E-07	4.28E-07
50	0.20	0.80	0.25	54.0	3.95E-07	3.89E-07	3.78E-07	3.87E-07
50	0.20	0.80	0.00	54.0	3.38E-07	3.36E-07	3.31E-07	3.35E-07

## Appendix C1

### $i_E/h$ values of double-walled cofferdams

**Table C1.1** Normalised exit hydraulic gradient  $i_E/h$  of double-walled cofferdams

Creep length $C$ (m)	$i_E/h$ ( $m^{-1}$ )						
	$LR/T = 0.10$	$LR/T = 0.15$	$LR/T = 0.20$	$LR/T = 0.25$	$LR/T = 0.30$	$LR/T = 0.35$	$LR/T = 0.40$
4.0	0.234	0.205	0.190	0.181	0.174	0.169	0.166
3.6	0.264	0.234	0.219	0.210	0.203	0.197	0.194
3.2	0.310	0.278	0.263	0.254	0.246	0.240	0.236
2.8	0.388	0.354	0.339	0.331	0.323	0.315	0.311
2.4	0.573	0.533	0.514	0.512	0.489	0.487	0.482
8.0	0.149	0.130	0.117	0.108	0.102	0.097	0.094
7.2	0.170	0.147	0.133	0.123	0.117	0.112	0.108
6.4	0.199	0.172	0.156	0.146	0.140	0.135	0.131
5.6	0.246	0.215	0.199	0.188	0.181	0.176	0.172
4.8	0.372	0.325	0.305	0.293	0.284	0.286	0.284
12.0	0.112	0.099	0.089	0.082	0.076	0.072	0.068
10.8	0.129	0.112	0.101	0.092	0.086	0.082	0.078
9.6	0.153	0.131	0.117	0.108	0.102	0.097	0.093
8.4	0.189	0.162	0.146	0.137	0.130	0.125	0.121
7.2	0.269	0.237	0.219	0.208	0.201	0.195	0.192
16.0	0.090	0.080	0.073	0.067	0.062	0.058	0.055
14.4	0.105	0.092	0.083	0.076	0.070	0.066	0.062
12.8	0.126	0.108	0.097	0.088	0.082	0.077	0.073
11.2	0.158	0.134	0.119	0.109	0.102	0.097	0.094
9.6	0.223	0.191	0.176	0.163	0.156	0.151	0.146
20.0	0.075	0.067	0.062	0.057	0.053	0.049	0.046
18.0	0.088	0.078	0.070	0.064	0.059	0.055	0.052
16.0	0.106	0.093	0.082	0.075	0.069	0.064	0.061
14.0	0.135	0.115	0.101	0.092	0.085	0.080	0.077
12.0	0.191	0.161	0.146	0.134	0.127	0.122	0.118
24.0	0.064	0.058	0.053	0.049	0.045	0.042	0.040
21.6	0.076	0.067	0.061	0.056	0.051	0.048	0.044
19.2	0.092	0.081	0.072	0.065	0.059	0.055	0.051
16.8	0.119	0.100	0.088	0.079	0.073	0.068	0.064
14.4	0.169	0.140	0.124	0.113	0.106	0.102	0.098
28.0	0.056	0.051	0.046	0.043	0.040	0.037	0.034
25.2	0.066	0.059	0.053	0.049	0.045	0.041	0.038
22.4	0.081	0.071	0.063	0.057	0.051	0.047	0.044
19.6	0.105	0.088	0.077	0.069	0.062	0.058	0.054
16.8	0.150	0.122	0.107	0.097	0.090	0.086	0.083
32.0	0.049	0.044	0.041	0.037	0.034	0.032	0.029
28.8	0.058	0.052	0.047	0.042	0.038	0.035	0.033
25.6	0.072	0.062	0.055	0.049	0.044	0.040	0.037
22.4	0.093	0.078	0.067	0.059	0.053	0.049	0.046
19.2	0.132	0.106	0.091	0.082	0.076	0.073	0.070
36.0	0.043	0.038	0.034	0.031	0.028	0.026	0.024
32.4	0.051	0.044	0.039	0.035	0.031	0.029	0.026
28.8	0.062	0.053	0.046	0.040	0.036	0.032	0.030
25.2	0.080	0.065	0.055	0.048	0.042	0.039	0.036
21.6	0.112	0.087	0.074	0.066	0.062	0.060	0.058

Creep length $C$ (m)	$i_E/h$ (m <sup>-1</sup> )						
	$LR/T = 0.50$	$LR/T = 0.60$	$LR/T = 0.70$	$LR/T = 0.80$	$LR/T = 1.00$	$LR/T = 1.50$	$LR/T = \infty$
4.0	0.160	0.157	0.155	0.154	0.151	0.149	0.149
3.6	0.188	0.185	0.183	0.182	0.179	0.177	0.177
3.2	0.231	0.228	0.225	0.224	0.221	0.220	0.219
2.8	0.305	0.303	0.298	0.299	0.295	0.293	0.293
2.4	0.478	0.469	0.464	0.473	0.462	0.458	0.468
8.0	0.088	0.085	0.082	0.081	0.078	0.077	0.076
7.2	0.103	0.100	0.097	0.095	0.093	0.091	0.091
6.4	0.126	0.122	0.120	0.118	0.116	0.114	0.114
5.6	0.167	0.163	0.160	0.159	0.157	0.156	0.155
4.8	0.268	0.269	0.269	0.259	0.258	0.257	0.257
12.0	0.063	0.060	0.057	0.055	0.053	0.051	0.051
10.8	0.073	0.069	0.067	0.065	0.063	0.061	0.061
9.6	0.088	0.084	0.082	0.080	0.078	0.077	0.076
8.4	0.115	0.112	0.109	0.108	0.106	0.105	0.105
7.2	0.185	0.181	0.178	0.177	0.177	0.175	0.174
16.0	0.050	0.047	0.044	0.042	0.040	0.038	0.038
14.4	0.057	0.053	0.051	0.049	0.047	0.046	0.045
12.8	0.068	0.065	0.062	0.061	0.059	0.057	0.057
11.2	0.088	0.085	0.083	0.082	0.080	0.079	0.079
9.6	0.141	0.138	0.136	0.135	0.133	0.132	0.133
20.0	0.042	0.038	0.036	0.034	0.032	0.030	0.029
18.0	0.047	0.044	0.041	0.040	0.038	0.036	0.036
16.0	0.056	0.052	0.050	0.048	0.047	0.046	0.045
14.0	0.072	0.068	0.066	0.065	0.064	0.063	0.063
12.0	0.114	0.111	0.109	0.108	0.107	0.107	0.107
24.0	0.035	0.032	0.030	0.028	0.026	0.024	0.024
21.6	0.040	0.036	0.034	0.033	0.031	0.029	0.029
19.2	0.047	0.043	0.041	0.040	0.038	0.037	0.037
16.8	0.059	0.056	0.055	0.054	0.053	0.052	0.052
14.4	0.094	0.092	0.091	0.090	0.090	0.089	0.089
28.0	0.030	0.027	0.025	0.024	0.022	0.020	0.019
25.2	0.034	0.031	0.029	0.027	0.025	0.024	0.024
22.4	0.039	0.036	0.034	0.033	0.032	0.031	0.031
19.6	0.050	0.047	0.046	0.045	0.044	0.044	0.044
16.8	0.080	0.078	0.077	0.077	0.077	0.076	0.076
32.0	0.026	0.023	0.021	0.019	0.018	0.016	0.016
28.8	0.028	0.026	0.024	0.022	0.021	0.020	0.019
25.6	0.033	0.030	0.028	0.027	0.026	0.026	0.025
22.4	0.042	0.039	0.038	0.038	0.037	0.037	0.037
19.2	0.068	0.067	0.067	0.067	0.066	0.066	0.066
36.0	0.021	0.018	0.016	0.015	0.014	0.012	0.012
32.4	0.023	0.020	0.018	0.017	0.016	0.015	0.015
28.8	0.026	0.024	0.022	0.021	0.021	0.020	0.020
25.2	0.033	0.031	0.031	0.030	0.030	0.030	0.030
21.6	0.057	0.057	0.057	0.057	0.057	0.057	0.056

## Appendix C2

### $i_E/h$ values of circular cofferdams

**Table C2.1** Normalised exit hydraulic gradient  $i_E/h$  of circular cofferdams

Creep length $C$ (m)	$i_E/h$ ( $m^{-1}$ )						
	$rR/T = 0.10$	$rR/T = 0.15$	$rR/T = 0.20$	$rR/T = 0.25$	$rR/T = 0.30$	$rR/T = 0.35$	$rR/T = 0.40$
4.0	0.320	0.283	0.260	0.245	0.232	0.223	0.216
3.6	0.371	0.327	0.300	0.283	0.269	0.258	0.250
3.2	0.444	0.390	0.360	0.340	0.324	0.311	0.302
2.8	0.567	0.498	0.462	0.439	0.420	0.403	0.391
2.4	0.843	0.744	0.691	0.668	0.624	0.610	0.594
8.0	0.193	0.175	0.161	0.151	0.143	0.136	0.130
7.2	0.228	0.204	0.187	0.174	0.165	0.157	0.151
6.4	0.279	0.247	0.225	0.210	0.198	0.189	0.182
5.6	0.365	0.320	0.291	0.271	0.256	0.245	0.236
4.8	0.576	0.490	0.445	0.416	0.395	0.389	0.378
12.0	0.138	0.128	0.120	0.113	0.107	0.102	0.098
10.8	0.166	0.152	0.141	0.132	0.124	0.118	0.113
9.6	0.207	0.186	0.171	0.159	0.149	0.142	0.136
8.4	0.277	0.244	0.221	0.205	0.193	0.183	0.175
7.2	0.432	0.374	0.338	0.314	0.297	0.283	0.273
16.0	0.108	0.102	0.096	0.091	0.087	0.083	0.079
14.4	0.131	0.122	0.114	0.107	0.101	0.096	0.092
12.8	0.166	0.151	0.140	0.130	0.122	0.116	0.110
11.2	0.226	0.200	0.183	0.169	0.158	0.149	0.142
9.6	0.361	0.311	0.283	0.258	0.242	0.230	0.219
20.0	0.089	0.084	0.080	0.076	0.073	0.070	0.067
18.0	0.108	0.101	0.096	0.090	0.086	0.081	0.078
16.0	0.138	0.127	0.118	0.110	0.104	0.098	0.093
14.0	0.191	0.171	0.156	0.144	0.135	0.127	0.120
12.0	0.309	0.268	0.242	0.221	0.206	0.194	0.184
24.0	0.075	0.072	0.069	0.066	0.063	0.060	0.058
21.6	0.092	0.087	0.082	0.078	0.074	0.070	0.067
19.2	0.118	0.110	0.102	0.096	0.090	0.085	0.081
16.8	0.165	0.149	0.136	0.126	0.117	0.110	0.104
14.4	0.273	0.236	0.211	0.193	0.179	0.167	0.158
28.0	0.065	0.063	0.060	0.057	0.055	0.053	0.050
25.2	0.080	0.076	0.072	0.068	0.065	0.062	0.059
22.4	0.103	0.096	0.090	0.085	0.079	0.075	0.071
19.6	0.145	0.132	0.121	0.111	0.103	0.096	0.091
16.8	0.244	0.211	0.188	0.170	0.157	0.146	0.137
32.0	0.058	0.055	0.053	0.050	0.048	0.046	0.044
28.8	0.071	0.067	0.063	0.060	0.057	0.054	0.051
25.6	0.091	0.085	0.080	0.074	0.070	0.065	0.061
22.4	0.129	0.117	0.107	0.098	0.090	0.083	0.078
19.2	0.219	0.189	0.166	0.149	0.135	0.125	0.117
36.0	0.051	0.049	0.046	0.044	0.041	0.039	0.037
32.4	0.063	0.059	0.055	0.052	0.048	0.045	0.043
28.8	0.081	0.075	0.069	0.063	0.059	0.054	0.050
25.2	0.114	0.102	0.092	0.083	0.075	0.068	0.063
21.6	0.193	0.162	0.140	0.123	0.110	0.101	0.094

Creep length $C$ (m)	$i_E/h$ (m <sup>-1</sup> )							
	$rR/T = 0.50$	$rR/T = 0.60$	$rR/T = 0.70$	$rR/T = 0.80$	$rR/T = 1.00$	$rR/T = 1.50$	$rR/T = 2.0$	$rR/T = \infty$
4.0	0.205	0.197	0.191	0.186	0.178	0.168	0.163	0.149
3.6	0.238	0.229	0.222	0.217	0.209	0.197	0.192	0.177
3.2	0.289	0.279	0.271	0.265	0.256	0.243	0.237	0.219
2.8	0.378	0.367	0.355	0.348	0.337	0.321	0.314	0.293
2.4	0.583	0.559	0.541	0.542	0.519	0.495	0.497	0.468
8.0	0.122	0.115	0.110	0.106	0.100	0.091	0.087	0.076
7.2	0.141	0.134	0.128	0.124	0.117	0.108	0.103	0.091
6.4	0.170	0.162	0.156	0.151	0.143	0.133	0.128	0.114
5.6	0.223	0.212	0.205	0.199	0.190	0.178	0.172	0.155
4.8	0.359	0.346	0.331	0.315	0.304	0.288	0.280	0.257
12.0	0.091	0.085	0.081	0.077	0.072	0.064	0.060	0.051
10.8	0.105	0.098	0.093	0.089	0.083	0.075	0.071	0.061
9.6	0.126	0.118	0.113	0.108	0.101	0.092	0.088	0.076
8.4	0.163	0.154	0.148	0.142	0.134	0.124	0.118	0.105
7.2	0.254	0.242	0.233	0.225	0.215	0.201	0.193	0.174
16.0	0.073	0.069	0.065	0.061	0.056	0.049	0.046	0.038
14.4	0.085	0.079	0.074	0.071	0.065	0.058	0.054	0.045
12.8	0.101	0.095	0.090	0.085	0.079	0.071	0.067	0.057
11.2	0.131	0.123	0.117	0.112	0.105	0.095	0.091	0.079
9.6	0.203	0.192	0.184	0.178	0.168	0.155	0.150	0.133
20.0	0.062	0.058	0.054	0.051	0.046	0.040	0.037	0.029
18.0	0.071	0.066	0.062	0.059	0.054	0.047	0.043	0.036
16.0	0.086	0.079	0.074	0.071	0.065	0.057	0.054	0.045
14.0	0.110	0.103	0.096	0.092	0.085	0.077	0.073	0.063
12.0	0.170	0.160	0.151	0.146	0.137	0.126	0.121	0.107
24.0	0.053	0.049	0.046	0.043	0.039	0.033	0.030	0.024
21.6	0.062	0.057	0.053	0.050	0.045	0.039	0.036	0.029
19.2	0.074	0.068	0.063	0.060	0.054	0.048	0.045	0.037
16.8	0.094	0.087	0.082	0.077	0.072	0.064	0.061	0.052
14.4	0.145	0.135	0.128	0.122	0.116	0.106	0.102	0.089
28.0	0.046	0.043	0.040	0.037	0.033	0.027	0.025	0.019
25.2	0.053	0.049	0.045	0.042	0.038	0.032	0.030	0.024
22.4	0.064	0.058	0.054	0.051	0.046	0.040	0.037	0.031
19.6	0.081	0.075	0.070	0.066	0.061	0.054	0.051	0.044
16.8	0.124	0.116	0.109	0.105	0.099	0.091	0.087	0.076
32.0	0.040	0.037	0.034	0.031	0.028	0.023	0.020	0.016
28.8	0.046	0.042	0.038	0.036	0.032	0.027	0.024	0.019
25.6	0.055	0.049	0.046	0.042	0.038	0.033	0.031	0.025
22.4	0.069	0.063	0.058	0.055	0.051	0.045	0.043	0.037
19.2	0.106	0.098	0.093	0.089	0.084	0.078	0.075	0.066
36.0	0.033	0.030	0.027	0.025	0.022	0.018	0.016	0.012
32.4	0.038	0.034	0.031	0.028	0.025	0.021	0.019	0.015
28.8	0.044	0.040	0.036	0.033	0.030	0.026	0.024	0.020
25.2	0.055	0.050	0.046	0.044	0.040	0.036	0.035	0.030
21.6	0.086	0.080	0.076	0.074	0.070	0.065	0.063	0.056

## Appendix D1

### Relation of double-walled cofferdam flow rate to the rectangular flow rate

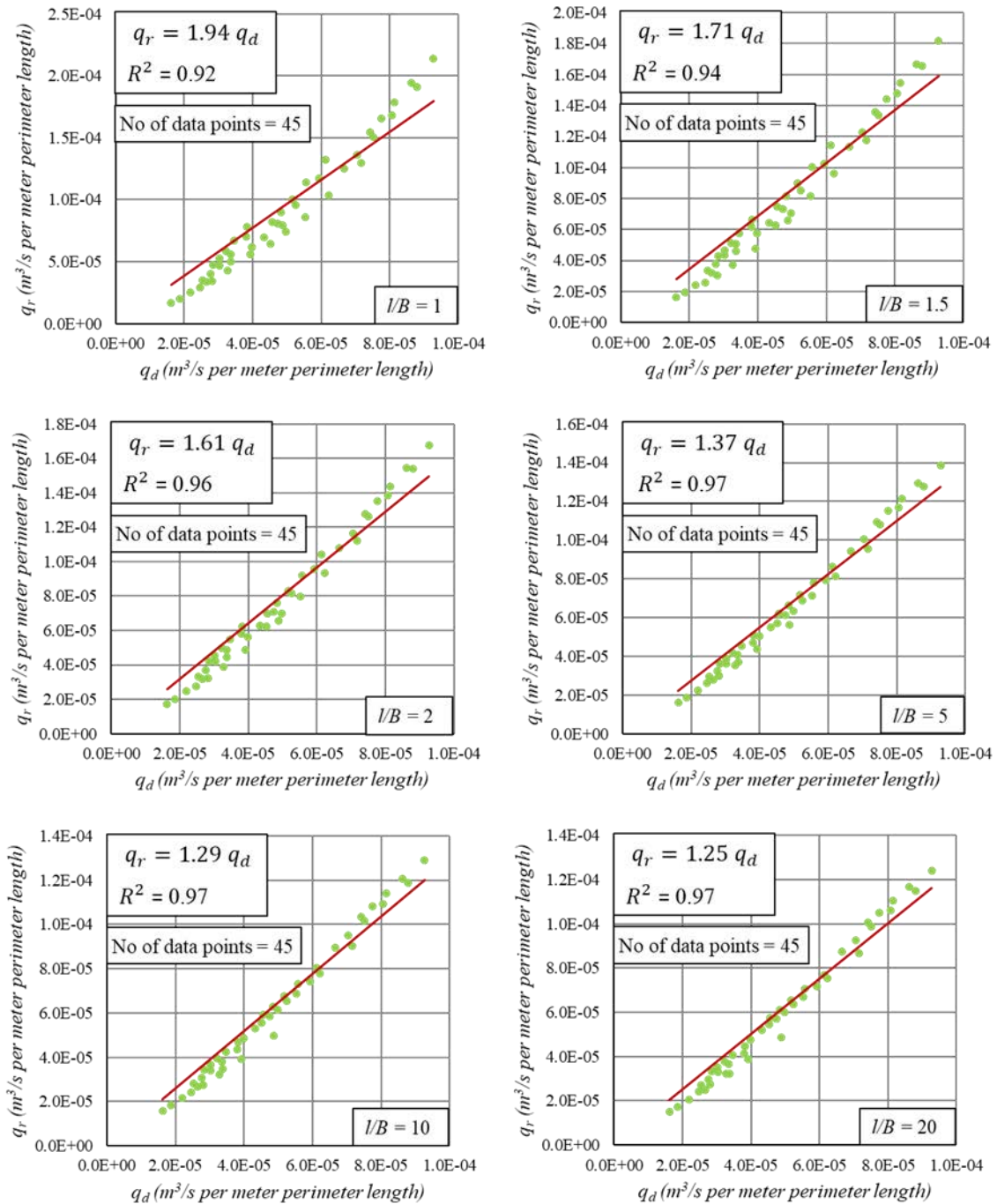


**Fig. D1.1** Relationship between double-walled flow rate to the 3D flow rate into rectangular cofferdam

Appendix D2

Relation of double-walled cofferdam  $i_E$  to the  $i_{EL}$  of rectangular cofferdams

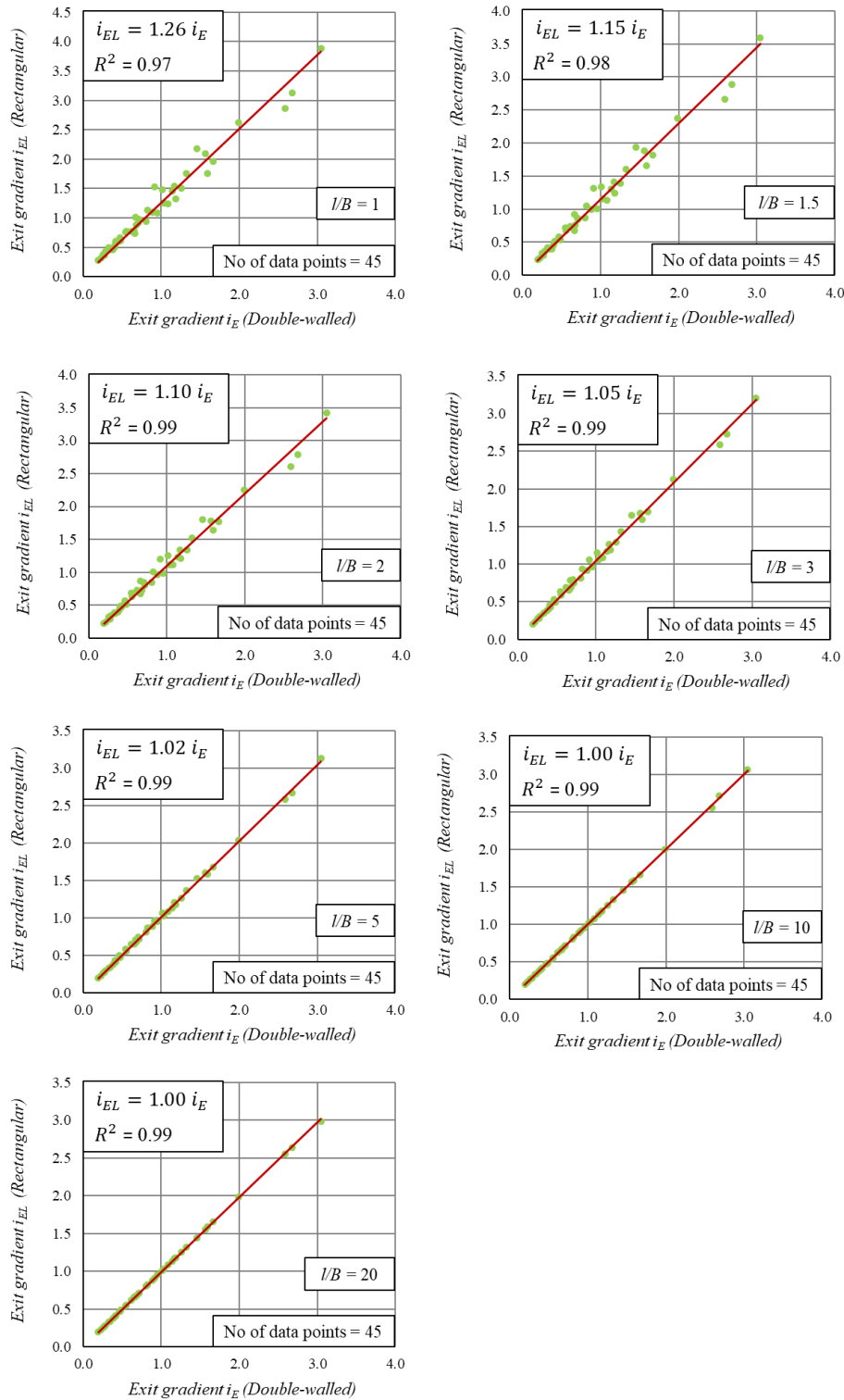
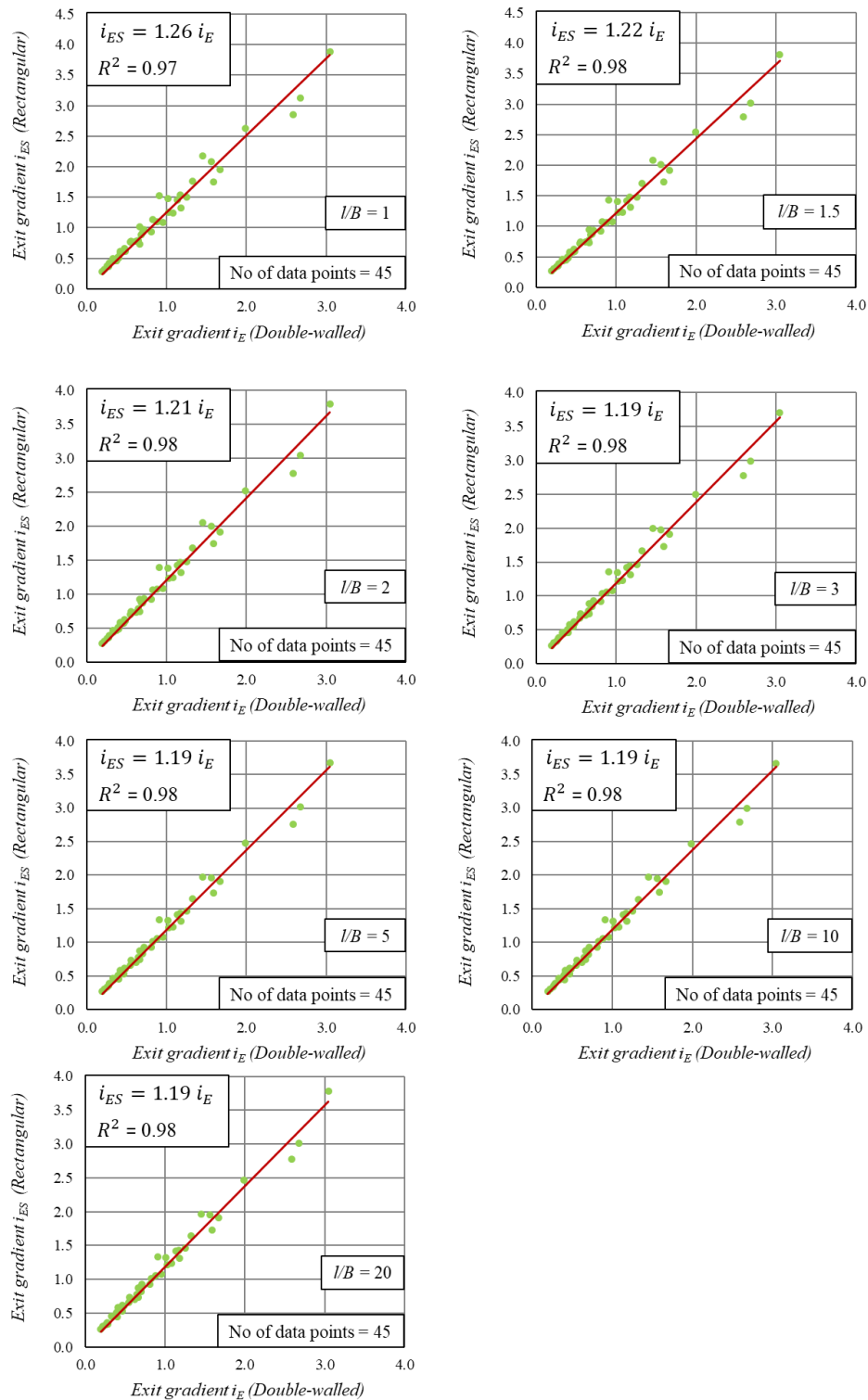


Fig. D2.1 Relationship between double-walled  $i_E$  to the actual  $i_{EL}$  of rectangular cofferdams

### Appendix D3

### Relation of double-walled cofferdam $i_E$ to the $i_{ES}$ of rectangular cofferdams



**Fig. D3.1** Relationship between double-walled  $i_E$  to the actual  $i_{ES}$  of rectangular cofferdams

## Appendix D4

### Relation of double-walled cofferdam $i_E$ to the $i_{EC}$ of rectangular cofferdams

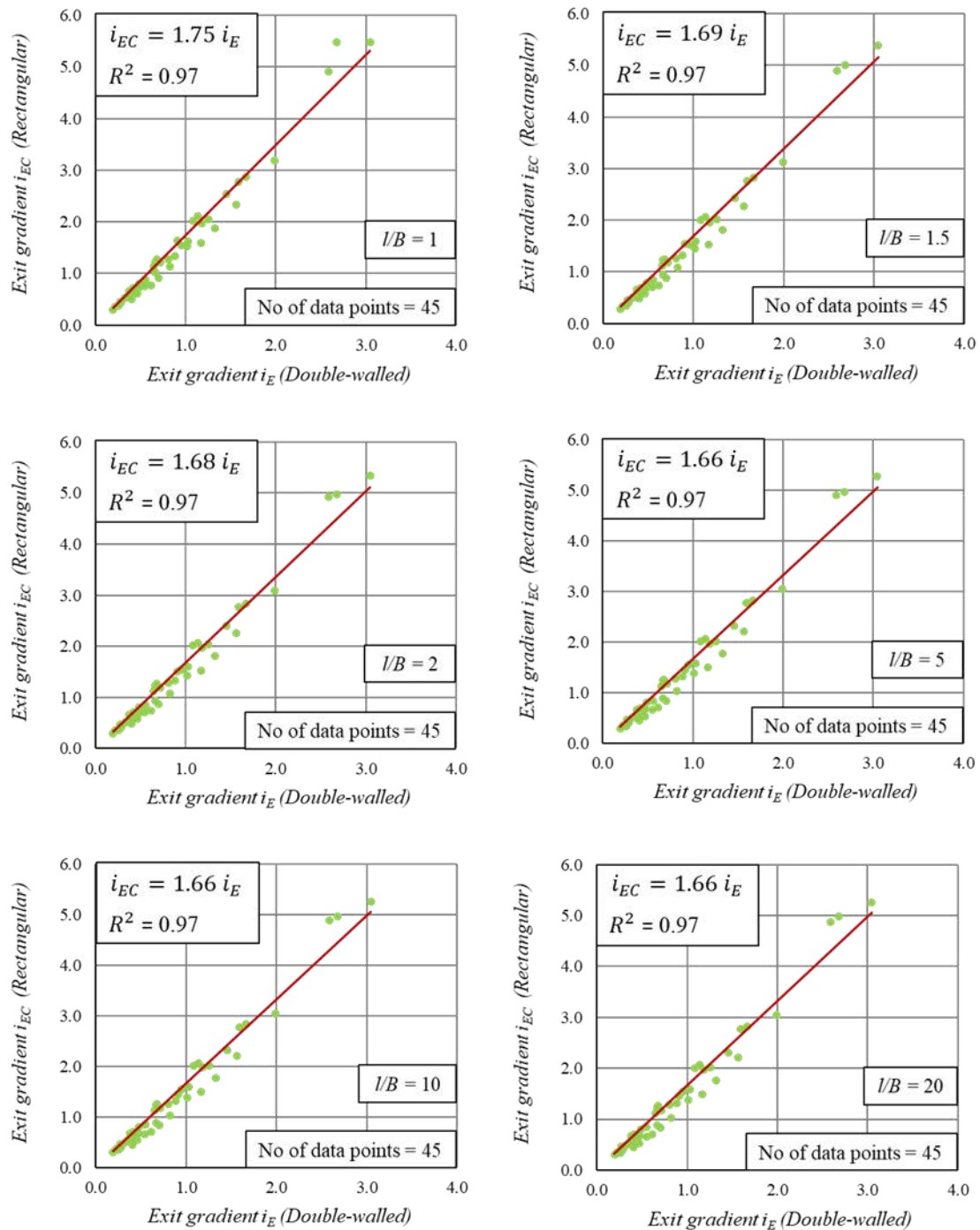


Fig. D4.1 Relationship between double-walled  $i_E$  to the actual  $i_{EC}$  of rectangular cofferdams